

REPORT DOCUMENTATION PAGE

1a. REPORT SECURITY CLASSIFICATION Unclassified			1b. RESTRICTIVE MARKINGS		
2a. SECURITY CLASSIFICATION AUTHORITY			3. DISTRIBUTION/AVAILABILITY OF REPORT Approved for distribution and unlimited public release		
2b. DECLASSIFICATION/DOWNGRADING SCHEDULE					
4. PERFORMING ORGANIZATION REPORT NUMBER(S) Report 6			5. MONITORING ORGANIZATION REPORT NUMBER(S)		
6a. NAME OF PERFORMING ORGANIZATION Dept. of Chemical Engineering University of Illinois		6b. OFFICE SYMBOL (If applicable)	7a. NAME OF MONITORING ORGANIZATION Office of Naval Research		
6c. ADDRESS (City, State and ZIP Code) 205 Roger Adams Lab 1209 W. California Street Urbana, Illinois 61801			7b. ADDRESS (City, State and ZIP Code) Arlington, Virginia 22217		
8a. NAME OF FUNDING/SPONSORING ORGANIZATION		8b. OFFICE SYMBOL (If applicable)	9. PROCUREMENT INSTRUMENT IDENTIFICATION NUMBER N00014-82-K-0324		
8c. ADDRESS (City, State and ZIP Code)			10. SOURCE OF FUNDING NOS.		
			PROGRAM ELEMENT NO.	PROJECT NO.	TASK NO.
			NR 657-728		
11. TITLE (Include Security Classification) Velocity Measurements for Turbulent Non- Flow Over Solid Walls -- Unclassified					
12. PERSONAL AUTHOR(S) Frederick, Kenneth A. and Thomas J. Hanratty, Project Supervisor					
13a. TYPE OF REPORT Progress		13b. TIME COVERED FROM 1982 TO 1985		14. DATE OF REPORT (Yr., Mo., Day) 1985, December 18	
				15. PAGE COUNT 264	
16. SUPPLEMENTARY NOTATION					
17. COSATI CODES			18. SUBJECT TERMS (Continue on reverse if necessary and identify by block number)		
FIELD	GROUP	SUB. GR.			
			turbulence, waves, laser-Doppler velocimetry		
19. ABSTRACT (Continue on reverse if necessary and identify by block number)					
See reverse side					
20. DISTRIBUTION/AVAILABILITY OF ABSTRACT UNCLASSIFIED/UNLIMITED <input type="checkbox"/> SAME AS RPT. <input type="checkbox"/> DTIC USERS <input type="checkbox"/>			21. ABSTRACT SECURITY CLASSIFICATION		
22a. NAME OF RESPONSIBLE INDIVIDUAL			22b. TELEPHONE NUMBER (Include Area Code)		22c. OFFICE SYMBOL

Velocity Measurements for Turbulent Nonseparated Flow Over Solid Waves

Laser-Doppler velocimetry measurements have been made of nonseparated velocity fields over solid sinusoidal wavy surfaces. Time-averaged velocity and turbulent intensity data are given.

The measurements were conducted over waves on the bottom wall of a rectangular channel with a cross section of twenty four by two inches, the two inch dimension being vertical. Two sets of velocity data were obtained at conditions corresponding to flows where linear and nonlinear shear stress responses are observed. The conditions were wave steepnesses $2a/\lambda$, and channel Reynolds numbers of 0.03125, 6400, and 0.05, 38,800 respectively. The wavelength of the waves was two inches.

The viscous wall region was of particular interest. Sufficient measurements were taken to give an accurate representation of both the streamwise and normal variations of the viscous wall region. The data was Fourier analyzed to determine the extent of nonlinearities, the wavelength averaged flowfields, and the amplitudes and phases of the velocity responses. The physical meaning of the data is interpreted in terms of pressure gradient effects along the wave surfaces. Comparisons of the data with predictions from simple eddy viscosity models are also given.

VELOCITY MEASUREMENTS FOR TURBULENT
NONSEPARATED FLOW OVER SOLID WAVES

PREPARED BY
KENNETH ARTHUR FREDERICK
THOMAS J. HANRATTY, PROJECT SUPERVISOR
FOR
THE OFFICE OF NAVAL RESEARCH, ARLINGTON, VA 22217
CONTRACT N00014-82-K-0324
PROJECT NR 657-728



REPORT 6,

DEPARTMENT OF CHEMICAL ENGINEERING
~~UNIVERSITY OF ILLINOIS~~ *University*
URBANA, ILLINOIS
61801

JUNE, 1986

APPROVED FOR PUBLIC RELEASE, DISTRIBUTION UNLIMITED

VELOCITY MEASUREMENTS FOR TURBULENT NONSEPARATED
FLOW OVER SOLID WAVES

Prepared by

Kenneth Arthur Frederick
Thomas J. Hanratty, Project Supervisor

for

The Office of Naval Research, Arlington, VA 22217
Contract N00014-82-K-0324
Project NR 657-728

Report 6

Department of Chemical Engineering
University of Illinois
Urbana, Illinois
61801

December, 1985

Approved for public release, distribution unlimited

TABLE OF CONTENTS

<u>Chapter</u>		<u>Page</u>
1	INTRODUCTION.....	1
2	LITERATURE REVIEW.....	6
3	THEORY.....	13
	I. Nonlinear Channel Analysis.....	13
	A. Governing Equations.....	13
	B. Numerical Solution.....	15
	II. Models for Turbulent Stresses.....	28
	A. Model C [*]	29
	B. Model D [*]	29
	III. Test of Channel Analysis.....	32
4	EXPERIMENTAL EQUIPMENT AND PROCEDURES.....	39
	I. Flow Loop and Test Section.....	39
	II. Modifications to Optical Traverse.....	43
	III. LDV System and Data Acquisition.....	49
5	EXPERIMENTAL RESULTS.....	55
	I. Flat Channel Data.....	55
	A. Friction Factors.....	55
	B. Mean Velocities.....	57
	C. Turbulent Intensities.....	57
	II. Flow Regime Map.....	60
	III. Results for Wave of Steepness $2a_d/\lambda = 0.03125$	62
	IV. Results for Wave of Steepness $2a_d/\lambda = 0.05$	73

<u>Chapter</u>		<u>Page</u>
6	DISCUSSION OF EXPERIMENTAL RESULTS AND COMPARISON WITH THEORY.....	95
	I. Wave of Steepness $2a_d/\lambda = 0.03125$	95
	A. Wall Stresses.....	95
	1. Surface Shear Stress.....	95
	2. Surface Pressure.....	99
	3. Drag.....	99
	B. Wavelength Averaged Mean Velocity.....	104
	C. Mean Velocity Profiles.....	107
	D. Mean Velocity Responses at Constant Heights above Wave.....	114
	E. Prediction of Surface Shear Stress Response from LDV Measurements.....	123
	F. Wave-Induced Velocity Perturbations.....	126
	G. Streamwise Intensities.....	134
	II. Wave of Steepness $2a_d/\lambda = 0.05$	142
	A. Wall Stresses.....	142
	1. Surface Shear Stress.....	142
	2. Surface Pressure.....	150
	3. Drag.....	150
	B. Wavelength Averaged Mean Velocity.....	150
	C. Mean Velocity Profiles.....	155
	D. Mean Velocity Responses at Constant Heights above Wave.....	161
	E. Wave-Induced Velocity Perturbations.....	168
7	SUMMARY AND CONCLUSIONS.....	176
	I. Goals and Approach.....	176
	II. Results.....	178
	NOMENCLATURE.....	187
	REFERENCES.....	191
	APPENDIX	
A	LISTING OF NONLINEAR CHANNEL COMPUTER PROGRAM.....	195
B	TABULATED FLAT CHANNEL INTENSITY MEASUREMENTS.....	227
C	TABULATED VELOCITY MEASUREMENTS OVER WAVES.....	229
D	COMPARISON OF LINEAR THEORY WITH VELOCITY MEASUREMENTS.....	260

LIST OF TABLES

<u>Table</u>		<u>Page</u>
3.1	Numerical Parameters and Vertical Resolution.....	21
3.2	Storage Requirements and Run Times.....	27
6.1	A Comparison of Surface Shear Stress Measurements with Predictions of Nonlinear Channel Analysis, $2a_d/\lambda = 0.03125$, $Re_b = 6400$, $2h_d/\lambda = 1.0$	98
6.2	Surface Pressure Results of Nonlinear Channel Analysis, $2a_d/\lambda = 0.03125$, $Re_b = 6400$, $2h_d/\lambda = 1.0$	101
6.3	Drag Coefficients, $2a_d/\lambda = 0.03125$, $Re_b = 6400$, $2h_d/\lambda = 1.0$	103
6.4	Predictions of First Harmonic of Surface Shear Stress Response, $2a_d/\lambda = 0.05$, $Re_b = 38,800$, $2h_d/\lambda = 1.0$	149
6.5	Surface Pressure Results of Nonlinear Channel Analysis, $2a_d/\lambda = 0.05$, $Re_b = 38,000$ $2h_d/\lambda = 1.0$	152
6.6	Drag Coefficients, $2a_d/\lambda = 0.05$, $Re_b = 38,800$, $2h_d/\lambda = 1.0$	153
B.1	Flat Channel Intensity Data, $Re_b = 11,000$	228
C.1	Time-Averaged Velocity*Data, $x_d/\lambda = 0.1$, $2a_d/\lambda = 0.03125$, $\alpha_d v/u^* = 0.008$	230
C.2	Time-Averaged Velocity*Data, $x_d/\lambda = 0.2$, $2a_d/\lambda = 0.03125$, $\alpha_d v/u^* = 0.008$	231
C.3	Time-Averaged Velocity*Data, $x_d/\lambda = 0.3$, $2a_d/\lambda = 0.03125$, $\alpha_d v/u^* = 0.008$	232
C.4	Time-Averaged Velocity*Data, $x_d/\lambda = 0.4$, $2a_d/\lambda = 0.03125$, $\alpha_d v/u^* = 0.008$	233
C.5	Time-Averaged Velocity*Data, $x_d/\lambda = 0.5$, $2a_d/\lambda = 0.03125$, $\alpha_d v/u^* = 0.008$	234
C.6	Time-Averaged Velocity*Data, $x_d/\lambda = 0.6$, $2a_d/\lambda = 0.03125$, $\alpha_d v/u^* = 0.008$	235

<u>Table</u>		<u>Page</u>
C.7	Time-Averaged Velocity Data, $x_d/\lambda = 0.7$, $2a_d/\lambda = 0.03125$, $\alpha_d v/u^* = 0.008$	236
C.8	Time-Averaged Velocity Data, $x_d/\lambda = 0.8$, $2a_d/\lambda = 0.03125$, $\alpha_d v/u^* = 0.008$	237
C.9	Time-Averaged Velocity Data, $x_d/\lambda = 0.9$, $2a_d/\lambda = 0.03125$, $\alpha_d v/u^* = 0.008$	238
C.10	Time-Averaged Velocity Data, $x_d/\lambda = 1.0$, $2a_d/\lambda = 0.03125$, $\alpha_d v/u^* = 0.008$	239
C.11	Intensity Data, $x_d/\lambda = 0.1$, $2a_d/\lambda = 0.03125$, $\alpha_d v/u^* = 0.008$	240
C.12	Intensity Data, $x_d/\lambda = 0.2$, $2a_d/\lambda = 0.03125$, $\alpha_d v/u^* = 0.008$	241
C.13	Intensity Data, $x_d/\lambda = 0.3$, $2a_d/\lambda = 0.03125$, $\alpha_d v/u^* = 0.008$	242
C.14	Intensity Data, $x_d/\lambda = 0.4$, $2a_d/\lambda = 0.03125$, $\alpha_d v/u^* = 0.008$	243
C.15	Intensity Data, $x_d/\lambda = 0.5$, $2a_d/\lambda = 0.03125$, $\alpha_d v/u^* = 0.008$	244
C.16	Intensity Data, $x_d/\lambda = 0.6$, $2a_d/\lambda = 0.03125$, $\alpha_d \lambda/u^* = 0.008$	245
C.17	Intensity Data, $x_d/\lambda = 0.7$, $2a_d/\lambda = 0.03125$, $\alpha_d \lambda/u^* = 0.008$	246
C.18	Intensity Data, $x_d/\lambda = 0.8$, $2a_d/\lambda = 0.03125$, $\alpha_d \lambda/u^* = 0.008$	247
C.19	Intensity Data, $x_d/\lambda = 0.9$, $2a_d/\lambda = 0.03125$, $\alpha_d v/u^* = 0.008$	248
C.20	Intensity Data, $x_d/\lambda = 1.0$, $2a_d/\lambda = 0.03125$, $\alpha_d v/u^* = 0.008$	249
C.21	Time-Averaged Velocity Data, $x_d/\lambda = 0.1$, $2a_d/\lambda = 0.050$, $\alpha_d v/u^* = 0.00165$	250
C.22	Time-Averaged Velocity Data, $x_d/\lambda = 0.2$, $2a_d/\lambda = 0.050$, $\alpha_d v/u^* = 0.00165$	251
C.23	Time-Averaged Velocity Data, $x_d/\lambda = 0.3$, $2a_d/\lambda = 0.050$, $\alpha_d v/u^* = 0.00165$	252

<u>Table</u>		<u>Page</u>
C.24	Time-Averaged Velocity Data, $x_d/\lambda = 0.4$, $2a_d/\lambda = 0.050$, $\alpha_d v/u^* = 0.00165$	253
C.25	Time-Averaged Velocity Data, $x_d/\lambda = 0.5$, $2a_d/\lambda = 0.050$, $\alpha_d v/u^* = 0.00165$	254
C.26	Time-Averaged Velocity Data, $x_d/\lambda = 0.6$, $2a_d/\lambda = 0.050$, $\alpha_d v/u^* = 0.00165$	255
C.27	Time-Averaged Velocity Data, $x_d/\lambda = 0.7$, $2a_d/\lambda = 0.050$, $\alpha_d v/u^* = 0.00165$	256
C.28	Time-Averaged Velocity Data, $x_d/\lambda = 0.8$, $2a_d/\lambda = 0.050$, $\alpha_d v/u^* = 0.00165$	257
C.29	Time-Averaged Velocity Data, $x_d/\lambda = 0.9$, $2a_d/\lambda = 0.050$, $\alpha_d v/u^* = 0.00165$	258
C.30	Time-Averaged Velocity Data, $x_d/\lambda = 1.0$, $2a_d/\lambda = 0.050$, $\alpha_d v/u^* = 0.00165$	259

LIST OF FIGURES

<u>Figure</u>		<u>Page</u>
2.1	Flow Regime Map for Two-Dimensional Solid Sinusoidal Waves.....	7
3.1	Physical and Transformed Regions.....	16
3.2	Stretched Coordinate System in Physical Domain, $2a_d/\lambda = 0.05$, $b = 5$, 9×81 Mesh.....	20
3.3	Discrete Flat Channel Profile, $Re_b = 6400$, $b = 5$, 81 Vertical Points.....	23
3.4	Discrete Flat Channel Profile, $Re_b = 38,800$, $b = 15$, 151 Vertical Points.....	24
3.5	Methods of Evaluating y'_d in Cess Profile, equation (3.31) (Wave Amplitude Exaggerated).....	30
3.6	Cess Eddy Viscosity Profile (Flat Channel), $Re_b = 6400$, $\kappa = 0.48$, $A = 33$	31
3.7	Surface Shear Stress Amplitude, Comparison of Boundary Layer and Channel Analyses for Small Amplitude Waves, Model D^* ($k_1 = -35$, $k_L = 1800$).....	34
3.8	Phase Angle of Surface Shear Stress, Comparison of Boundary Layer and Channel Analyses for Small Amplitude Waves, Model D^* ($k_1 = -35$, $k_L = 1800$).....	35
3.9	Surface Pressure Amplitude, Comparison of Boundary Layer and Channel Analyses for Small Amplitude Waves, Model D^* ($k_1 = -35$, $k_L = 1800$).....	36
3.10	Phase Angle of Surface Pressure, Comparison of Boundary Layer and Channel Analyses for Small Amplitude Waves, Model D^* ($k_1 = -35$, $k_L = 1800$).....	37
4.1	Schematic of Flow Loop.....	41
4.2	Optical Traversing Mechanism.....	44
4.3	Detail of Lower Lead Screw Shaft Assembly.....	46
4.4	Top View of Mechanical Connection Between Lead Screw Shafts.....	47

<u>Figure</u>		<u>Page</u>
5.15	Streamwise Intensity Measurements, $x_d/\lambda = 0.1$, $2a_d/\lambda = 0.03125$, $Re_b = 6400$, $2h_d/\lambda = 1.0$	74
5.16	Streamwise Intensity Measurements, $x_d/\lambda = 0.2$, $2a_d/\lambda = 0.03125$, $Re_b = 6400$, $2h_d/\lambda = 1.0$	75
5.17	Streamwise Intensity Measurements, $x_d/\lambda = 0.3$, $2a_d/\lambda = 0.03125$, $Re_b = 6400$, $2h_d/\lambda = 1.0$	76
5.18	Streamwise Intensity Measurements, $x_d/\lambda = 0.4$, $2a_d/\lambda = 0.03125$, $Re_b = 6400$, $2h_d/\lambda = 1.0$	77
5.19	Streamwise Intensity Measurements, $x_d/\lambda = 0.5$, $2a_d/\lambda = 0.03125$, $Re_b = 6400$, $2h_d/\lambda = 1.0$	78
5.20	Streamwise Intensity Measurements, $x_d/\lambda = 0.6$, $2a_d/\lambda = 0.03125$, $Re_b = 6400$, $2h_d/\lambda = 1.0$	79
5.21	Streamwise Intensity Measurements, $x_d/\lambda = 0.7$, $2a_d/\lambda = 0.03125$, $Re_b = 6400$, $2h_d/\lambda = 1.0$	80
5.22	Streamwise Intensity Measurements, $x_d/\lambda = 0.8$, $2a_d/\lambda = 0.03125$, $Re_b = 6400$, $2h_d/\lambda = 1.0$	81
5.23	Streamwise Intensity Measurements, $x_d/\lambda = 0.9$, $2a_d/\lambda = 0.03125$, $Re_b = 6400$, $2h_d/\lambda = 1.0$	82
5.24	Streamwise Intensity Measurements, $x_d/\lambda = 1.0$, $2a_d/\lambda = 0.03125$, $Re_b = 6400$, $2h_d/\lambda = 1.0$	83
5.25	Mean Velocity Measurements, $x_d/\lambda = 0.1$, $2a_d/\lambda = 0.05$, $Re_b = 38,800$, $2h_d/\lambda = 1.0$	84
5.26	Mean Velocity Measurements, $x_d/\lambda = 0.2$, $2a_d/\lambda = 0.05$, $Re_b = 38,800$, $2h_d/\lambda = 1.0$	85
5.27	Mean Velocity Measurements, $x_d/\lambda = 0.3$, $2a_d/\lambda = 0.05$, $Re_b = 38,800$, $2h_d/\lambda = 1.0$	86
5.28	Mean Velocity Measurements, $x_d/\lambda = 0.4$, $2a_d/\lambda = 0.05$, $Re_b = 38,800$, $2h_d/\lambda = 1.0$	87
5.29	Mean Velocity Measurements, $x_d/\lambda = 0.5$, $2a_d/\lambda = 0.05$, $Re_b = 38,800$, $2h_d/\lambda = 1.0$	88
5.30	Mean Velocity Measurements, $x_d/\lambda = 0.6$, $2a_d/\lambda = 0.05$, $Re_b = 38,800$, $2h_d/\lambda = 1.0$	89
5.31	Mean Velocity Measurements, $x_d/\lambda = 0.7$, $2a_d/\lambda = 0.05$, $Re_b = 38,800$, $2h_d/\lambda = 1.0$	90
5.32	Mean Velocity Measurements, $x_d/\lambda = 0.8$, $2a_d/\lambda = 0.05$, $Re_b = 38,800$, $2h_d/\lambda = 1.0$	91

<u>Figure</u>		<u>Page</u>
4.5	Side View of Lead Screw Shaft Crank Assembly.....	48
4.6	Top View of Horizontal Traversing Mechanism.....	50
4.7	Laser-Doppler Velocimeter System.....	52
4.8	Schematic of Receiving Optics.....	53
5.1	Fanning Friction Factor for Flat Channel.....	56
5.2	Comparison of Flat Channel Velocity Data of Thorsness with Cess Profile.....	58
5.3	Flat Channel Streamwise Intensity Profile, $Re_b = 11,000$	59
5.4	Location of LDV Data on Flow Regime Map.....	61
5.5	Mean Velocity Measurements, $x_d/\lambda = 0.1$, $2a_d/\lambda = 0.03125$, $Re_b = 6400$, $2h_d/\lambda = 1.0$	63
5.6	Mean Velocity Measurements, $x_d/\lambda = 0.2$, $2a_d/\lambda = 0.03125$, $Re_b = 6400$, $2h_d/\lambda = 1.0$	64
5.7	Mean Velocity Measurements, $x_d/\lambda = 0.3$, $2a_d/\lambda = 0.03125$, $Re_b = 6400$, $2h_d/\lambda = 1.0$	65
5.8	Mean Velocity Measurements, $x_d/\lambda = 0.4$, $2a_d/\lambda = 0.03125$, $Re_b = 6400$, $2h_d/\lambda = 1.0$	66
5.9	Mean Velocity Measurements, $x_d/\lambda = 0.5$, $2a_d/\lambda = 0.03125$, $Re_b = 6400$, $2h_d/\lambda = 1.0$	67
5.10	Mean Velocity Measurements, $x_d/\lambda = 0.6$, $2a_d/\lambda = 0.03125$, $Re_b = 6400$, $2h_d/\lambda = 1.0$	68
5.11	Mean Velocity Measurements, $x_d/\lambda = 0.7$, $2a_d/\lambda = 0.03125$, $Re_b = 6400$, $2h_d/\lambda = 1.0$	69
5.12	Mean Velocity Measurements, $x_d/\lambda = 0.8$, $2a_d/\lambda = 0.03125$, $Re_b = 6400$, $2h_d/\lambda = 1.0$	70
5.13	Mean Velocity Measurements, $x_d/\lambda = 0.9$, $2a_d/\lambda = 0.03125$, $Re_b = 6400$, $2h_d/\lambda = 1.0$	71
5.14	Mean Velocity Measurements, $x_d/\lambda = 1.0$, $2a_d/\lambda = 0.03125$, $Re_b = 6400$, $2h_d/\lambda = 1.0$	72

<u>Figure</u>		<u>Page</u>
5.33	Mean Velocity Measurements, $x_d/\lambda = 0.9$, $2a_d/\lambda = 0.05$, $Re_b = 38,800$, $2h_d/\lambda = 1.0$	92
5.34	Mean Velocity Measurements, $x_d/\lambda = 1.0$, $2a_d/\lambda = 0.05$, $Re_b = 38,000$, $2h_d/\lambda = 1.0$	93
6.1	Shear Stress Response, $2a_d/\lambda = 0.3125$, $Re_b = 6400$, $2h_d/\lambda = 1.0$	96
6.2	Calculated Pressure Response, $2a_d/\lambda = 0.03125$, $Re_b = 6400$, $2h_d/\lambda = 1.0$	100
6.3	Wavelength Averaged Velocity Profiles, $2a_d/\lambda = 0.03125$, $Re_b = 6400$, $2h_d/\lambda = 1.0$	105
6.4	Typical Velocity Profile Used to Construct Wavelength Averaged Profile Along Cartesian Coordinates, $x_d/\lambda = 0.2$ (amplitude exaggerated).....	106
6.5	Typical Velocity Profile Used to Construct Wavelength Averaged Profile Along Curvilinear Coordinates, $\epsilon = \pi/4$ (amplitude exaggerated).....	108
6.6	Comparison of Mean Velocity Measurements with Channel Calculations, $x_d/\lambda = 0.5, 1.0$, $2a_d/\lambda = 0.03125$, $Re_b = 6400$, $2h_d/\lambda = 1.0$	109
6.7	Comparison of Mean Velocity Measurements with Channel Calculations, $x_d/\lambda = 0.4, 0.9$, $2a_d/\lambda = 0.03125$, $Re_b = 6400$, $2h_d/\lambda = 1.0$	110
6.8	Comparison of Mean Velocity Measurements with Channel Calculations, $x_d/\lambda = 0.3, 0.8$, $2a_d/\lambda = 0.03125$, $Re_b = 6400$, $2h_d/\lambda = 1.0$	111
6.9	Comparison of Mean Velocity Measurements with Channel Calculations, $x_d/\lambda = 0.2, 0.7$, $2a_d/\lambda = 0.03125$, $Re_b = 6400$, $2h_d/\lambda = 1.0$	112
6.10	Comparison of Mean Velocity Measurements with Channel Calculations, $x_d/\lambda = 0.1, 0.6$, $2a_d/\lambda = 0.03125$, $Re_b = 6400$, $2h_d/\lambda = 1.0$	113
6.11	Mean Velocity Responses at Constant Heights above Wave Surface, $2a_d/\lambda = 0.0312$, $Re_b = 6400$, $2h_d/\lambda = 1.0$	115
6.12	Velocity Amplitude Ratio of Second to First Harmonics, $2a_d/\lambda = 0.03125$, $Re_b = 6400$, $2h_d/\lambda = 1.0$	116

<u>Figure</u>		<u>Page</u>
6.13	Amplitudes of First and Second Harmonics of Velocity Response, $2a_d/\lambda = 0.03125$, $Re_b = 6400$, $2h_d/\lambda = 1.0$	117
6.14	Velocity Response at $y_d u^*/\nu = 9$, $2a_d/\lambda = 0.03125$, $Re_b = 6400$, $2h_d/\lambda = 1.0$	119
6.15	Velocity Response at $y_d u^*/\nu = 40$, $2a_d/\lambda = 0.03125$, $Re_b = 6400$, $2h_d/\lambda = 1.0$	120
6.16	Phase Angle of First Harmonic of Velocity Response, $2a_d/\lambda = 0.03125$, $Re_b = 6400$, $2h_d/\lambda = 1.0$	122
6.17	Comparison of Shear Stress Amplitude from Electrochemical and Extrapolated Velocity Measurements, $2a_d/\lambda = 0.03125$, $Re_b = 6400$, $2h_d/\lambda = 1.0$	124
6.18	Near Wall Region at $x_d/\lambda = 0.3$, $2a_d/\lambda = 0.03125$, $Re_b = 6400$, $2h_d/\lambda = 1.0$	125
6.19	Linear Extrapolation to Wall of Phase Angle of First Harmonic of Velocity Response, $2a_d/\lambda = 0.03125$, $Re_b = 6400$, $2h_d/\lambda = 1.0$	127
6.20	Wave-Induced Velocity Perturbations, $x_d/\lambda = 0.5, 1.0$, $2a_d/\lambda = 0.03125$, $Re_b = 6400$, $2h_d/\lambda = 1.0$	128
6.21	Wave-Induced Velocity Perturbations, $x_d/\lambda = 0.4, 0.9$, $2a_d/\lambda = 0.03125$, $Re_b = 6400$, $2h_d/\lambda = 1.0$	129
6.22	Wave-Induced Velocity Perturbations, $x_d/\lambda = 0.3, 0.8$, $2a_d/\lambda = 0.03125$, $Re_b = 6400$, $2h_d/\lambda = 1.0$	130
6.23	Wave-Induced Velocity Perturbations, $x_d/\lambda = 0.2, 0.7$, $2a_d/\lambda = 0.03125$, $Re_b = 6400$, $2h_d/\lambda = 1.0$	131
6.24	Wave-Induced Velocity Perturbations, $x_d/\lambda = 0.1, 0.6$, $2a_d/\lambda = 0.03125$, $Re_b = 6400$, $2h_d/\lambda = 1.0$	132
6.25	Comparison of Wavelength Averaged Intensity Profile with Flat Surface Intensity Profile.....	135
6.26	Envelope of Perturbations about Wavelength Averaged Intensity, $2a_d/\lambda = 0.03125$, $Re_b = 6400$, $2h_d/\lambda = 1.0$	137
6.27	Locus of Maximum Intensities, $2a_d/\lambda = 0.03125$, $Re_b = 6400$, $2h_d/\lambda = 1.0$	140

<u>Figure</u>		<u>Page</u>
6.28	Intensity Amplitude Ratio of Second to First Harmonics, $2a_d/\lambda = 0.03125$, $Re_b = 6400$, $2h_d/\lambda = 1.0$	141
6.29	Amplitudes of First and Second Harmonics of Intensity Response, $2a_d/\lambda = 0.03125$, $Re_b = 6400$, $2h_d/\lambda = 1.0$	143
6.30	Intensity Response at $y_d u^*/\nu = 24$, $2a_d/\lambda = 0.03125$, $Re_b = 6400$, $2h_d/\lambda = 1.0$	144
6.31	Intensity Response at $y_d u^*/\nu = 60$, $2a_d/\lambda = 0.03125$, $Re_b = 6400$, $2h_d/\lambda = 1.0$	145
6.32	Phase Angle of First Harmonic of Intensity Response, $2a_d/\lambda = 0.03125$, $Re_b = 6400$, $2h_d/\lambda = 1.0$	146
6.33	Calculated Surface Shear Stress Response, $2a_d/\lambda = 0.05$, $Re_b = 38,800$, $2h_d/\lambda = 1.0$	148
6.34	Calculated Pressure Response, $2a_d/\lambda = 0.05$, $Re_b = 38,800$, $2h_d/\lambda = 1.0$	151
6.35	Wavelength Averaged Velocity Profiles, $2a_d/\lambda = 0.05$, $Re_b = 38,800$, $2h_d/\lambda = 1.0$	154
6.36	Comparison of Mean Velocity Measurements with Channel Calculations, $x_d/\lambda = 0.5, 1.0$, $2a_d/\lambda = 0.05$, $Re_b = 38,800$, $2h_d/\lambda = 1.0$	156
6.37	Comparison of Mean Velocity Measurements with Channel Calculations, $x_d/\lambda = 0.4, 0.9$, $2a_d/\lambda = 0.05$, $Re_b = 38,800$, $2h_d/\lambda = 1.0$	157
6.38	Comparison of Mean Velocity Measurements with Channel Calculations, $x_d/\lambda = 0.3, 0.8$, $2a_d/\lambda = 0.05$, $Re_b = 38,800$, $2h_d/\lambda = 1.0$	158
6.39	Comparison of Mean Velocity Measurements with Channel Calculations, $x_d/\lambda = 0.2, 0.7$, $2a_d/\lambda = 0.05$, $Re_b = 38,800$, $2h_d/\lambda = 1.0$	159
6.40	Comparison of Mean Velocity Measurements with Channel Calculations, $x_d/\lambda = 0.1, 0.6$, $2a_d/\lambda = 0.05$, $Re_b = 38,800$, $2h_d/\lambda = 1.0$	160
6.41	Mean Velocity Responses at Constant Heights above Wave Surface, $2a_d/\lambda = 0.05$, $Re_b = 38,800$, $2h_d/\lambda = 1.0$	162
6.42	Velocity Amplitude Ratio of Second to First Harmonics, $2a_d/\lambda = 0.05$, $Re_b = 38,800$, $2h_d/\lambda = 1.0$	163

Figure		Page
6.43	Amplitude of First and Second Harmonics of Velocity Response, $2a_d/\lambda = 0.05$, $Re_b = 38,800$, $2h_d/\lambda = 1.0$	164
6.44	Velocity Response at $y_d u^*/\nu = 26$, $2a_d/\lambda = 0.05$, $Re_b = 38,800$, $2h_d/\lambda = 1.0$	165
6.45	Velocity Response at $y_d u^* = 100$, $2a_d/\lambda = 0.05$, $Re_b = 38,800$, $2h_d/\lambda = 1.0$	166
6.46	Phase Angle of First Harmonic of Velocity Response, $2a_d/\lambda = 0.05$, $Re_b = 38,800$, $2h_d/\lambda = 1.0$	169
6.47	Wave-Induced Velocity Perturbations, $x_d/\lambda = 0.5, 1.0$, $2a_d/\lambda = 0.05$, $Re_b = 38,800$, $2h_d/\lambda = 1.0$	171
6.48	Wave-Induced Velocity Perturbations, $x_d/\lambda = 0.4, 0.9$, $2a_d/\lambda = 0.05$, $Re_b = 38,800$, $2h_d/\lambda = 1.0$	172
6.49	Wave-Induced Velocity Perturbations, $x_d/\lambda = 0.3, 0.8$, $2a_d/\lambda = 0.05$, $Re_b = 38,800$, $2h_d/\lambda = 1.0$	173
6.50	Wave-Induced Velocity Perturbations, $x_d/\lambda = 0.2, 0.7$, $2a_d/\lambda = 0.05$, $Re_b = 38,800$, $2h_d/\lambda = 1.0$	174
6.51	Wave-Induced Velocity Perturbations, $x_d/\lambda = 0.1, 0.6$, $2a_d/\lambda = 0.05$, $Re_b = 38,800$, $2h_d/\lambda = 1.0$	175
D.1	Comparison of Linear Theory with Measurements, $ \hat{u}_d _1$ ($2a_d/\lambda = 0.03125$, $\alpha_d \nu/u^* = 0.008$).....	261
D.2	Comparison of Linear Theory with Measurements, $\theta_{\hat{u},1}$ ($2a_d/\lambda = 0.03125$, $\alpha_d \nu/u^* = 0.008$).....	262
D.3	Comparison of Linear Theory with Measurements, $ \hat{u}_d _1$ ($2a_d/\lambda = 0.05$, $\alpha_d \nu/u^* = 0.00165$).....	263
D.4	Comparison of Linear Theory with Measurements, $\theta_{\hat{u},1}$ ($2a_d/\lambda = 0.05$, $\alpha_d \nu/u^* = 0.00165$).....	264

CHAPTER 1

INTRODUCTION

When a turbulent fluid interacts with a wave spatial variations occur in the surface stresses and the velocity field. These variations affect the transport of heat, mass, and momentum at the interfacial boundary. The prediction of the flowfield over a wave is important to the understanding of many natural and industrial processes.

The pressure distribution along a wave surface is of major interest in the problem of wave generation on large bodies of water and in determining when atomization occurs in two phase flows. Shear stress variations play an important role in sediment transport in rivers and in describing interfacial instabilities on thin liquid films. A knowledge of the surface stresses along a wave is also critical in predicting the motion of desert sand dunes and the dissolution patterns found in underwater caverns and melting ice.

Previous investigations in this laboratory by Cook [17], Morrisroe [33], Zilker [48], Thorsness [44], and Abrams [2] have concentrated on the measurement of the pressure and shear stress along a solid sinusoidal wave. Experiments were performed with waves having height to wavelength ratios of $2a_d/\lambda = 0.0125, 0.03125, 0.05, 0.125, 0.200$ and with a range of flowrates so that $0.0058 < \alpha_d u^*/\nu < 0.01$ where α_d is the wavenumber. It was found that for $2a_d/\lambda < 0.033$ and $a_d u^*/\nu < 27$ the shear stress is perturbed linearly with wave amplitude. That is, the responses can be described by single harmonics with characteristic amplitudes and phases. For $a_d u^*/\nu > 27$ shear stress responses are nonlinear since the profiles become distorted and

can no longer be described by single harmonics. Pressure responses were observed to be linear for all nonseparated flows. Separation can occur for waves with $2a_d/\lambda > 0.033$ and the size of the reversed flow region increases with increasing $2a_d/\lambda$ and with increasing $\alpha_d v/u^*$. The reversed flow region with $2a_d/\lambda = 0.05$ waves is very thin and was observed to disappear approximately at the value of $\alpha_d v/u^*$ predicted by the solution of the linear momentum equations.

The above observations are consistent with pressure and shear stress measurements conducted over waves in other laboratories. Additional pressure measurements were performed by Stanton et al [43], Motzfeld [34], Larras and Claria [27], Zagustin [47], Kendall [24], Sigal [41], Beebe [8], Cary et al. [12] and Lin et al. [30] and other shear stress data were obtained by Kendall [24], Sigal [41], and Beebe [8].

Considerable progress has been made in the modelling of the pressure and shear stress distributions along waves that have small enough amplitudes to produce a linear response. The analysis for this case is greatly simplified since the momentum equations can be linearized. The critical issue is the specification of the wave induced Reynolds stresses. The best model to date is the eddy viscosity Model D^{*} developed by Thorsness [44] and Abrams [2]. This model uses the mixing length hypothesis of Lyod, Moffat, and Kays [31]. The effects of pressure gradient and relaxation are taken into account by an empirical method that uses one lag constant. Model D^{*} provides a good prediction of the pressure and shear stress over a wide range of dimensionless wavenumbers, $\alpha_d v/u^*$.

Measurements of the velocity field over a wave are not as numerous and detailed as those of surface stresses. Motzfeld [34], Kendall [24], Hsu and Kennedy [20], Sigal [41], and Zilker [48] investigated the flowfield above waves under nonseparated flow conditions. Separated flow over waves has been studied by Beebe [8], Zilker [48], Buckles [10], and Kuzan [25]. Only the separated flow studies of Buckles and Kuzan involved sufficient measurements to give an accurate representation of the spatial variation of the flowfield and measured close enough to the wave surface to detect wave-induced perturbations within the lower viscous wall region.

The primary purpose of this thesis is to extend the previous experimental studies by obtaining detailed measurements of the velocity field above waves with nonseparated flows. Of particular interest are measurements within the viscous wall region which can be used as a test of the turbulence models of Thorsness [44] and Abrams [2]. Previous tests of these models have been limited to comparisons with surface stress data. Two sets of velocity measurements were obtained at conditions corresponding to flows where linear and nonlinear shear stress responses are observed. The conditions are $2a_d/\lambda = 0.03125$, $\alpha_d v/u^* = 0.008$, $a_d u^*/v = 12.3$ and $2a_d/\lambda = 0.05$, $\alpha_d v/u^* = 0.00165$, $a_d u^*/v = 95.2$ respectively.

The measurements were made in a water channel with a rectangular cross section of 2.0 in. \times 24.0 in. The overall channel length was about thirty-five feet, with the last five feet at the downstream end being the test section. The bottom surface of this section was removable and had wave profiles of wavelength two inches machined

across it. Tests were conducted over the eighth wave in a series of ten waves. The velocity data consisted of time-averaged and turbulent intensity profiles in the streamwise direction.

Detailed measurements of the viscous wall region were made with the laser-Doppler velocimeter (LDV) techniques developed by Buckles [10]. The technique of obtaining velocities with LDV has several advantages over the classical hot film and hot wire methods which were used by Kendall [24], Sigal [41], Beebe [8], and Zilker [48]. A LDV requires no calibration, does not disturb the flow with a physical probe, can detect momentary flow reversals, and can operate in highly turbulent flows. The key feature of the LDV used in this study is an optics system containing two beam expanders. The beam expanders provided a small enough measurement volume to perform velocity measurements as close to the wave surface as $y_d u^* / \nu$, equal to two and ten at the dimensionless wave-numbers, $\alpha_d \nu / u^*$, of 0.008 and 0.00165 respectively. Fifteen to twenty data points were taken vertically within the viscous wall region. Good spatial resolution in the horizontal direction was achieved by conducting velocity measurements every tenth of a wavelength.

The velocity measurements were obtained over finite amplitude waves where the application of linear theory is uncertain. Therefore a nonlinear computer code was developed to predict the flow-field above finite amplitude waves. The code solves the nonlinear Reynolds-averaged Navier-Stokes equations using spectral methods in the flow direction and finite differences in the normal

direction. The code is a modification of the boundary layer program of McLean [32] to the flow geometry of waves on the lower wall of a rectangular channel. Previous linear and nonlinear wavy surface codes developed in this laboratory [1, 2, 45] have been limited to the prediction of boundary layer flows.

A comparison of the velocity measurements with linear and non-linear calculations using the turbulence models of Thorsness [44] and Abrams [2] provides considerable physical insight into the nature of nonseparated flow over a wave surface.

CHAPTER 2

LITERATURE REVIEW

This chapter reviews the literature on velocity measurements over solid and rigid two-dimensional sinusoidal wavy surfaces. The discussion, which is facilitated by using the flow regime map of Abrams, Frederick and Hanratty [3], is presented in the chronological order in which the measurements were made.

The flow regime map is shown in Figure 2.1. The vertical axis, $2a_d/\lambda$, is the wave steepness and the horizontal axis is the wave-number, $2\pi/\lambda$, made dimensionless with respect to wall parameters. The wall parameters are the friction velocity, $u^* = \sqrt{\tau_w/\rho}$, and the kinematic viscosity, ν , of the fluid. The observed behavior for flow over solid sinusoidal waves can be divided into three regions: a region where the flows are separated, a nonseparated region where the shear stress response is linear, and a nonseparated region where the shear stress response is nonlinear. Velocity measurements have been obtained in all three regions.

The first velocity measurements over a wavy surface were conducted by Motzfeld [34]. A pitot tube was used in a low-speed wind tunnel to obtain mean streamwise velocity profiles above two sinusoidal waveforms containing six waves with $\lambda = 300$ mm and values of $2a_d/\lambda$ equal to 0.05 and 0.100 respectively. Profiles were taken at several x_d/λ positions and strong deviations from the flat plate profile were observed. The major limitation of this study was that measurements close to the wave surface could not be obtained with the pitot tube technique. From Figure 2.1 it is seen that both sets of measurements were obtained for nonlinear nonseparated flows.

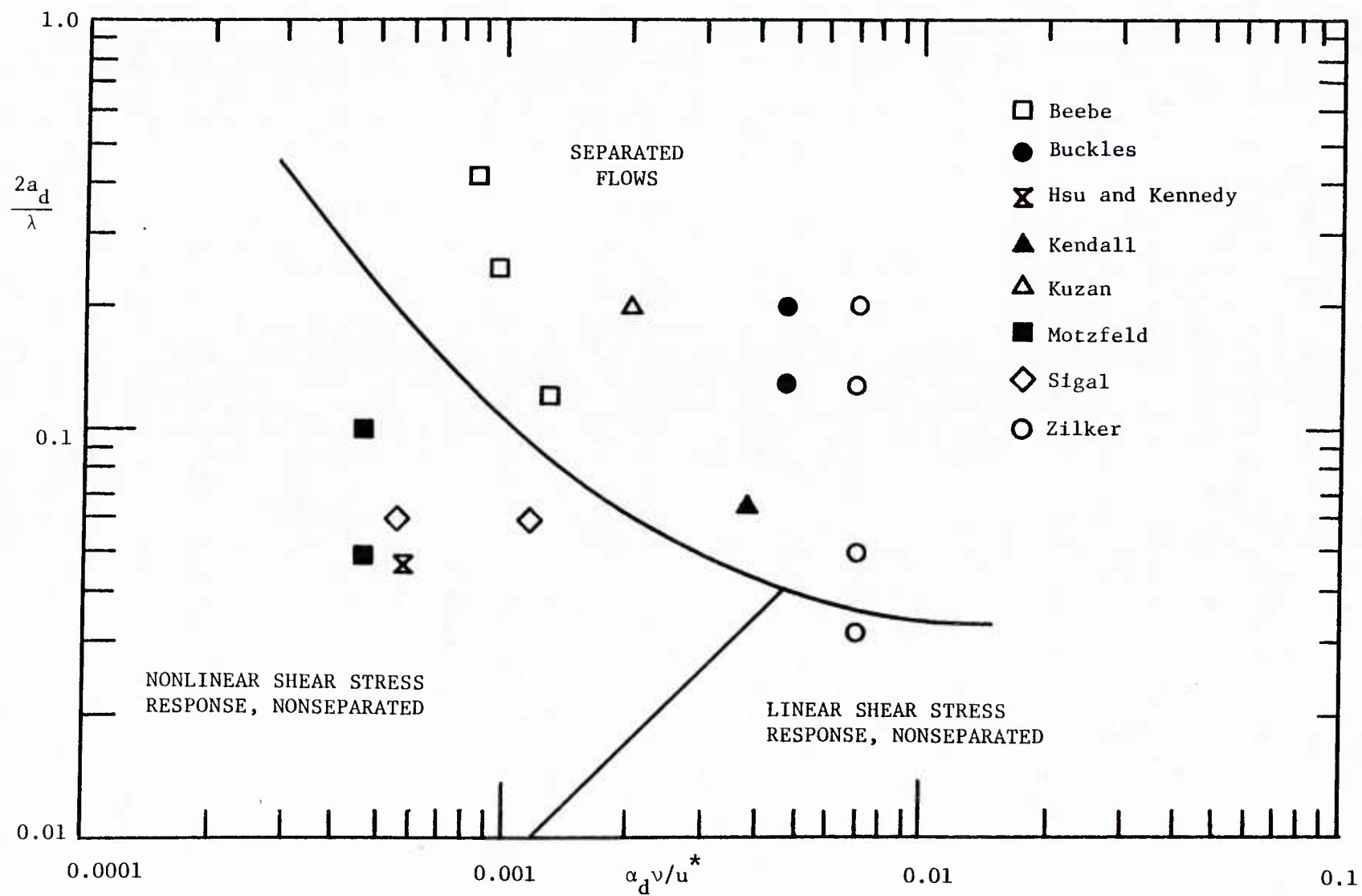


Figure 2.1 Flow Regime Map for Two-Dimensional Solid Sinusoidal Waves

Kendall [24] used hot wire probes to measure the velocity field above a smooth wavy neoprene rubber sheet that comprised a portion of the bottom floor of a low turbulence wind tunnel. The sheet was mechanically deformed into twelve sinusoidal waves which could progress upwind or downwind at a controlled speed. The wavelength of the waves was four inches and the steepness, $2a_d/\lambda$, was equal to 0.0625. Only one set of average velocity measurements was reported at zero wave speed. Two streamwise velocity profiles were obtained at the limits of excursion of the cyclic velocity perturbation about the wavelength averaged flowfield. The maximum and minimum perturbations occurred at $x_d/\lambda = 0.96$ and $x_d/\lambda = 0.35$ respectively. Figure 2.1 shows that these data are located in the separated flow regime. However, no reversed flows were observed even at the closest measurement point of $y_d u^*/\nu = 12.4$. This is consistent with the flow visualization experiments of Zilker [48] which indicate that the separated region is extremely thin for the wave steepness and flowrate used by Kendall.

Hsu and Kennedy [20] studied turbulent air flow in wavy pipes. The wavy pipes had an average diameter of 0.408 ft. and were constructed by forming fiberglass onto wooden mandrels. Hot wire probes were used to investigate the flowfield over waves with steepnesses, $2a_d/\lambda$, equal to 0.0222 and 0.0444 and wavelengths of 1.67 ft. and 0.83 ft. respectively. A constant Reynolds number of 1.13×10^5 based on the average pipe diameter was maintained in the experiments.

Longitudinal components of the mean and turbulent velocities were measured with a single-wire probe. Tangential and radial

components, as well as Reynolds stresses, were obtained with a cross-wire probe. Profiles were taken at 1/8th wavelength increments in the flow direction. Each profile consisted of only about ten velocity measurements. The closest measurement to the wavy surface was at approximately y_+^* , equal to 120. It was observed that the mean velocity profiles at positions symmetrical about the location of minimum (or maximum) diameter are nearly identical. Turbulent intensities remained constant along the pipe within a central core covering about sixty percent of the radius. The data of Hsu and Kennedy is located in the nonlinear shear stress response region of Figure 2.1.

Sigal [41] made velocity measurements over two geometrically similar wavy surfaces in a turbulent boundary layer of a low-speed wind tunnel. The waves were constructed of smooth aluminum sheeting deformed to a sinusoidal shape. The two wavy sheets each contained five waves of steepness, $2a_d/\lambda$, equal to 0.055 and had wavelengths of six and twelve inches respectively. Measurements of the average and fluctuating velocities parallel to the wave surface were obtained with a single sensor hot wire probe. In addition, average and fluctuating velocities in the streamwise and normal directions as well as Reynolds stresses were obtained with an x-array hot wire probe. The closest measurements to the wave surface were at about y_+^* equal to ten.

Profiles were taken at only four positions along each wave surface above the locations where

- 1) C'_p is a minimum,
- 2) C'_p equals zero and the pressure gradient is negative,
- 3) C'_p is a maximum,
- and 4) C'_p equals zero and the pressure gradient is positive,

where C'_p is the local wall pressure coefficient. The four locations correspond to x_d/λ positions of approximately 0.0, 0.25, 0.50, and 0.75 respectively. Figure 2.1 shows the location of Sigal's data in the nonlinear shear stress response region of the flow regime map.

Velocity profiles at the crests and troughs showed strong positive and negative perturbations respectively about the flat plate profile. These disturbances extended to several thousand y -plus units, $y_d^+ u^*/\nu$, above the wave surface. In contrast, the profiles corresponding to C'_p equal to zero showed smaller perturbations that became negligible at about y -plus equal to 300. For both pairs of profiles the positive and negative deviations are approximately equal in magnitude. The wavelength average profiles are in close agreement with the flat plate profile. Strong streamwise variations in the turbulent intensities were also noted.

Beebe [8] investigated large amplitude wavy surfaces as a particular form of surface roughness. Waves with λ equal to 4.2 inches and $2a_d/\lambda$ equal to 0.119, 0.238, and 0.405 were constructed out of styrofoam and covered with felt. Average streamwise velocity profiles were taken over the crests with a pitot tube. Turbulent intensities and Reynolds stresses were also measured above the crests with a two-wire probe. All measurements were performed at conditions within the separated flow region of Figure 2.1 but no velocities within the

the separated bubble could be obtained with the pitot tube and hot wire techniques.

The first detailed set of velocity measurements in this laboratory were obtained by Zilker [48] over smooth Plexiglas waves with $2a_d/\lambda$ equal to 0.0125, 0.03125, 0.05, 0.125 and 0.200. Each wave test surface contained ten waves of wavelength two inches and was part of the bottom wall of a rectangular channel. A split film sensor was used to obtain average and fluctuating streamwise velocities. Normal velocities, normal fluctuations and Reynolds stresses were also measured but are subject to a degree of uncertainty since the normal velocities had unrealistic values at the center of the channel. Profiles were taken at one-tenth wavelength increments in the streamwise direction. All measurements were made at a Reynolds number of 8000 based on the half channel height.

Figure 2.1 shows that the above flowrate places the two waves of smallest amplitude within the linear shear stress response region. The wave with $2a_d/\lambda$ equal to 0.0125 did not perturb the flowfield enough to differentiate profiles at any x_d/λ position from flat channel results. Average velocity profile data obtained over the 0.03125 wave surface began to reflect the presence of the sinusoidal boundary.

Flow visualization experiments indicated that reversed flow regions existed for the waves with $2a_d/\lambda$ equal to 0.05, 0.125, and 0.200. The separated region for the 0.05 wave was very thin and thought to be below the lowest velocity measurement at approximately $y_d u^*/\nu$ equal to ten. This is confirmed by recent LDV measurements at the same conditions by Kuzan [] which show that the time

averaged velocity field does not reverse as close to the wave surface as $y_d u^* / \nu$ equal to two. The reversed flow portions of the flowfields over the 0.125 and 0.200 waves were much larger and could not be studied since split film sensors do not distinguish between positive and negative velocities.

Buckles [10] conducted the first detailed study of separated flow over a wavy surface. The measurements of Zilker were extended to include the reversed flow regions above waves with $2a_d/\lambda = 0.125$ and 0.200. A LDV was used to detect negative velocities. Average and fluctuating velocities were obtained at a Reynolds number of 12,000 based on the half channel height. Profiles were taken at streamwise increments no greater than one-tenth of a wavelength beginning as close to the wave surface as y -plus, $y_d u^* / \nu$, equal to 3.5. The size, shape, and extent of the time-averaged separation bubble was determined for both waves. The thickest point of the separated region over the 0.200 wave was found to be of the order of the wave amplitude. The separation bubble above the 0.125 wave is about one-third the thickness. It was noted that there is no position above the wave surfaces where the flow is separated at all times. Similarities between separated flow over waves and a classical shear layer were also observed.

Kuzan [25] extended Buckles work by studying the effect of flowrate on the separation bubble. LDV measurements were taken above a wave with $2a_d/\lambda$ equal to 0.200 at a Reynolds number of 30,000. The separated region was observed to shrink uniformly as the Reynolds number increases. That is, the separation bubble was inclined in the trough at the same angle for the two flowrates tested.

CHAPTER 3

THEORY

This chapter is in three sections. Section I presents a nonlinear analysis for turbulent flow over finite amplitude waves in a rectangular channel. In Section II the turbulent stress models used in the above theory are described. Section III gives a check of the nonlinear analysis by comparing surface stress results for very small amplitude waves with the linear theory of Thorsness [44] and Abrams [2] and with literature data. A comparison of the nonlinear analysis with the LDV measurements over finite amplitude waves is given in Chapter 6.

I. Nonlinear Channel Analysis

The linear theory of Thorsness [44] and Abrams [2] is strictly valid only for boundary layer flows with waves of infinitesimal amplitude. This section discusses a nonlinear analysis and a computational method for extending the calculations of Thorsness and Abrams to the case of finite amplitude waves on the bottom wall of a rectangular channel. The method is a modification of the boundary layer analysis of McLean [32].

A. Governing Equations

Prediction of the turbulent flowfield over waves of finite amplitude was achieved by solving the nonlinear Reynolds-averaged Navier-Stokes equations. These momentum equations are shown below for two-dimensional steady-state incompressible flow in Cartesian coordinates:

$$\begin{aligned}
u_d \frac{\partial u_d}{\partial x_d} + v_d \frac{\partial u_d}{\partial y_d} = -\frac{1}{\rho} \frac{\partial p_d}{\partial x_d} + \nu \left(\frac{\partial^2 u_d}{\partial x_d^2} + \frac{\partial^2 u_d}{\partial y_d^2} \right) \\
+ \frac{\partial}{\partial x_d} (-\overline{u'_d u'_d}) + \frac{\partial}{\partial y_d} (-\overline{u'_d v'_d})
\end{aligned} \quad (3.1)$$

$$\begin{aligned}
u_d \frac{\partial v_d}{\partial x_d} + v_d \frac{\partial v_d}{\partial y_d} = -\frac{1}{\rho} \frac{\partial p_d}{\partial y_d} + \nu \left(\frac{\partial^2 v_d}{\partial x_d^2} + \frac{\partial^2 v_d}{\partial y_d^2} \right) \\
+ \frac{\partial}{\partial x_d} (-\overline{u'_d v'_d}) + \frac{\partial}{\partial y_d} (-\overline{v'_d v'_d})
\end{aligned} \quad (3.2)$$

where u_d, u'_d and v_d, v'_d are time-averaged and fluctuating velocities in the x_d and y_d directions respectively. The subscript "d" refers to dimensional variables.

The wave surface is the sinusoid

$$y_d = a_d \cos(\alpha_d x_d), \quad (3.3)$$

where a_d is the wave amplitude, $\alpha_d = 2\pi/\lambda$ is the wavenumber and λ is the wavelength.

The boundary conditions at the wave surface and the top wall of the channel are no slip and may be written as

$$u_d(x_d, a_d \cos \alpha_d x_d) = v_d(x_d, a_d \cos \alpha_d x_d) = 0 \quad (3.4)$$

and

$$u_d(x_d, y_T) = v_d(x_d, y_T) = 0. \quad (3.5)$$

where y_T is the coordinate of the top wall of the channel. In the horizontal direction the boundary conditions are periodic and given by

$$u_d(0, y_d) = u_d(\lambda, y_d), \quad (3.6)$$

and

$$v_d(0, y_d) = v_d(\lambda, y_d). \quad (3.7)$$

B. Numerical Solution

It is desirable to perform computations on a rectangular region. This was accomplished by a conformal mapping of the physical domain $0 \leq x_d \leq \lambda$; $a_d \cos(\alpha_d x_d) \leq y_d \leq y_T$ to the rectangular region $0 \leq \varepsilon \leq 2\pi$; $0 \leq \eta \leq \eta_T$, where η_T is the transformed coordinate of the top wall of the channel. The map is given by the following orthogonal transformation developed by Caponi et al. [11]:

$$\alpha_d x_d = \varepsilon + \sum_{i=1}^{\infty} \frac{b_i}{i} \sin i \varepsilon \left(\frac{\cosh i (\eta_T - \eta)}{\sinh i \eta_T} \right), \quad (3.8)$$

$$\alpha_d y_d = \eta + b_0 - \sum_{i=1}^{\infty} \frac{b_i}{i} \cos i \varepsilon \left(\frac{\sinh i (\eta_T - \eta)}{\sinh i \eta_T} \right). \quad (3.9)$$

The coefficients b_i can be chosen to approximate any given periodic and symmetrical surface. Eleven terms were found to be sufficient to fit the wave surface $y_d = a_d \cos \alpha_d x_d$ for $2a_d/\lambda \leq 0.05$. Figure 3.1 shows the physical and transformed regions. Equations (3.8) and (3.9) can easily be modified to accommodate asymmetric surfaces [32].

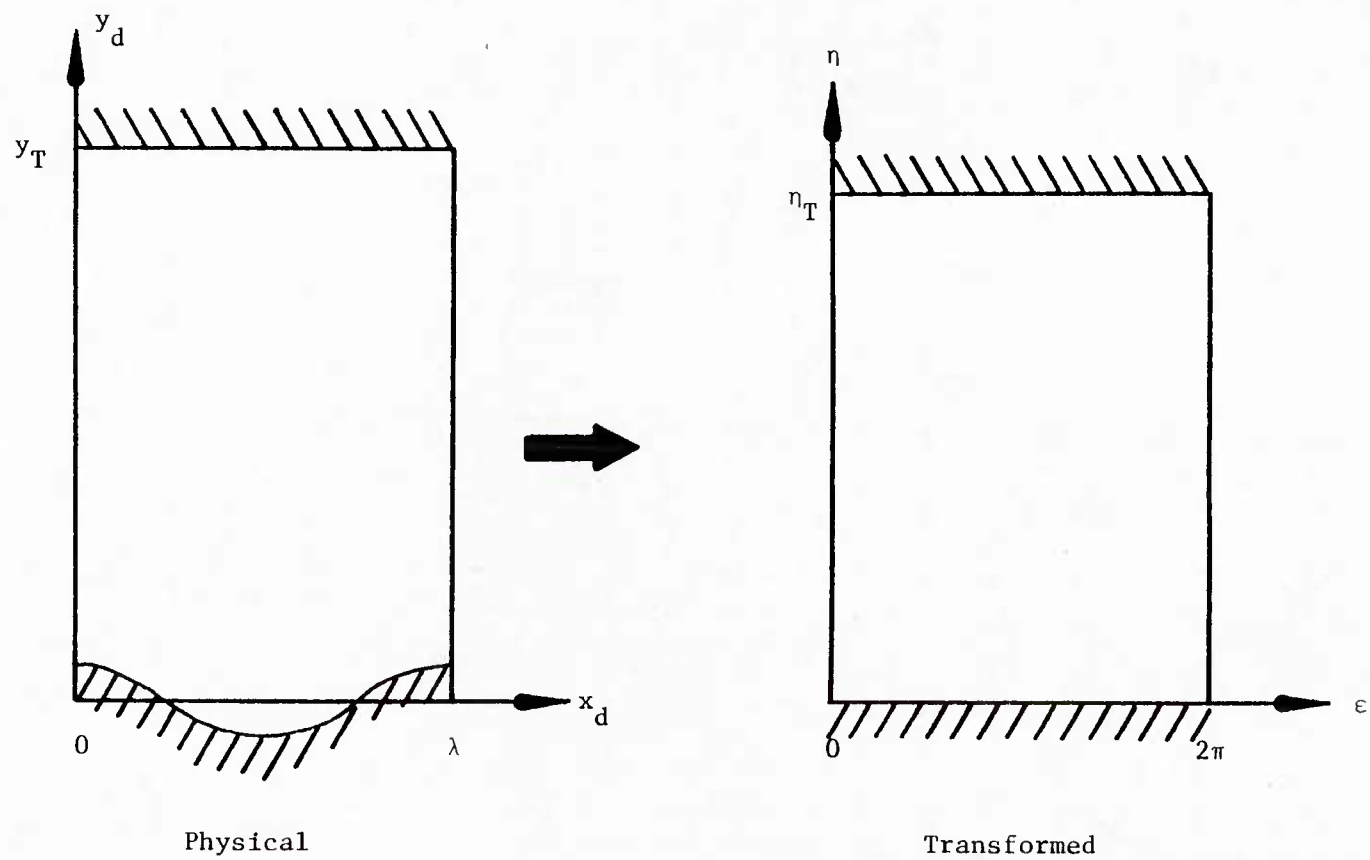


Figure 3.1 Physical and Transformed Regions

The momentum equations (3.1) and (3.2) were solved in streamfunction-vorticity form. The streamfunction, ψ_d , and the vorticity, ω_d , are defined by,

$$\omega_d = \frac{\partial v_d}{\partial x_d} - \frac{\partial u_d}{\partial y_d}, \quad (3.10)$$

$$u_d = \frac{\partial \psi_d}{\partial y_d}, \quad (3.11)$$

and

$$v_d = - \frac{\partial \psi_d}{\partial x_d}. \quad (3.12)$$

McLean [32] has shown that in the transformed coordinates, (ϵ, η) , the equations of motion become

$$\omega_d = -J \left(\frac{\partial^2 \psi_d}{\partial \epsilon^2} + \frac{\partial^2 \psi_d}{\partial \eta^2} \right), \quad (3.13)$$

and

$$\begin{aligned} \frac{\partial \omega_d}{\partial \epsilon} \frac{\partial \psi_d}{\partial \eta} - \frac{\partial \omega_d}{\partial \eta} \frac{\partial \psi_d}{\partial \epsilon} &= \left(\frac{\partial^2}{\partial \epsilon^2} + \frac{\partial^2}{\partial \eta^2} \right) \left[(v + v_t) \omega_d \right] \\ &+ \frac{2}{J} \left[\frac{\partial^2 \psi_d}{\partial x_d^2} \frac{\partial^2 v_t}{\partial y_d^2} - 2 \frac{\partial^2 \psi_d}{\partial x_d \partial y_d} \frac{\partial^2 v_t}{\partial x_d \partial y_d} + \frac{\partial^2 \psi_d}{\partial y_d^2} \frac{\partial^2 v_t}{\partial x_d^2} \right], \end{aligned} \quad (3.14)$$

where the Jacobian, J , is defined by

$$J = \left(\frac{\partial^2 x_d}{\partial \epsilon^2} + \frac{\partial^2 x_d}{\partial \eta^2} \right)^{-1}. \quad (3.15)$$

In the derivation of equation (3.14) the turbulent stress terms in equations (3.1) and (3.2) have been modeled with an isotropic eddy viscosity according to the following constitutive equations:

$$-\overline{u'_d u'_d} = \frac{1}{\rho} R_{x_d x_d} = \nu_t 2 S_{x_d x_d} = \nu_t 2 \frac{\partial u_d}{\partial x_d}, \quad (3.16)$$

$$-\overline{v'_d v'_d} = \frac{1}{\rho} R_{y_d y_d} = \nu_t 2 S_{y_d y_d} = \nu_t 2 \frac{\partial v_d}{\partial y_d}, \quad (3.17)$$

and

$$-\overline{u'_d v'_d} = R_{x_d y_d} = \nu_t 2 S_{x_d y_d} = \nu_t \left(\frac{\partial u_d}{\partial y_d} + \frac{\partial v_d}{\partial x_d} \right). \quad (3.18)$$

Models for the eddy viscosity are described in Section II.

The no slip boundary conditions in the transformed region are

$$\frac{\partial \psi_d}{\partial \eta}(\epsilon, 0) = \frac{\partial \psi_d}{\partial \epsilon}(\epsilon, 0) = 0 \quad (3.19)$$

and

$$\frac{\partial \psi_d}{\partial \eta}(\epsilon, \eta_T) = \frac{\partial \psi_d}{\partial \epsilon}(\epsilon, \eta_T) = 0 \quad (3.20)$$

at the top and bottom walls respectively. In the horizontal direction the periodic boundary conditions become

$$\psi_d(0, \eta) = \psi_d(2\pi, \eta) \quad (3.21)$$

and

$$\omega_d(0, \eta) = \omega_d(2\pi, \eta) . \quad (3.22)$$

In order to resolve the steep velocity gradients near the two surfaces, the vertical coordinates were stretched according to the following equation:

$$\eta = \eta_T \left[\frac{\tan^{-1}[-b(1 - 2z)] - \tan^{-1}[-b]}{2 \tan^{-1} [+b]} \right] \quad (3.23)$$

where z is the unstretched coordinate and b is a stretching parameter. Figure 3.2 shows an example of the stretched coordinate system in the physical domain for $2a_d/\lambda = 0.05$ and $b = 5$ with a 9×81 mesh. Details of the coordinate system in the near wall region, which is not visible in this figure due to the fine spacing, is discussed below.

Table 3.1 shows the stretching parameters and the number of vertical points used for the computational studies of the two wave steepnesses investigated. These parameters provide the necessary grid spacing to resolve accurately the flowfield in the vertical direction. Resolution was verified by reducing the number of grid points from 151 to 81 for the case of $2a_d/\lambda = 0.05$ and $Re_b = 38,800$. Predictions of surface stresses and velocities differed by only about one percent.

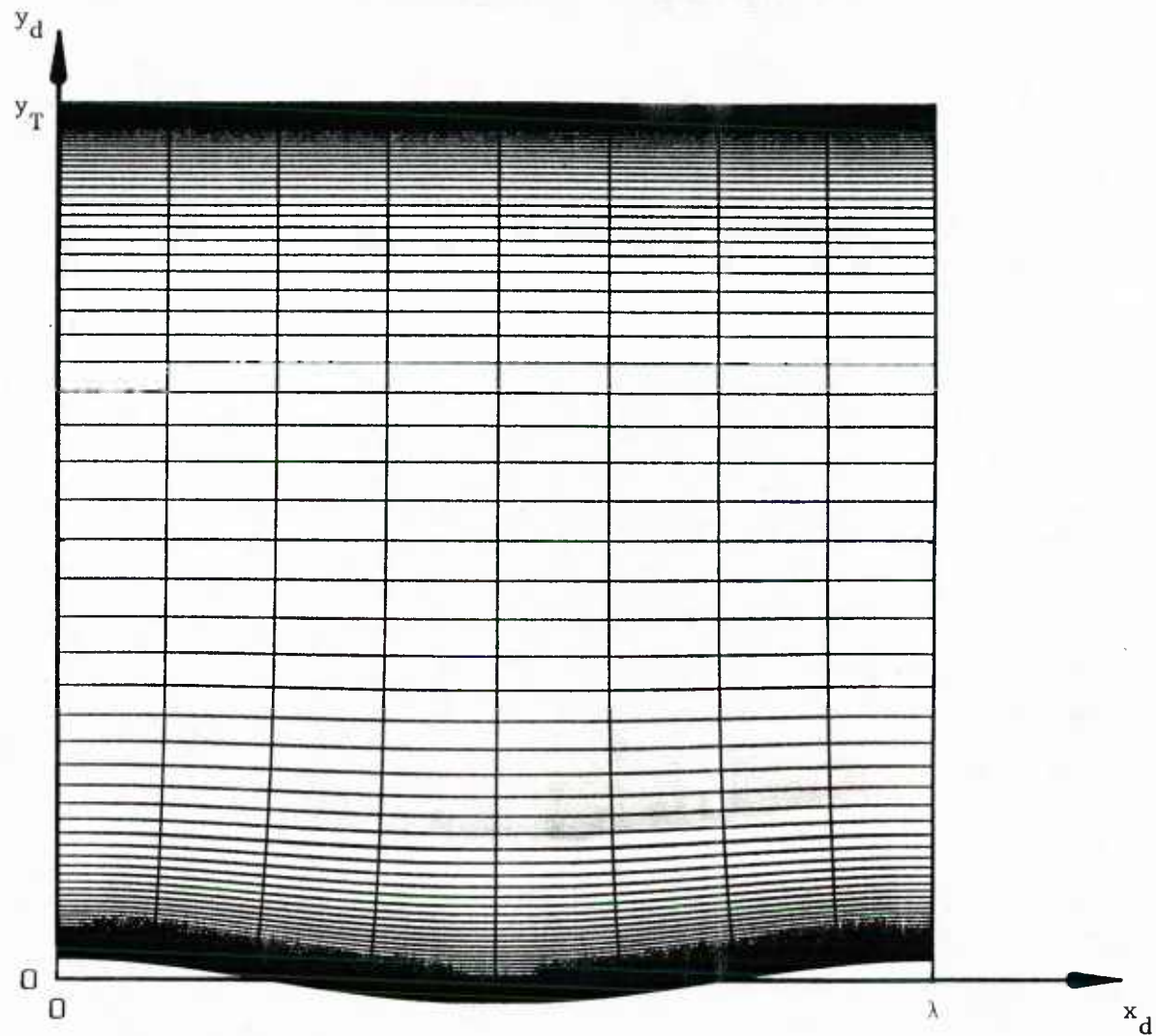


Figure 3.2 Stretched Coordinate System in Physical Domain,
 $2a_d/\lambda = 0.05$, $b = 5$, 9×81 Mesh

Flow Conditions	Stretching Parameter	# Vertical Points	# Points in Viscous Sublayer	# Points in Viscous Wall Region
$2a_d/\lambda = 0.03125$ $Re_b = 6400$	5	81	3	17
$2a_d/\lambda = 0.05$ $Re_b = 38,800$	15	151	4	24

Table 3.1 Numerical Parameters and Vertical Resolution

The resolution is illustrated in Figures 3.3 and 3.4 which show the discrete velocity profiles obtained using the parameters in Table 3.1 in a flat channel with $Re_b = 6400$ and $38,800$ respectively. These flat channel profiles represent the average vertical resolution found over one wavelength. The resolution is slightly higher at the crests and slightly lower over the troughs due to the transformed coordinates and the change in cross sectional area. Note that there are 3,4 grid points in the viscous sublayer ($y_d u^* / \nu < 5$) and 17,24 grid points in the viscous wall region ($y_d u^* / \nu < 40$) for $Re_b = 6400$ and $38,800$ respectively. These numbers are also included in Table 3.1.

Numerically, the vertical derivatives are evaluated by finite differences. The first, second and third derivatives are approximated as

$$\frac{\partial \phi}{\partial \eta} \approx \frac{\phi_{n,m+1} - \phi_{n,m-1}}{2\Delta z} \left(\frac{\partial z}{\partial \eta} \right) \quad (3.24)$$

$$\begin{aligned} \frac{\partial^2 \phi}{\partial \eta^2} \approx & \frac{\phi_{n,m+1} - 2\phi_{n,m} + \phi_{n,m-1}}{(\Delta z)^2} \left(\frac{\partial z}{\partial \eta} \right)^2 \\ & + \frac{\phi_{n,m+1} - \phi_{n,m-1}}{2\Delta z} \left(\frac{\partial^2 z}{\partial \eta^2} \right) \end{aligned} \quad (3.25)$$

and

$$\begin{aligned} \frac{\partial^3 \phi}{\partial \eta^3} \approx & \frac{\phi_{n,m+2} - 2\phi_{n,m+1} + 2\phi_{n,m-1} - \phi_{n,m-2}}{(\Delta z)^3} \frac{1}{2} \left(\frac{\partial z}{\partial \eta} \right)^3 \\ & + \frac{\phi_{n,m+1} - 2\phi_{n,m} + \phi_{n,m-1}}{(\Delta z)^2} 3 \left(\frac{\partial z}{\partial \eta} \right) \left(\frac{\partial^2 z}{\partial \eta^2} \right) + \frac{\phi_{n,m+1} - \phi_{n,m-1}}{2\Delta z} \left(\frac{\partial^3 z}{\partial \eta^3} \right) \end{aligned} \quad (3.26)$$

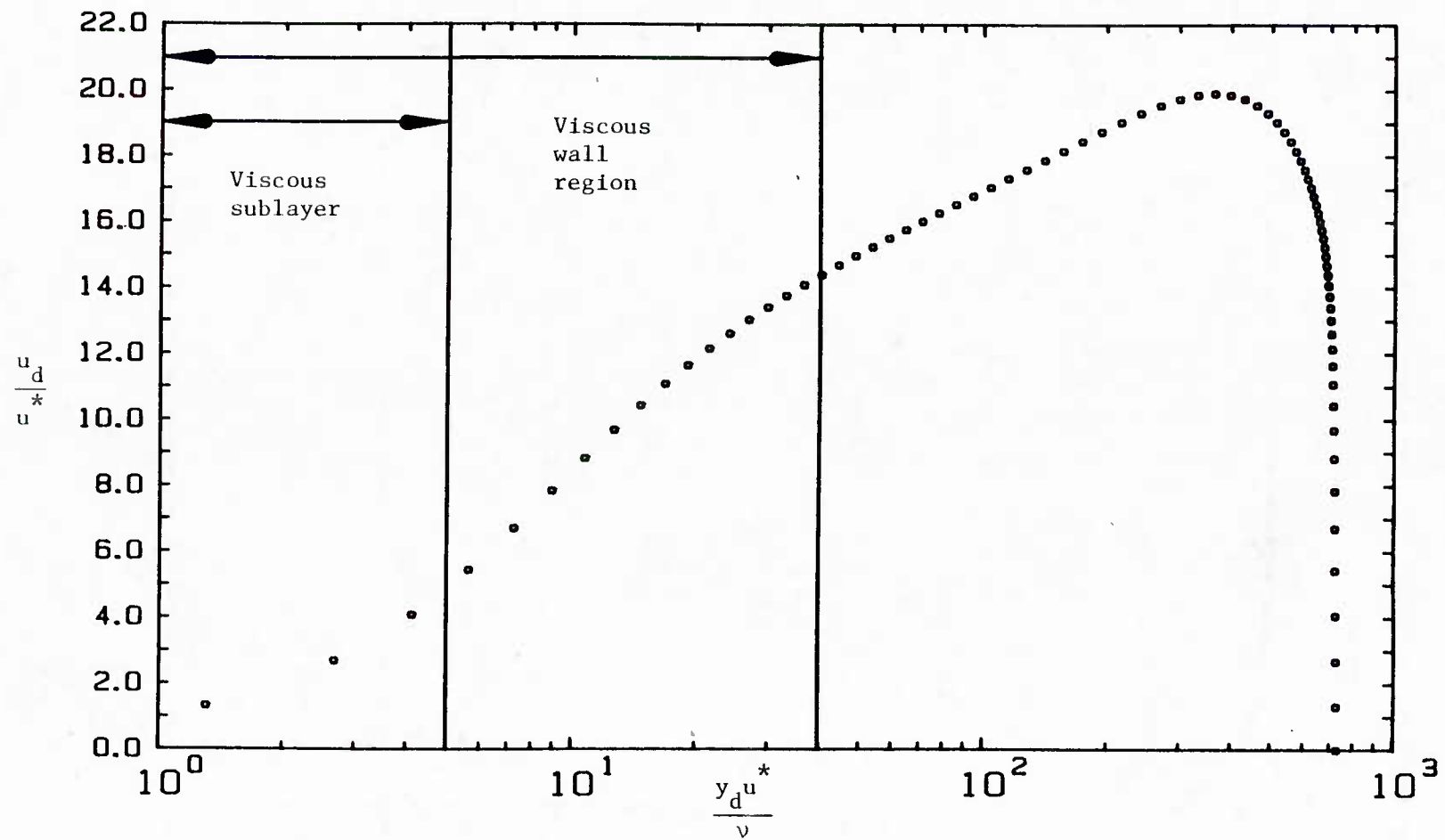


Figure 3.3 Discrete Flat Channel Profile, $Re_b = 6400$, $b = 5$,
81 Vertical Points

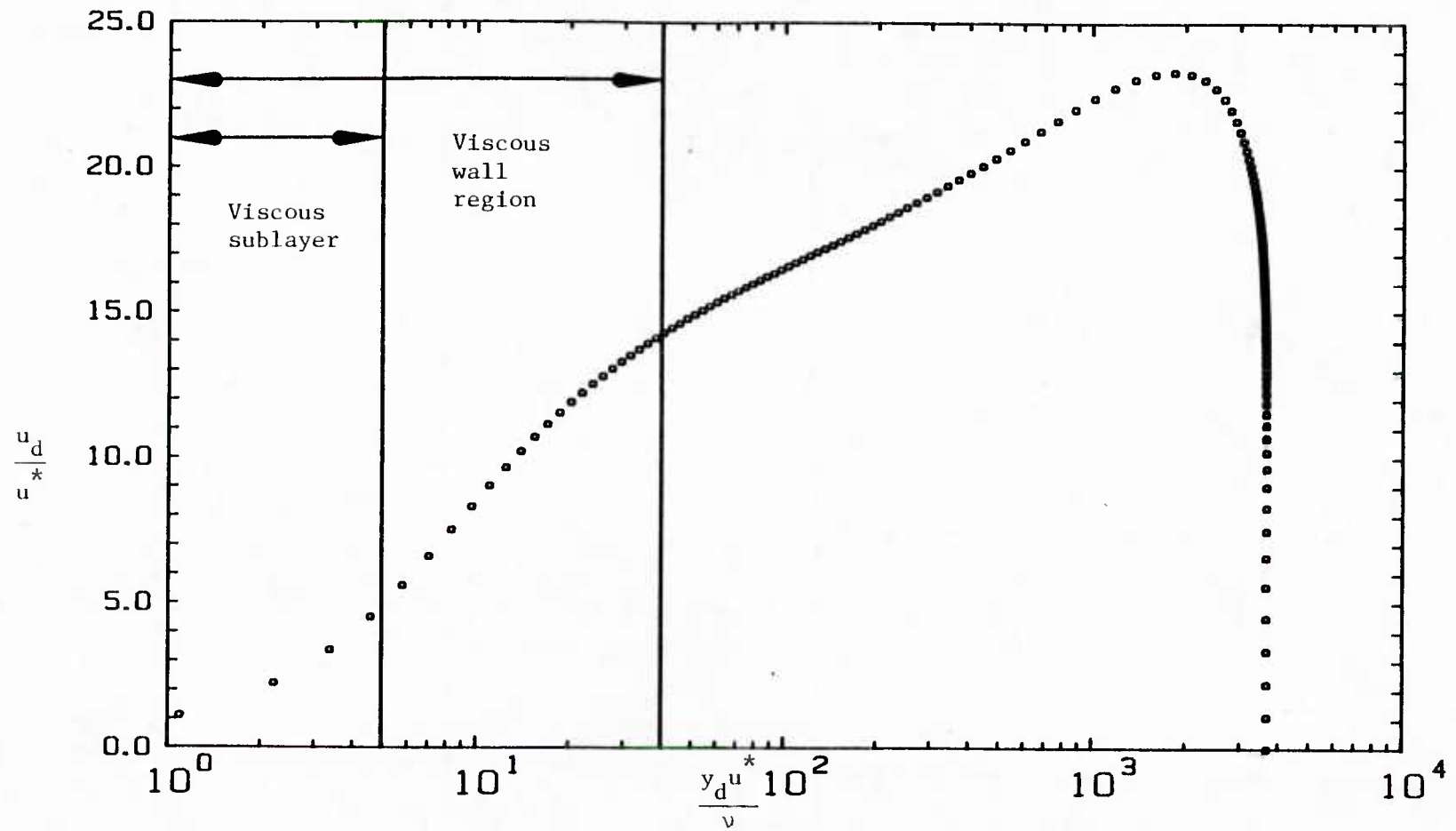


Figure 3.4 Discrete Flat Channel Profile, $Re_b = 38,800$, $b = 15$, 151 Vertical Points

where $\phi_{n,m}$ refers to either the streamfunction ψ_d or the vorticity ω_d . The derivatives of z arise because of the coordinate stretching.

The horizontal derivatives are evaluated by spectral methods. Since the flowfield is assumed to be periodic, the streamfunction and vorticity may be represented by the following discrete Fourier series at constant η :

$$\phi(\epsilon_j) \Big|_{\eta} = \sum_{k=-N/2}^{N/2-1} \gamma_k e^{ik\epsilon_j} \quad (3.27)$$

where $N+1$ is the number of points in the horizontal direction (crest to crest), $\epsilon_j = 2\pi j/N$, and $0 \leq j \leq N$. The Fourier coefficients, γ_k , are calculated by a fast Fourier transform routine. The horizontal derivatives are given by,

$$\frac{\partial \phi(\epsilon_j)}{\partial \epsilon} \Big|_{\eta} = \sum_{k=-N/2}^{N/2-1} ik \gamma_k e^{ik\epsilon_j} \quad (3.28)$$

and

$$\frac{\partial^2 \phi(\epsilon_j)}{\partial \epsilon^2} \Big|_{\eta} = \sum_{k=-N/2}^{N/2-1} (-k^2) \gamma_k e^{ik\epsilon_j} \quad (3.39)$$

Good spatial resolution in the horizontal direction was obtained with nine points (crest to crest) and four Fourier harmonics. The nine spectral points are equivalent to approximately 18 finite difference points. A rough rule of thumb given by Orszag [35] is that a finite difference method requires a factor of 2 more resolution in each spatial direction than a spectral method to achieve 5-10

percent accuracy. Tests with 17 points and 8 harmonics gave the same results for waves with $2a_d/\lambda = 0.05$.

The discretised equations were solved by Newton's method. Since the Jacobian matrix has substantial zero structure, a sparse matrix solver developed by Stadtherr [42] was used to lower storage requirements. A summary of the approximate storage requirements and run times on a VAX 11/780 is given in Table 3.2. The numbers in parentheses refer to values obtained by treating the Jacobian matrix as full. It should be noted that although the sparse matrix solver substantially lowered the storage requirements, no reduction in run times was observed. All runs were performed in double precision.

Cartesian streamwise velocities were calculated from results in transformed coordinates by use of the following chain rule equation:

$$u_d(x_d, y_d) = \frac{\partial \psi_d}{\partial y_d} = \frac{\partial \psi_d}{\partial \eta} \frac{\partial \eta}{\partial y_d} + \frac{\partial \psi_d}{\partial \epsilon} \frac{\partial \epsilon}{\partial y_d} \quad (3.30)$$

A complete listing of the nonlinear channel computer code is given in Appendix A.

Flow Conditions	Mesh	Storage Requirement (M bytes)	Run Time (CPU hours)
$2a_d/\lambda = 0.03125$ $Re_b = 6400$	9 x 81	1.2 (4.0)	5 (5)
$2a_d/\lambda = 0.05$ $Re_b = 38,800$	9 x 151	2.4	20

Table 3.2 Storage Requirements and Run Times

II. Models for Turbulent Stresses

A channel flow consists of a wall region and a core region where the eddy viscosities behave differently. The following equation by Reynolds and Tiederman [38] was used to describe the eddy viscosity:

$$\frac{\nu_t}{\nu} = \frac{1}{2} \left[1 + \frac{4}{9} \kappa^2 \left(\frac{y'_d u^*}{\nu} \right)^2 \left(1 - \frac{y'_d}{2h_d} \right)^2 \left(3 - 4 \frac{y'_d}{h_d} + 2 \left(\frac{y'_d}{h_d} \right)^2 \right)^2 \right. \\ \left. \left[1 - \exp \left(\frac{-y'_d \tau_d^{1/2}}{\rho^{1/2} \nu A} \right) \right]^2 \right]^{1/2} - \frac{1}{2} \quad (3.31)$$

where h_d is the average half channel height, κ is the von Karman constant, and τ_d is the local shear stress in the fluid. The van Driest parameter, A , is a measure of the thickness of the viscous wall region. Equation (3.31) is an adaptation for a channel of an expression first suggested by Cess [13] for pipe flow. The expression is a combination of van Driest's [46] wall region law and Reichardt's [36] middle law. The Cess profile provides a smooth transition between the inner and core regions because it is continuous and analytic.

In equation (3.31) the variable y'_d refers to a physical distance from either the wave surface or the top wall of the channel. In this analysis y'_d is measured from the wave surface for grid points at or below the center line of constant η . Above this line y'_d is measured from the top wall. Three methods of evaluating y'_d were investigated:

- 1) along a line of constant ϵ ,
- 2) along a line normal to the surface,
- and 3) along a vertical line to the surface.

Figure 3.5 illustrates the three types of distances. The three distances are identical for waves of infinitesimal amplitude.

It should be noted that for a channel it is not appropriate to model the eddy viscosity with a mixing length as did Thorsness and Abrams for a boundary layer flow. Mixing length theories predict zero eddy viscosity at the channel center. Measurements show that the eddy viscosity is large and nearly constant in the core region. Figure 3.6 shows the Cess eddy viscosity profile for a flat channel with $Re_b = 6400$, $\kappa = 0.48$ and $A = 33$.

The nonlinear channel calculations were performed with turbulence Models C^* and D^* developed by Thorsness [44] and Abrams [2].

A. Model C^*

Model C^* is simply the Cess eddy viscosity profile, equation (3.31), with the flat channel value of the van Driest parameter, A . Although the value of A is constant, the eddy viscosity varies slightly in the flow direction since it is a function of the local shear stress. Turbulent stresses change along the wave due to variations in both the eddy viscosity and the local rate of strain. See equations (3.16)-(3.18).

B. Model D^*

Model D^* is an extension of Model C^* in which pressure gradient effects on the turbulence are taken into account. In this model the

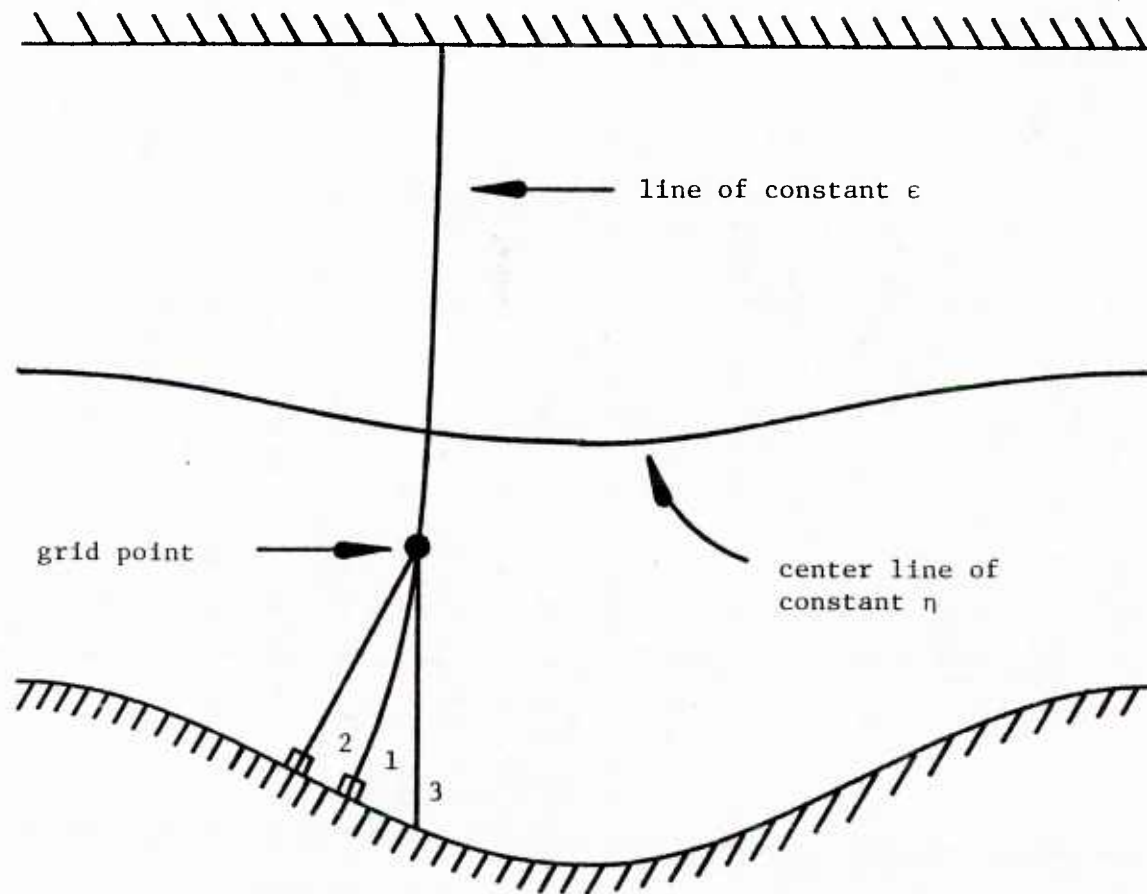


Figure 3.5 Methods of Evaluating y'_d in Cess Profile, equation (3.31)
(Wave Amplitude Exaggerated)

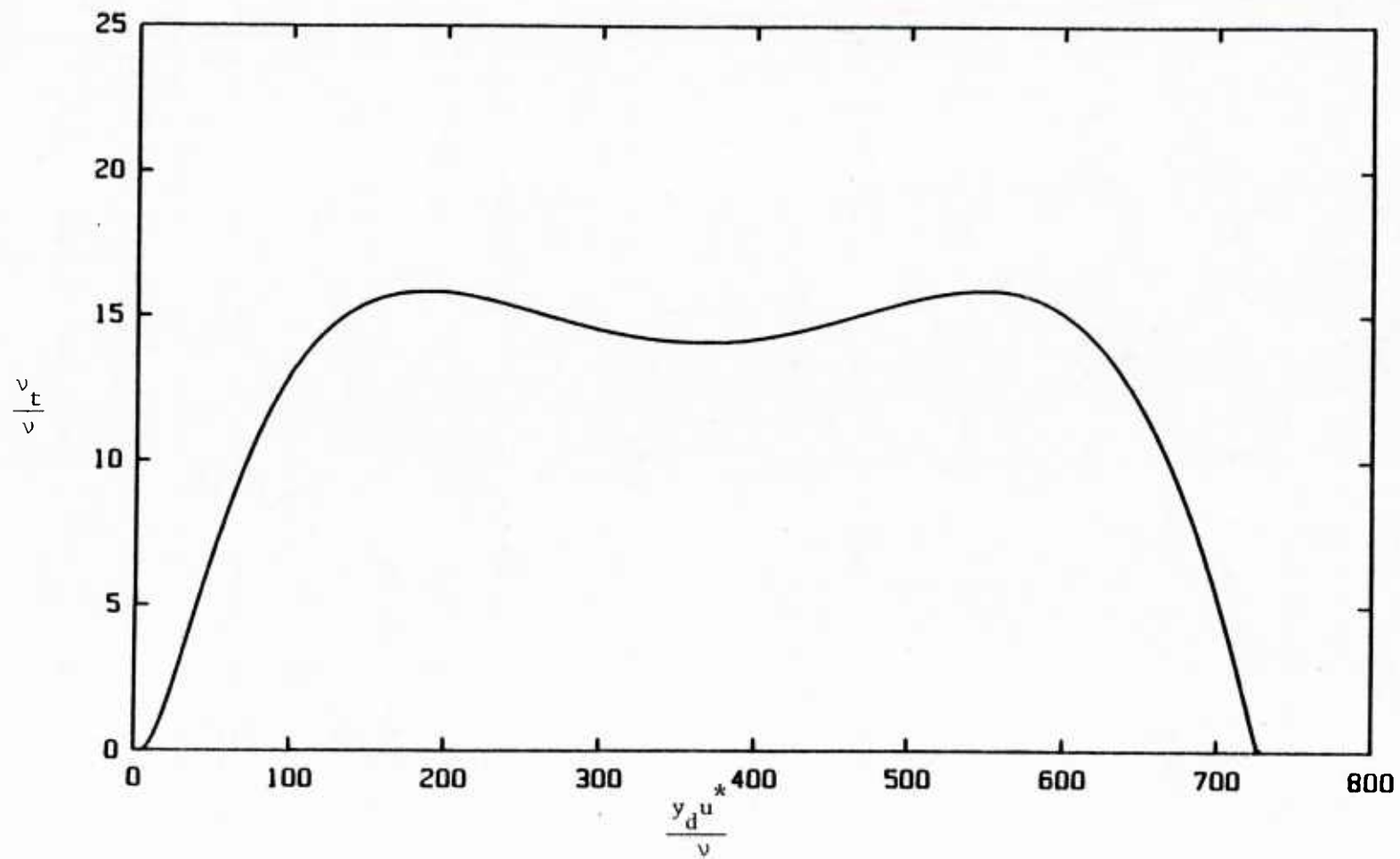


Figure 3.6 Cess Eddy Viscosity Profile (Flat Channel),
 $Re_b = 6400$, $\kappa = 0.48$, $A = 33$

van Driest parameter, A , is used as a scale factor that governs the thickness of the viscous wall region. The viscous wall region thickens with increasing negative pressure gradient and thins with increasing positive pressure gradient. For equilibrium boundary layers Loyd, Moffat and Kays [31] suggest the following functional dependence on A on the dimensionless pressure gradient, $p^+ = (dp_d/dx_d)(\nu/\rho u^*)^3$,

$$A = \bar{A} \left[1 + p^+ k_1 + p^{+2} k_2 + \dots \right] \quad (3.32)$$

where \bar{A} is the flat channel value of A and k_1 and k_2 are empirical constants. Loyd et al. have argued that for a nonequilibrium condition, such as exists in flow over waves, an effective pressure gradient, p_{eff}^+ , should be used in equation (3.21) where

$$\frac{d p_{eff}^+}{d \left(\frac{x_d u^*}{\nu} \right)} = \frac{p^+ - p_{eff}^+}{k_L} \quad (3.33)$$

and k_L is an empirical lag constant. This, in effect, introduces a lag between the imposition of a nonzero pressure gradient and a change of scale in the viscous wall region.

III. Test of Channel Analysis

The nonlinear channel analysis was tested by comparing surface stress results for the limiting case of very small amplitude waves with the linear boundary layer analysis of Thorsness [44] and Abrams [2] and with literature data. The channel calculations were performed

with $2h_d/\lambda = 1.0$, $2a_d/\lambda = 0.001$, $\kappa = 0.48$, and $A = 33$. The channel height to wavelength ratio, $2h_d/\lambda$, was chosen to correspond to that of the channel in this laboratory. The dimensionless wave amplitudes ranged from $a_d u^*/\nu = 0.0314$ at $\alpha_d \nu/u^* = 0.1$ to $a_d u^*/\nu = 6.28$ at $\alpha_d \nu/u^* = 0.0005$. Since $a_d u^*/\nu$ was always much less than 27 a linear response was ensured. Selection of the Cess profile constants, κ and A , is discussed in Chapter 5, Section I. All of the calculations presented in this section used turbulence Model D^{*} with $k_1 = -35$, $k_2 = 0$, and $k_L = 1800$ as suggested by Abrams [2].

Predictions of the amplitude of the shear stress responses are given in Figure 3.7 compared with the data of Abrams [2]. Abrams obtained linear shear stress responses in a channel with $2h_d/\lambda = 1.0$ and $2a_d/\lambda = 0.014$. This figure shows that with turbulence constants $k_1 = -35$ and $k_L = 1800$ the channel analysis provides the best fit to the data. The boundary layer calculations underpredict the data and were found by Thorsness [44] to be low for the range of constants $-60 < k_1 < -15$ and $1500 < k_L < 6000$.

Phase angles of the shear stress are given in Figure 3.8. Again, for $k_1 = -35$ and $k_L = 1800$, the best fit to the data is seen with the channel analysis. Better agreement might be obtained with a slight reduction of k_L . However, the lengthy nature of the channel calculations prohibited fine tuning of the turbulence constants.

Amplitudes and phases of pressure responses are shown in Figures 3.9 and 3.10 compared with literature data. The amplitudes predicted by the boundary layer and channel analyses are in close agreement. However, significant differences in the phase angles are observed

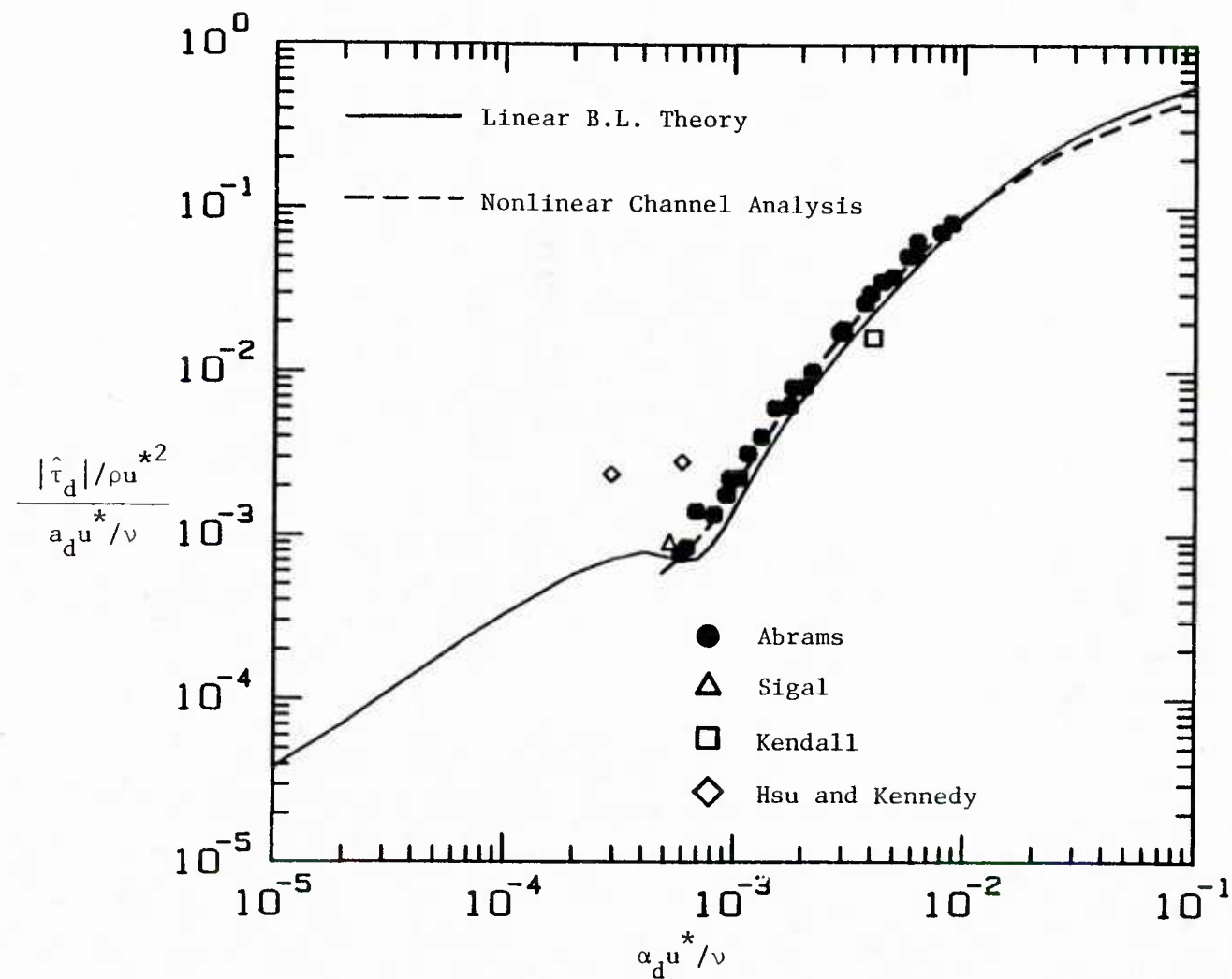


Figure 3.7 Surface Shear Stress Amplitude, Comparison of Boundary Layer and Channel Analyses for Small Amplitude Waves, Model D* ($k_1 = -35$, $k_L = 1800$)

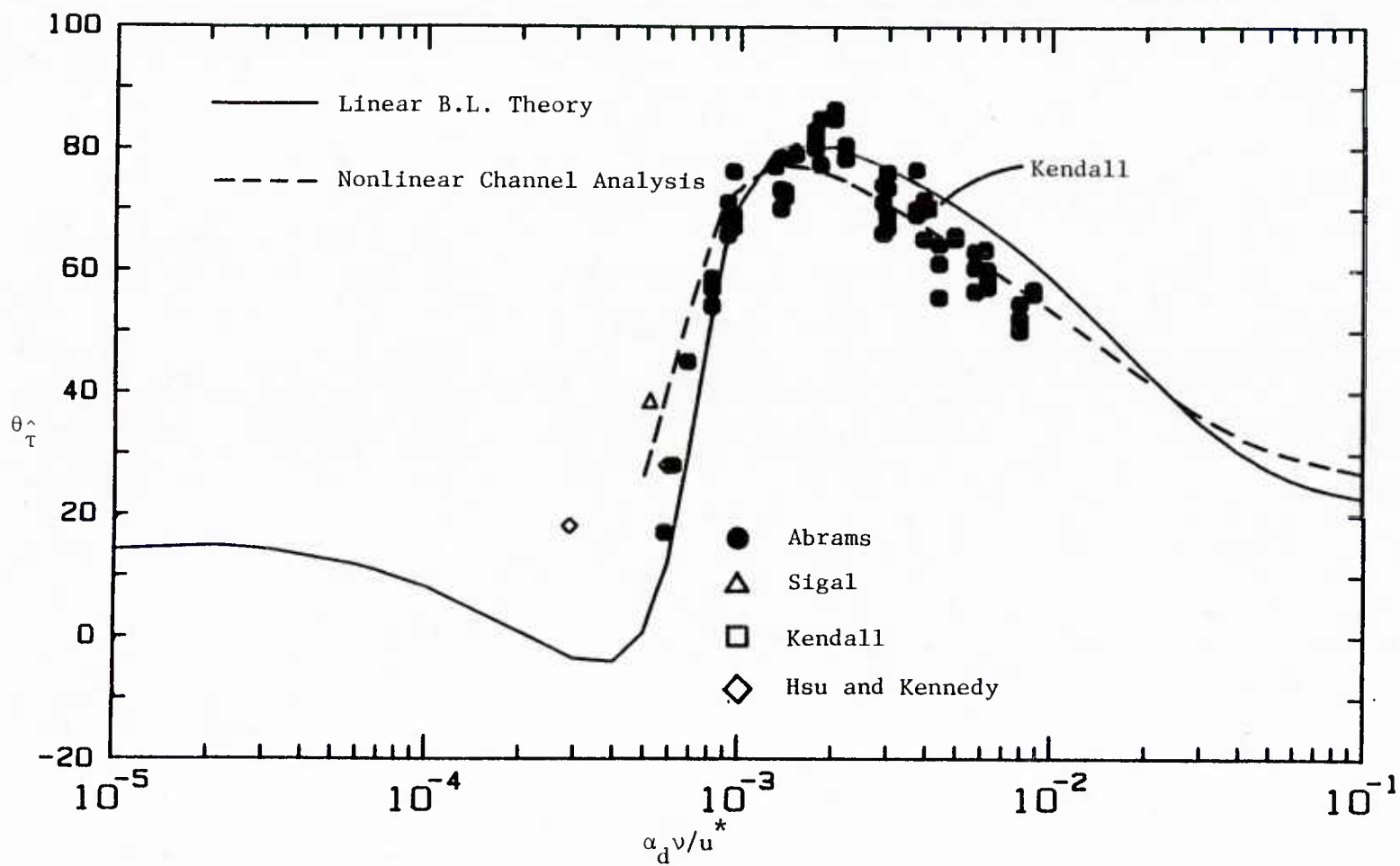


Figure 3.8 Phase Angle of Surface Shear Stress, Comparison of Boundary Layer and Channel Analyses for Small Amplitude Waves, Model D*
 $(k_1 = -35, k_L = 1800)$

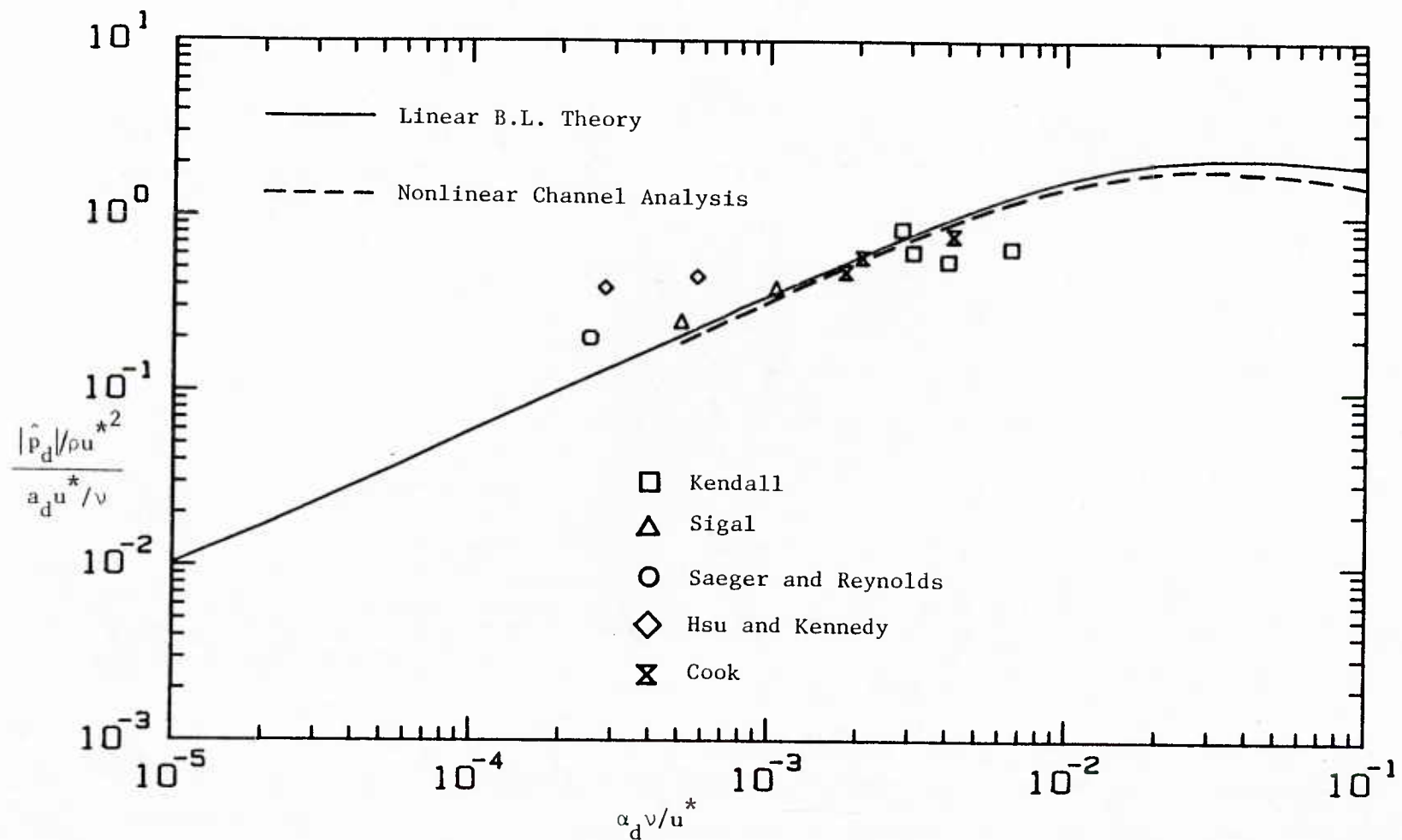


Figure 3.9 Surface Pressure Amplitude, Comparison of Boundary Layer and Channel Analyses for Small Amplitude Waves, Model D* ($k_1 = -35$, $k_1 = 1800$)

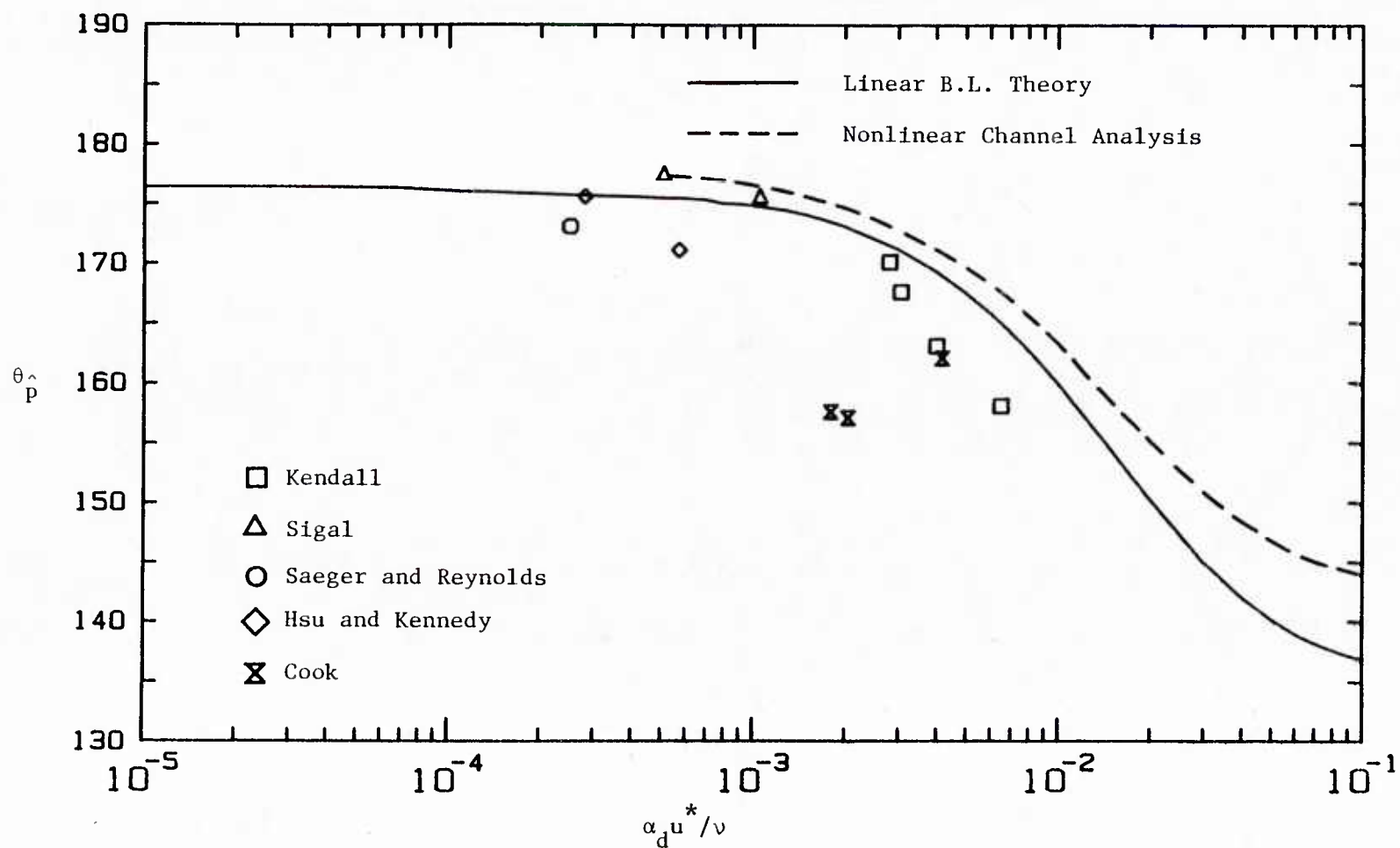


Figure 3.10 Phase Angle of Surface Pressure, Comparison of Boundary Layer and Channel Analyses for Small Amplitude Waves, Model D*
 $(k_1 = -35, k_L = 1800)$

between the two methods of calculation. At very small $\alpha_d v/u^*$, where the flow is in equilibrium with the wave, zero phase shift in the pressure field is expected ($\theta_p = 180^\circ$). Here the channel analysis appears to be qualitatively more correct than the boundary layer analysis as it predicts a closer approach to 180° . At large $\alpha_d v/u^*$ the two theories differ greatly. This is not surprising because the boundary layer analysis of Thorsness and Abrams assumes a deep logarithmic layer while the logarithmic layer in a channel is very thin under these conditions. A quantitative check of the accuracy of the pressure calculations is not possible. This is because few pressure measurements have been made over wavy surfaces and those available show large scatter. Comparisons with theory are further complicated since the literature data were obtained in many different flow geometries including boundary layers, channels, and pipes.

CHAPTER 4

EXPERIMENTAL EQUIPMENT AND PROCEDURES

The purpose of the experimental work was to obtain velocity profiles in the viscous wall region ($y_d u^* / \nu < 40$) for turbulent flow over a solid sinusoidal wavy surface with small enough amplitude that the flow does not separate. The major disturbances in the flowfield are expected to be within this thin region. The profiles will give a better physical understanding of how the presence of a wavy surface perturbs a turbulent flowfield and can be used as a test of the turbulence models of Thorsness [45] and Abrams [2].

Fluid velocities were measured using laser-Doppler velocimetry. This method was chosen because it is a non-obtrusive measurement technique with a small enough "probe" size to resolve the viscous wall region.

Section I of this chapter describes the flow loop and test section. Section II discusses the optical traverse and section III describes the LDV system and data acquisition.

I. Flow Loop and Test Section

The experiments were carried out in a horizontal rectangular water channel originally built by Cook [17] and later modified by Zilker [48] and Buckles [10]. A detailed description of this flow loop may be found in a thesis by Buckles [9]. Consequently the description here is limited to the essential features.

A schematic of the flow loop is shown in Figure 4.1. The rectangular channel has a cross section 2 in. high and 2 ft. wide and a length of 27.5 ft.

Figure 4.1 Schematic of Low Loop

1. Test section window
2. Removable wave surface
3. Removable blanking plate
4. Honeycomb
5. Round to rectangular diffusers
6. Annubar flow meter
7. Butterfly throttling valve
8. Bypass diaphragm valve
9. Small pump
10. Large pump

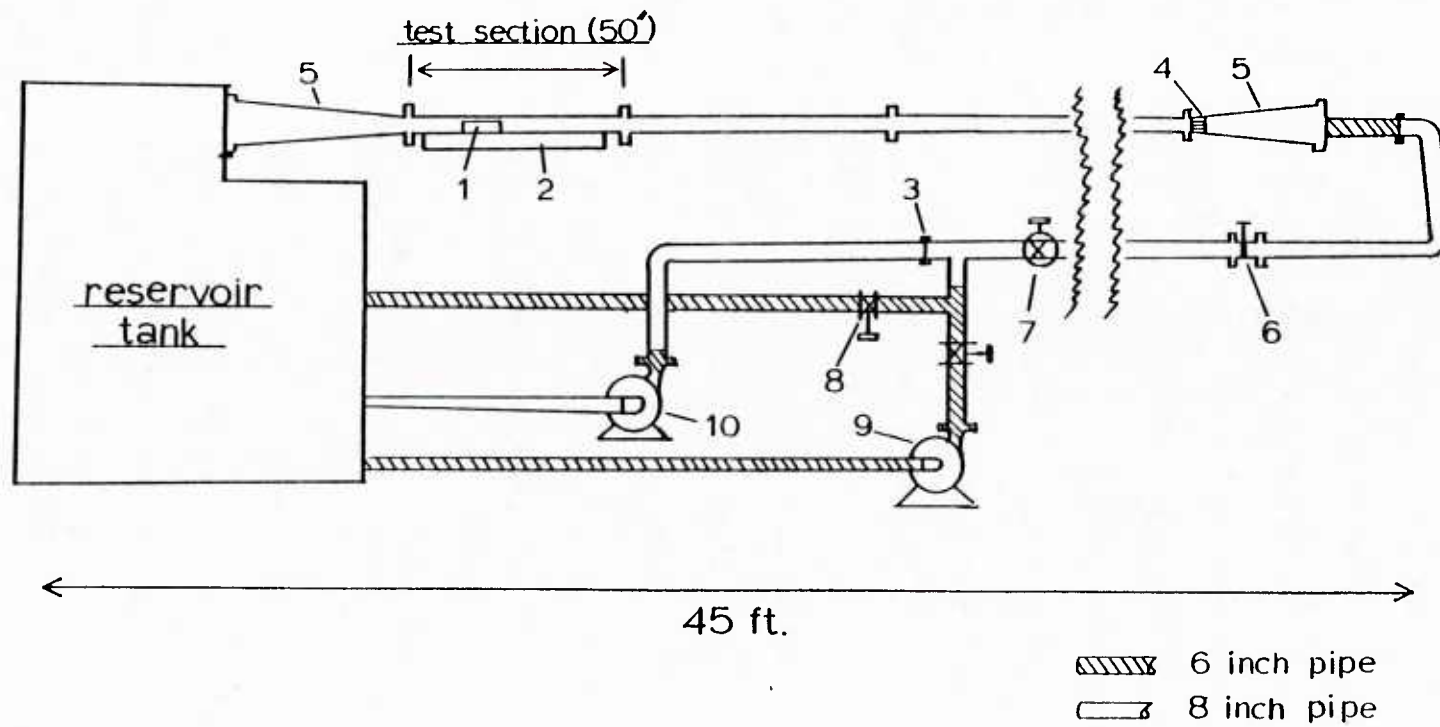


Figure 4.1 Schematic of Flow Loop

The first 23.5 ft. of the channel is made of stainless steel and provides approximately 70 hydraulic diameters for flow development before the test section. The existence of fully developed turbulent flow at the entrance to the test section has been verified by Zilker [48] and Thorsness [44]. The channel is also wide enough that the mean flow is essentially two-dimensional.

The pump is a Worthington 6CNG84 centrifugal pump with a 5 h.p. motor that can deliver flow rates of up to 800 g.p.m. This flow rate corresponds to a channel Reynolds number of 42,000 based on the half channel height and the bulk velocity.

The downstream end of the channel is a 58 in. long Plexiglas test section in which the velocity measurements were performed. The top wall of this section is flat and a portion of the bottom wall consists of a 24 in. by 27 in. removable sinusoidal wavy surface. The waves were machined with the mean wave level at the level of the lower wall. This was to ensure that there was no change in the mean cross-sectional area. Each side of the test section contains a 5 in. \times 1-1/2 in. glass window to allow the laser beams of the LDV system to pass through one side of the channel and be viewed by the receiving optics on the other side.

Velocity measurements were obtained over waves of amplitude 0.03125 in. and 0.05 in. at Reynolds numbers of 6400 and 38,800 respectively. Each wave surface contained ten waves of wavelength two inches and the tests were conducted over the eighth wave at one-tenth wavelength increments. Details of the construction of the wave surfaces may be found in theses by Zilker [48] and Cook [17].

II. Modifications to Optical Traverse

Buckles [10] constructed a traversing mechanism for movement of the LDV system in the normal and streamwise directions. The traverse was modified to increase its accuracy of movement and to decrease its susceptibility to vibration. Accurate vibration free movement was necessary to conduct measurements close enough to a wave surface to resolve the viscous wall region.

The mechanism's vertical motion is on twin stainless steel precision ground shafts. They are mounted vertically and parallel to each other on opposite sides of the unistrut structure that supports the flow loop. On each shaft are two linear ball bearing pillow blocks. The bearing blocks are mounted to a vertically movable rigid cage constructed of aluminum I-beams. Connected to the top of this cage are a pair of eleven foot I-beams that run perpendicular to the channel test section. This pair of beams in the optical bed for the LDV system. Buckles suspended the entire structure by 1/4 inch steel cables in a sling-type design that raised and lowered the traverse with a scissors jack. It was found that this suspension design did not provide an even enough lifting force on both sides of the cage to prevent binding in the shaft bearings. As a result the optical bed underwent a small amplitude seesaw type motion when moved vertically. The play in the shaft bearings also made the traverse susceptible to vibration.

The seesaw motion was corrected by supporting the I-beam cage and optical bed on two lead screws. A drawing of the design is shown in Figure 4.2.

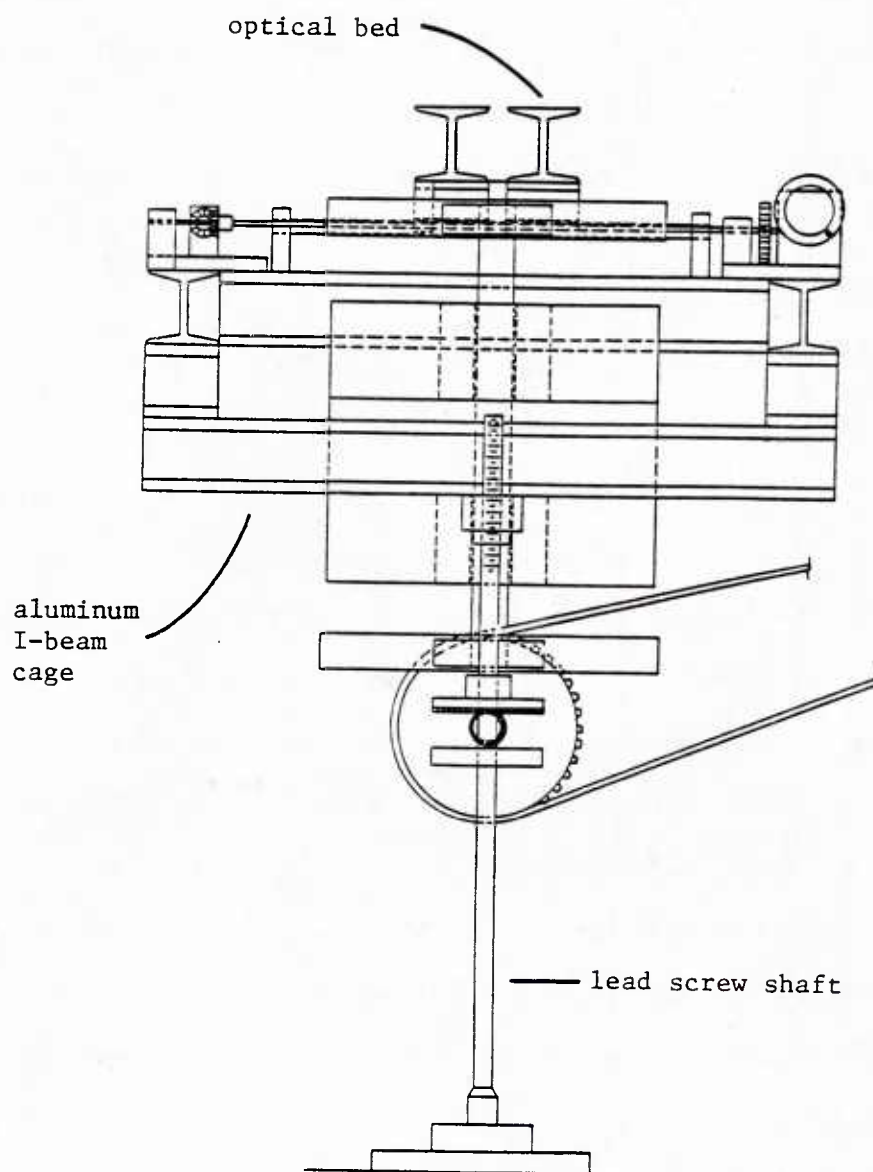


Figure 4.2 Optical Traversing Mechanism

Each lead screw is 8-1/2 inches long, one inch in diameter and turns through a 2-1/2 inch diameter brass nut that is attached to the cage. The lead screws are pinned to one inch diameter stainless steel shafts which are mounted vertically and parallel to each other with a separation distance of 5 feet.

The shafts are supported by a stainless steel collar and rotate freely in flat race thrust bearings (Figure 4.3). A radial bearing is mounted under the thrust bearings to keep the shafts aligned vertically. The entire lower shaft assembly sits on a 3-1/4 in. \times 5-1/4 in. \times 1-1/2 in. aluminum block which is attached to a second 6 in. \times 12 in. \times 1 in. aluminum block that is bolted to the floor.

To ensure that the lead screw shafts turn in unison and raise the optical bed evenly, they are connected mechanically by a system of four bevel gears and a horizontal 5/8 in. steel rod. A 9 in. sprocket is mounted on the rod. This sprocket is turned by a 2 in. sprocket on the end of a 4 ft. roller chain. See Figures 4.4 and 4.5. A hand crank is attached to the smaller sprocket.

The bevel gears on the lead screw shafts and rod have a 4:1 gear ratio. The gear ratio between the two sprockets is also 4:1. Thus a single turn on the hand crank will rotate the lead screw shaft 1/16th of a revolution. This rotation will raise or lower the I-beam cage and optical bed 0.0125 in. since there are 5 turns per inch on the lead screws. It was found that the smallest distance that the bed could accurately be moved was 0.0005 in.

The rigidity of the lead screw design eliminated most of the vertical vibrations inherent in the suspension design.

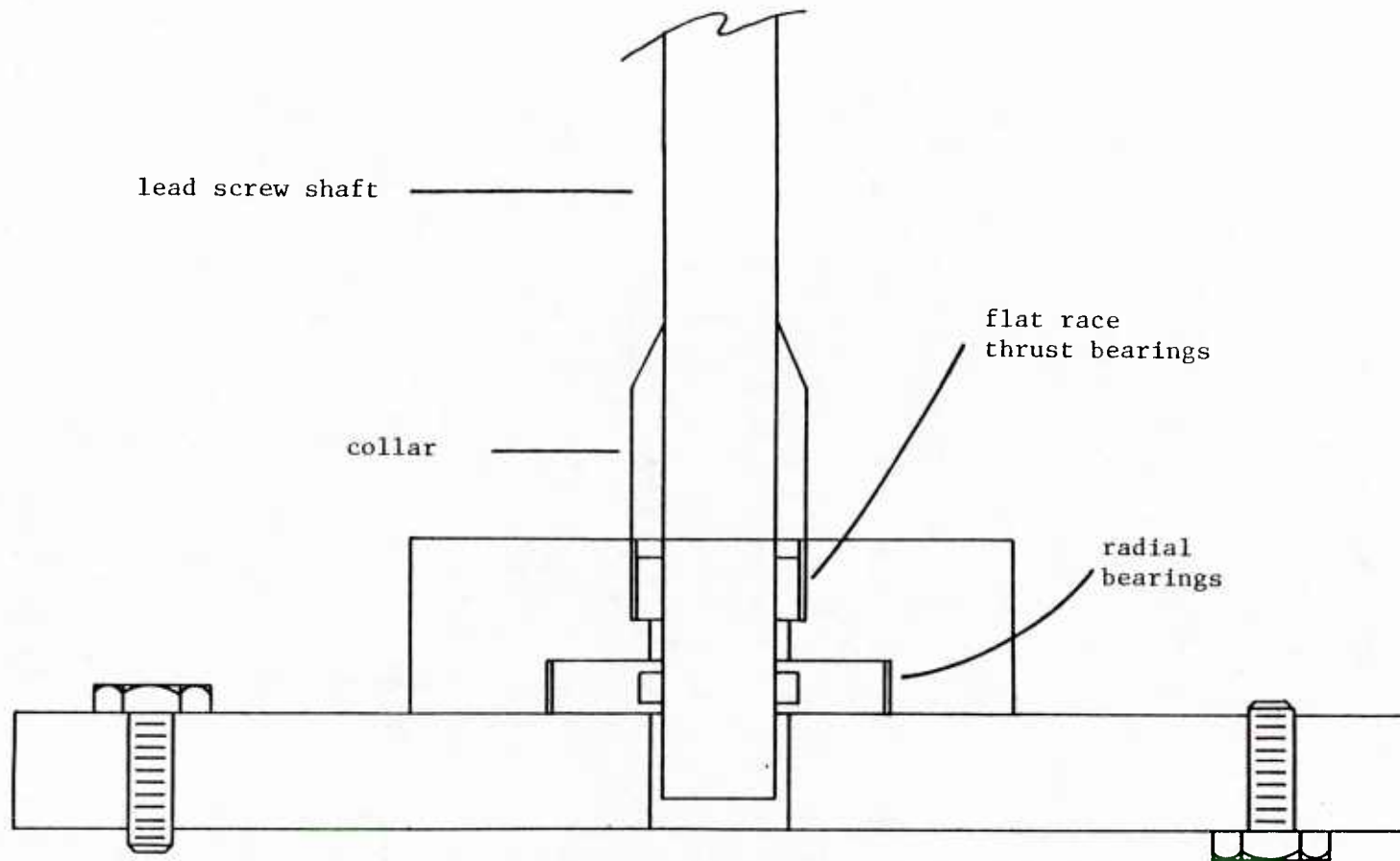


Figure 4.3 Detail of Lower Lead Screw Shaft Assembly

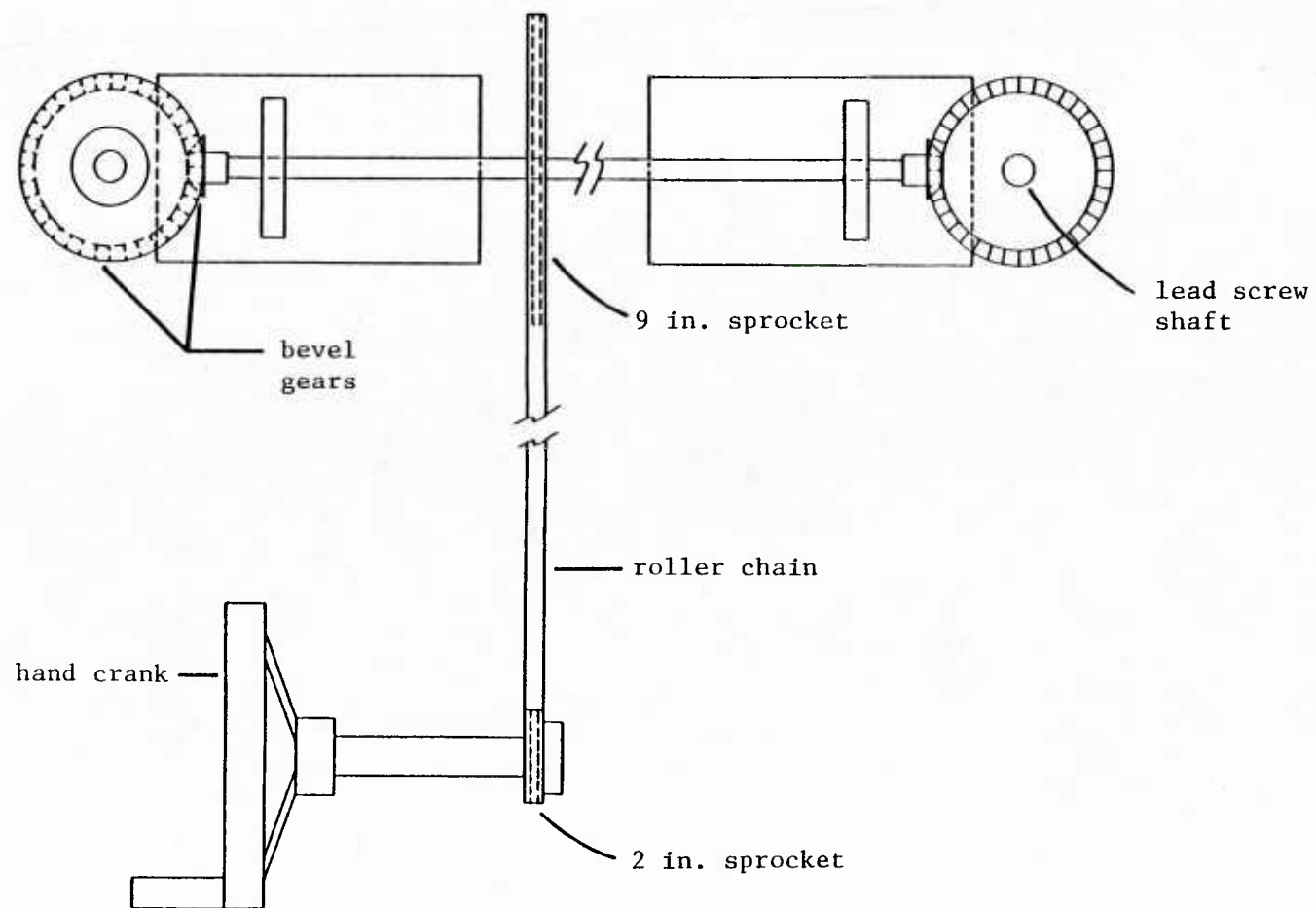


Figure 4.4 Top View of Mechanical Connection Between Lead Screw Shafts

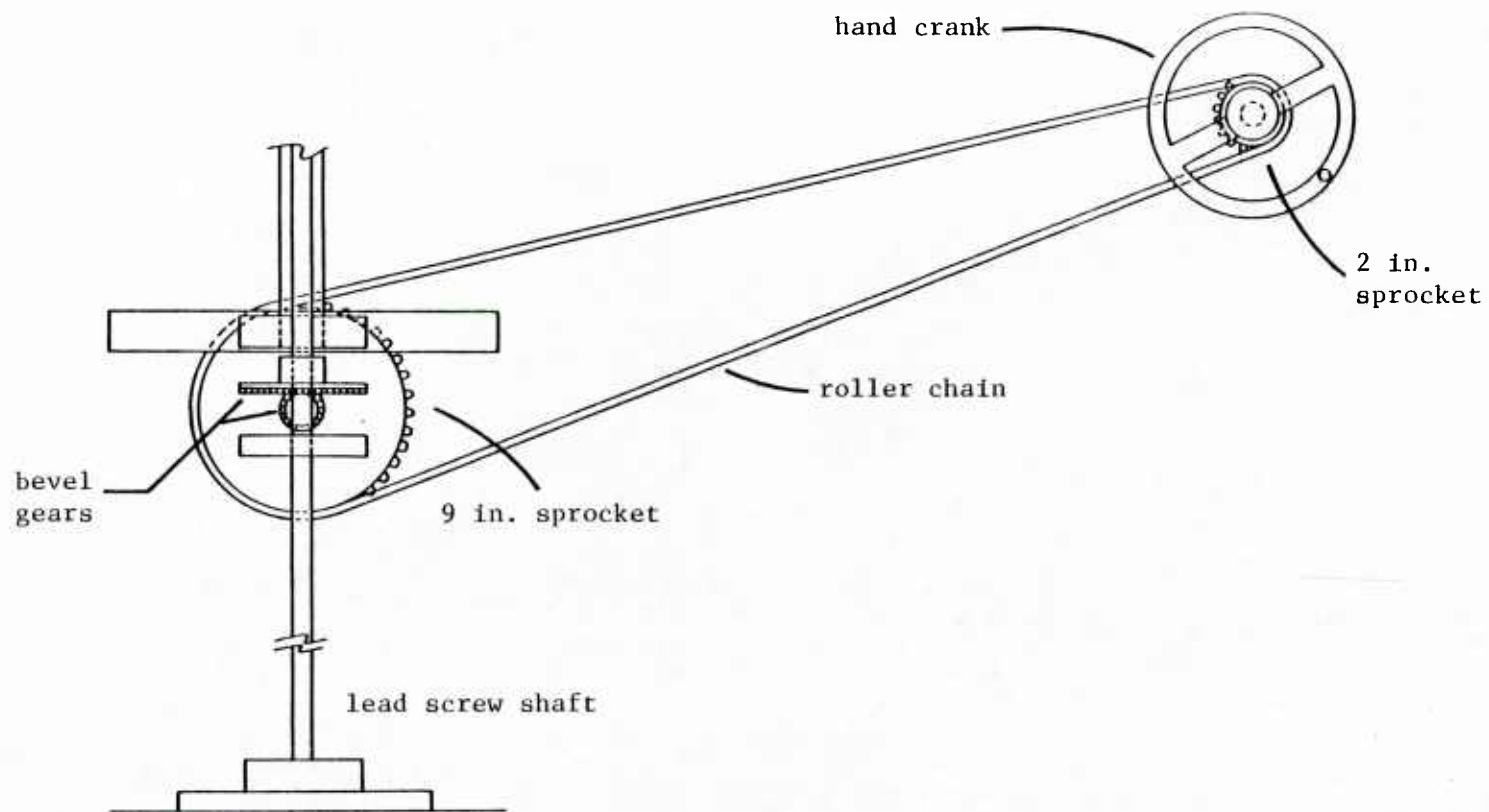


Figure 4.5 Side View of Lead Screw Shaft Crank Assembly

It was also necessary to modify the manner in which the traverse was moved in the horizontal direction. In the design of Buckles [9] the optical bed was moved horizontally on linear bearings with a pulley system using thin steel cables. This pulley system did not hold the bed stationary. The bed was free to move a little in the horizontal direction because the cables would stretch slightly when the heavy bed vibrated.

The horizontal vibration was substantially reduced by eliminating the pulley system and moving the optical bed on a second pair of lead screws. The new horizontal traverse design is shown in Figure 4.6. The pair of lead screws are pinned on each side to 1/2 in. stainless steel rods that are mounted horizontally and parallel to each other on the I-beam cage. As in the case of the vertical lead screws, these rods turn in unison because they are connected mechanically by a system of 4 bevel gears and a 3/8 in. steel rod. The lead screws turn through 1 in. \times 1-1/4 in. \times 2 in. brass nuts attached to the bed and the rods are rotated by turning a hand crank on a reduction gearbox. The entire horizontal traverse system is geared so that a single turn on the hand crank moves the optical bed 0.025 in.

III. LDV System and Data Acquisition

The velocity measurements were obtained using a single-channel dual-beam laser-Doppler velocimeter operated in the forward-scatter mode. The LDV system used was identical to that of Buckles [9] except for the receiving optics. Therefore only a brief description of the system and its operation will be given here. Also, for a

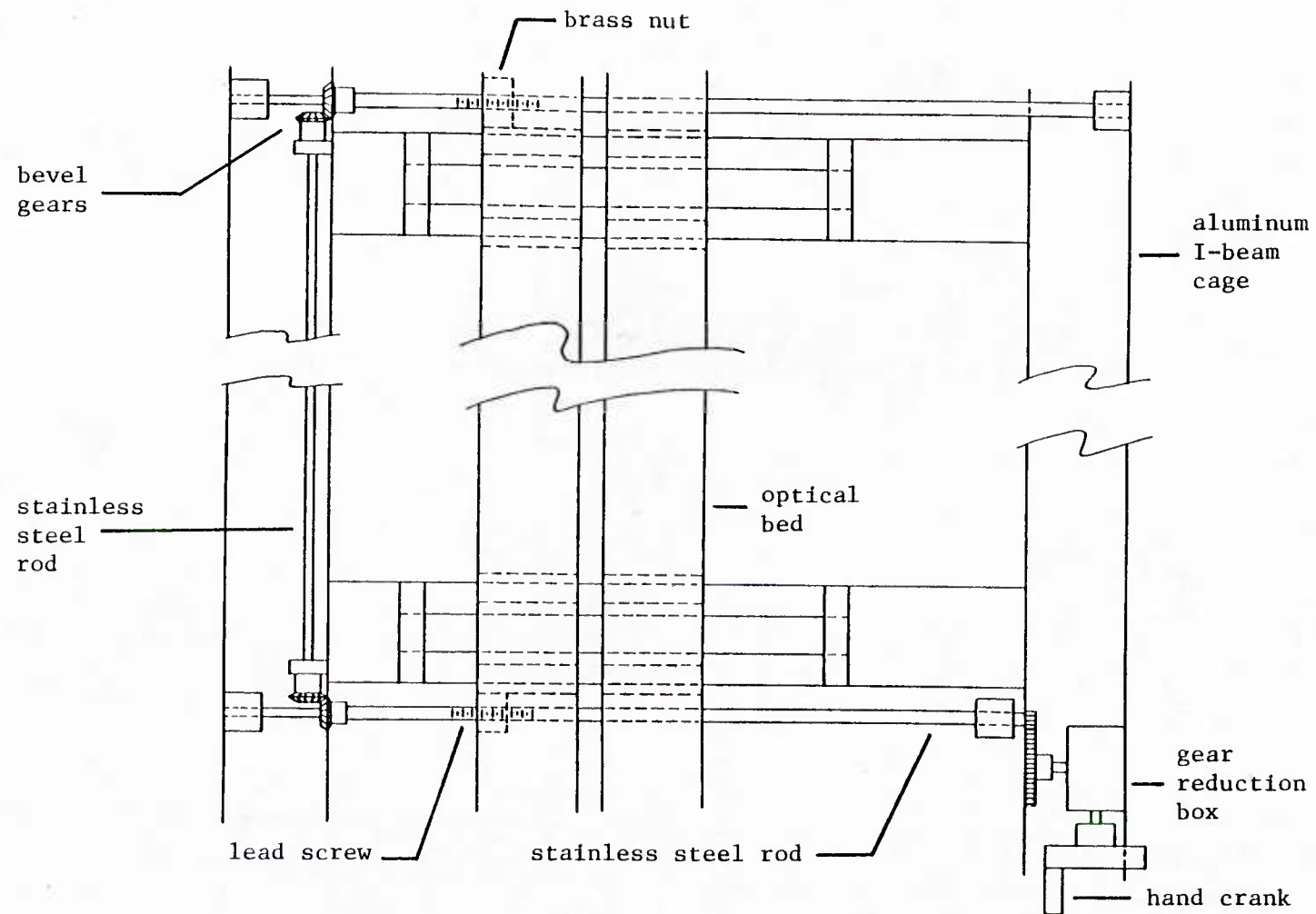


Figure 4.6 Top View of Horizontal Traversing Mechanism

complete description of LDV theory, the reader is referred to a report by Adrian [5].

The LDV system is shown in Figure 4.7. The system views the flowfield from the side of the channel. It consists of a 15 mW Spectra Physics He-Ne laser and TSI Inc. optics and a photomultiplier tube. A single laser beam is split by prisms into two beams in the horizontal plane. The beams are focused by a 250 mm focal-length transmitting lens and intersect to form the measurement volume where fluid velocity is determined. Two 2.27:1 beam expansion units were placed in series before the transmitting lens to reduce the measurement volume dimensions. The measurement volume, defined by the e^{-2} intensity distribution of the illuminating beams, is an ellipsoid with axes 3.5×10^{-3} cm, 3.5×10^{-3} cm, and 3.8×10^{-2} cm in the streamwise, normal and traverse directions.

The receiving optics is a TSI Model 9142-2 polarization separator. A schematic of this unit is shown in Figure 4.8. The unit can be used to collect and separate scattered light into two polarities that are perpendicular to each other. Light is collected with a 350 mm focal-length lens and focused by a 200 mm lens onto a mirror where it is reflected into a polarization splitter. The splitter sends horizontally polarized light to one photomultiplier tube and vertically polarized light to a second tube. The entire receiving optics unit is part of a LDV system manufactured by TSI to measure two velocity components that are distinguished by their polarities. However, for the experiments in this thesis a single component transmitting system was used where all of the scattered

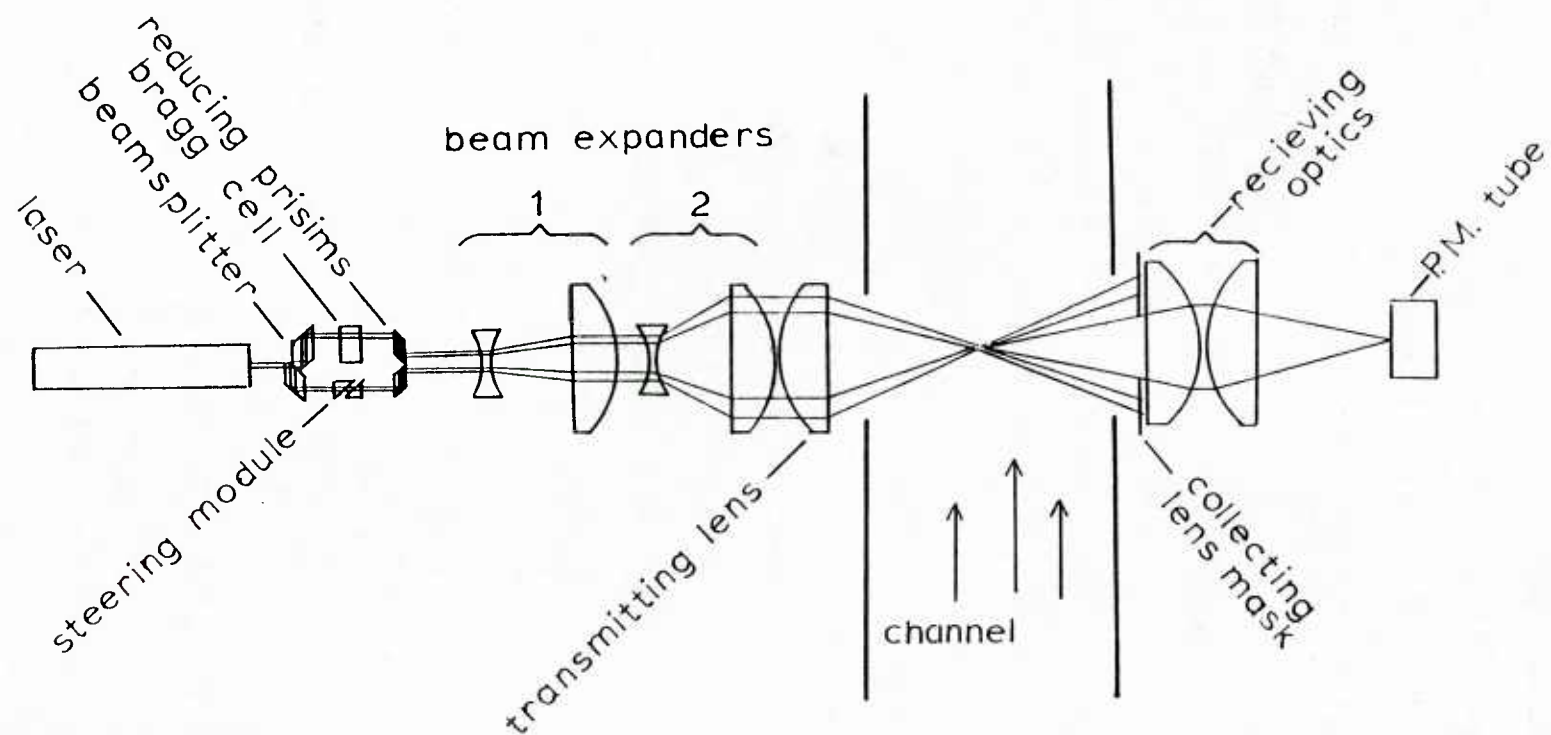


Figure 4.7 Laser-Doppler Velocimeter System

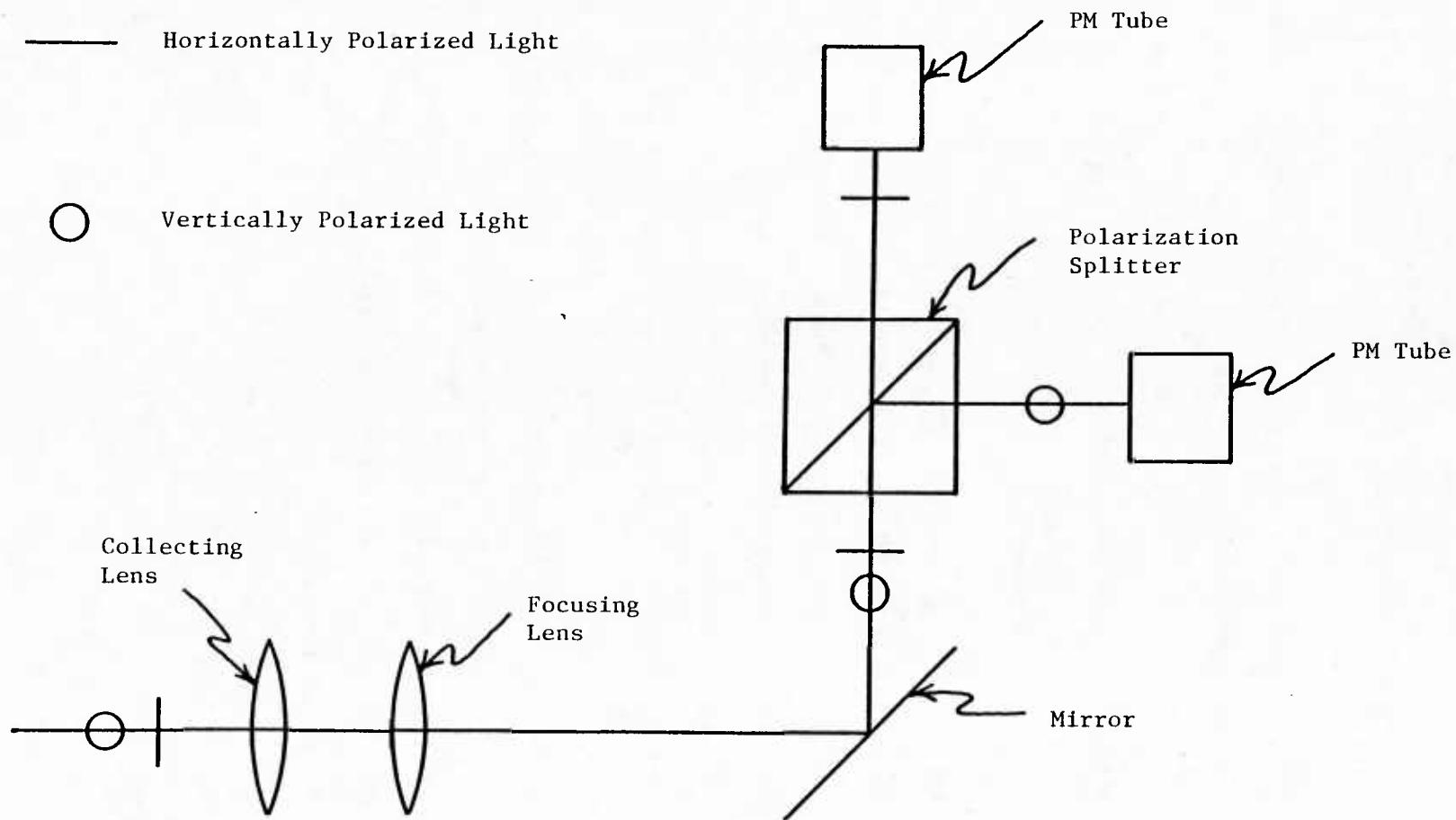


Figure 4.8 Schematic of Receiving Optics

light was vertically polarized. Consequently only one photomultiplier tube was used. The polarization separator was set up in anticipation of future two-component LDV measurements.

The Doppler signals were frequency shifted by 200-500 KHz to increase the count rate, lower fringe biasing and to detect negative velocities if present. Pedestal components were removed prior to processing with a 100 KHz high-pass filter. The signal processor was a TSI Model 1090 frequency tracker operated on its 500 KHz and 5MHz ranges.

The water was prepared by filtering out all particles larger than 3 μm in diameter and adding 0.5 μm white latex paint spheres manufactured by Dow Chemical Co. The concentration of these seed particles was such that on the average only one particle was in the measurement volume at any given time. Under these conditions data rates of 2000-4000 and 4000-8000 samples per second were achieved at Reynolds numbers of 6400 and 38,800 respectively. The resulting signals from the tracker had "high data density" (Adrain [5]); i.e. there were many velocity samples per Taylor microscale of the flow. In this region of operation the signals could be assumed to be continuous. They were filtered at 1 KHz to remove noise and sampled at 80 Hz by an 8-bit A/D converter. Mean velocities and mean root mean square fluctuations were calculated by averaging batches of 4000 samples.

CHAPTER 5

EXPERIMENTAL RESULTS

I. Flat Channel Data

A. Friction Factors

The velocity measurements presented in this thesis are made nondimensional with respect to wall parameters. Velocities are made dimensionless with flat channel friction velocities, $u^* = \sqrt{\frac{\tau_w}{\rho}}$, obtained from the flat channel electrochemical shear stress data of Thorsness [44]. Distances above the wave surface are made dimensionless with respect to ν/u^* , where ν is the kinematic viscosity. Figure 5.1 shows Thorsness' Fanning friction factor data versus a Reynolds number, Re_b , based on the half channel height, h_d , and the bulk velocity, U_b . The data are well fitted by the Blasius type equation

$$f = 0.0612 Re_b^{-1/4} \quad (5.1)$$

Equation 5.1 is identical to that obtained by Cohen [15] for air flow in a one inch rectangular channel. The friction velocity is defined as a function of the friction factor according to the following equation

$$u^* = U_b \sqrt{f/2} \quad (5.2)$$

The channel calculations are also normalized with wall parameters. However, in order to keep the calculations self consistent and independent of the data, the friction velocities used were obtained

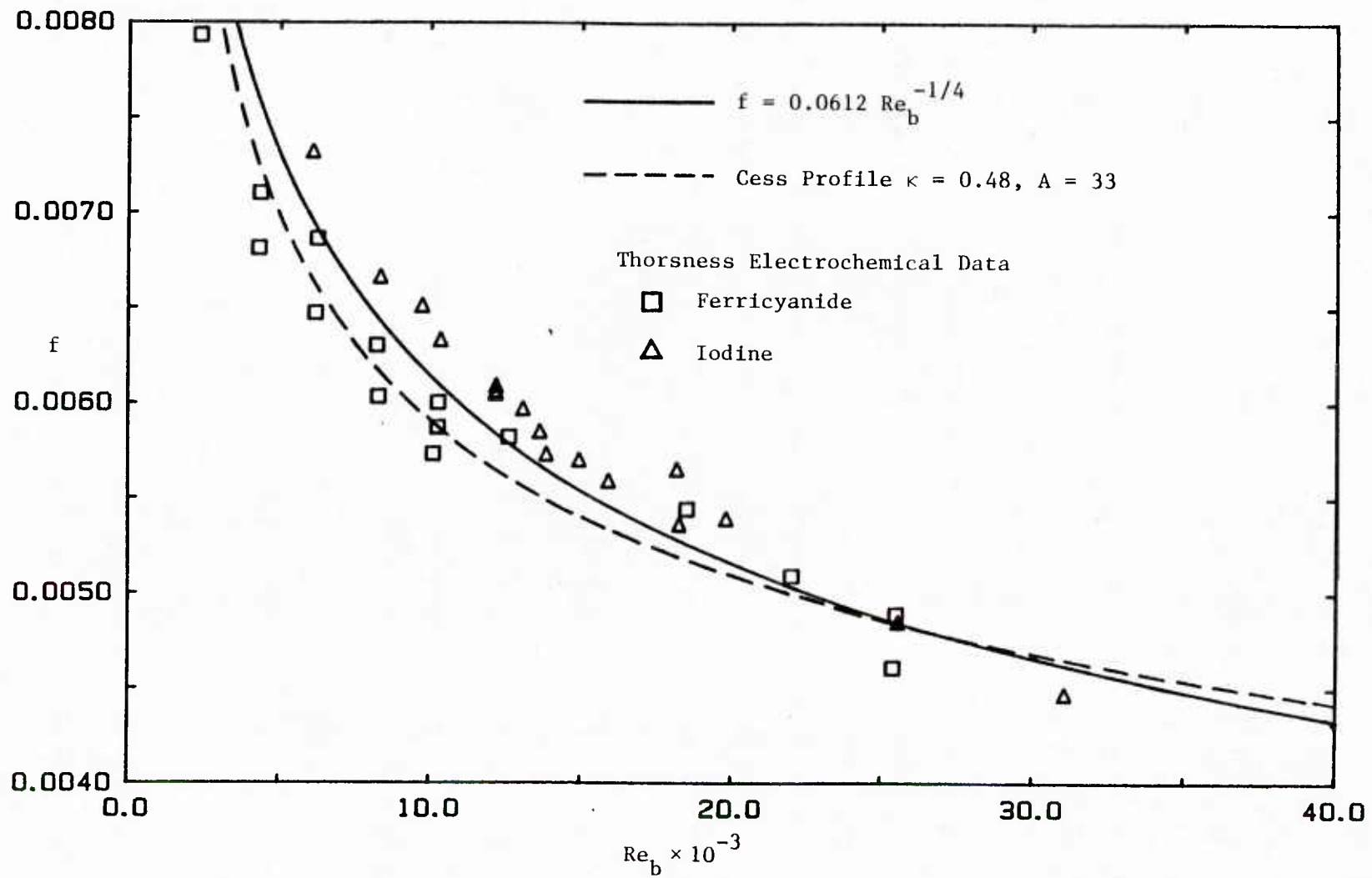


Figure 5.1 Fanning Friction Factor for Flat Channel

by applying the Cess profile to a flat channel. The flat channel friction factor-Reynolds number relationship predicted by the Cess profile with $\kappa = 0.48$ and $A = 33$ is also shown in Figure 5.1. Good agreement with the friction factor data is observed.

The values of the von Karman constant and the van Driest parameter were selected to give the best fit to equation (5.1). These values differ from the generally accepted values of $\kappa = 0.41$ and $A \approx 25$. It is believed that these constants can be adjusted freely for the Cess profile because they lose some physical meaning due to the matching process in the derivation of this equation.

Values of $\kappa = 0.48$ and $A = 33$ were used for all wavy surface channel calculations.

B. Mean Velocities

Thorsness [44] obtained flat channel velocity profiles at several bulk Reynolds numbers, Re_b , ranging from 5190 to 29,600. Figure 5.2 shows a comparison of Thorsness' data at the extremes of this range with Cess profiles using $\kappa = 0.48$ and $A = 33$. Good agreement is observed. A good prediction of flat channel velocity profiles with the Cess equation is a prerequisite for applying this eddy viscosity model to the more complicated flow over wavy surfaces.

C. Turbulent Intensities

In order to test the ability of the LDV system to measure accurately turbulent intensities, measurements of the streamwise intensity, $\sqrt{u_d'^2} / u^*$, were obtained in a flat channel. Figure 5.3 shows intensity data at $Re_b = 11,000$. A maximum intensity of 2.7 in wall units is observed at $y_d u^* / \nu = 14$. This agrees closely with the

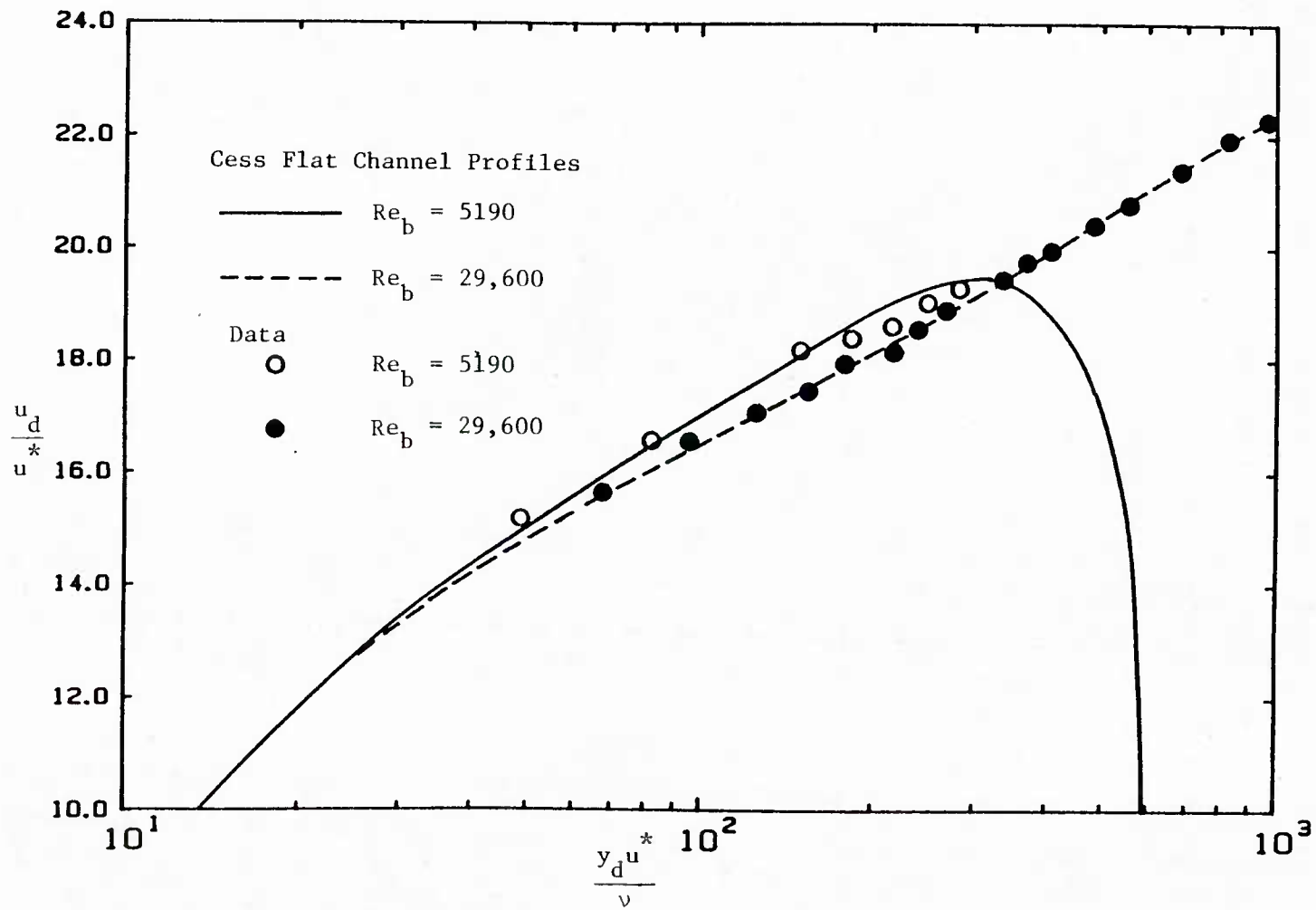


Figure 5.2 Comparison of Flat Channel Velocity Data of Thorsness with Cess Profile

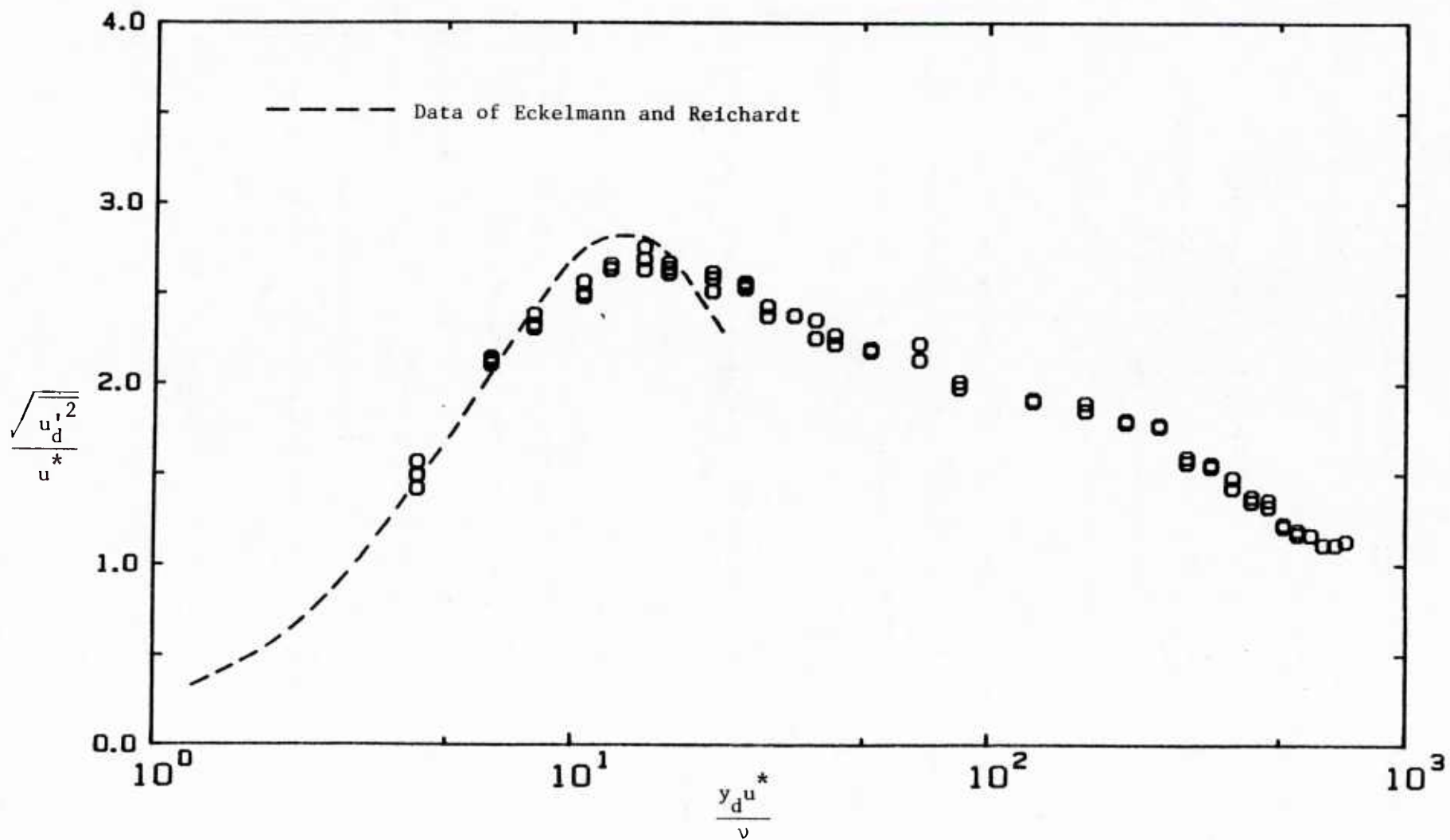


Figure 5.3 Flat Channel Streamwise Intensity Profile, $Re_b = 11,000$

measurements of Eckelmann and Reichardt [18], which are also shown in Figure 5.3. In other channel investigations Compte-Bellot [16], Clark [14], Hussain and Reynolds [21], and Reischman and Tiederman [37] found maximum intensities ranging from 2.5 - 3.3 at $y_d u^* / \nu$ locations of 12-15. The centerline intensity of 1.1 is slightly higher than values from the above literature which range from 0.75-1.0. A possible source of the increased intensity is vibrations of the optical traverse and test section.

It should be noted that the literature intensity measurements were obtained over a wide range of Reynolds numbers. However, comparisons with the data in Figure 5.3 are valid since both the maximum and centerline intensities are relatively insensitive to flowrate when normalized with wall parameters.

A tabulation of the flat channel intensity data may be found in Appendix B.

II. Flow Regime Map

Two sets of velocity measurements over waves were taken, one each in the linear and nonlinear shear stress response regions discussed in Chapter 2. The set of data in the linear region was obtained over a wave of steepness $2a_d/\lambda = 0.03125$ with a dimensionless wavenumber of $\alpha_d \nu / u^* = 0.008$ ($Re_b = 6400$). For the nonlinear set $2a_d/\lambda$ was equal to 0.05 and $\alpha_d \nu / u^*$ was equal to 0.00165 ($Re_b = 38,800$). Figure 5.4 shows the location of the two sets of data on the flow regime map.

The data consist of time averaged velocity profiles and profiles of the root mean square value of the fluctuating streamwise intensity.

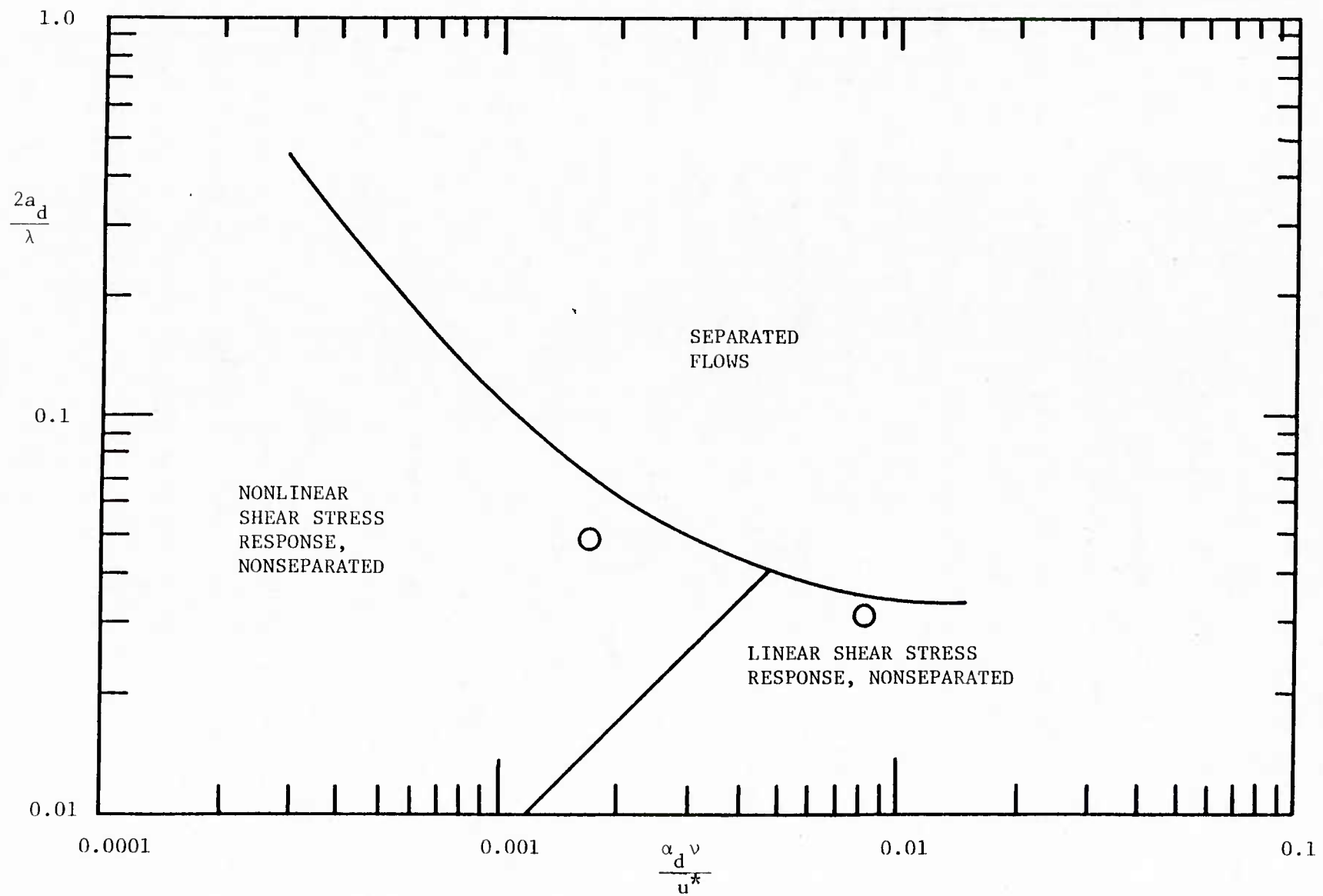


Figure 5.4 Location of LDV Data on Flow Regime Map

An analysis and discussion of the data and a comparison with the turbulence models described in Chapter 3 is given in Chapter 6.

III. Results for Wave of Steepness $2a_d/\lambda = 0.03125$.

The wave steepness $2a_d/\lambda = 0.03125$ and the wavenumber $\alpha_d v/u^* = 0.008$ were chosen for the first set of data because a linear velocity field response was expected under these conditions. A wave of lower steepness would have produced a closer approximation to a linear flowfield. However, the wave of $2a_d/\lambda = 0.03125$ was used because split film measurements of Zilker [48] indicated that a wave with $2a_d/\lambda = 0.0125$ did not cause large enough changes in the velocity profiles to be distinguished from a flat plate profile. A larger amplitude wave was not used since separation may have resulted (Zilker [48]). The wavenumber $\alpha_d v/u^* = 0.008$ corresponds to the lowest steady flowrate that can be obtained with the flow loop. Higher flowrates produce a more nonlinear flowfield by increasing the dimensionless wave amplitude, $a_d u^*/v$. The dimensionless wave amplitude is equal to 12.3. Zilker [48] observed linear shear stress responses for $a_d u^*/v < 27$.

Measurements of the mean velocity profiles at the ten x_d/λ positions are shown in Figures 5.5-5.14. Each profile was obtained by traversing the LDV vertically from near the wave surface to the channel centerline. The closest data to the wave are at $y_d u^*/v = 2$. Closer measurements were not possible due to vibrations of the wave, extraneous laser light reflections off the wave surface, and the measurement volume diameter of 0.5 wall units. The channel centerline

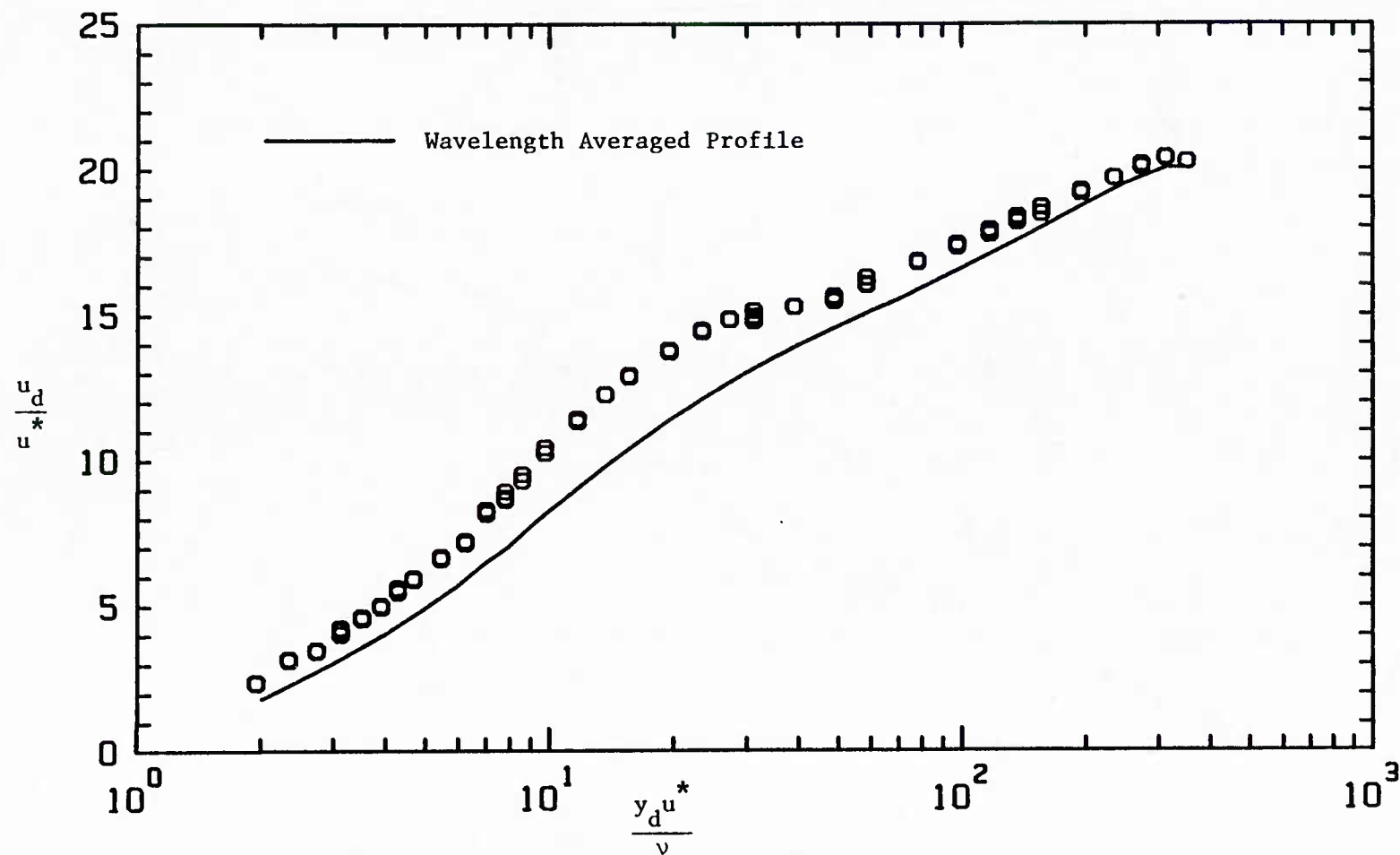


Figure 5.5 Mean Velocity Measurements, $x_d/\lambda = 0.1$, $2a_d/\lambda = 0.03125$,
 $Re_b = 6400$, $2h_d/\lambda = 1.0$

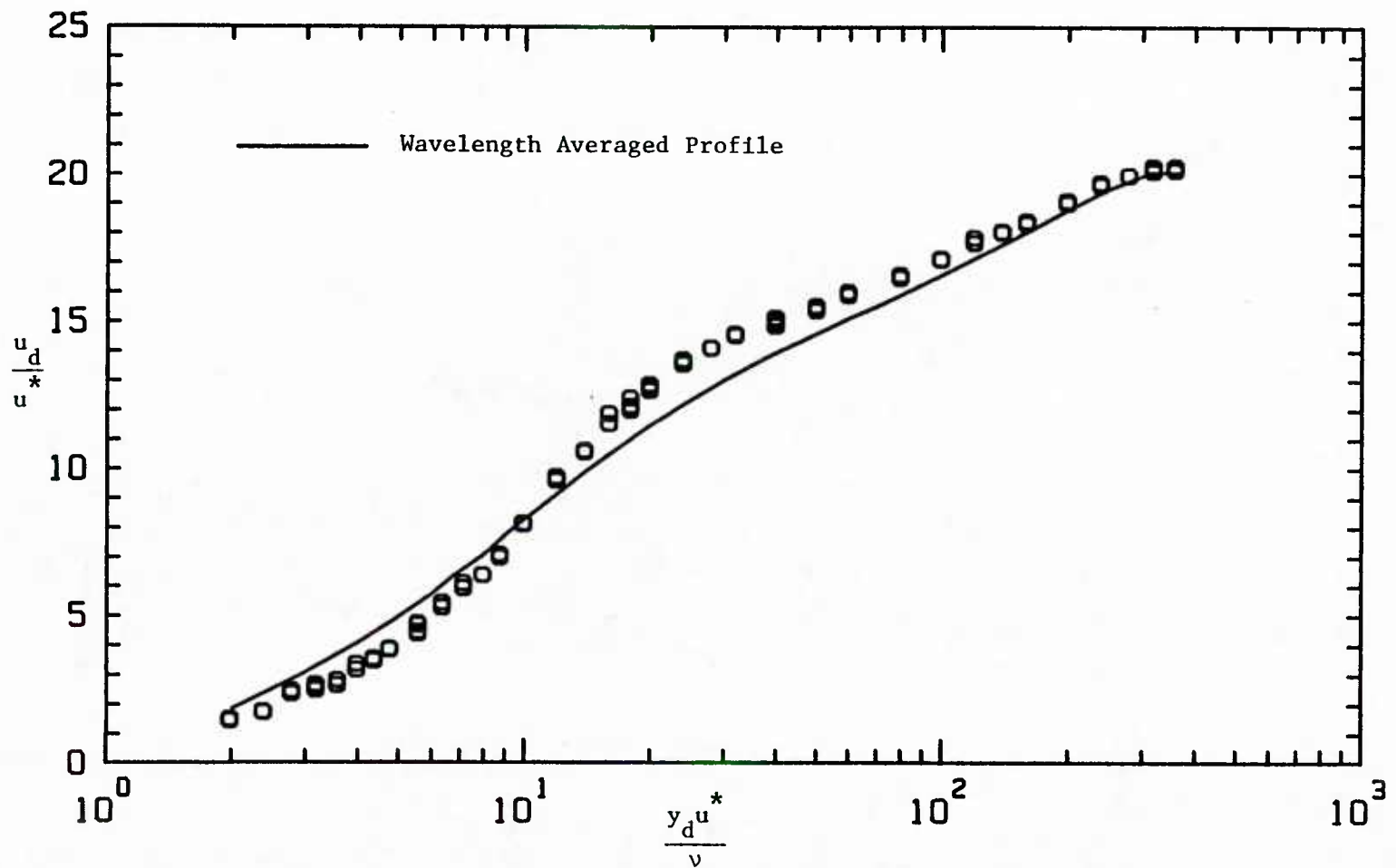


Figure 5.6 Mean Velocity Measurements, $x_d/\lambda = 0.2$, $2a_d/\lambda = 0.03125$,
 $Re_b = 6400$, $2h_d/\lambda = 1.0$

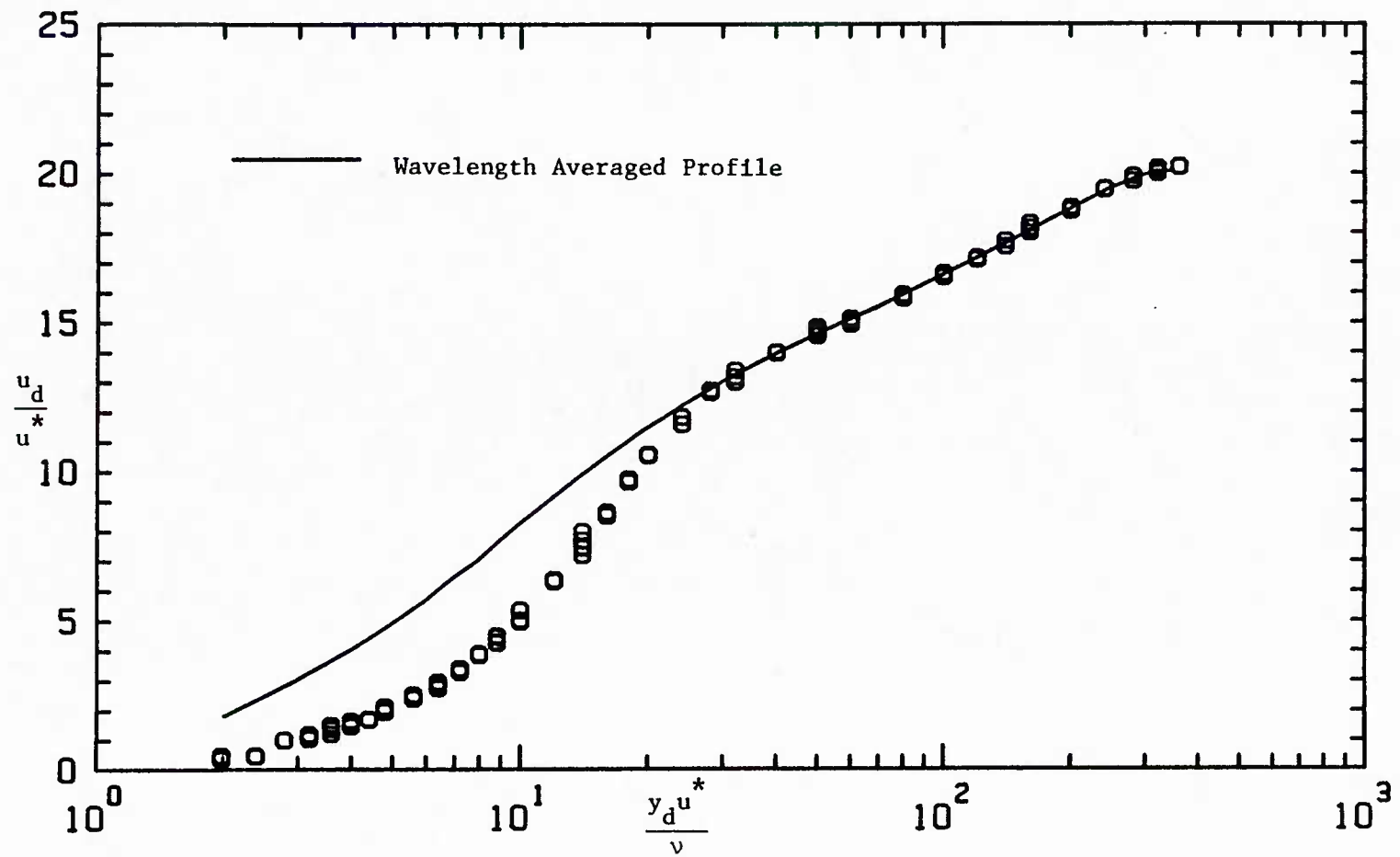


Figure 5.7 Mean Velocity Measurements, $x_d/\lambda = 0.3$, $2a_d/\lambda = 0.03125$,
 $Re_b = 6400$, $2h_d/\lambda = 1.0$

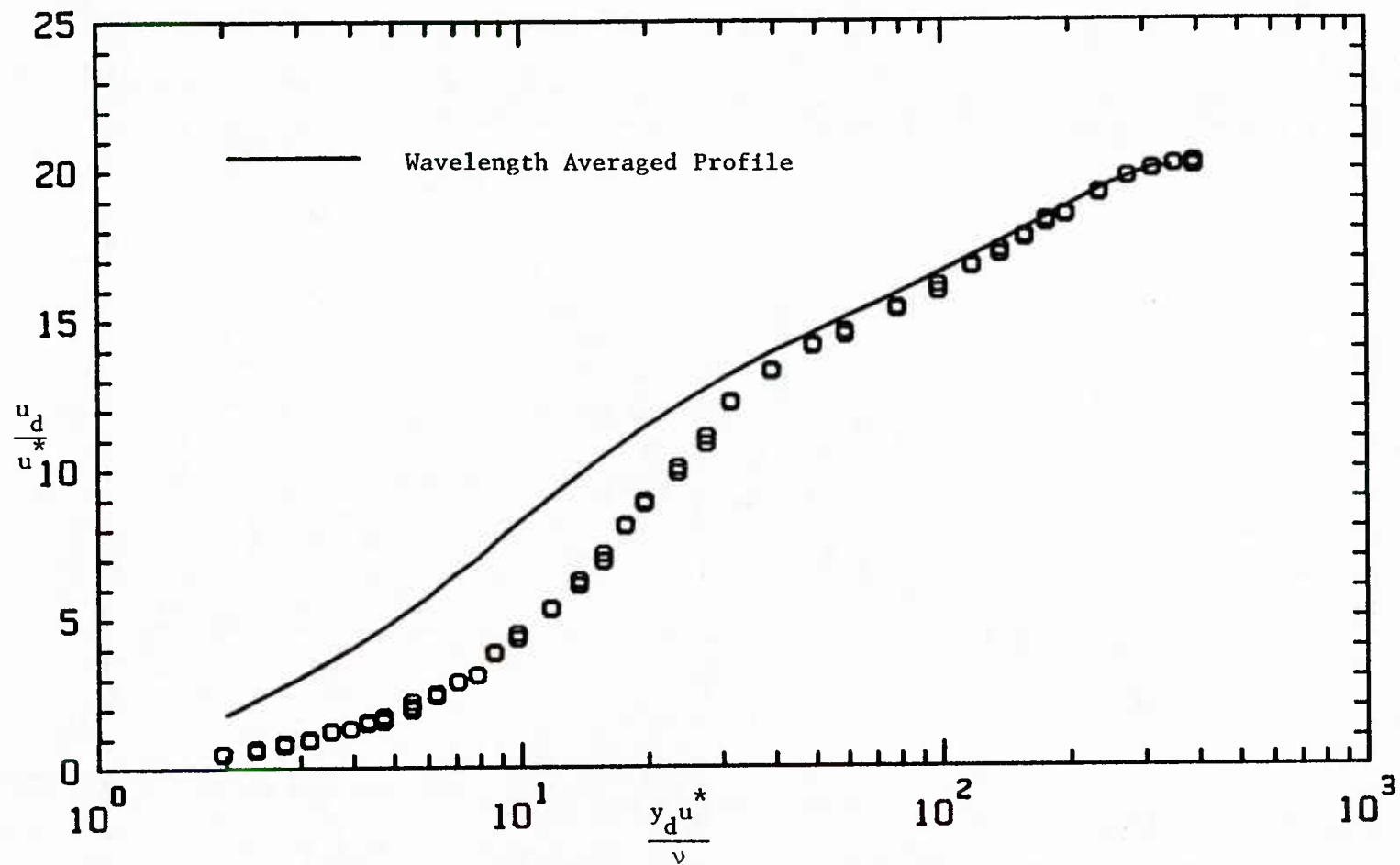


Figure 5.8 Mean Velocity Measurements, $x_d/\lambda = 0.4$, $2a_d/\lambda = 0.03125$,
 $Re_b = 6400$, $2h_d/\lambda = 1.0$

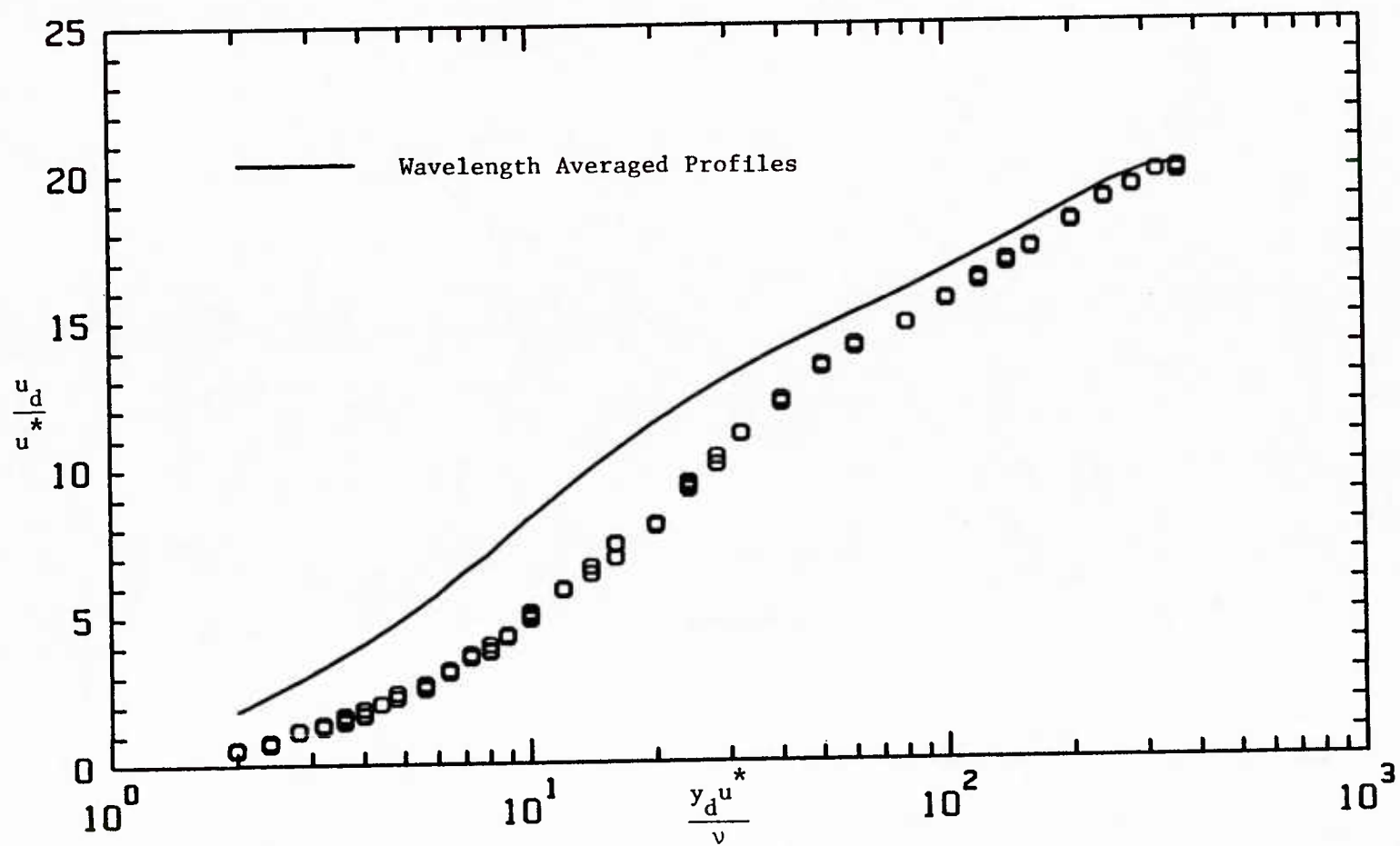


Figure 5.9 Mean Velocity Measurements, $x_d/\lambda = 0.5$, $2a_d/\lambda = 0.03125$,
 $Re_b = 6400$, $2h_d/\lambda = 1.0$

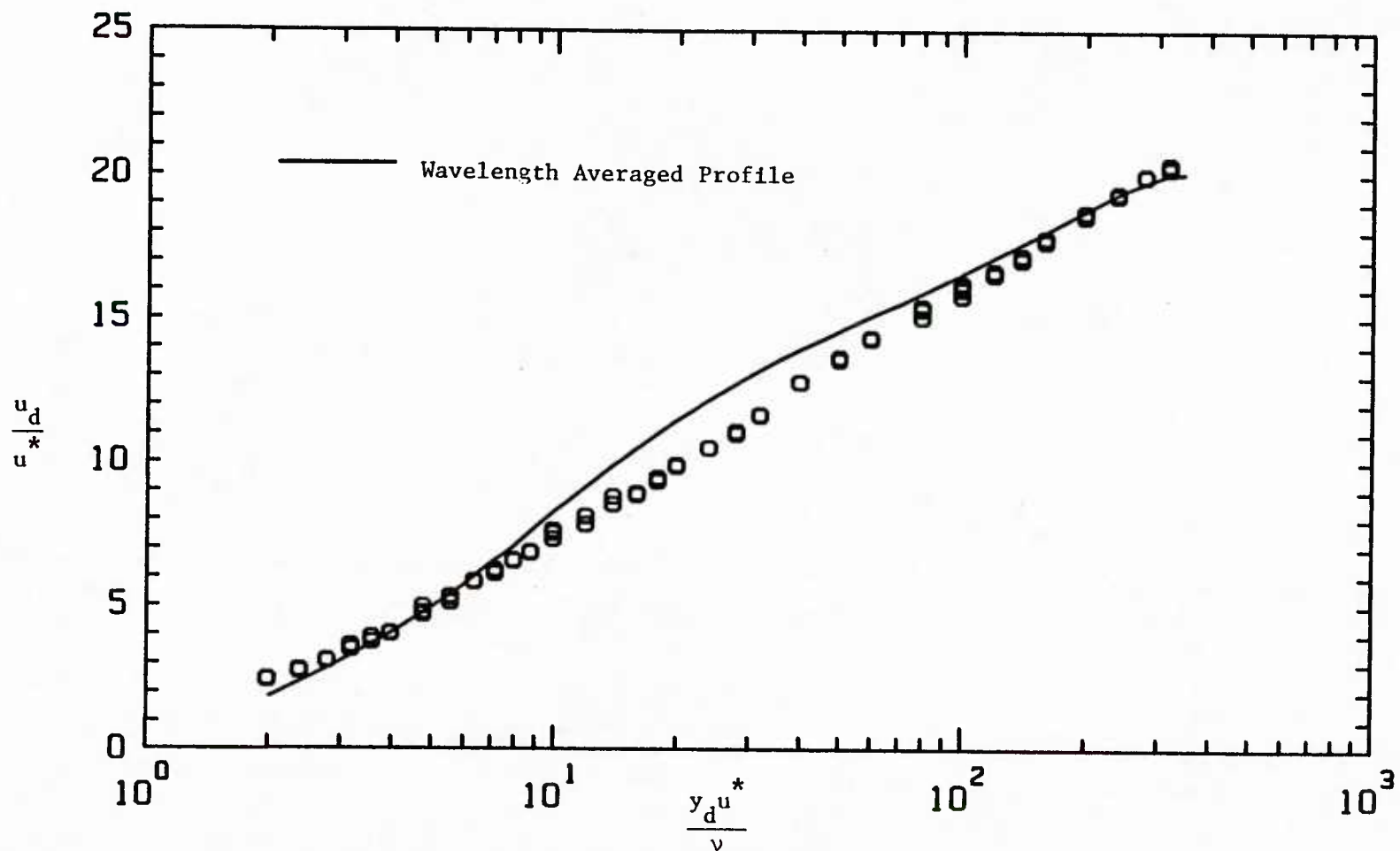


Figure 5.10 Mean Velocity Measurements, $x_d/\lambda = 0.6$, $2a_d/\lambda = 0.03125$,
 $Re_b = 6400$, $2h_d/\lambda = 1.0$

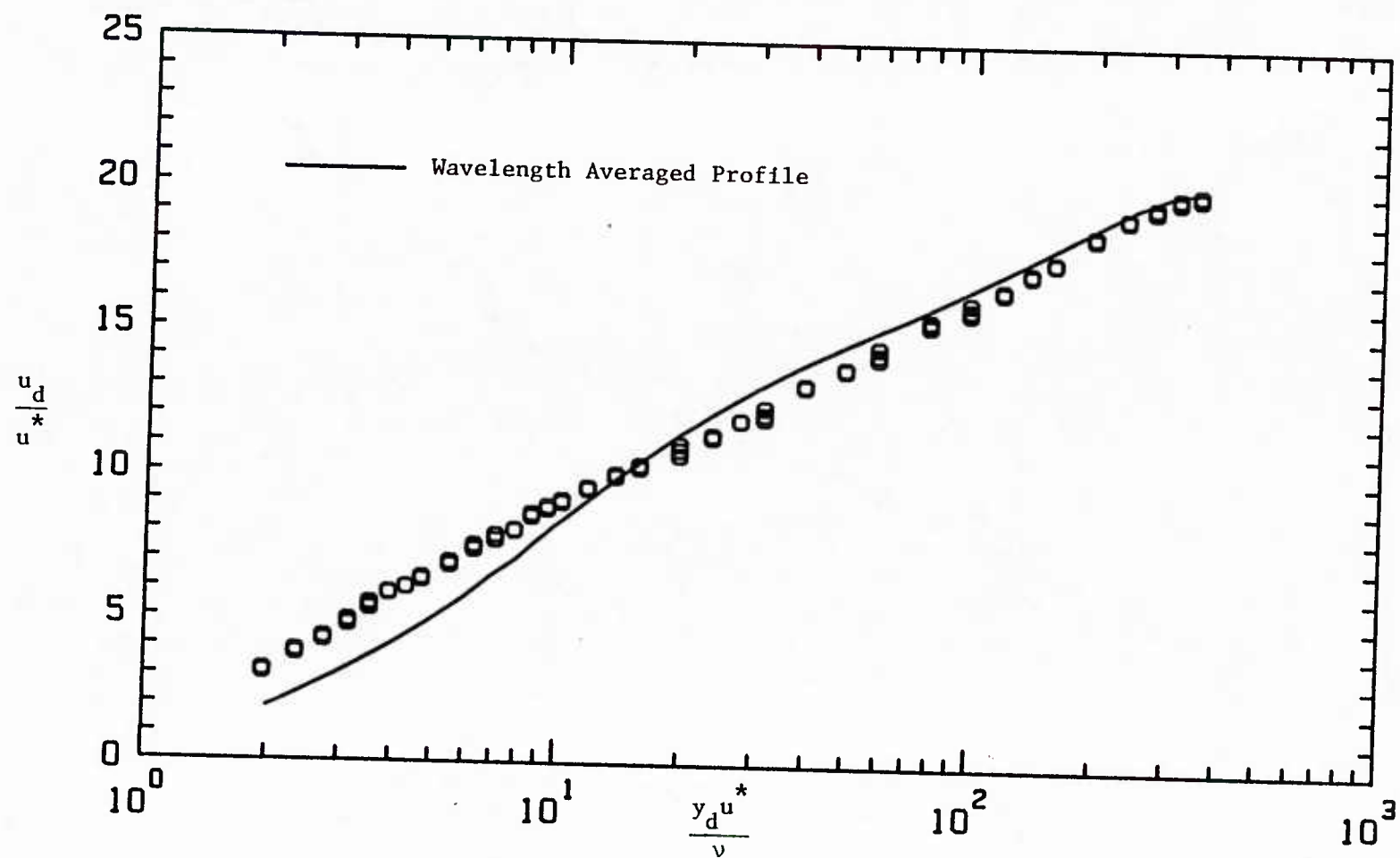


Figure 5.11 Mean Velocity Measurements, $x_d/\lambda = 0.7$, $2a_d/\lambda = 0.03125$
 $Re_b = 6400$, $2h_d/\lambda = 1.0$

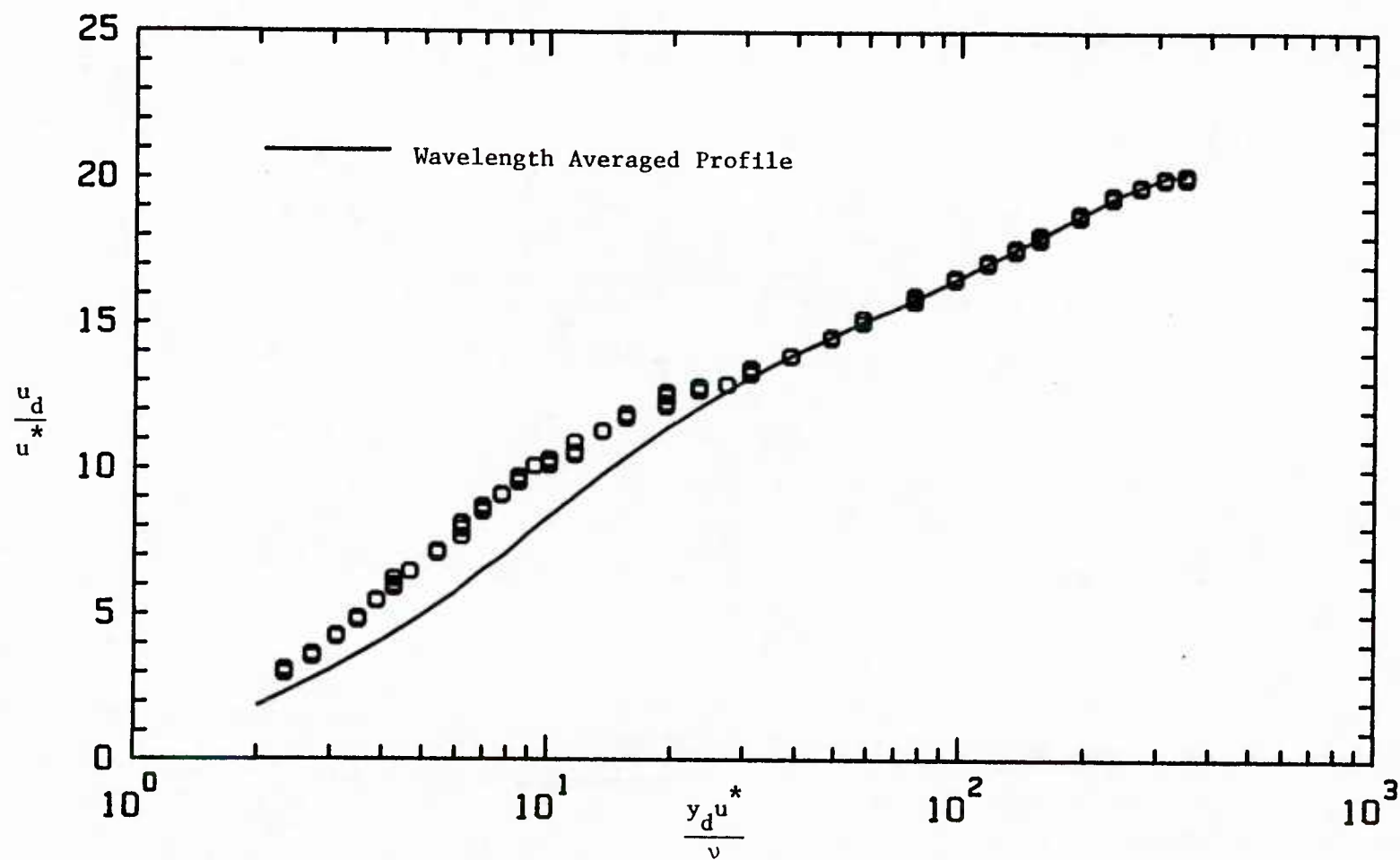


Figure 5.12 Mean Velocity Measurements, $x_d/\lambda = 0.8$, $2a_d/\lambda = 0.03125$,
 $Re_b = 6400$, $2h_d/\lambda = 1.0$

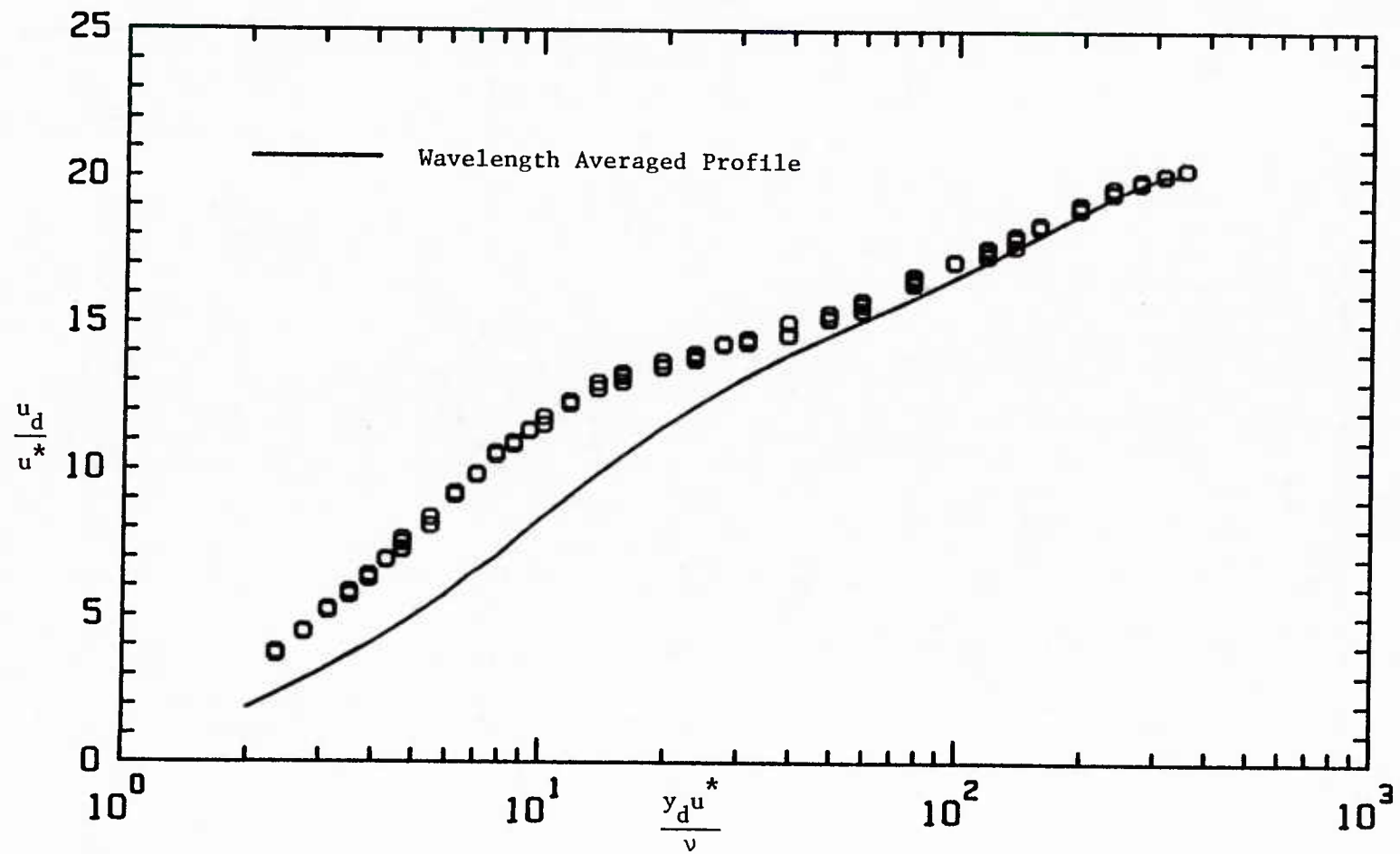


Figure 5.13 Mean Velocity Measurements, $x_d/\lambda = 0.9$, $2a_d/\lambda = 0.03125$,
 $Re_b = 6400$, $2h_d/\lambda = 1.0$

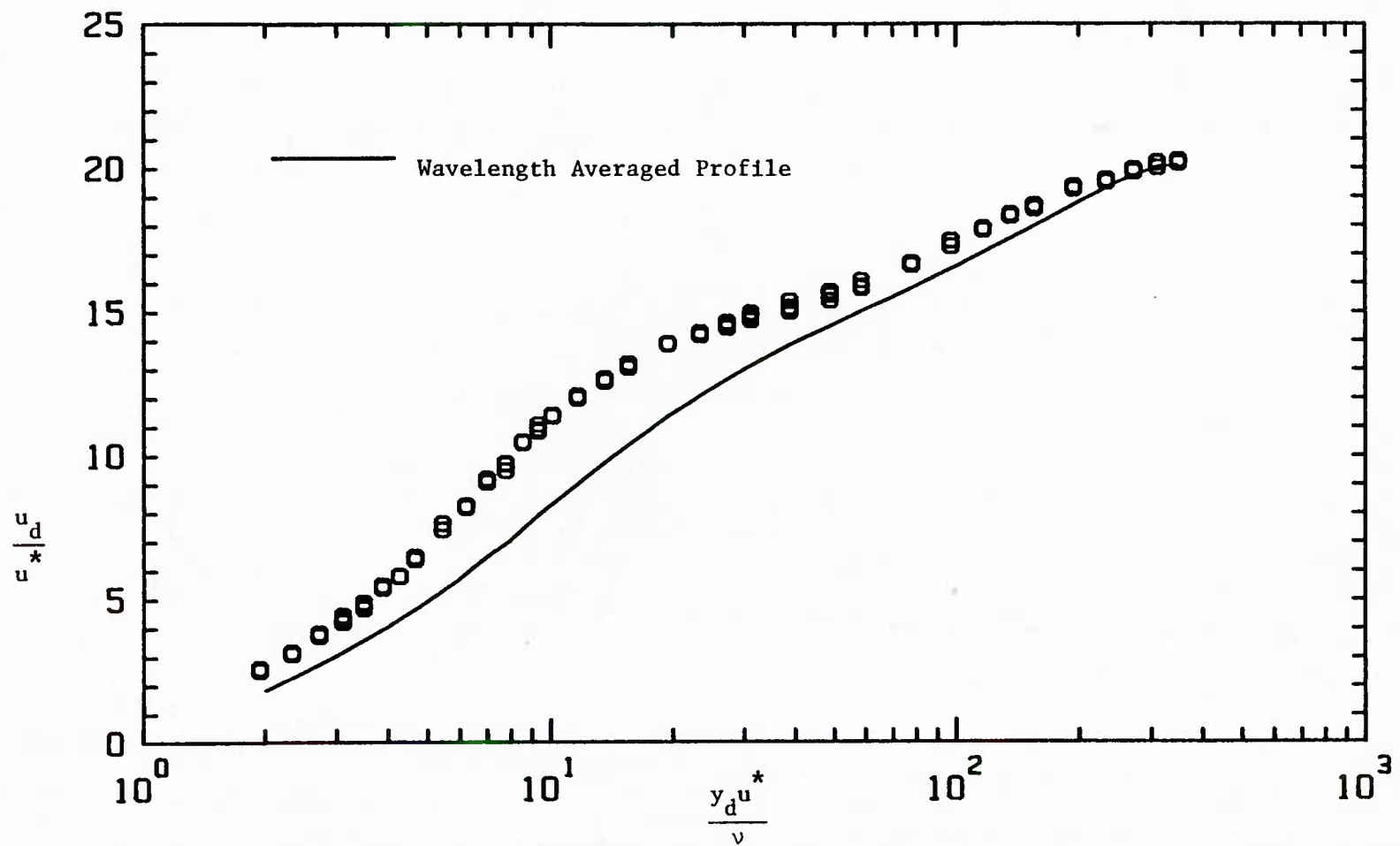


Figure 5.14 Mean Velocity Measurements, $x_d/\lambda = 1.0$, $2a_d/\lambda = 0.03125$,
 $Re_b = 6400$, $2h_d/\lambda = 1.0$

is about $365 y_d u^* / \nu$ units above the average wave height. Approximately twenty measurements were taken within the viscous wall region at each x_d / λ position. The uncertainties in the distance, $y_d u^* / \nu$, and the velocity, u_d / u^* , are about 0.40 and 0.25 dimensionless units respectively.

Figure 5.5-5.14 also contain the wavelength averaged profile as a reference for observing disturbances about the mean flowfield. The calculation of the average profile is discussed in Chapter 6, Section I.B. The most striking feature of these figures is that there is a lag in the reaction of the fluid to the wave which increases with increasing height.

Profiles of the streamwise intensity are given in Figures 5.15-5.24 compared with the reference wavelength averaged intensity profile. These figures show that the outer portion of the viscous wall region lags the inner portion in reacting to the wave. A detailed discussion of this behavior is given in Chapter 6, Section I.G.

IV. Results for Wave of Steepness $2a_d / \lambda = 0.05$

The conditions for the second set of data, $2a_d / \lambda = 0.05$ and $\alpha_d \nu / u^* = 0.00165$, were chosen because a highly nonlinear nonseparated flowfield was expected for these conditions. Measurements of this flowfield should provide a good test of the nonlinear channel analysis for waves of finite amplitude and of turbulence Models C* and D*. These models have not previously been applied to predict the velocity field over waves of finite amplitude with nonseparated flows.

Mean velocity profiles are shown in Figures 5.25-5.34 compared with the wavelength averaged profile. The closest measurement to the

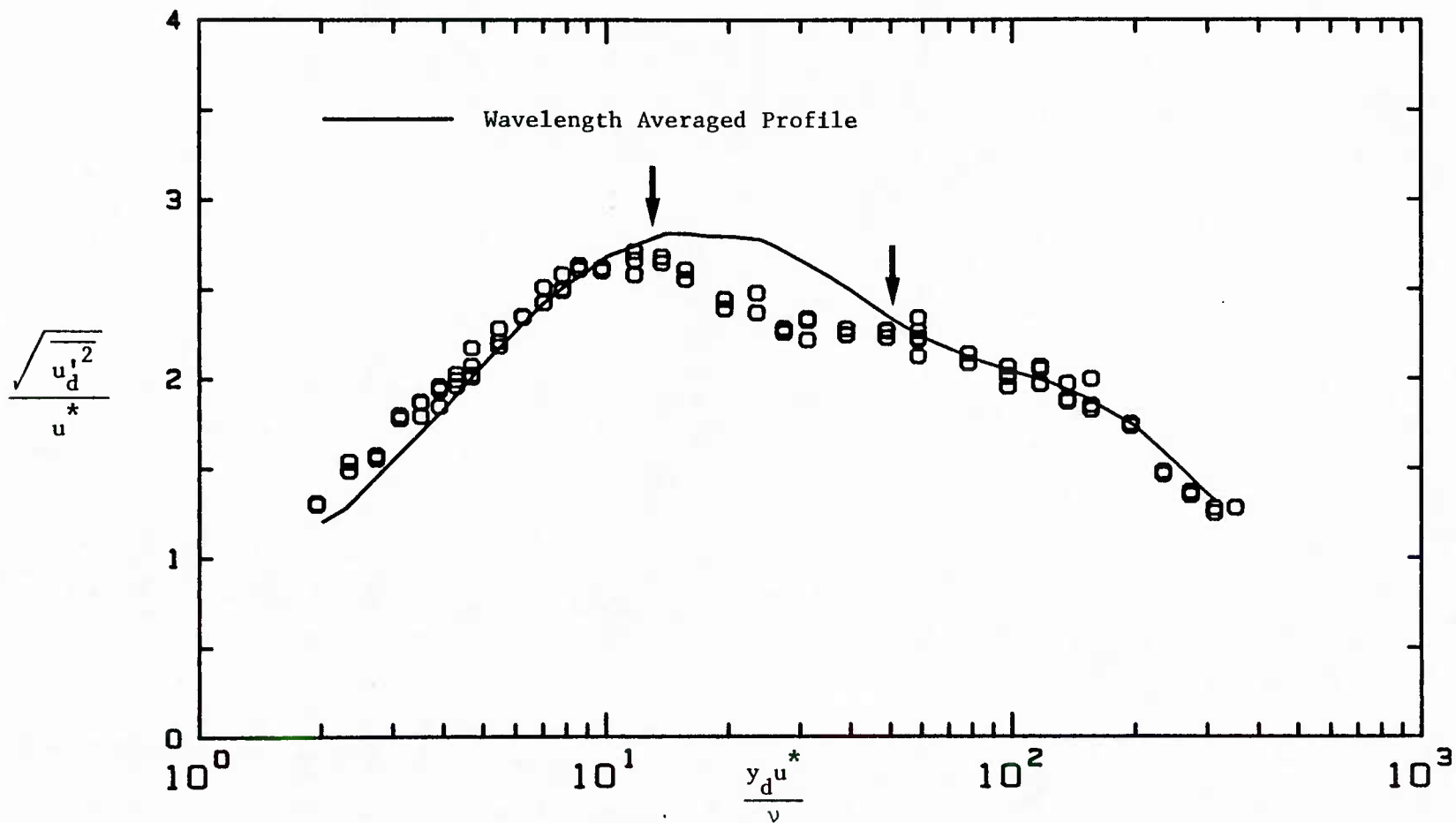


Figure 5.15 Streamwise Intensity Measurements, $x_d/\lambda = 0.1$,
 $2a_d/\lambda = 0.03125$, $Re_b = 6400$, $2h_d/\lambda = 1.0$

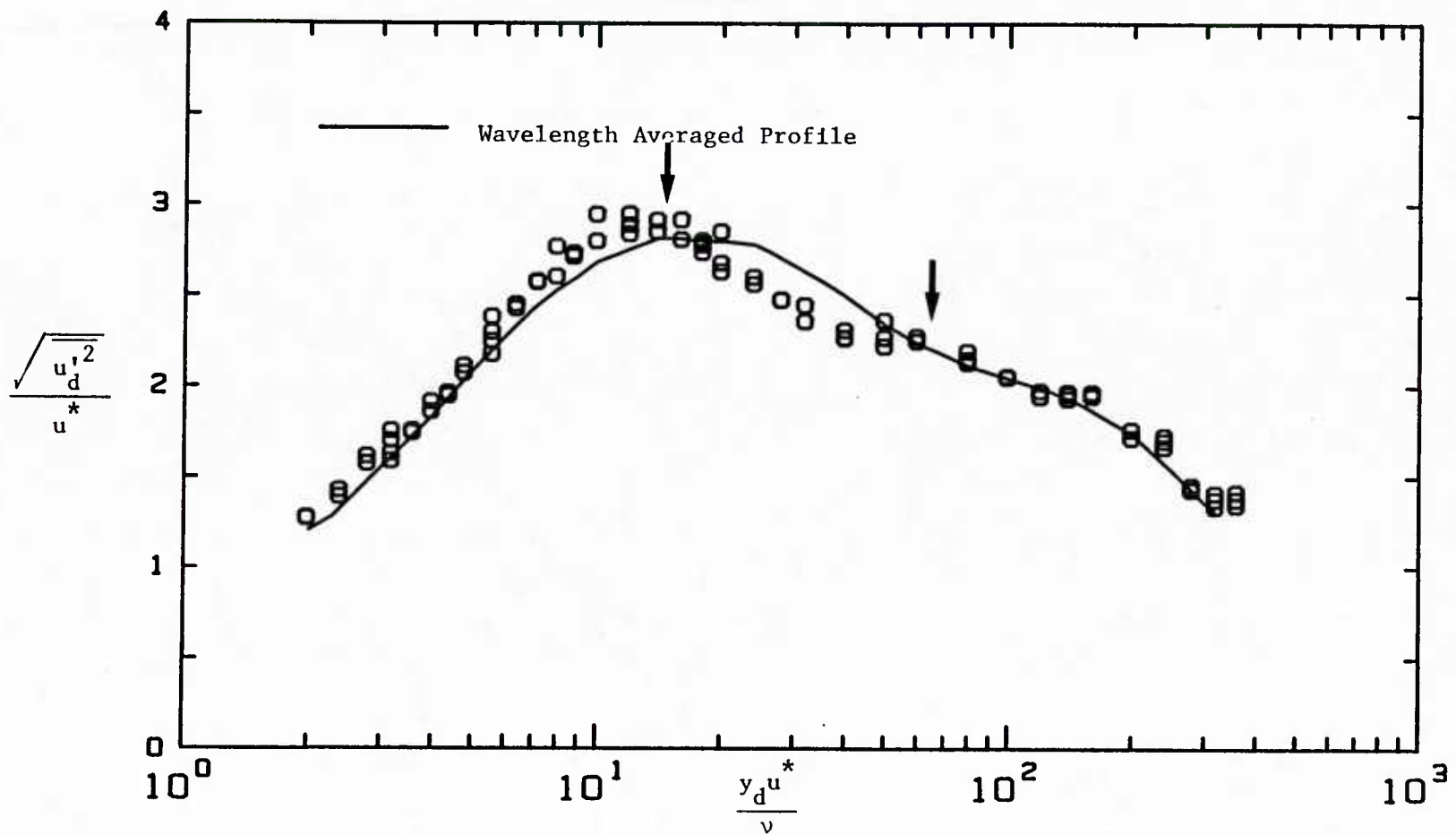


Figure 5.16 Streamwise Intensity Measurements, $x_d/\lambda = 0.2$, $2a_d/\lambda = 0.03125$, $Re_b = 6400$, $2h_d/\lambda = 1.0$

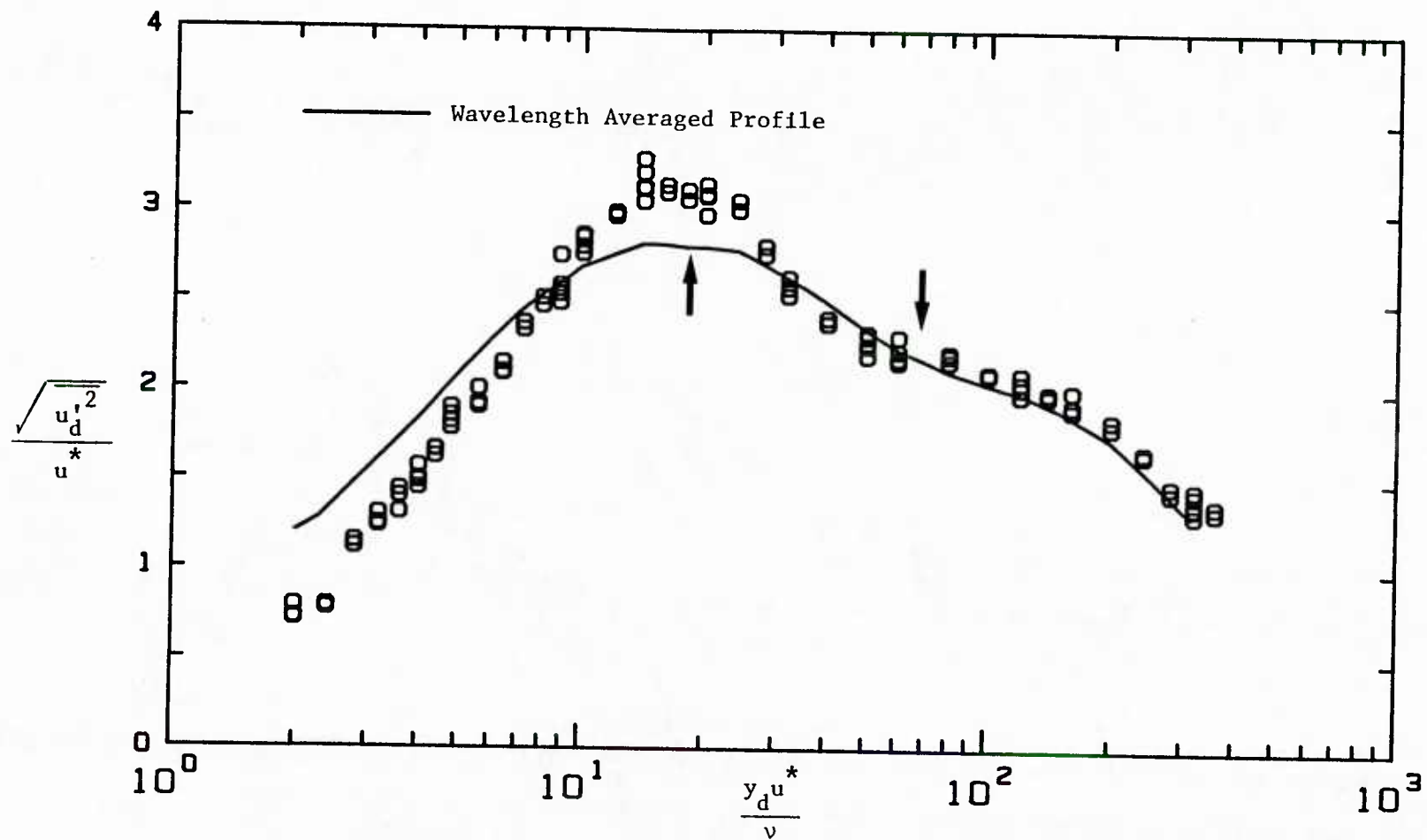


Figure 5.17 Streamwise Intensity Measurements, $x_d/\lambda = 0.3$, $2a_d/\lambda = 0.03125$,
 $Re_b = 6400$, $2h_d/\lambda = 1.0$

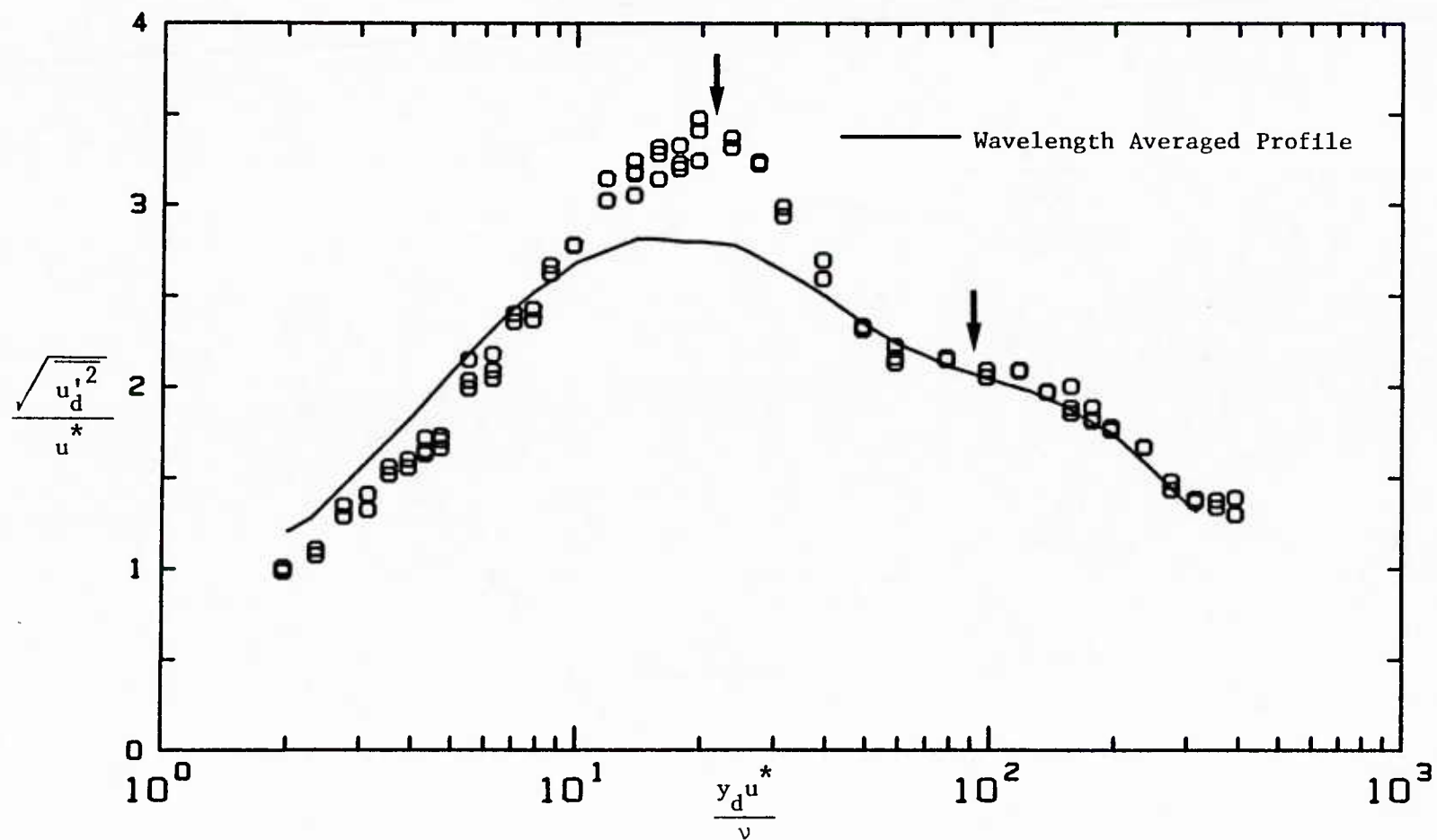


Figure 5.18 Streamwise Intensity Measurements, $x_d/\lambda = 0.4$, $2a_d/\lambda = 0.03125$,
 $Re_b = 6400$, $2h_d/\lambda = 1.0$

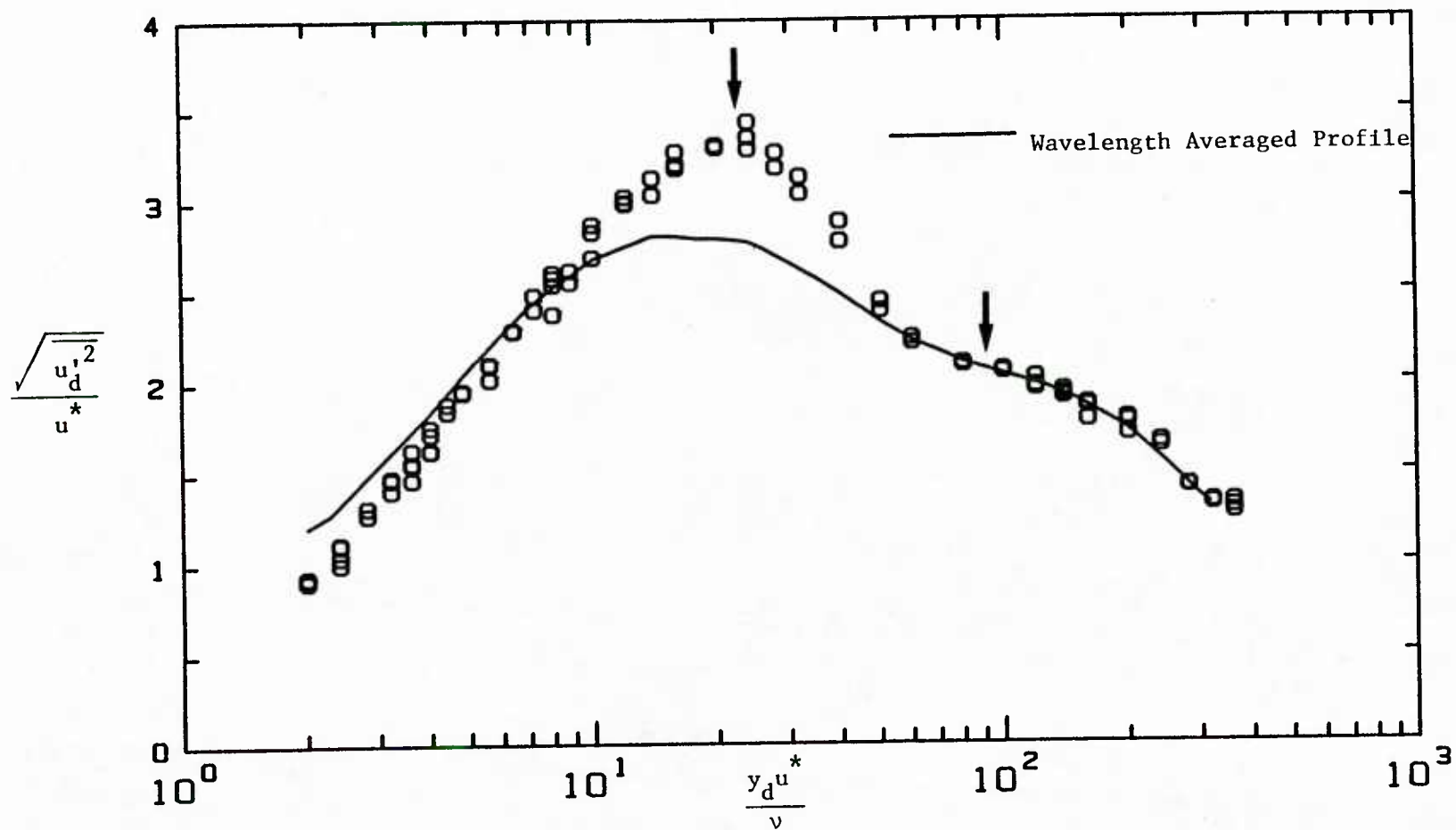


Figure 5.19 Streamwise Intensity Measurements, $x_d/\lambda = 0.5$, $2a_d/\lambda = 0.03125$, $Re_b = 6400$, $2h_d/\lambda = 1.0$

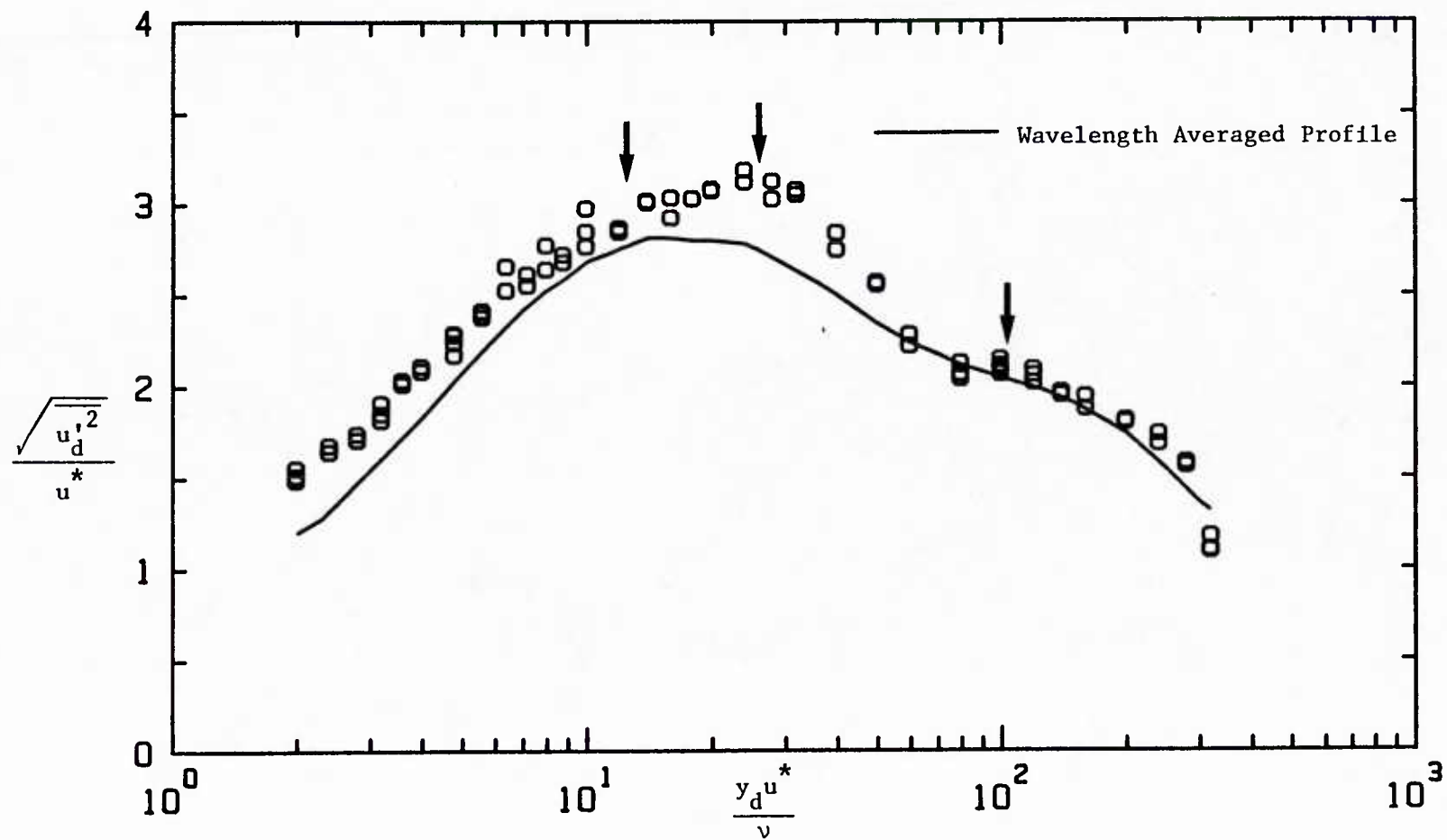


Figure 5.20 Streamwise Intensity Measurements, $x_d/\lambda = 0.6$,
 $2a_d/\lambda = 0.03125$, $Re_b = 6400$, $2h_d/\lambda = 1.0$

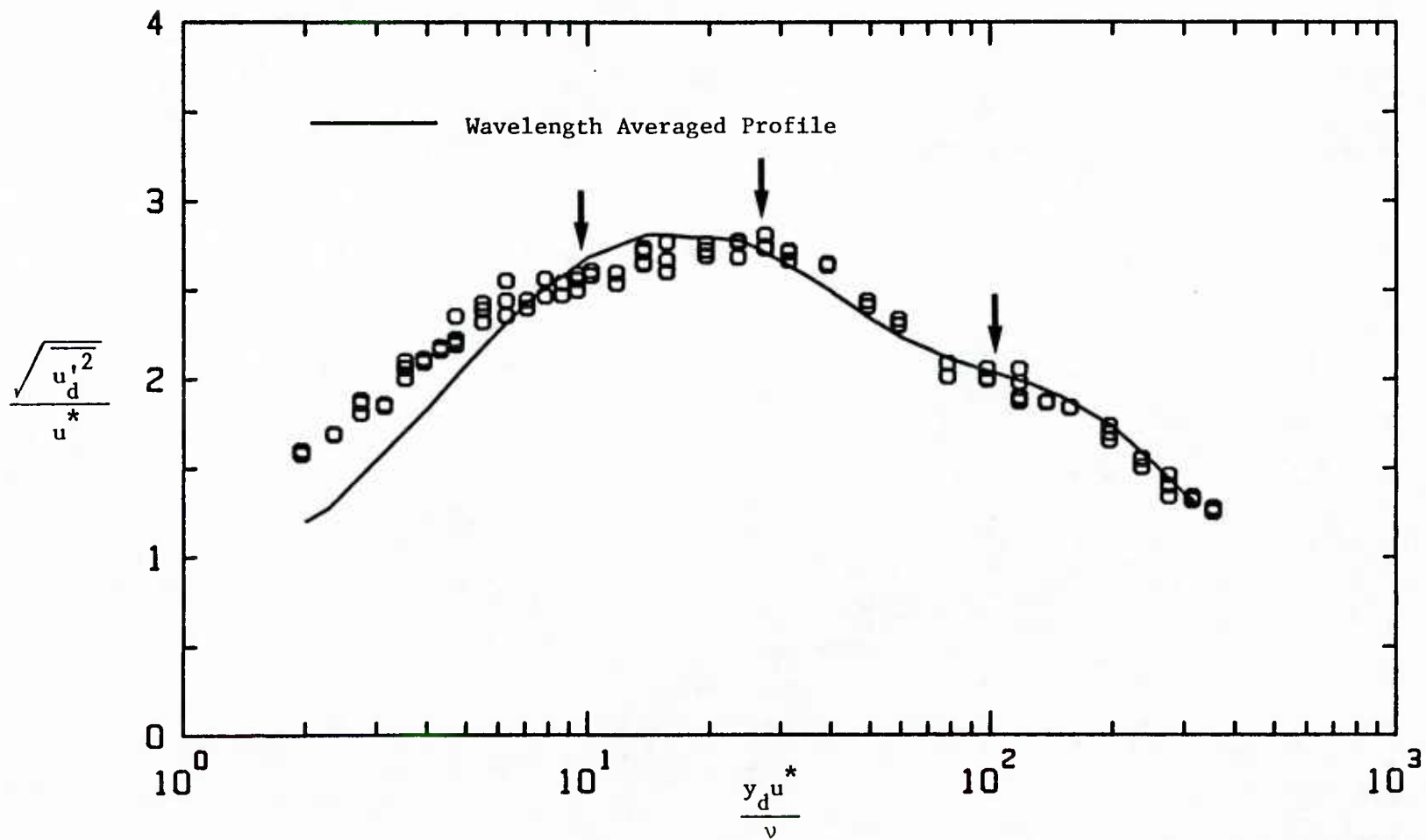


Figure 5.21 Streamwise Intensity Measurements, $x_d/\lambda = 0.7$,
 $2a_d/\lambda = 0.03125$, $Re_b = 6400$, $2h_d/\lambda = 1.0$

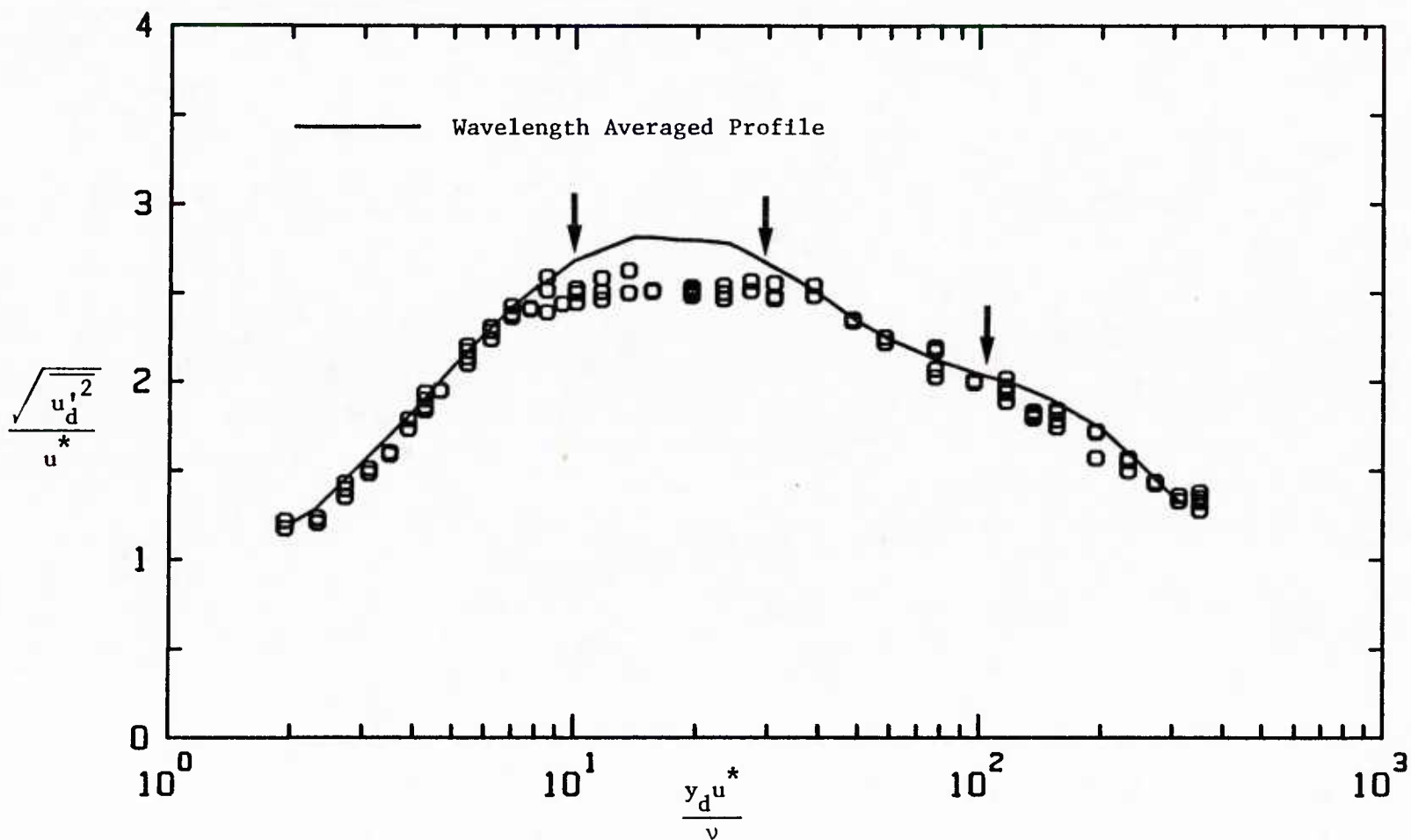


Figure 5.22 Streamwise Intensity Measurements, $x_d/\lambda = 0.8$, $2a_d/\lambda = 0.03125$,
 $Re_b = 6400$, $2h_d/\lambda = 1.0$

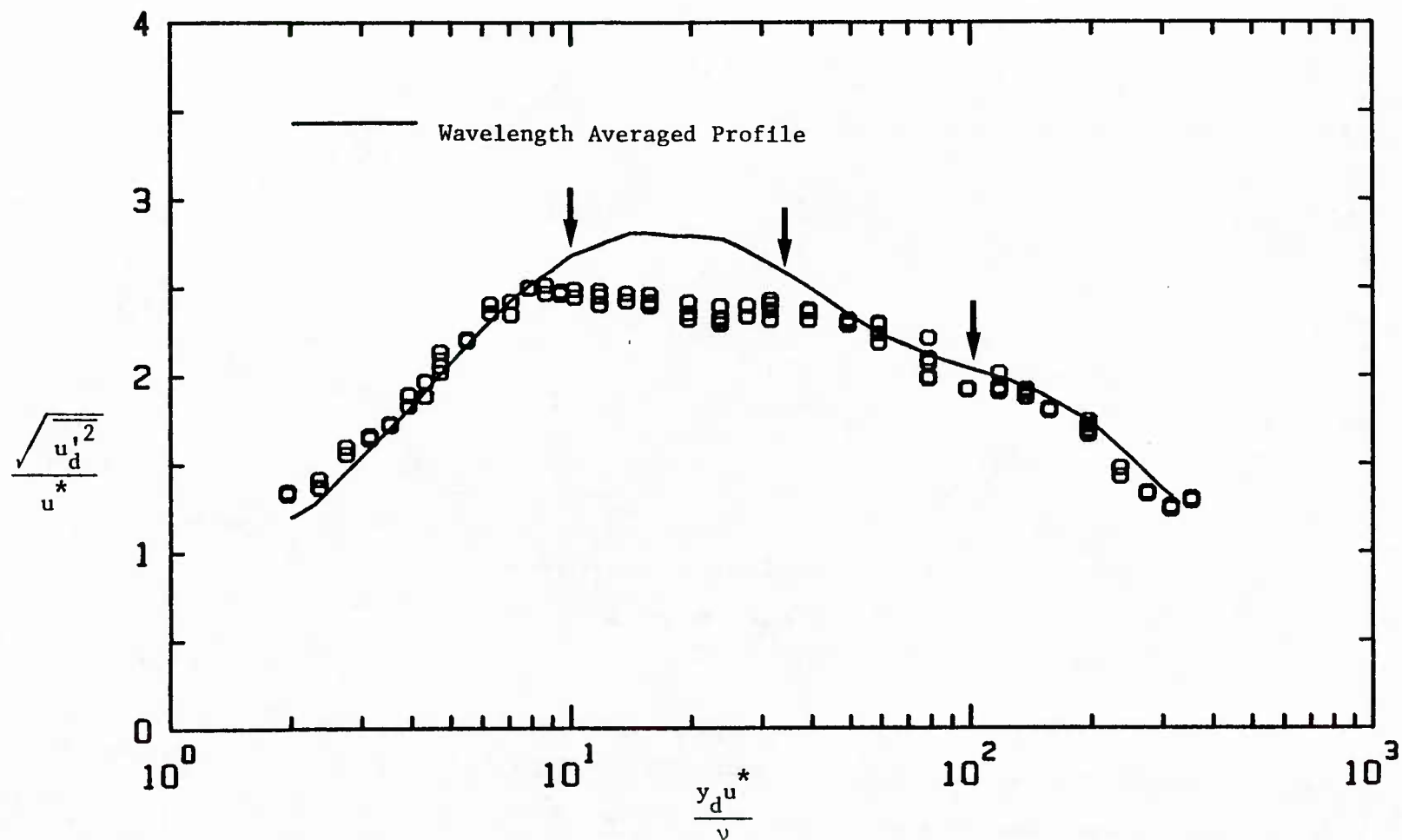


Figure 5.23 Streamwise Intensity Measurements, $x_d/\lambda = 0.9$, $2a_d/\lambda = 0.03125$,
 $Re_b = 6400$, $2h_d/\lambda = 1.0$

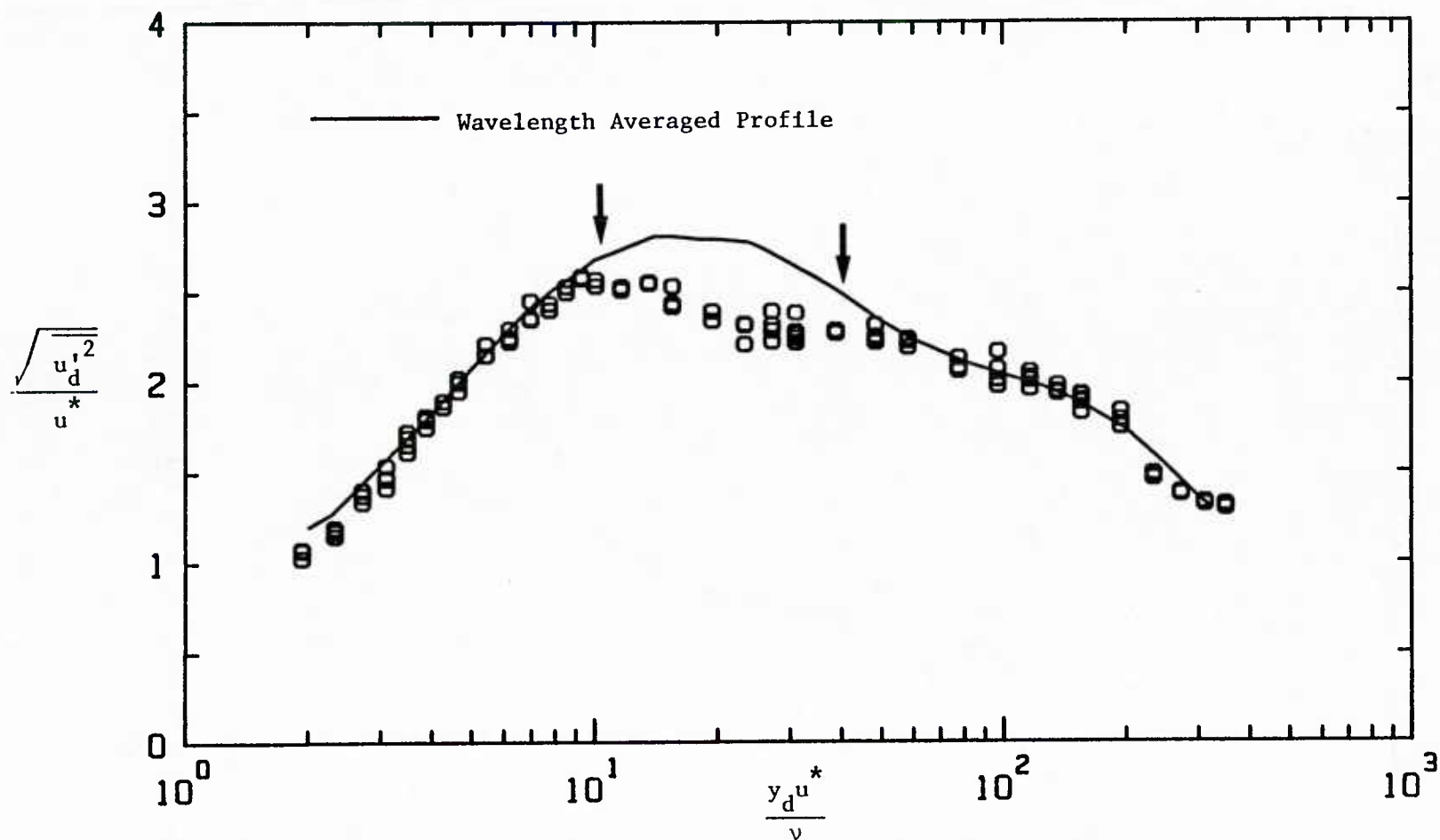


Figure 5.24 Streamwise Intensity Measurements, $x_d/\lambda = 1.0$,
 $2a_d/\lambda = 0.03125$, $Re_b = 6400$, $2h_d/\lambda = 1.0$

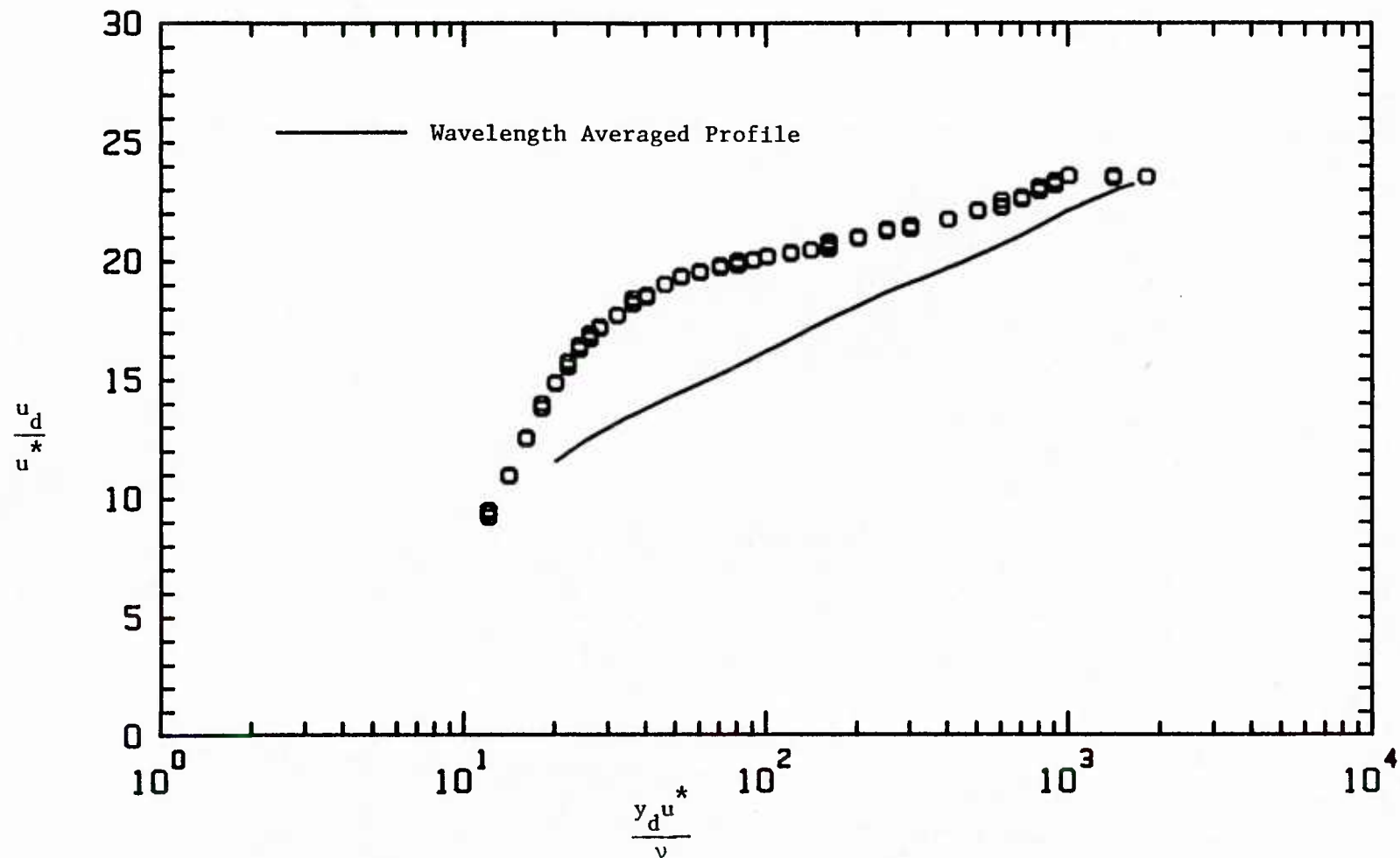


Figure 5.25 Mean Velocity Measurements, $x_d/\lambda = 0.1$, $2a_d/\lambda = 0.05$,
 $Re_b = 38,800$, $2h_d/\lambda = 1.0$

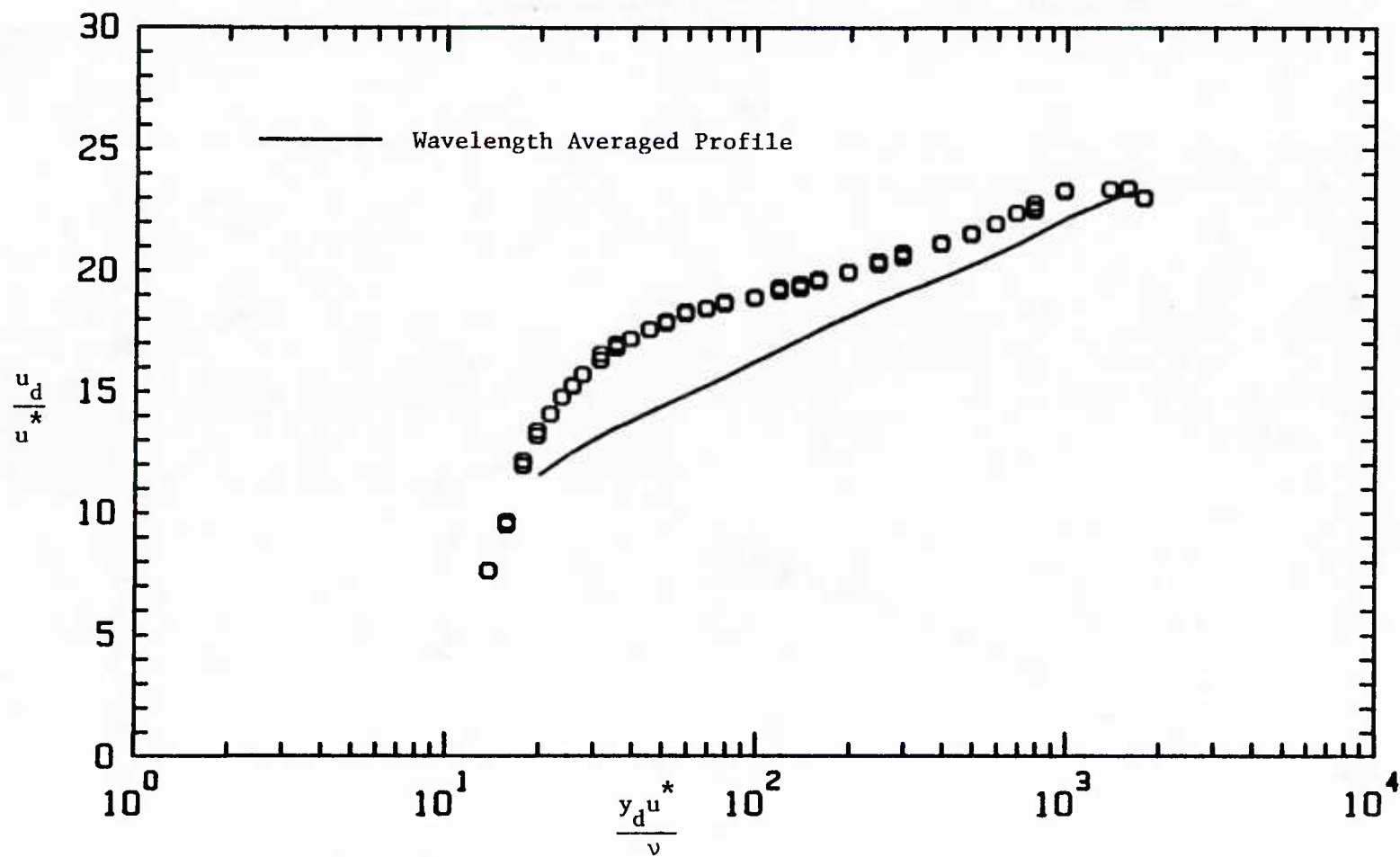


Figure 5.26 Mean Velocity Measurements, $x_d/\lambda = 0.2$, $2a_d/\lambda = 0.05$,
 $Re_b = 38,800$, $2h_d/\lambda = 1.0$

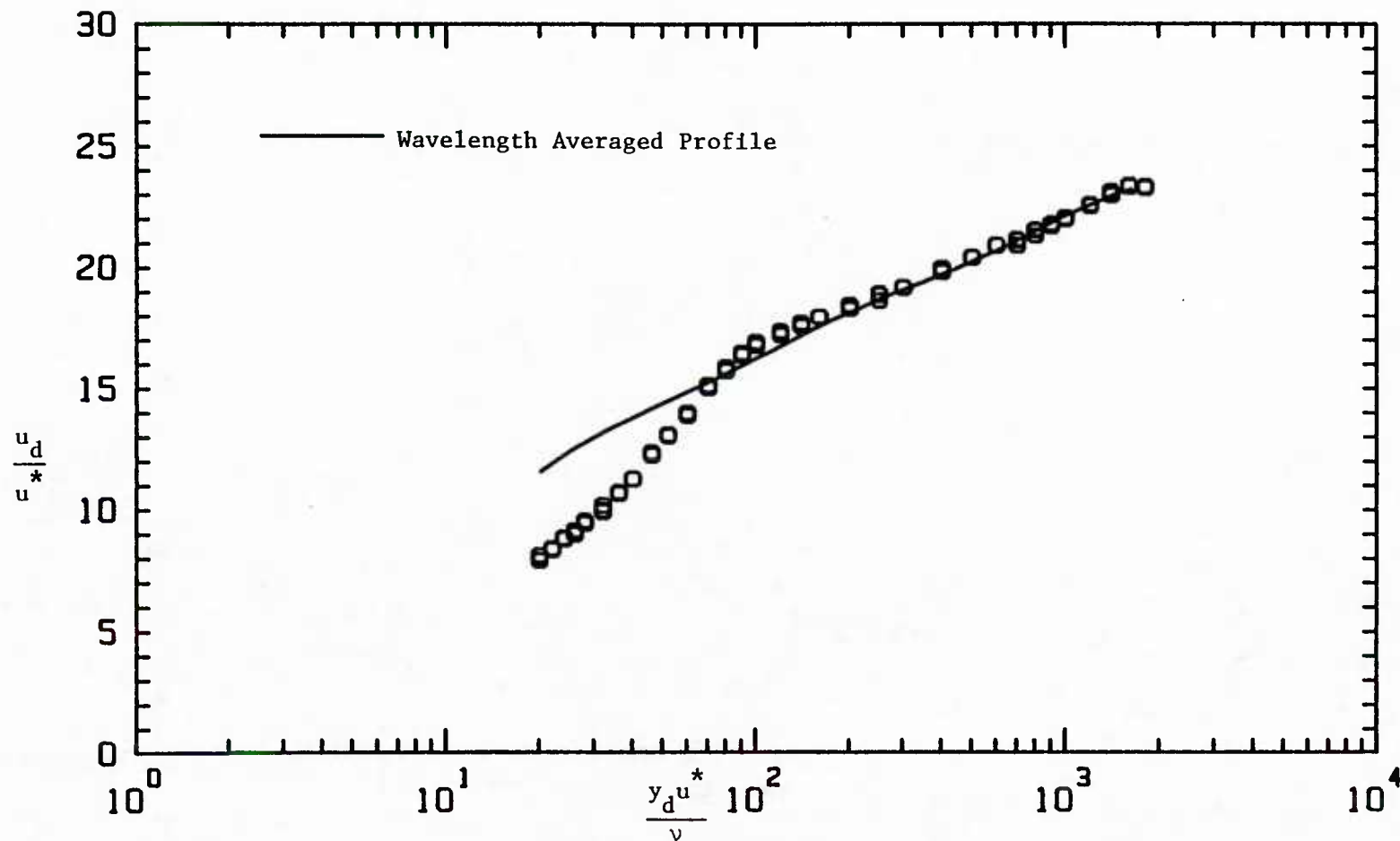


Figure 5.27 Mean Velocity Measurements, $x_d/\lambda = 0.3$, $2a_d/\lambda = 0.05$,
 $Re_b = 38,800$, $2h_d/\lambda = 1.0$

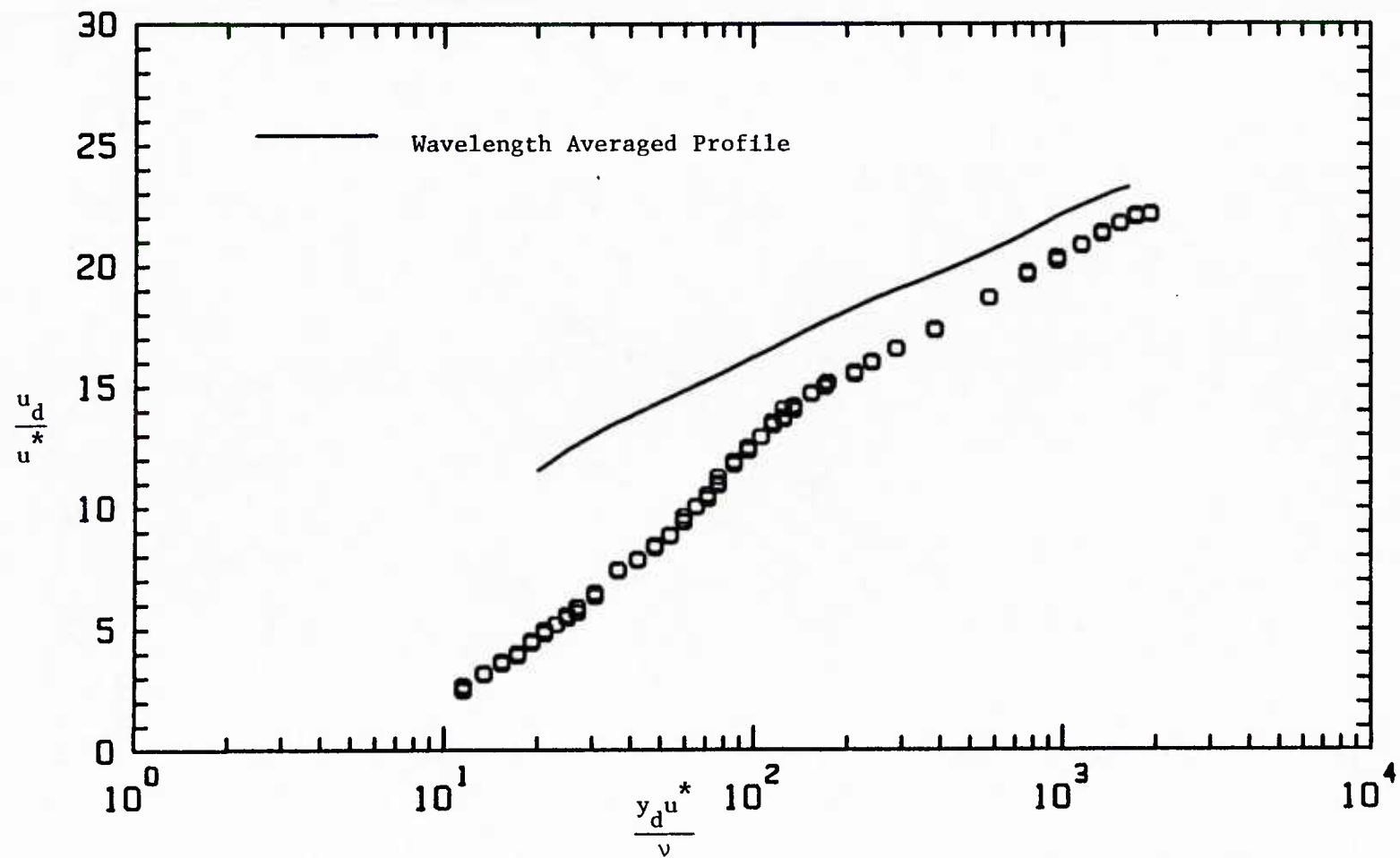


Figure 5.28 Mean Velocity Measurements, $x_d/\lambda = 0.4$, $2a_d/\lambda = 0.05$,
 $Re_b = 38,800$, $2h_d/\lambda = 1.0$

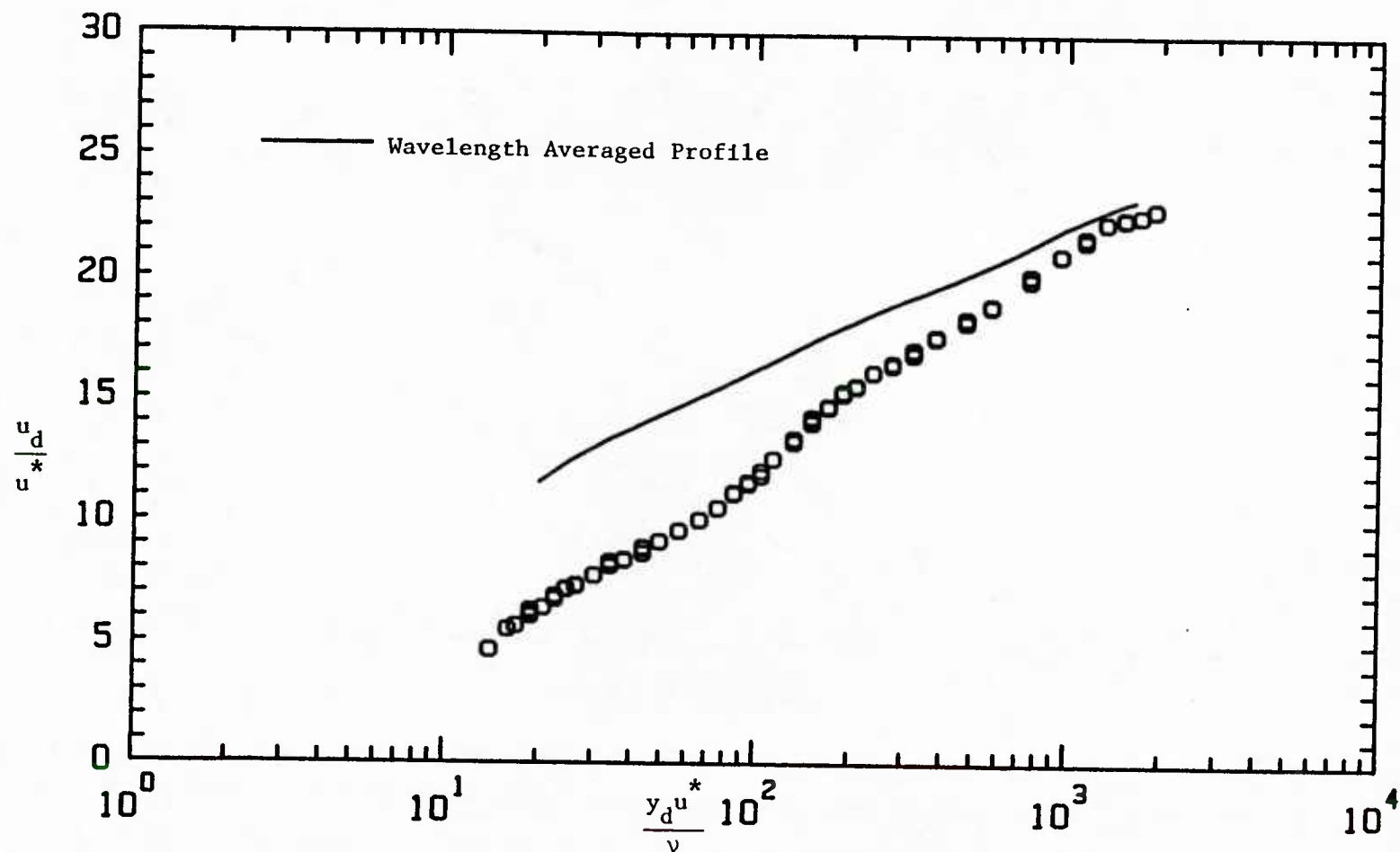


Figure 5.29 Mean Velocity Measurements, $x_d/\lambda = 0.5$, $2a_d/\lambda = 0.05$,
 $Re_b = 38,800$, $2h_d/\lambda = 1.0$

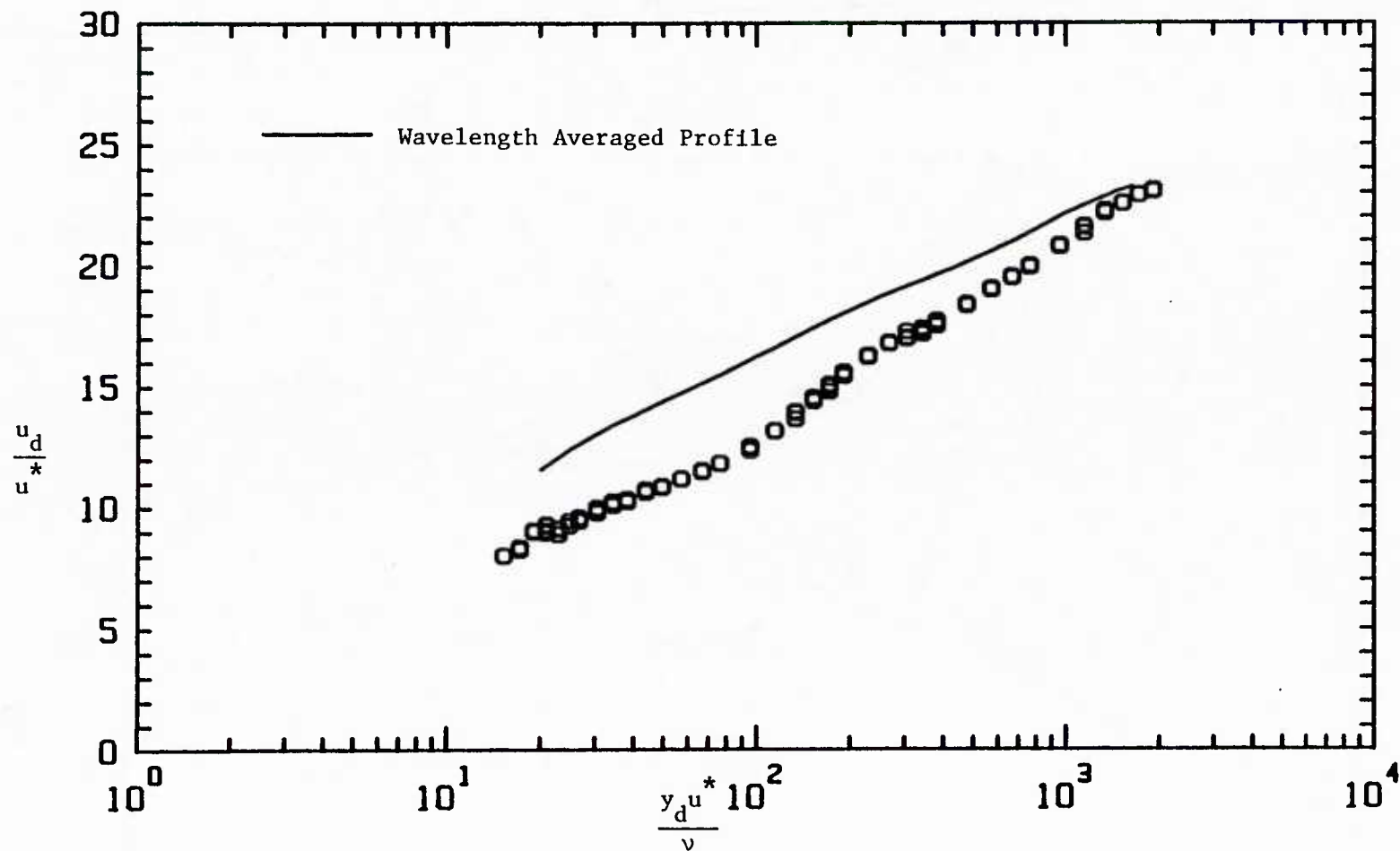


Figure 5.30 Mean Velocity Measurements, $x_d/\lambda = 0.6$, $2a_d/\lambda = 0.05$,
 $Re_b = 38,000$, $2h_d/\lambda = 1.0$

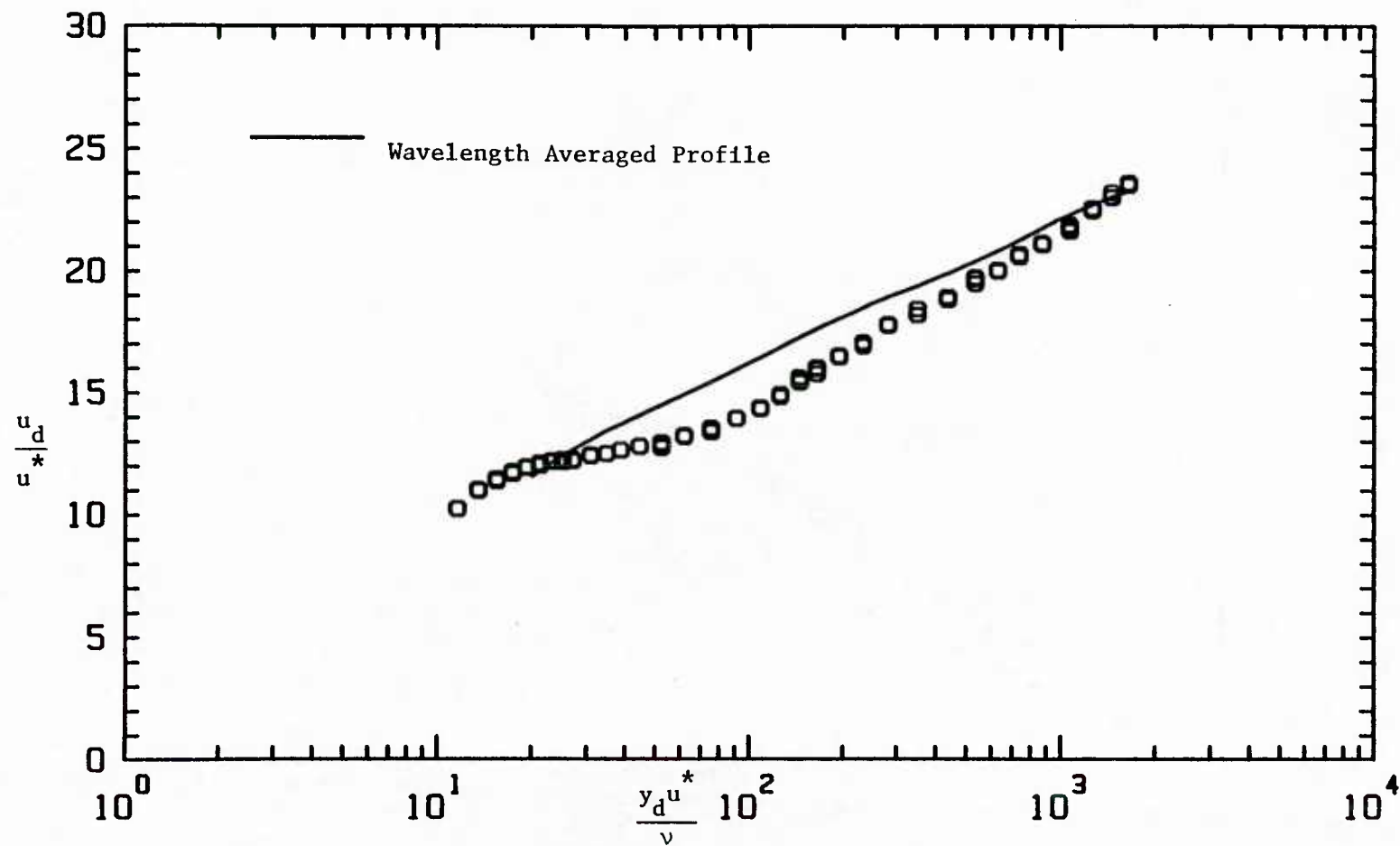


Figure 5.31 Mean Velocity Measurements, $x_d/\lambda = 0.7$, $2a_d/\lambda = 0.05$,
 $Re_b = 38,800$, $2h_d/\lambda = 1.0$

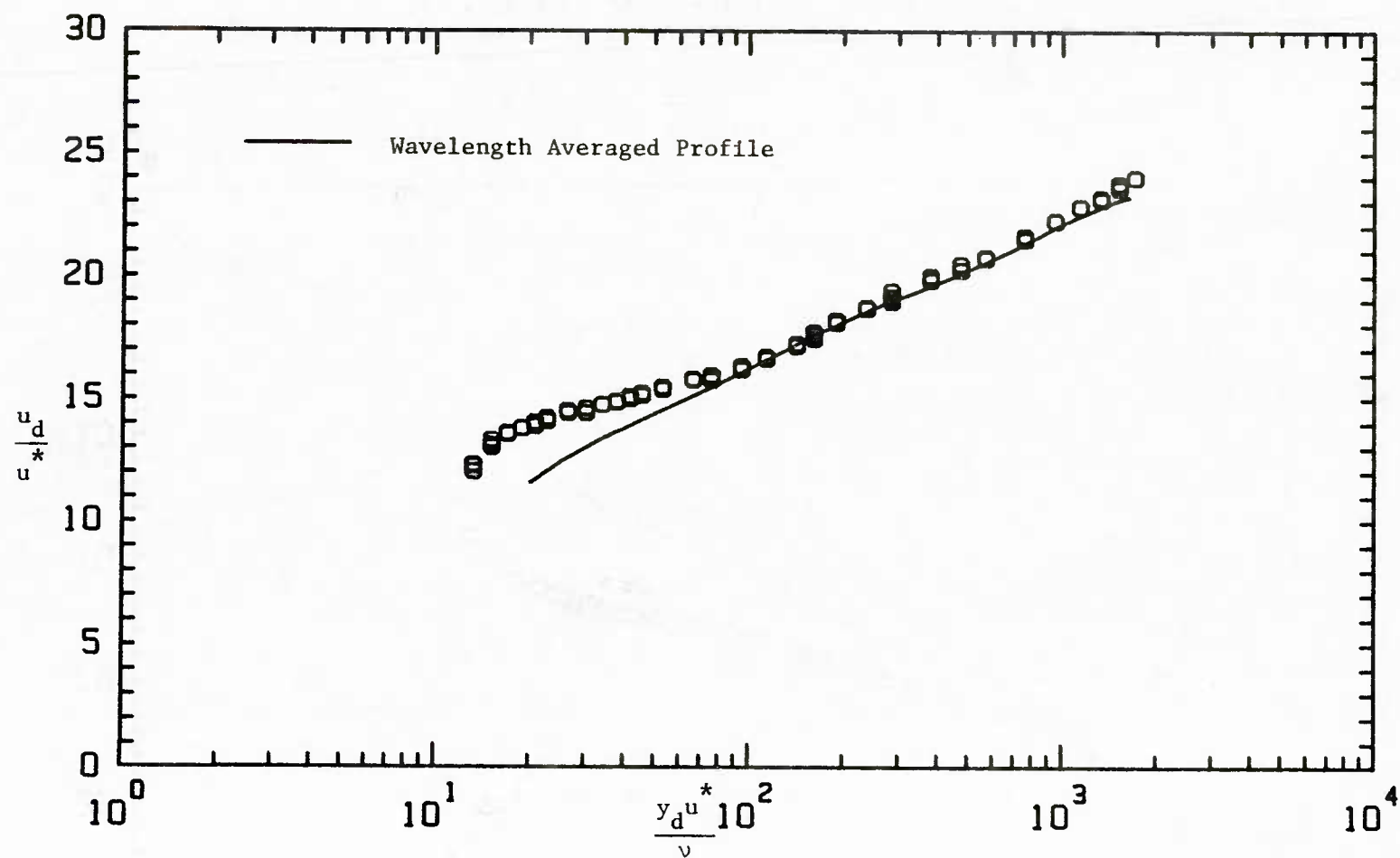


Figure 5.32 Mean Velocity Measurements, $x_d/\lambda = 0.8$, $2a_d/\lambda = 0.05$,
 $Re_b = 38,800$, $2h_d/\lambda = 1.0$

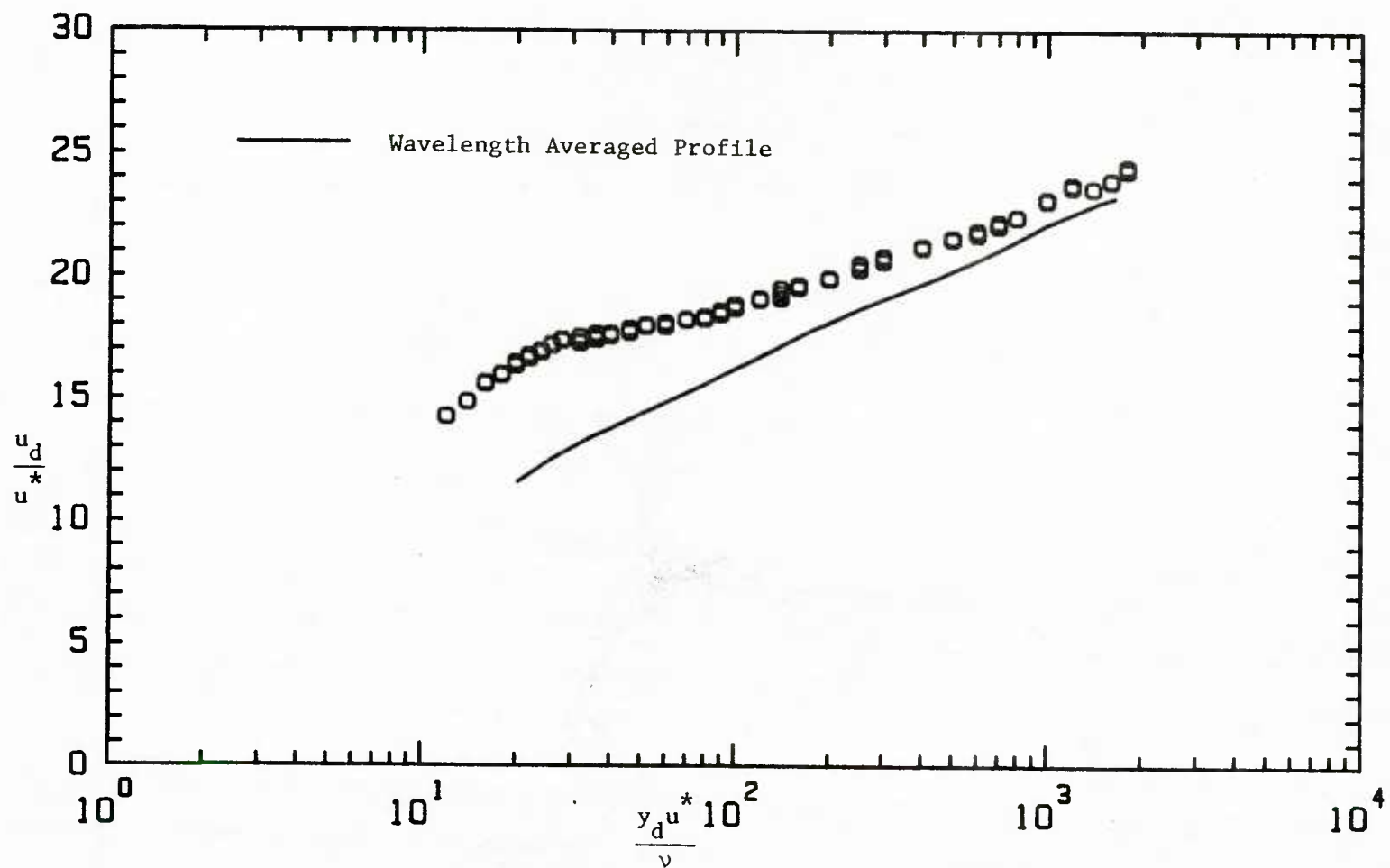


Figure 5.33 Mean Velocity Measurements, $x_d/\lambda = 0.9$, $2a_d/\lambda = 0.05$,
 $Re_b = 38,800$, $2h_d/\lambda = 1.0$

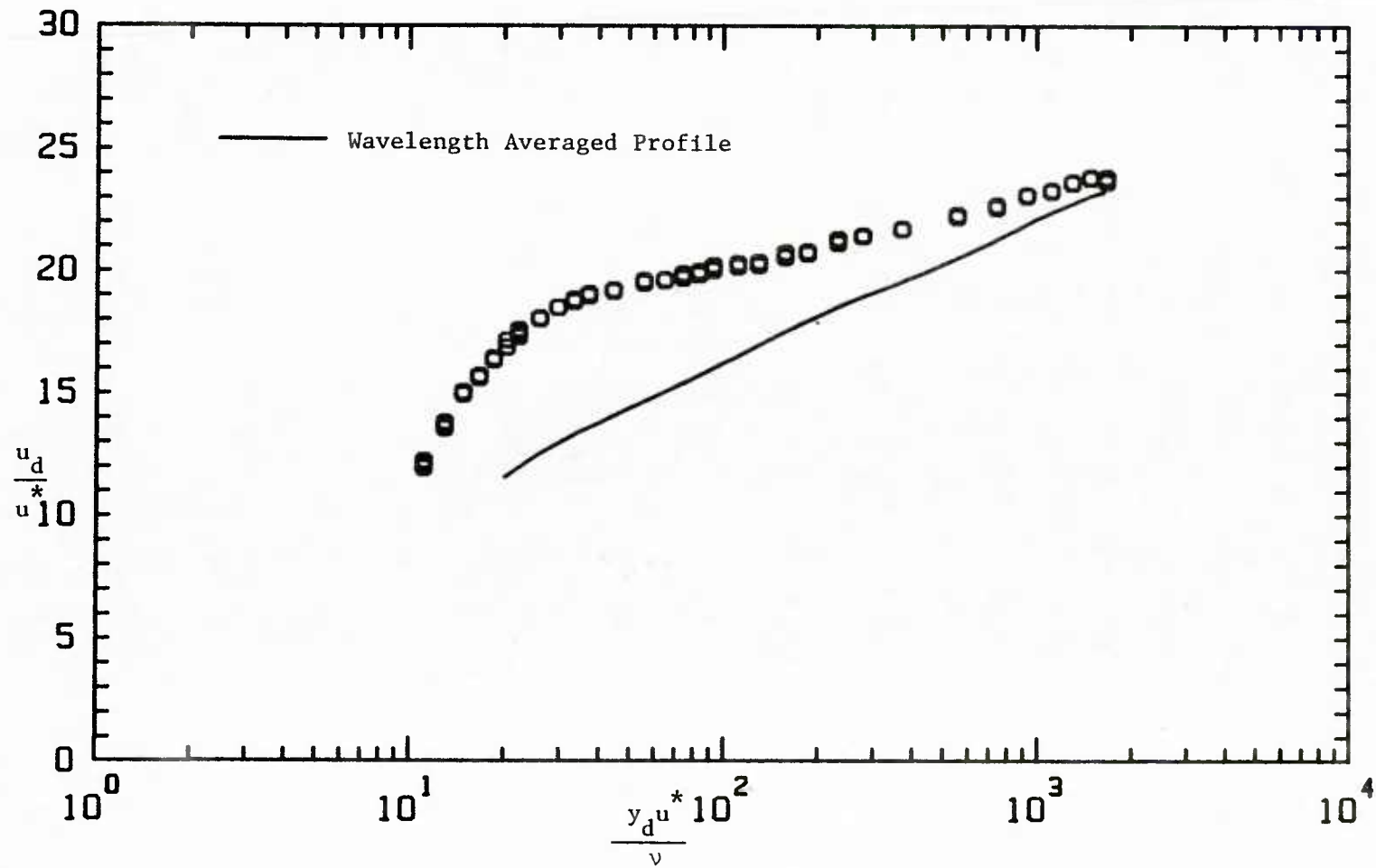


Figure 5.34 Mean Velocity Measurements, $x_d/\lambda = 1.0$, $2a_d/\lambda = 0.05$,
 $Re_b = 38,000$, $2h_d/\lambda = 1.0$

wave surface is $y_d u^* / \nu = 10$ and the channel centerline is about 1830 $y_d u^* / \nu$ units above the average wave height. The measurement volume diameter was 2.6 wall units. Approximately fifteen data points were obtained within the viscous wall region. The dimensionless wave amplitude, $a_d u^* / \nu$, is equal to 95.2. The uncertainties in $y_d u^* / \nu$ and u_d / u^* are about 2.0 and 0.4 dimensionless units respectively. As in the case of the $2a_d / \lambda = 0.03125$ wave, the reference wavelength averaged profile clearly shows that the reaction of the outer flow lags that of the inner flow.

Accurate measurements of the streamwise intensities over the 0.05 wave could not be obtained due to difficulties with the frequency tracker.

The data for the $2a_d / \lambda = 0.03125$ and 0.05 waves is tabulated in Appendix C.

CHAPTER 6

DISCUSSION OF EXPERIMENTAL RESULTS AND COMPARISON WITH THEORY

In this chapter the velocity measurements presented in the previous chapter are analyzed. When applicable the measurements are compared with predictions from the nonlinear channel code using the turbulence Models C^* and D^* developed by Thorsness, Morrisroe and Hanratty [45] and Abrams [2]. A summary of the major conclusions of this chapter is given in Chapter 7.

I. Wave of Steepness $2a_d/\lambda = 0.03125$

This section discusses the velocity data obtained over the wave of steepness $2a_d/\lambda = 0.03125$. The data are presented in several forms which are designed to show the linearity of the flowfield above this wave. The presentation includes wall stress profiles, wavelength averaged velocity profiles, mean velocity profiles, velocity responses at constant heights above the wave, profiles of wave-induced velocity perturbations and streamwise intensities.

A. Wall Stresses

1. Surface Shear Stress

Zilker [48] used electrochemical techniques to obtain surface shear stress measurements along the $2a_d/\lambda = 0.03125$ wave with the same flowrate, $Re_b = 6400$, as the velocity measurements presented in this thesis. Data for the eighth and ninth wavelengths are shown in Figure 6.1 The data were fitted to the following two harmonic Fourier series by performing a least squares analysis:

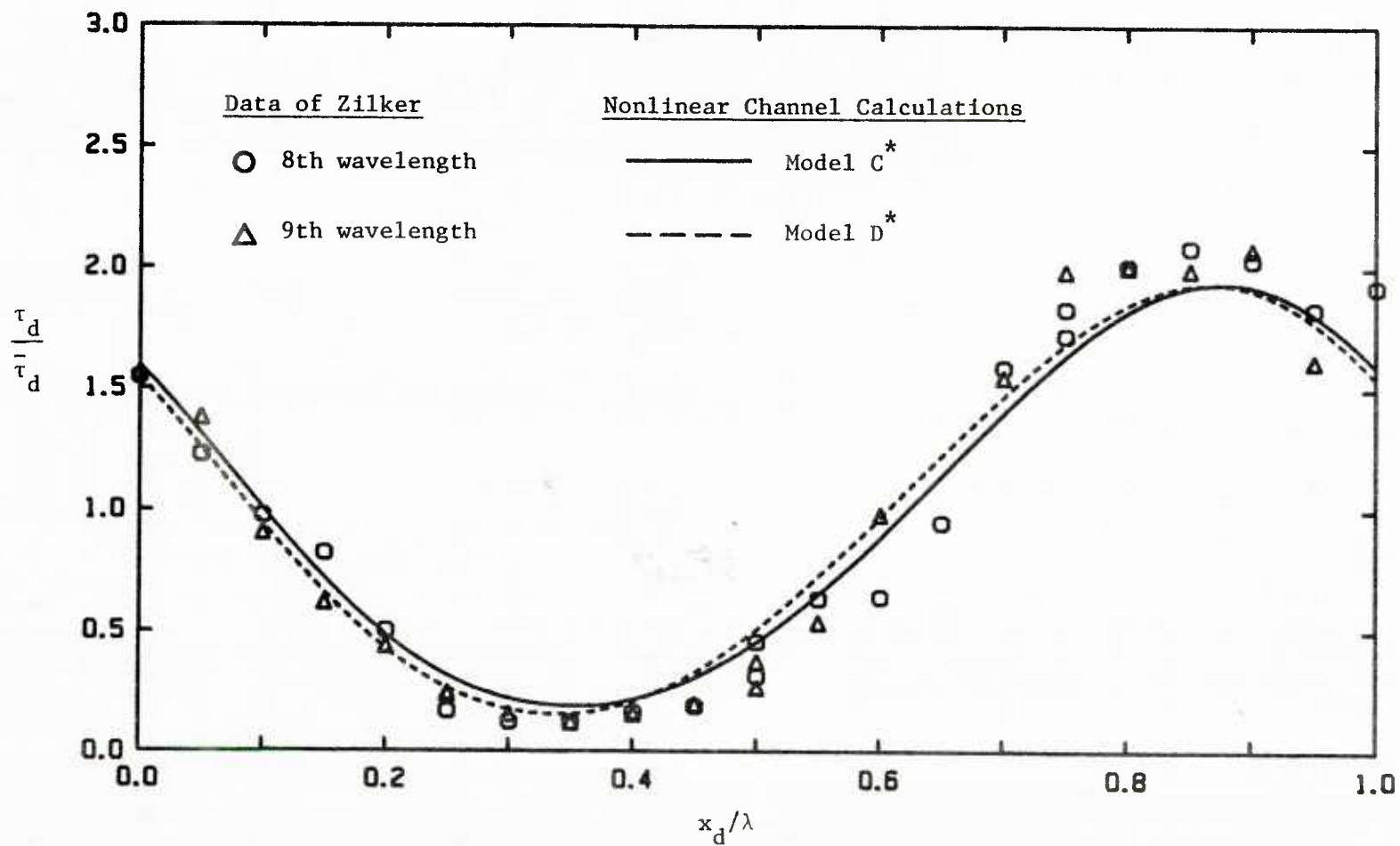


Figure 6.1 Shear Stress Response, $2a_d/\lambda = 0.03125$,
 $Re_b = 6400$, $2h_d/\lambda = 1.0$

$$\tau_d = \bar{\tau}_d + \sum_{n=0}^{N=2} c_n \sin\left(\frac{2\pi n x_d}{\lambda}\right) + d_n \cos\left(\frac{2\pi n x_d}{\lambda}\right). \quad (6.1)$$

The amplitudes and phases of the harmonics are defined from equation (6.1) as

$$|\hat{\tau}_d|_n = \sqrt{c_n^2 + d_n^2}, \quad (6.2)$$

and

$$\theta_{\hat{\tau},n} = \tan^{-1} \left(\frac{-d_n}{c_n} \right) \quad (6.3)$$

respectively. Table 6.1 shows the results of the Fourier fit. The wavelength averaged shear stress over the eighth and ninth waves, $\bar{\tau}_d / \rho u^{*2} = 1$, is the same as would exist if the wave was replaced by a flat surface. The amplitude and phase of the first harmonic are $|\hat{\tau}_d|_1 / \rho u^{*2} = 0.989$ and $\theta_{\hat{\tau},1} = 50.9^\circ$. The uncertainties in these quantities are approximately ± 5 percent and $\pm 5^\circ$ respectively. The ratio of the amplitude of the second harmonic to the first is $|\hat{\tau}_d|_2 / |\hat{\tau}_d|_1 = 0.099$. This indicates a borderline linear-nonlinear response since Zilker, Cook, and Hanratty [49] noted that an observable difference from a sinusoidal variation is obtained when $|\hat{\tau}_d|_2 / |\hat{\tau}_d|_1 \geq 0.116$.

The shear stress response predictions of the nonlinear channel analysis with turbulence Models C* and D* are also shown in Figure 6.1. A summary of a least squares Fourier analysis of these results is given in Table 6.1. Both models predict a linear response with a

	<u>Data</u>	<u>Model C</u> *	<u>Model D</u> *
$ \hat{\tau}_d _1 / \rho u^*{}^2$	0.989	0.7822	0.7919
$\theta_{\hat{\tau},1}$	50.9	49.8	54.5
$\bar{\tau}_d / \rho u^*{}^2$	1	0.895	0.893
$ \hat{\tau}_d _2 / \hat{\tau}_d _1$	0.099	0.0808	0.0673

Table 6.1 A Comparison of Surface Shear Stress Measurements
with Predictions of Nonlinear Channel Analysis,
 $2a_d/\lambda = 0.03125$, $Re_b = 6400$, $2h_d/\lambda = 1.0$

wavelength averaged shear stress reduction of about 10 percent. The amplitude and phase of the first harmonic for both models are within the experimental error of the shear stress measurements.

2. Surface Pressure

The behavior of the surface pressure for $2a_d/\lambda = 0.03125$, $2h_d/\lambda = 1.0$, and $Re_b = 6400$ is shown in Figure 6.2, as predicted by the nonlinear code with turbulence Models C* and D*. These discrete profiles were fitted to a Fourier series with two harmonics. The amplitudes and phase angles of the first harmonic are shown in Table 6.2. It should be noted that the local pressure drop due to the channel, from the upstream crest to each x_d/λ position, was added to the points in Figure 6.2 before the Fourier analysis. This ensured that only the wave-induced pressure was considered. A linear pressure drop due to the channel was assumed. In Table 6.2 it can be seen that Models C* and D* predict similar amplitudes and phases. No pressure data is available for comparison with the calculations.

3. Drag

The drag of the wave on the fluid can be determined from the distribution of the tangential and normal stresses at the wavy surface. The total horizontal, x_d , component of the force at the surface is given by:

$$F_{x_d} = \int_{A'} (p_d \sin \beta - \rho v \omega_d \cos \beta) dA' \quad (6.2)$$

where

$$\tan \beta = \frac{dy_d}{dx_d} \quad (6.3)$$

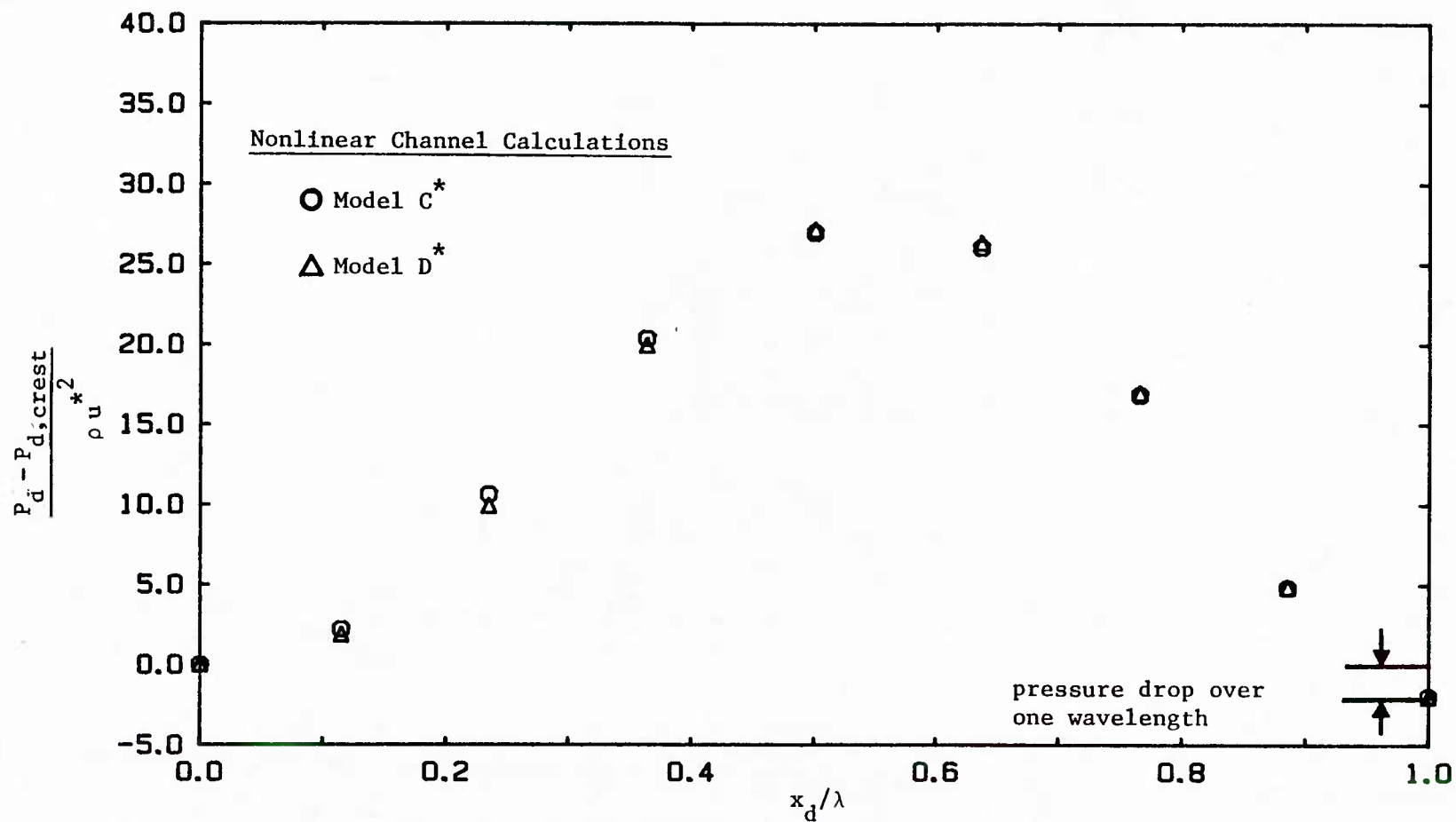


Figure 6.2 Calculated Pressure Response, $2a_d/\lambda = 0.03125$, $Re_b = 6400$, $2h_d/\lambda = 1.0$

	<u>Model C*</u>	<u>Model D*</u>
$ \hat{p}_d _1 / \rho u^{*2}$	14.38	14.58
$\theta_{\hat{p},1}$	165.2	163.7
$ \hat{p}_d _2 / \hat{p}_d _1$	0.0759	0.0644

Table 6.2 Surface Pressure Results of Nonlinear
Channel Analysis, $2a_d/\lambda = 0.03125$,
 $Re_b = 6400$, $2h_d/\lambda = 1.0$

is the slope of the wave surface and dA' is an infinitesimal area along the surface. It is convenient to study the components of this force by defining a skin friction drag coefficient, C_s , and a form drag coefficient, C_p , as follows:

$$C_s = - \frac{1}{\rho u_*^2} \frac{1}{\lambda} \int_0^\lambda \rho v \omega_d \cos \beta dS, \quad (6.4)$$

and

$$C_p = \frac{1}{\rho u_*^2} \frac{1}{\lambda} \int_0^\lambda p_d \sin \beta dS, \quad (6.5)$$

where dS is a distance along the wave. In the transformed coordinates these coefficients become,

$$C_s = - \frac{\alpha_d}{\rho u_*^2} \frac{1}{2\pi} \int_0^{2\pi} \rho v \omega_d x_\epsilon d\epsilon, \quad (6.6)$$

and

$$C_p = \frac{\alpha_d}{\rho u_*^2} \frac{1}{2\pi} \int_0^{2\pi} p_d y_\epsilon d\epsilon. \quad (6.7)$$

For a flat surface $C_s = 1$ and $C_p = 0$.

Drag coefficients predicted from the nonlinear channel analysis for the wave of steepness $2a_d/\lambda = 0.03125$ with $Re_b = 6400$ are shown in Table 6.3. It can be seen that with turbulence Models C^* and D^* there is approximately a 10 percent decrease in the skin friction drag

Turbulence Model	C_s	C_p	$\frac{C_s}{C_s + C_p}$	$\frac{C_p}{C_s + C_p}$	$C_s + C_p$
C^*	0.895	0.190	0.825	0.175	1.09
D^*	0.893	0.212	0.808	0.192	1.11

measurements of Zilker

$$C_s = 1.0 \pm 0.05$$

Table 6.3 Drag Coefficients, $2a_d/\lambda = 0.03125$,
 $Re_b = 6400$, $2h_d/\lambda = 1.0$

relative to a flat surface. However, the total drag for the wave surface increases by about 10 percent due to an increase in form drag. The form drag represents almost 20 percent of the total drag for both models.

Experimentally, Zilker et al. [49] found that $C_s = 1.0 \pm 0.05$ for the above wave and flow conditions. No pressure measurements are available to determine the form drag coefficient.

B. Wavelength Averaged Mean Velocity

An average representation of the flowfield over one wavelength of the wave with $2a_d/\lambda = 0.03125$ can be obtained by averaging the ten velocity profiles in Figures 5.5-5.14. The resulting wavelength averaged velocity profile is shown in Figure 6.3. The ten profiles used to construct this average are equally spaced profiles of the streamwise velocity with distances measured vertically from the wave surface as shown in Figure 6.4 for the position $x_d/\lambda = 0.2$. Predictions of the same type of wavelength averaged profile by the nonlinear channel code with turbulence Models C^* and D^* are also shown in Figure 6.3. No differences between Model C^* and D^* are observed. The wavelength averaged data are slightly higher than the theory. This difference is not believed to be significant because it is within the experimental error of the velocity measurements and within errors in the friction factor data of Thorsness [44] which were used to normalize the measurements.

A second type of wavelength averaged velocity profile above the wave surface was calculated from the theoretical results. In this case the profiles to be averaged are formed along the eight

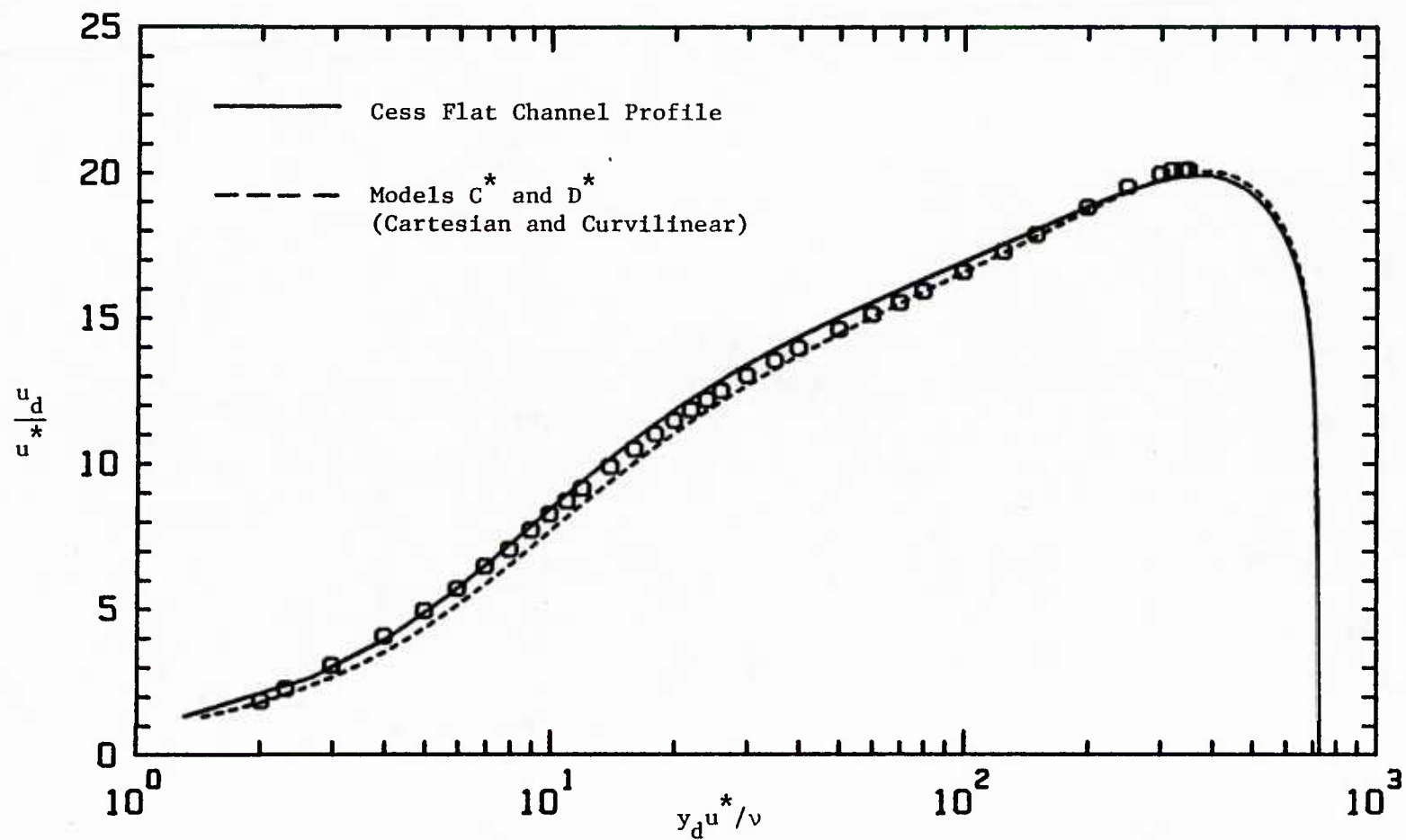


Figure 6.3 Wavelength Averaged Velocity Profiles, $2a_d/\lambda = 0.03125$, $Re_b = 6400$, $2h_d/\lambda = 1.0$

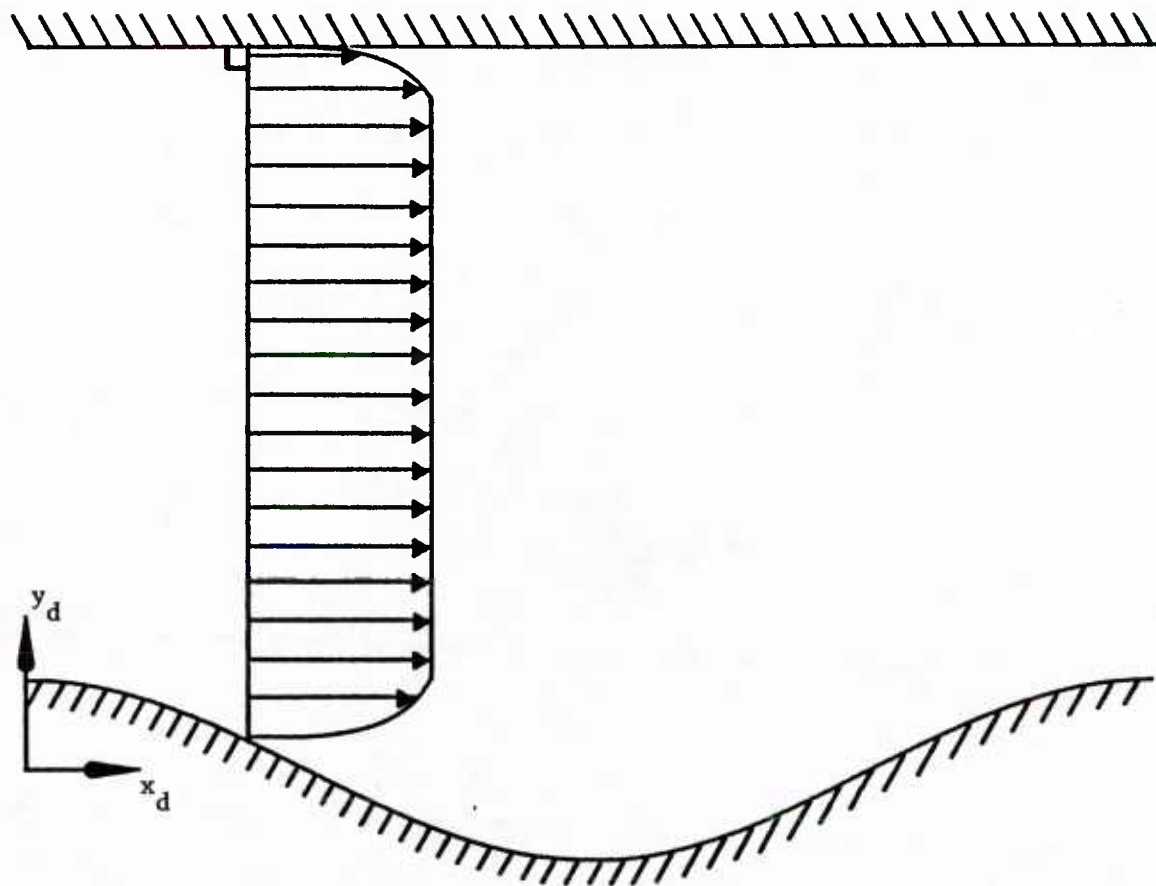


Figure 6.4 Typical Velocity Profile Used to Construct Wavelength Averaged Profile Along Cartesian Coordinates, $x_d/\lambda = 0.2$ (amplitude exaggerated)

curvilinear coordinate lines of constant ϵ . Distances from the wave surface are measured along these lines. All velocities are parallel to lines of constant η . That is, only velocity components in the ϵ -direction are considered. As an example of such a profile, Figure 6.5 shows the velocity profile along $\epsilon = \pi/4$. It is believed that a profile averaged along such curves is the proper wavelength averaged profile to compare with the flat channel profile. This is because profiles along the curvilinear coordinates reflect the geometry of the surface in contact with the flow. The flat channel profile is included in Figure 6.3. It was found that the wavelength averaged profile along curvilinear coordinates is nearly identical to the average profile in Cartesian coordinates. This is expected for waves of small steepness.

C. Mean Velocity Profiles

The mean velocity profiles at the ten x_d/λ positions are compared in Figures 6.6-6.10 with results of the nonlinear channel code using turbulence Models C^* and D^* . There are no significant differences between the two models for a wave with $2a_d/\lambda = 0.03125$ and $Re_b = 6400$. Reasonably good agreement between the experimental profiles and the models is observed. The most important result is that Model C^* , which is a straightforward application of the Cess eddy viscosity profile for a flat channel, predicts a good first approximation of the velocity field over a wave. A shortcoming of both Models C^* and D^* is that the models predict smaller deviations about the wavelength averaged profile than is observed.

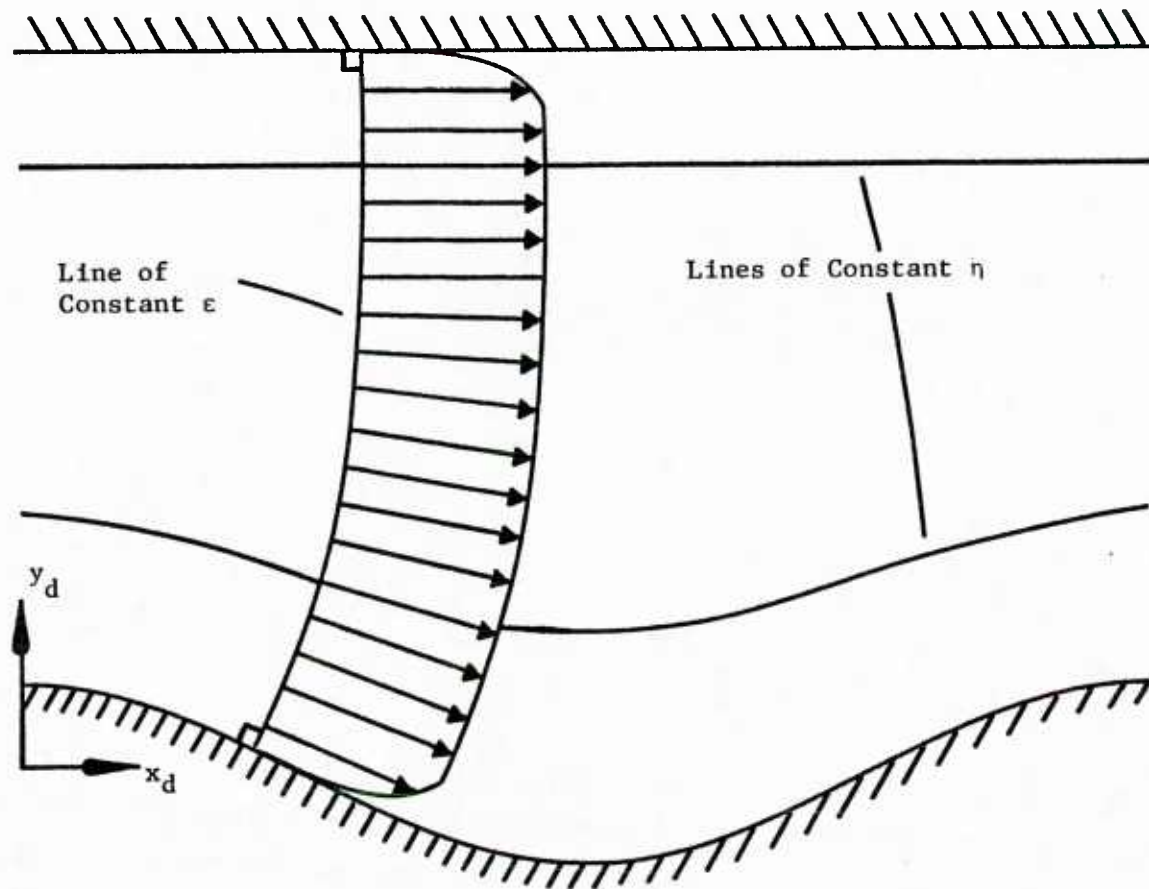


Figure 6.5 Typical Velocity Profile Used to Construct Wavelength Averaged Profile Along Curvilinear Coordinates, $\epsilon = \pi/4$ (amplitude exaggerated)

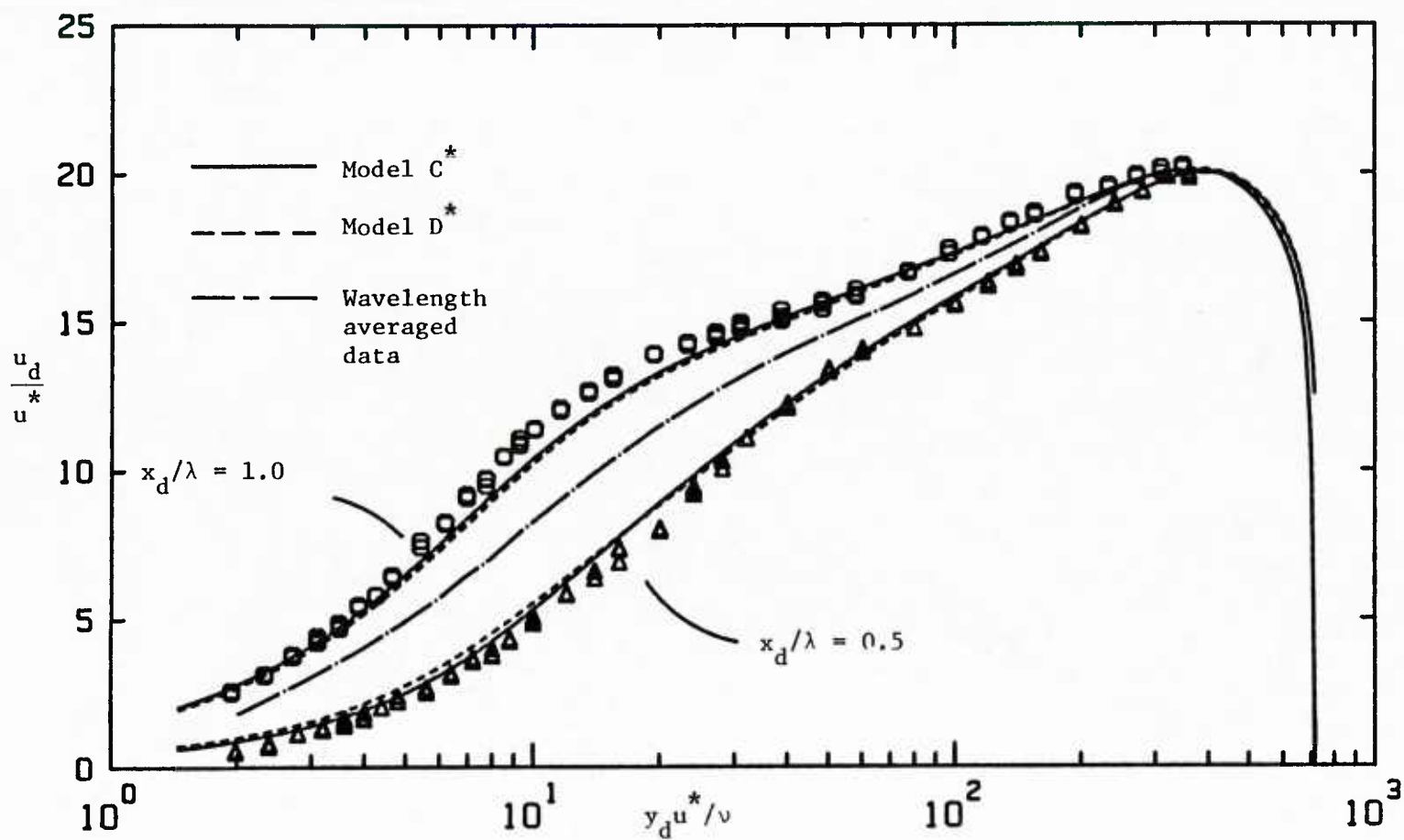


Figure 6.6 Comparison of Mean Velocity Measurements with Channel Calculations, $x_d / \lambda = 0.5, 1.0$, $2a_d / \lambda = 0.03125$, $Re_b = 6400$, $2h_d / \lambda = 1.0$

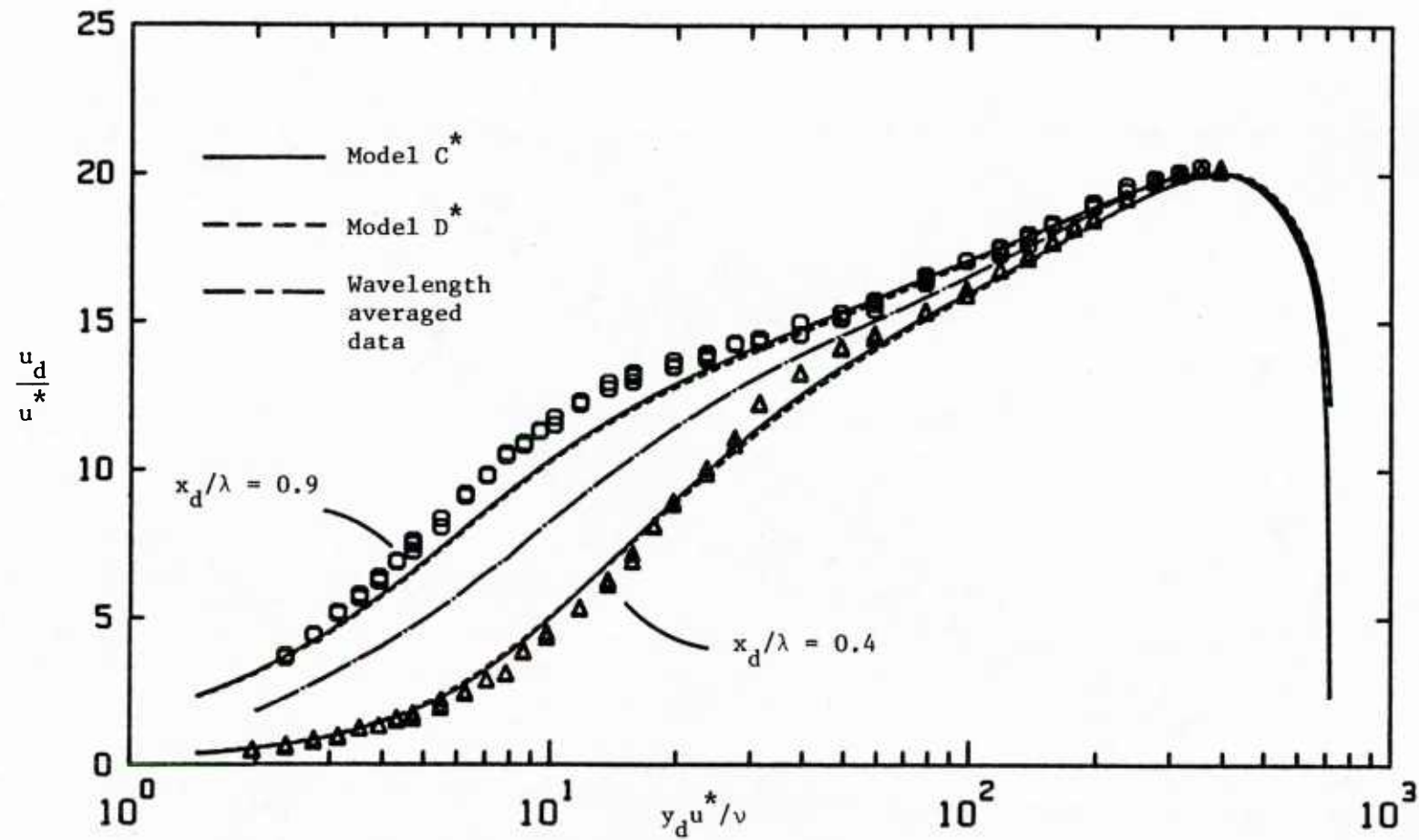


Figure 6.7 Comparison of Mean Velocity Measurements with Channel Calculations, $x_d/\lambda = 0.4, 0.9$, $2a_d/\lambda = 0.03125$, $Re_b = 6400$, $2h_d/\lambda = 1.0$

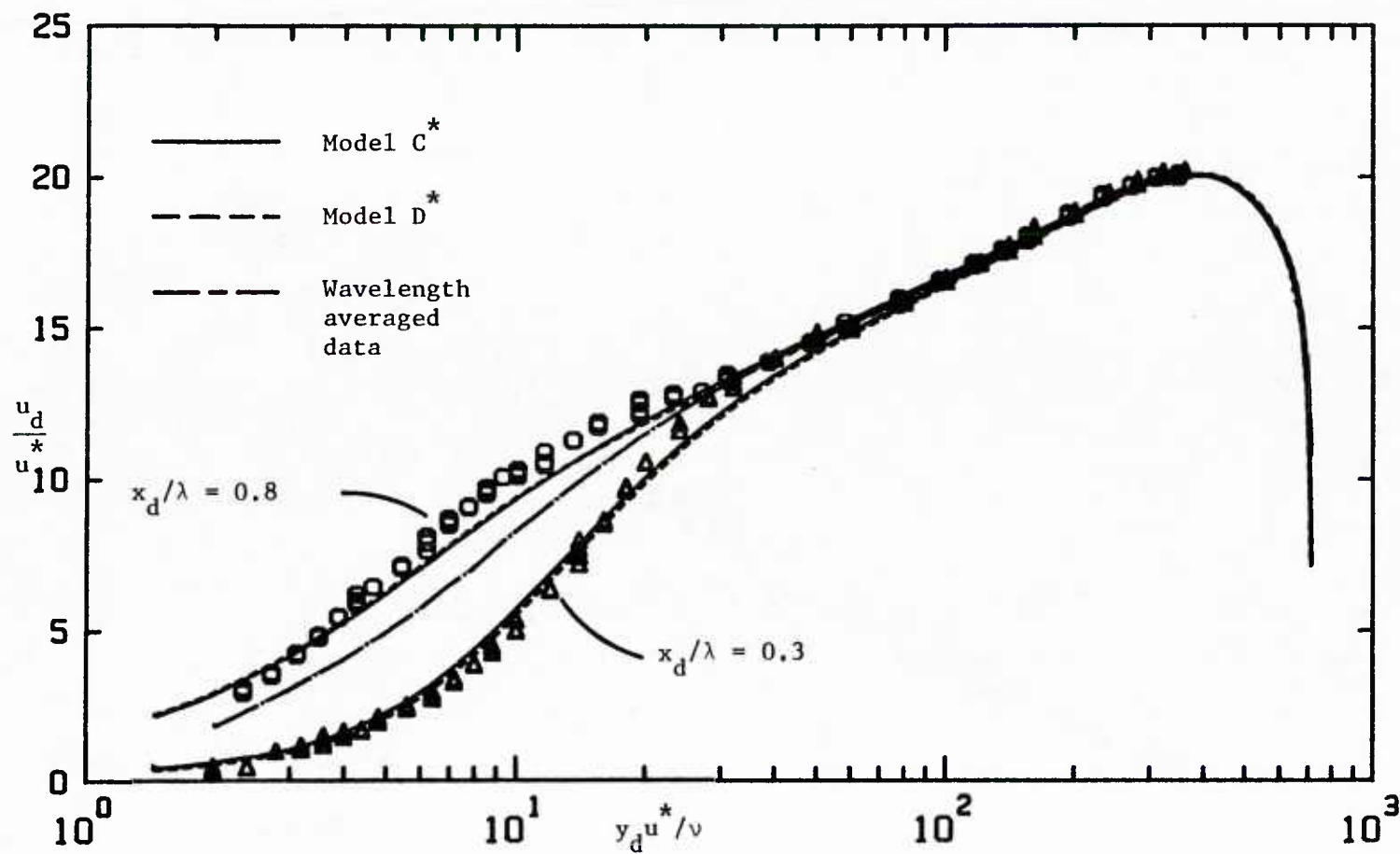


Figure 6.8 Comparison of Mean Velocity Measurements with Channel Calculations, $x_d/\lambda = 0.3, 0.8$, $2a_d/\lambda = 0.03125$, $Re_b = 6400$, $2h_d/\lambda = 1.0$

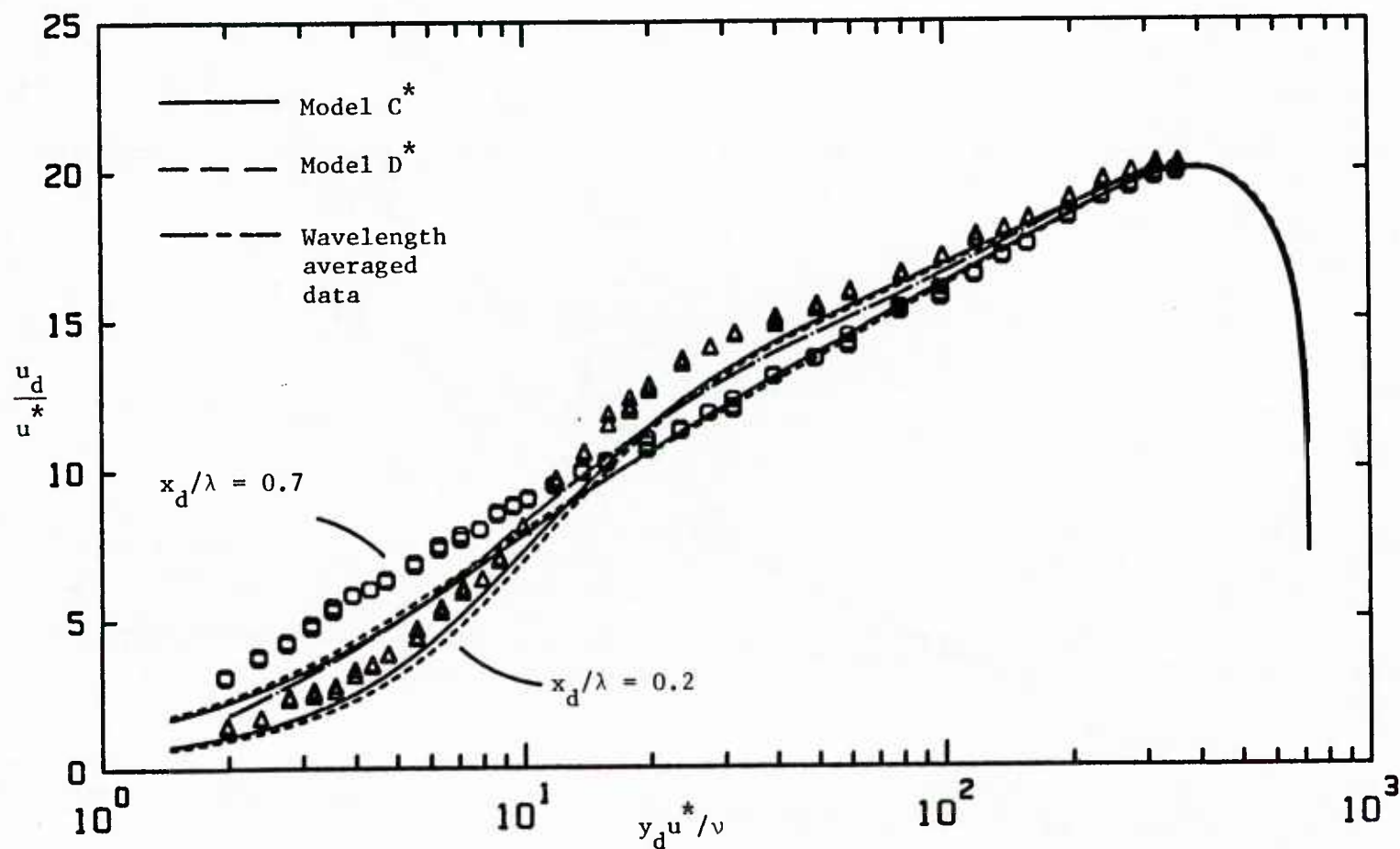


Figure 6.9 Comparison of Mean Velocity Measurements with Channel Calculations, $x_d / \lambda = 0.2, 0.7$, $2a_d / \lambda = 0.03125$, $Re_b = 6400$, $2h_d / \lambda = 1.0$

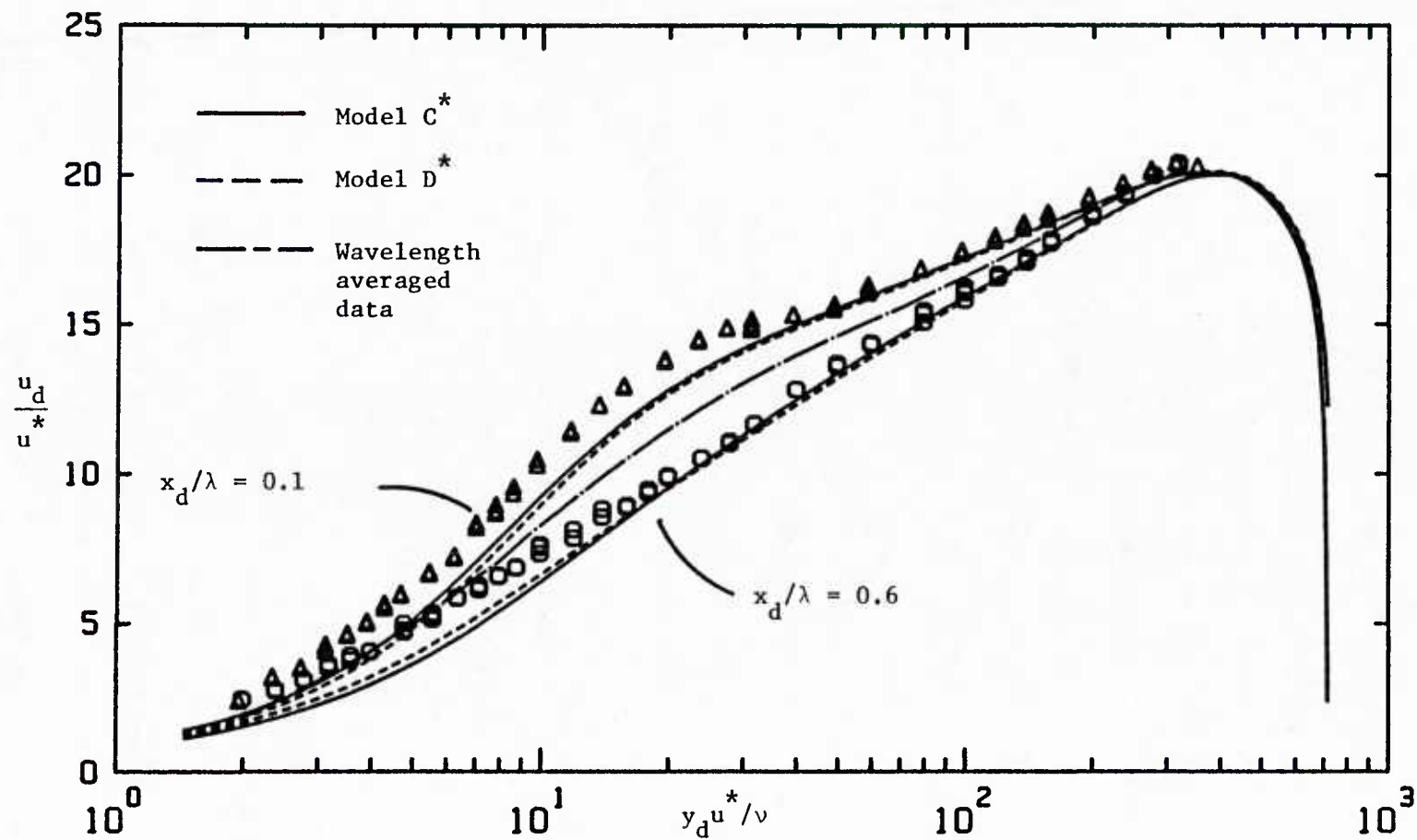


Figure 6.10 Comparison of Mean Velocity Measurements with Channel Calculations, $x_d / \lambda = 0.1, 0.6$, $2a_d / \lambda = 0.03125$, $Re_b = 6400$, $2h_d / \lambda = 1.0$

The calculated velocity profiles were found to be independent of the type of distance y_d' used in the Cess equation.

D. Mean Velocity Responses at Constant Heights above Wave

The entire time-averaged flowfield above the wave can be studied by plotting velocities at constant vertical heights above the surface. This is shown in Figure 6.11 with constant $y_d u^* / \nu$ values ranging from 5 to 300. It can be seen that the velocity field is perturbed approximately according to the shape of the wave. That is, a near linear response is observed with an associated phase and amplitude at each $y_d u^* / \nu$ value.

The curves in Figure 6.11 were least squares fitted to a two harmonic Fourier series to obtain quantitative information about the linearity of this flowfield. The ratio of the amplitudes of the second to first harmonics, $|\hat{u}_d|_2 / |\hat{u}_d|_1$, is shown in Figure 6.12 as a function of distance above the wave surface. The maximum ratio of 0.17 indicates a weakly nonlinear response. It is suspected that this ratio is slightly higher than the true ratio because any scatter in the data of Figure 6.11 is interpreted as nonlinearities by the Fourier analysis. Models C* and D* underpredict the observed nonlinearities.

The amplitudes of the first and second harmonics of the velocity response are shown in Figure 6.13. Here it is also clear that the first harmonic dominates the second harmonic at all $y_d u^* / \nu$ values. Both amplitudes are zero at the wall due to the no slip condition. The amplitude of the first harmonic increases rapidly to a maximum

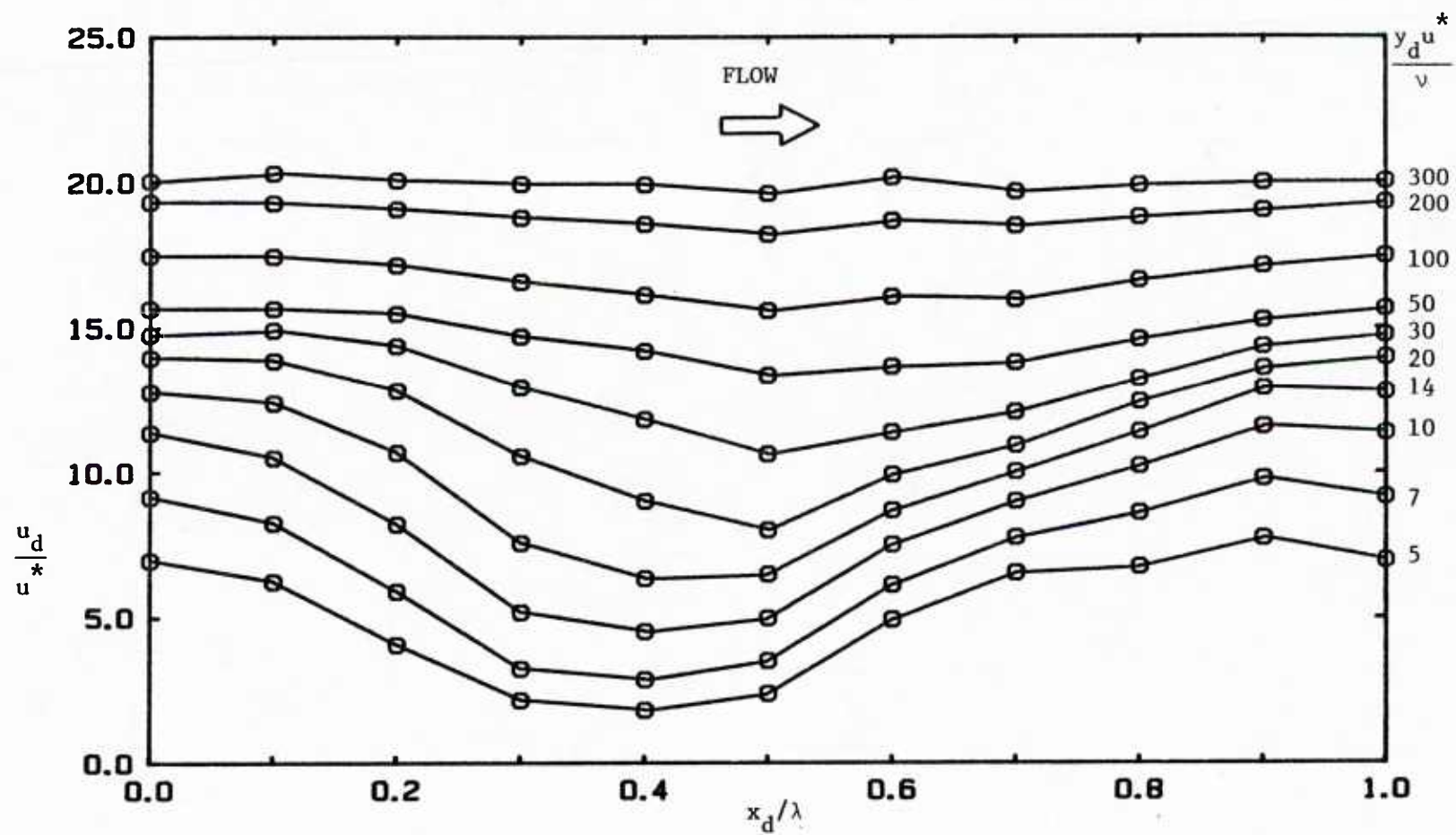


Figure 6.11 Mean Velocity Responses at Constant Heights above Wave Surface, $2a_d/\lambda = 0.0312$, $Re_b = 6400$, $2h_d/\lambda = 1.0$

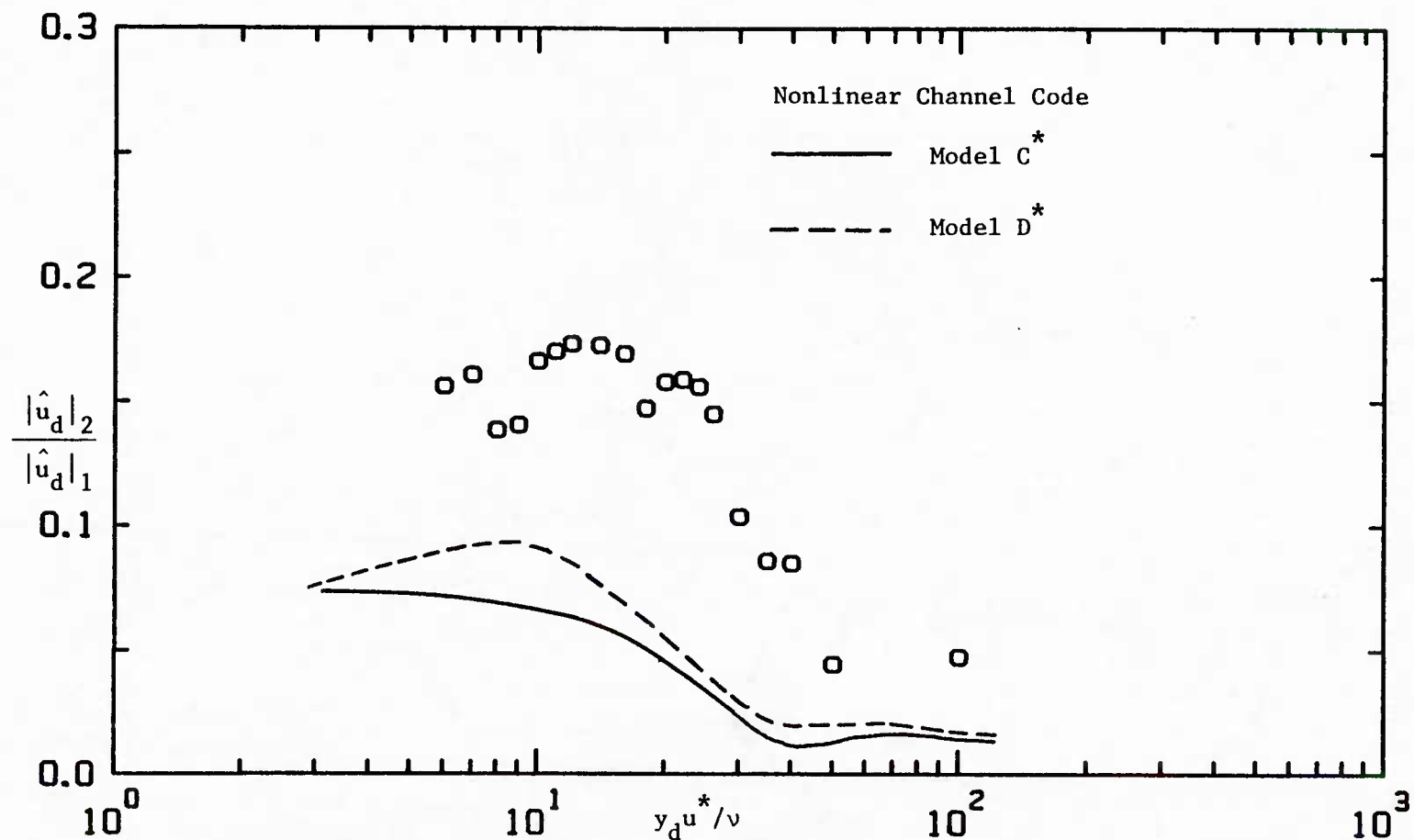


Figure 6.12 Velocity Amplitude Ratio of Second to First Harmonics,
 $2a_d/\lambda = 0.03125$, $Re_b = 6400$, $2h_d/\lambda = 1.0$

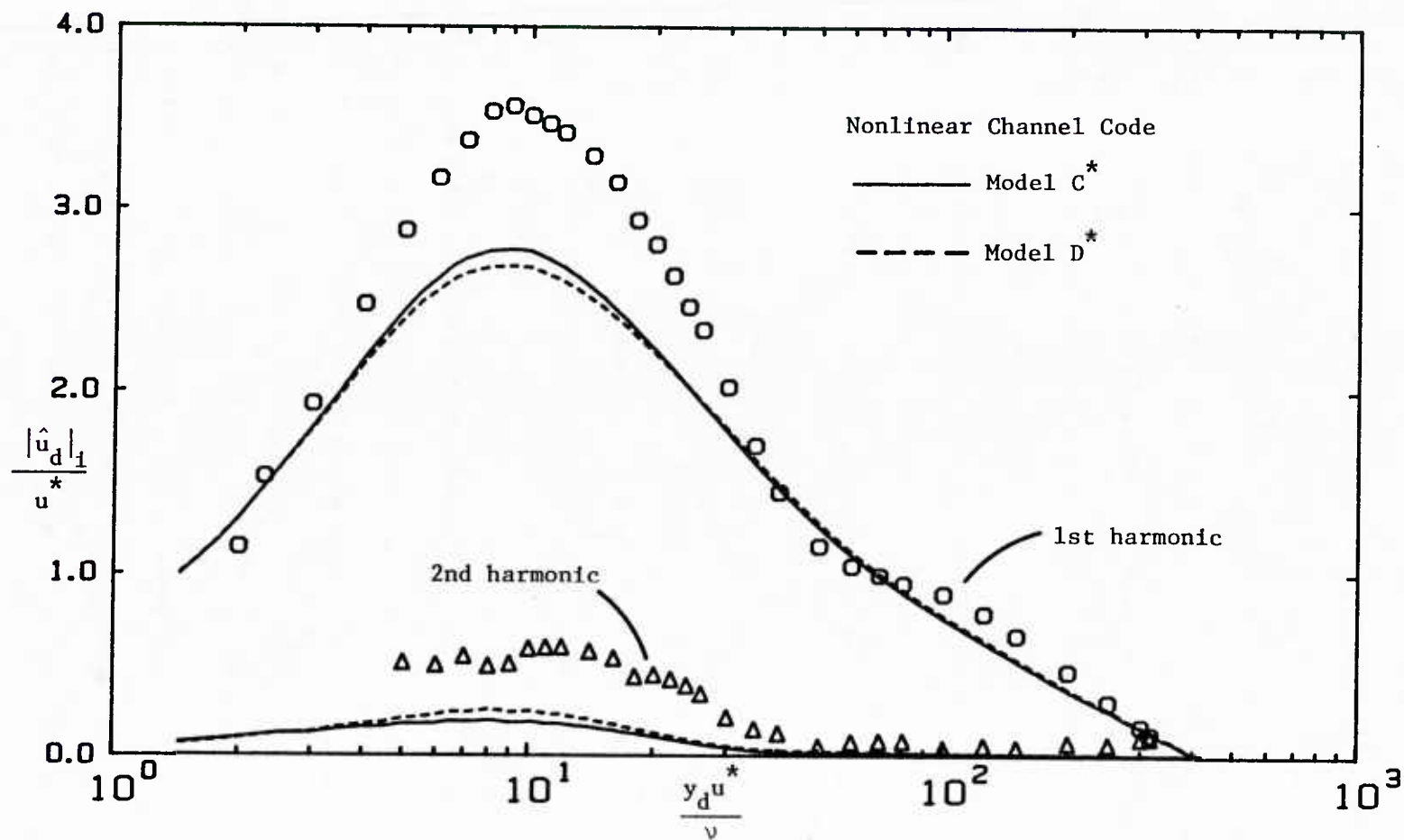


Figure 6.13 Amplitudes of First and Second Harmonics of Velocity Response, $2a_d/\lambda = 0.03125$, $Re_b = 6400$, $2h_d/\lambda = 1.0$

value of 3.6 at $y_d u^* / \nu$ equal to 9. This is also the approximate location of the maximum nonlinearity. Figure 6.14 shows the response at $y_d u^* / \nu = 9$ where it is Fourier fitted to one and two harmonics. Above $y_d u^* / \nu = 9$ the amplitude of the first harmonic decreases rapidly to about the edge of the viscous wall region and then gradually decreases to zero near the center of the channel, $y_d u^* / \nu \approx 365$. Disturbances are small far from the wave surface because here the fluid cannot "feel" the presence of the wave below it.

Nonlinearities also become negligible near the edge of the viscous wall region. The velocity response at $y_d u^* / \nu = 40$ is shown in Figure 6.15. Here it is seen that the Fourier fits to one and two harmonics are almost indistinguishable.

The amplitude predictions of Models C^* and D^* are also shown in Figure 6.13. Both models predict nearly identical first and second harmonic amplitudes with the same general shape as the data. However, the models significantly underestimate the amplitude observations for $4 < y_d u^* / \nu < 30$.

It should be noted here that there are turbulence models which predict larger velocity perturbations about the wavelength average than Models C^* and D^* . Abrams [2] used a linear analysis to investigate the effect of a quasilaminar model on the flowfield over a wave of infinitesimal amplitude in a boundary layer. A quasilaminar model assumes that all wave-induced turbulent quantities are zero. The computer code of Abrams was run with quasilaminar, C^* and D^* turbulence models for $\alpha_d \nu / u^* = 0.008$ (equivalent to $Re_b = 6400$).

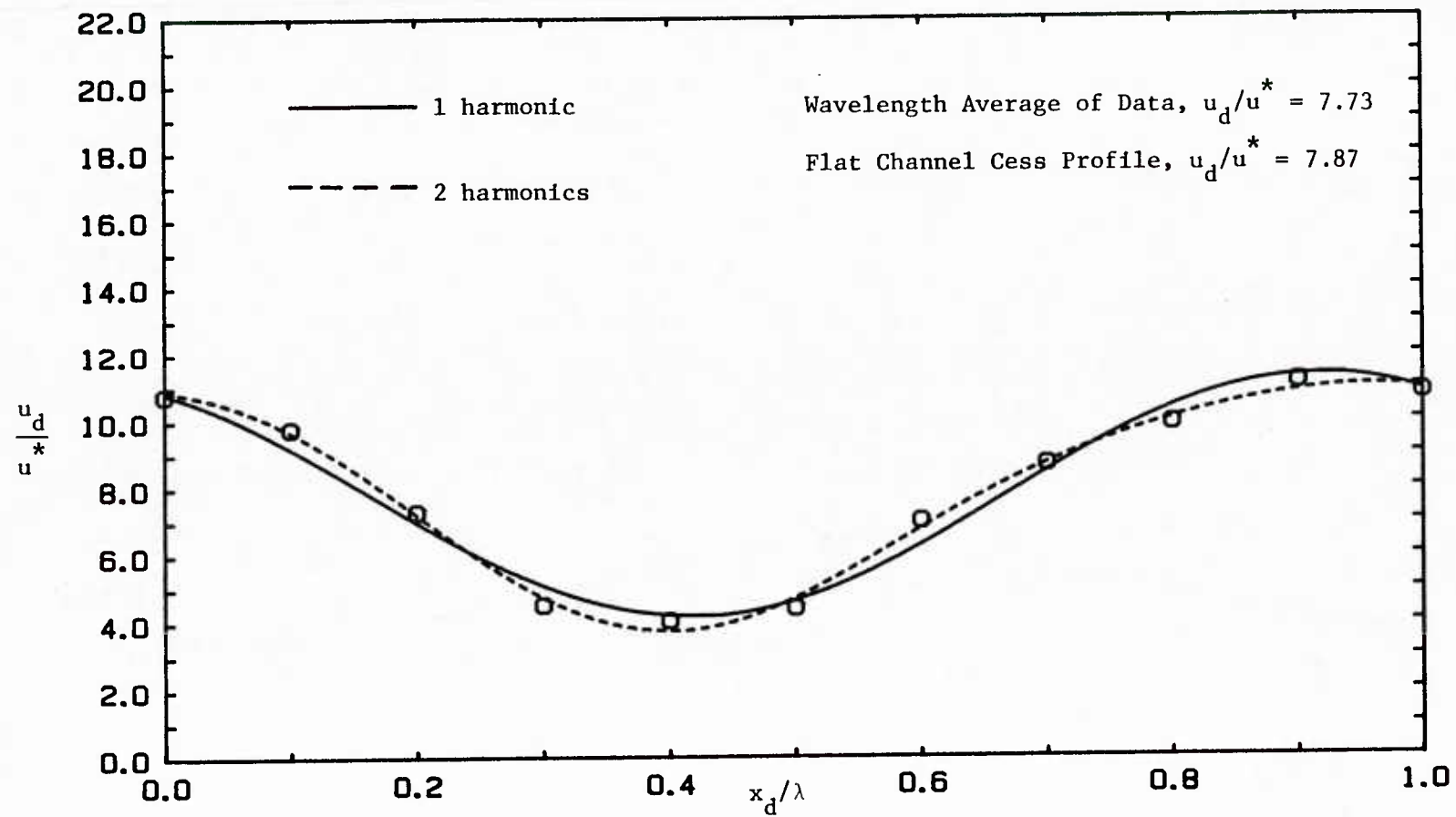


Figure 6.14 Velocity Response at $y_d u^*/\nu = 9$, $2a_d/\lambda = 0.03125$,
 $Re_b = 6400$, $2h_d/\lambda = 1.0$

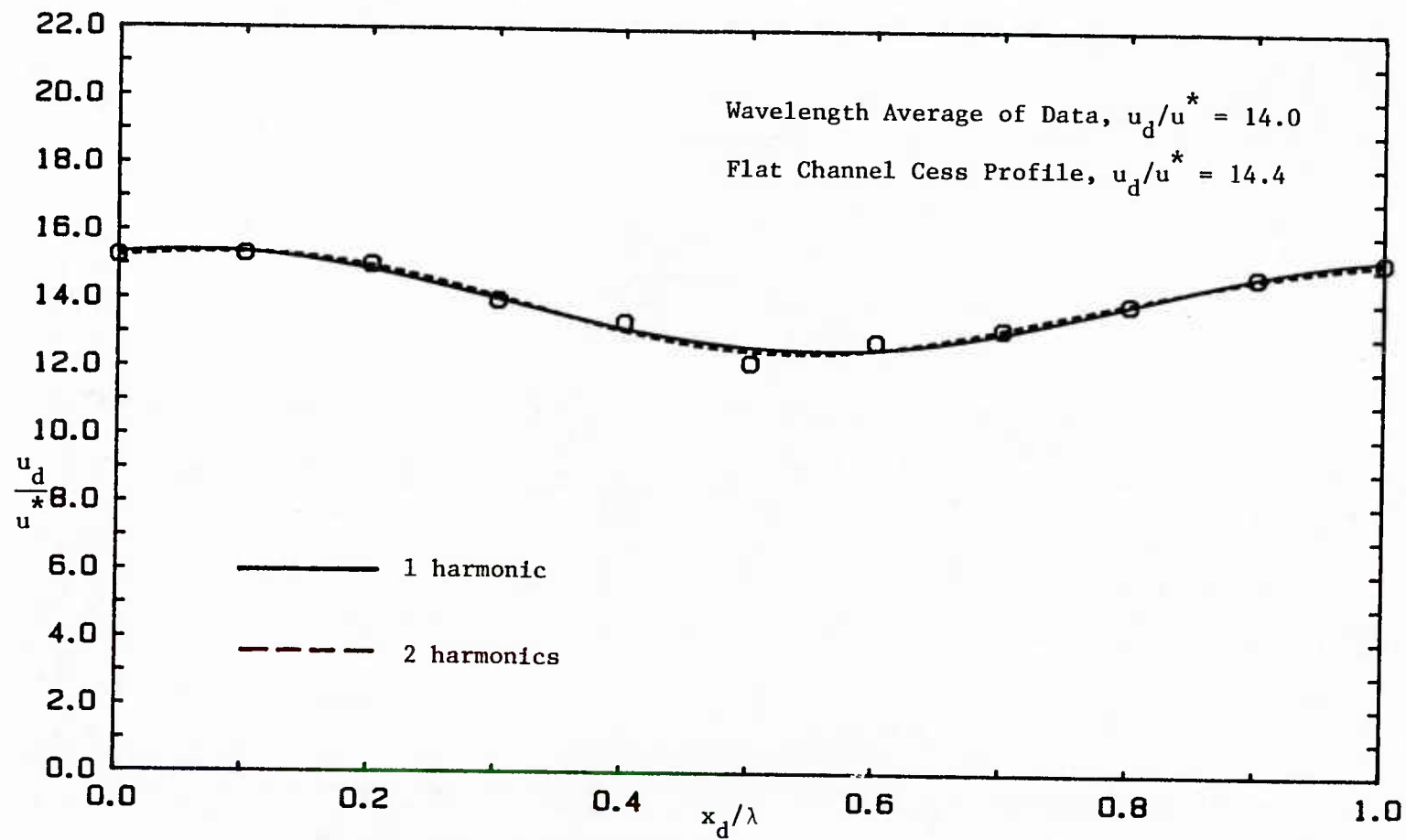


Figure 6.15 Velocity Response at $y_d u^*/\nu = 40$, $2a_d/\lambda = 0.03125$,
 $Re_b = 6400$, $2h_d/\lambda = 1.0$

It was found that the quasilaminar model predicts a maximum wave-induced amplitude which is 30 percent and 37 percent higher than Models C* and D* respectively. (Profiles of velocity perturbation amplitudes calculated from the linear analysis are given in Appendix D.) However, the quasilaminar model was not adapted to the nonlinear analysis for two reasons. First, Thorsness et al. [45] and Abrams and Hanratty [4] have shown that this model cannot predict the surface shear stress over a wide range of flowrates. The model is valid only for very large values of the dimensionless wave-number, $\alpha_d v/u^*$. Secondly, the quasilaminar model predicts only perturbations and can strictly be applied only to waves of infinitesimal amplitudes for which the wavelength averaged velocity is known.

The quasilaminar model is mentioned above because the findings of Abrams suggest that a very simple model, with smaller wave-induced variations of the turbulence outside the near wall region than Models C* and D*, may provide a better fit to the velocity field.

The phase angle of the first harmonic of the velocity response, $\theta_{u,1}$, is shown in Figure 6.16 as a function of $y_d u^*/v$. This phase angle is the shift of the maximum velocity upstream of the crest. The phase angle is a maximum at the wave surface and decreases rapidly within the viscous wall region. A drop of about 20° in the phase is seen between $y_d u^*/v = 2$ and 10. A minimum value of -25° is observed at about $y_d u^*/v = 50$ and the phase tends toward zero far from the wall where the influence of the wave on the fluid is not felt.

A comparison of $\theta_{u,1}$ predicted from turbulence Models C* and D* is also shown in Figure 6.16. Good agreement is observed with

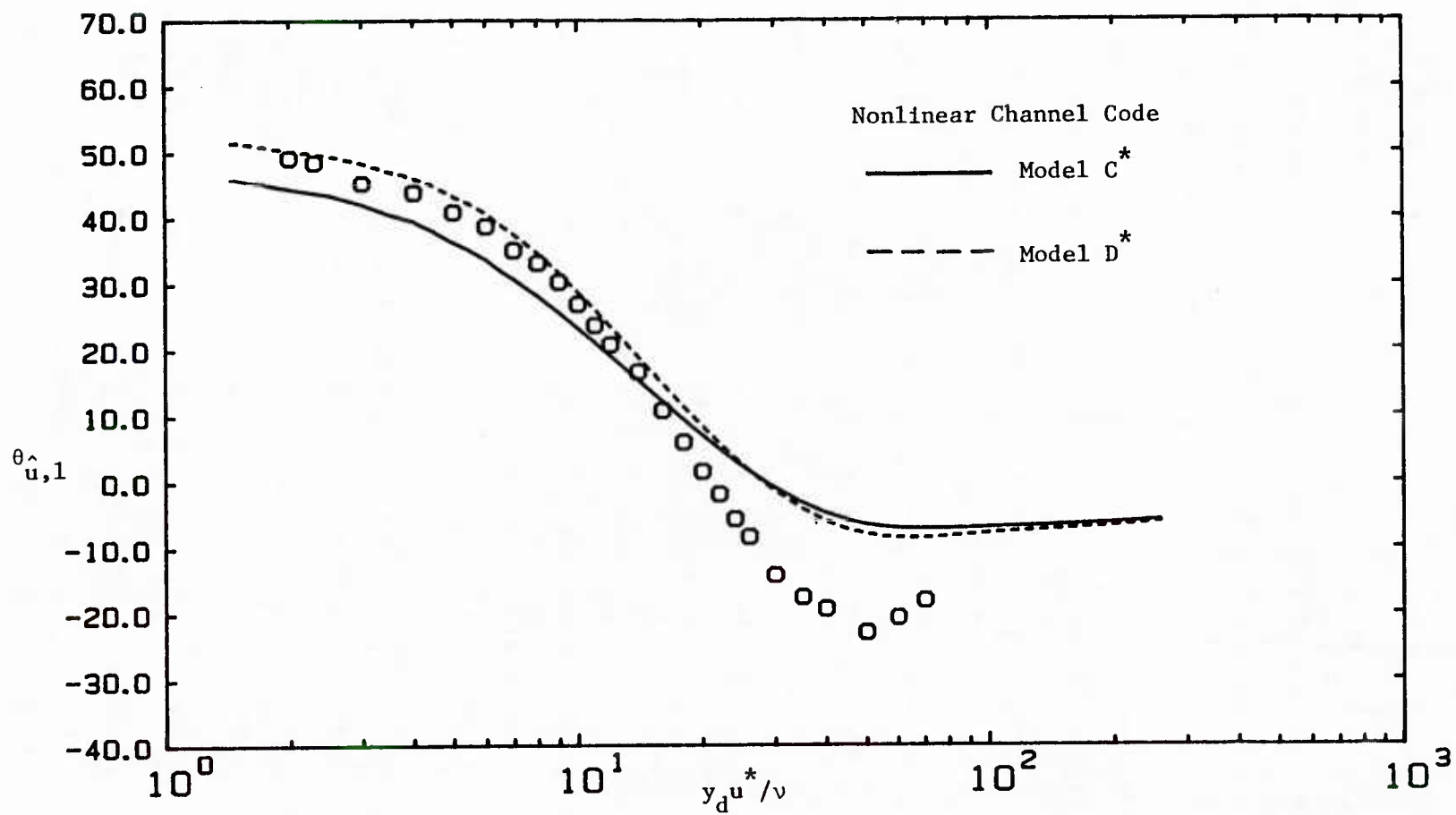


Figure 6.16 Phase Angle of First Harmonic of Velocity Response,
 $2a_d/\lambda = 0.03125$, $Re_b = 6400$, $2h_d/\lambda = 1.0$

both models for $y_d u^* / \nu < 20$. Neither model fits the data well outside the viscous wall region. However, the data may be in error here.

It is not possible to determine accurately phase angles in this region because scatter in the data becomes comparable to the amplitude of the velocity response for large $y_d u^* / \nu$.

E. Prediction of Surface Shear Stress Response from LDV Measurements

It is of interest to know whether the LDV data for $2a_d/\lambda = 0.03125$ and $Re_b = 6400$ are close enough to the wave surface to obtain the surface shear stress response. This subsection discusses determination of the amplitude and phase of the wall shear stress from the velocity measurements.

In Figure 6.13 the slope of $|\hat{u}_d|_1$ versus $y_d u^* / \nu$ at the wave surface is equal to the amplitude of the wave-induced shear stress. This quantity, $|\hat{\tau}_d|_1$, can be determined from the velocity data provided there are points close enough to the surface to extrapolate linearly. Figure 6.17 shows a comparison of the slope obtained by extrapolating the data with $|\hat{\tau}_d|_1$ from the electrochemical measurements of Zilker et al. [49]. It is found that the velocity data are not close enough to the wave surface to obtain the shear stress amplitude. This implies that the linear region in the velocity profiles does not extend to the closest measurements at $y_d u^* / \nu$ equal to two. A flat channel profile, by contrast, has a linear region that extends to a $y_d u^* / \nu$ value of five. The closeness of the wave-induced velocity perturbations to the wall indicates that both LDV and electrochemical techniques are necessary to study the near wall region. This point is illustrated in Figure 6.18 where mean velocity data at $x/\lambda = 0.3$ are compared

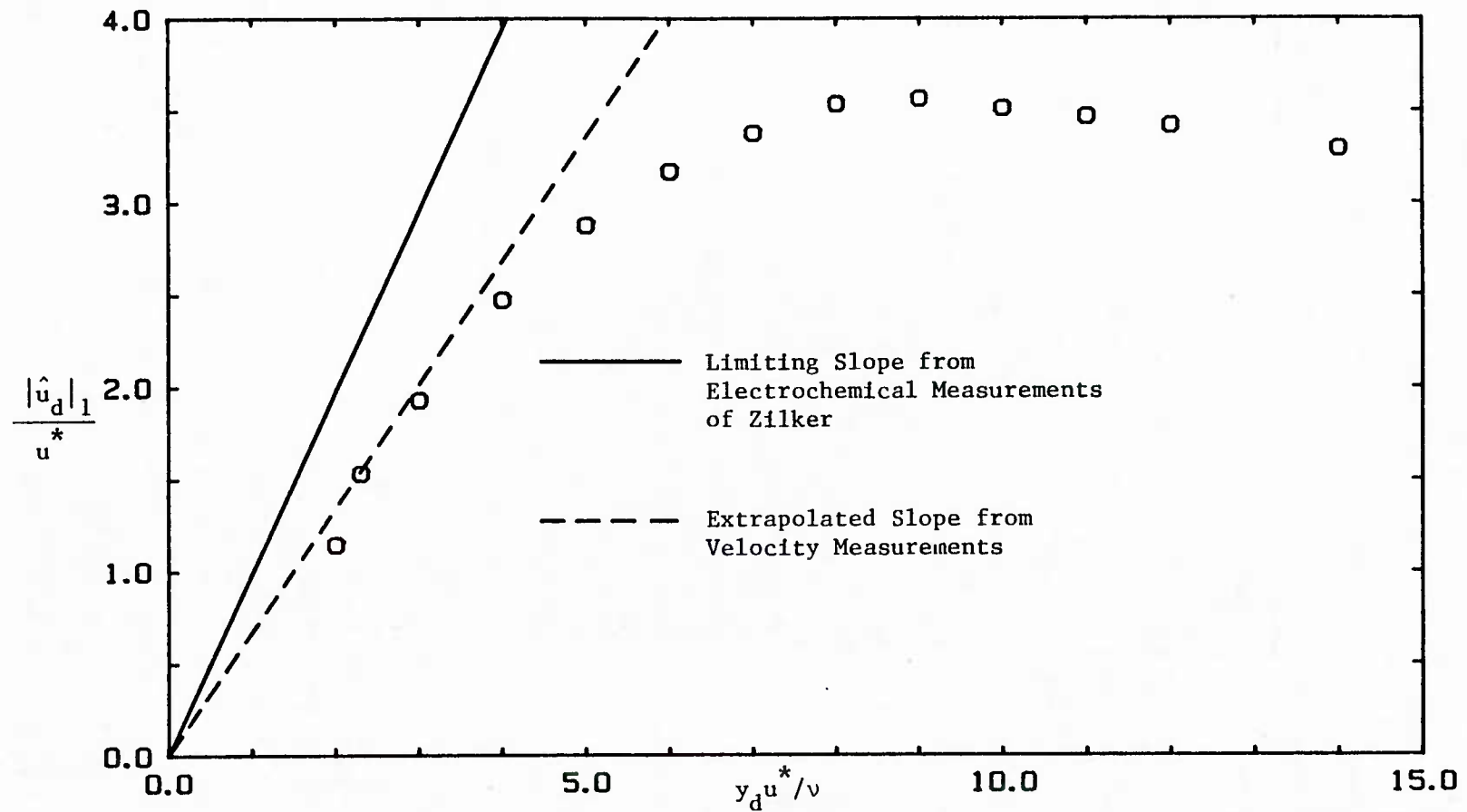


Figure 6.17 Comparison of Shear Stress Amplitude from Electrochemical and Extrapolated Velocity Measurements, $2a_d/\lambda = 0.03125$, $Re_b = 6400$, $2h_d/\lambda = 1.0$

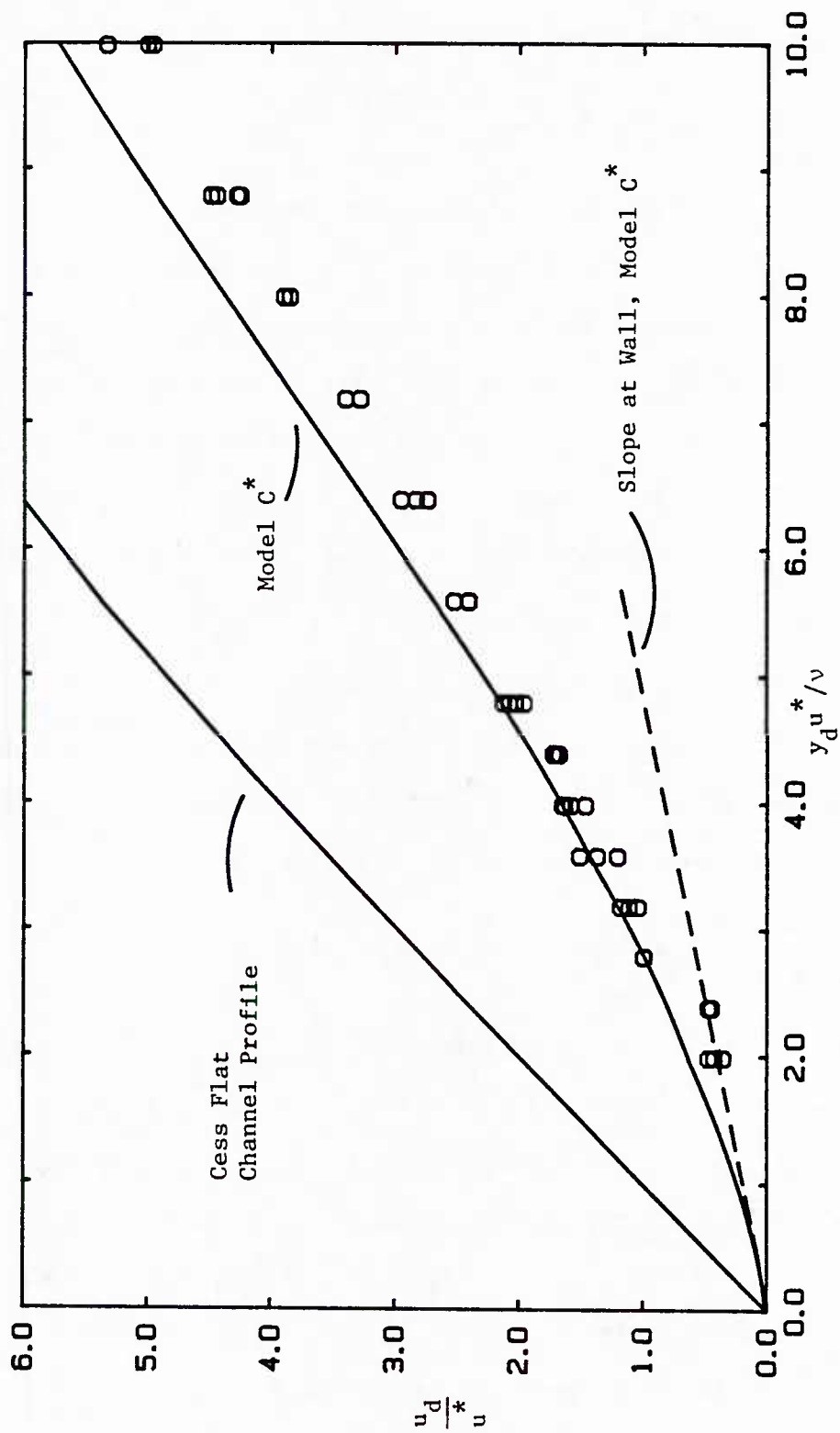


Figure 6.18 Near Wall Region at $x_d/\lambda = 0.3$, $2a_d/\lambda = 0.03125$, $Re_b = 6400$, $2h_d/\lambda = 1.0$

with the Cess flat channel profiles and the prediction of Model C^* . Model C^* , which was shown in Section I.A.1. to provide a good fit to the surface shear stress, is linear only to about $y_d u^*/\nu$ equal to one at this position.

The phase angle of the velocity at the wave surface is equal to the phase angle of the shear stress. The data in Figure 6.16 can be extrapolated linearly to the wall to obtain a shear stress phase angle, $\theta_{\tau,1}$, of 54 degrees. See Figure 6.19. The extrapolated and calculated phases are within the experimental error of the electrochemical measurements of Zilker et al. Thus for a wave with $2a_d/\lambda = 0.03125$ and $Re_b = 6400$, IDV techniques can be used to measure the phase angle, but not the amplitude, of the surface shear stress response.

F. Wave-Induced Velocity Perturbations

The flowfield over a wave surface may be thought of as a wave-induced perturbation about the wavelength averaged profile. Thus the flowfield is given as,

$$u_d(x_d, y_d) = \bar{U}_d(y_d) + \hat{u}_d(x_d, y_d) \quad (6.2)$$

where $\hat{u}_d(x_d, y_d)$ is the perturbation and $u_d(x_d, y_d)$ and $\bar{U}_d(y_d)$ are the total and wavelength averaged velocities respectively. Measured profiles of $\hat{u}_d(x_d, y_d)$ are shown in Figures 6.20-6.24. By presenting only the perturbations, rather than the total velocity profiles, the effect of the wave on the mean flowfield is isolated. The profiles were obtained by subtracting the experimental wavelength averaged profile in Figure 6.3 from the total velocity profiles in Figures 5.5-5.14.

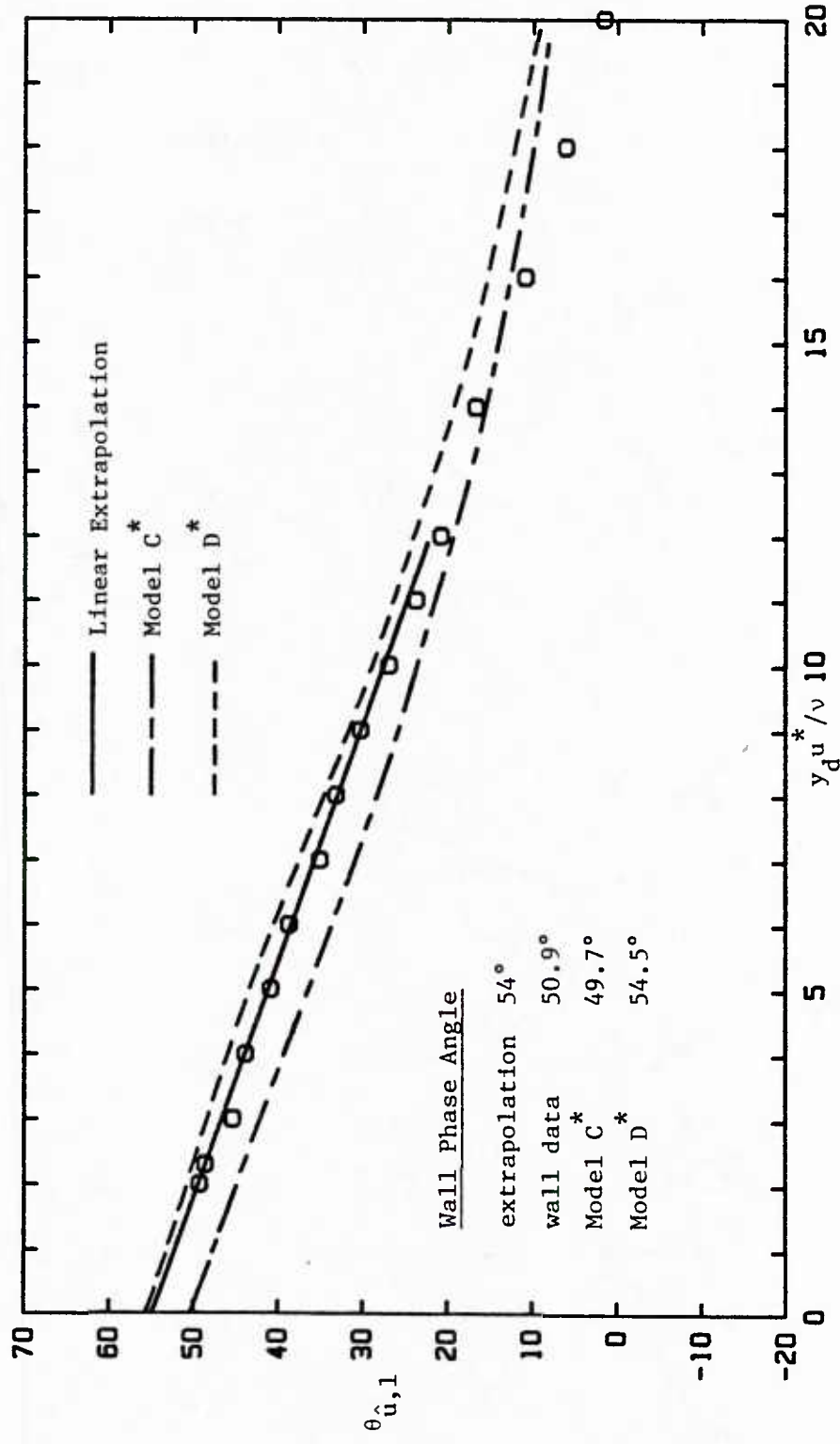


Figure 6.19 Linear Extrapolation to Wall of Phase Angle of First Harmonic of Velocity Response, $2a_d/\lambda = 0.03125$, $Re_b = 6400$, $2h_d/\lambda = 1.0$

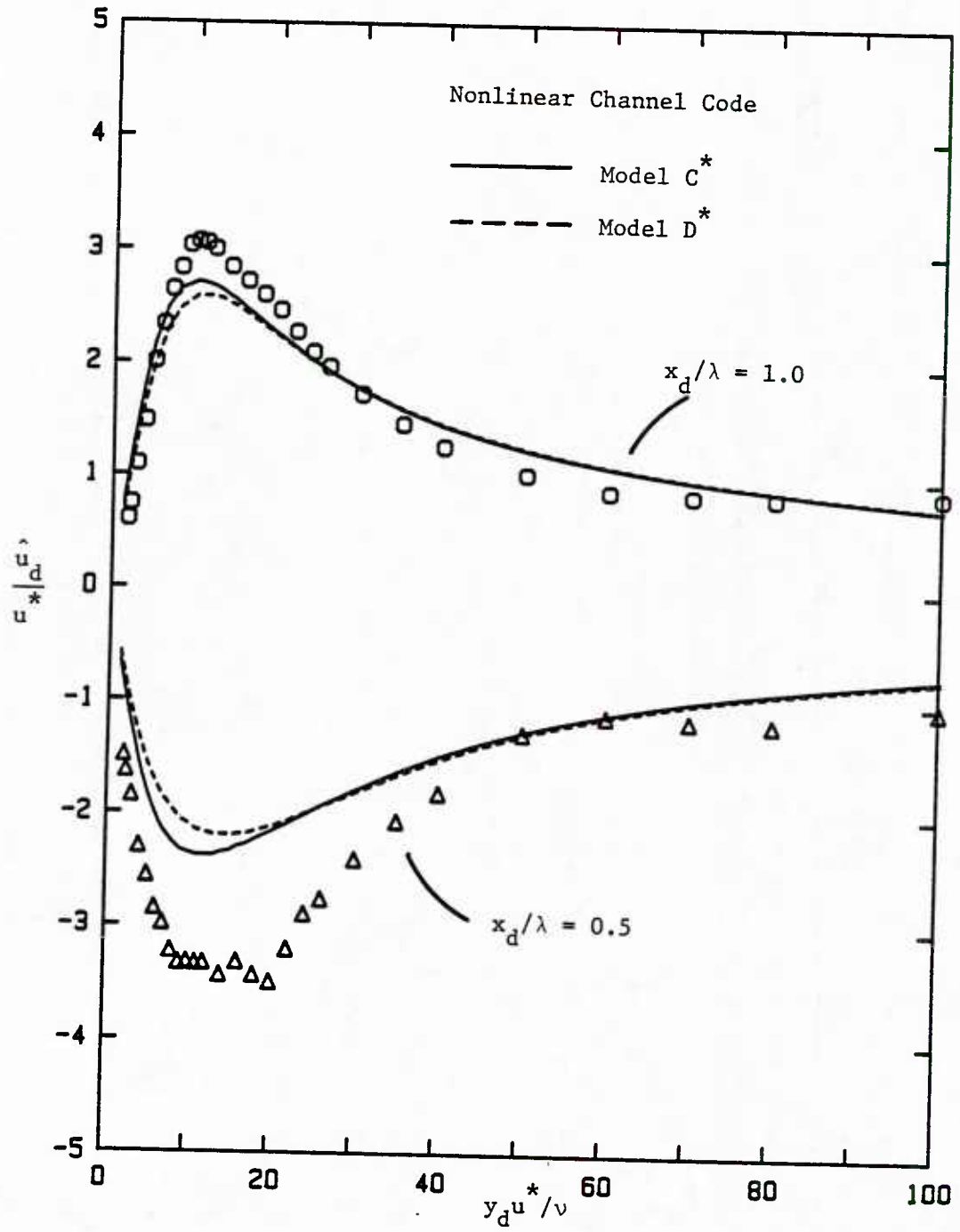


Figure 6.20 Wave-Induced Velocity Perturbations,
 $x_d/\lambda = 0.5, 1.0$, $2a_d/\lambda = 0.03125$,
 $Re_b = 6400$, $2h_d/\lambda = 1.0$

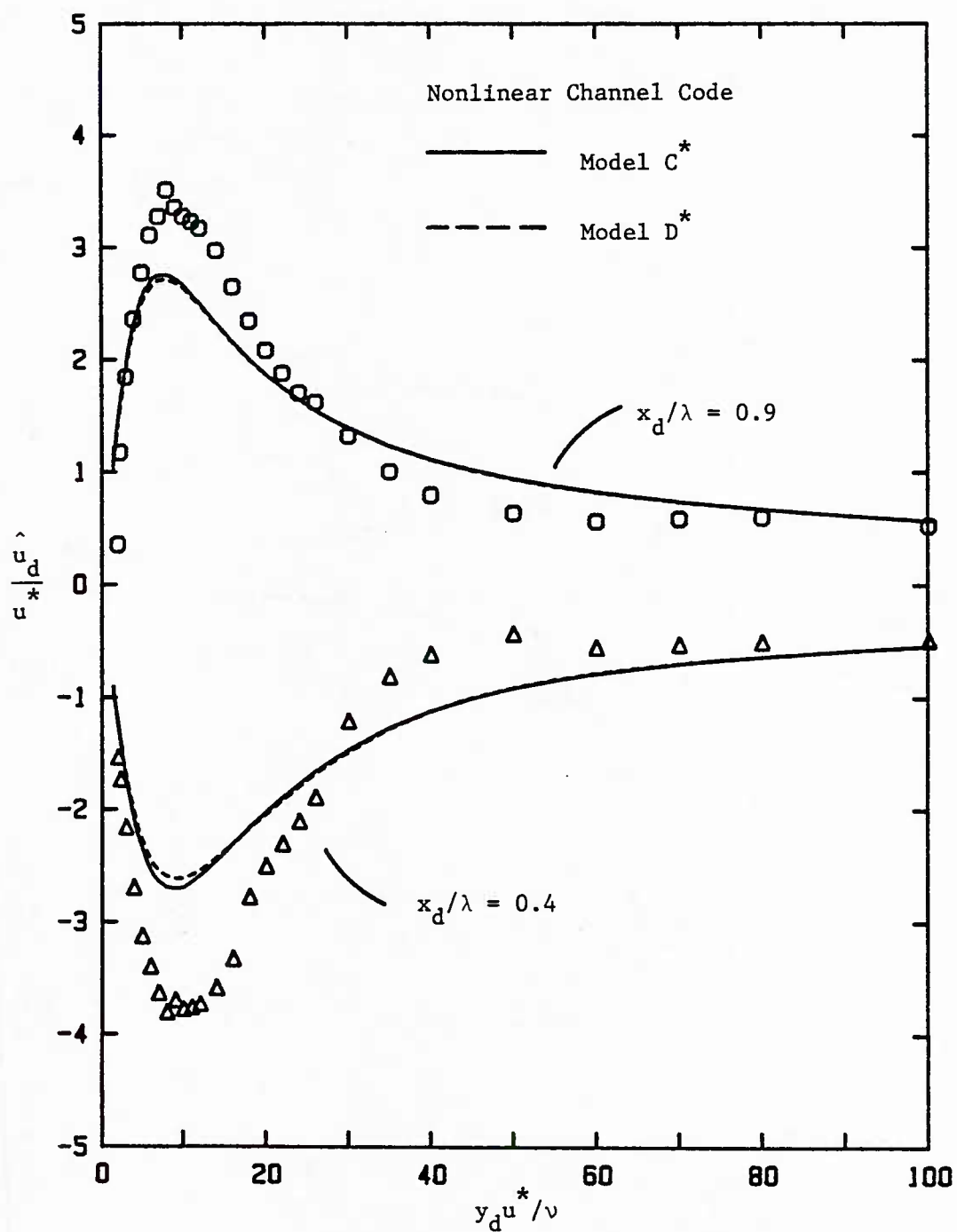


Figure 6.21 Wave-Induced Velocity Perturbations, $x_d/\lambda = 0.4, 0.9$, $2a_d/\lambda = 0.03125$, $Re_b = 6400$, $2h_d/\lambda = 1.0$

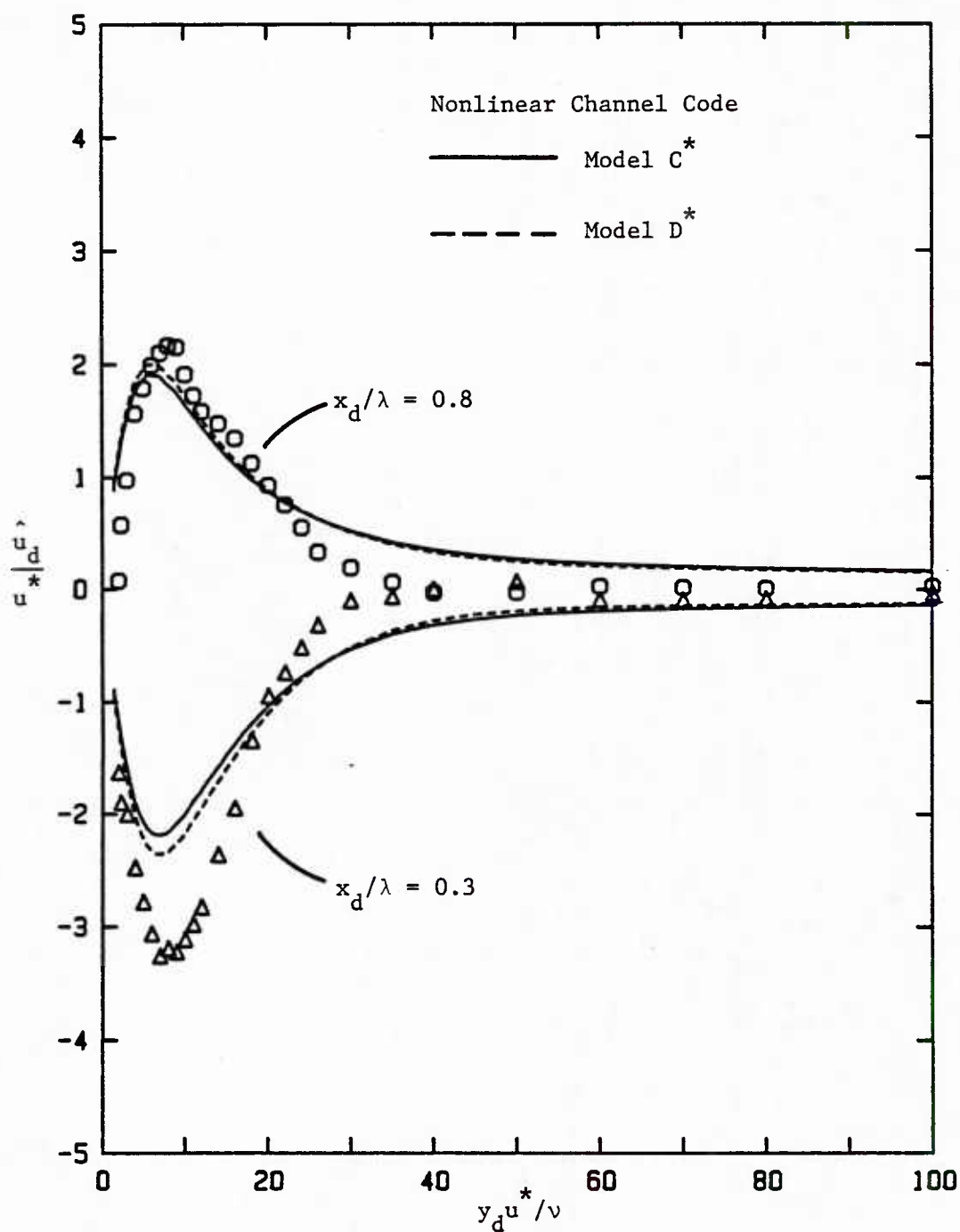


Figure 6.22 Wave-Induced Velocity Perturbations, $x_d/\lambda = 0.3, 0.8$, $2a_d/\lambda = 0.03125$, $Re_b = 6400$, $2h_d/\lambda = 1.0$

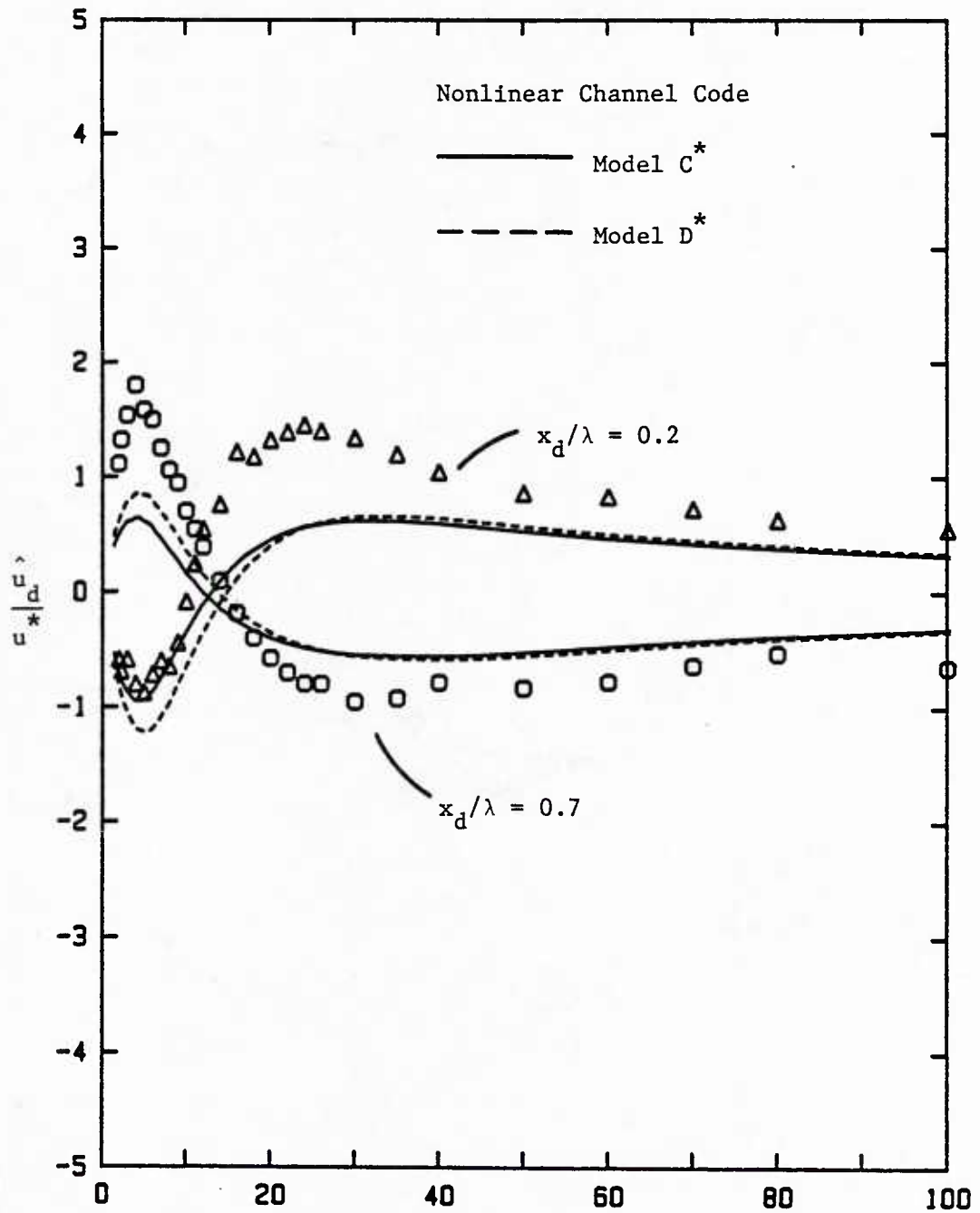


Figure 6.23 Wave-Induced Velocity Perturbations, $x_d/\lambda = 0.2$, 0.7 , $2a_d/\lambda = 0.03125$, $Re_b = 6400$, $2h_d/\lambda = 1.0$

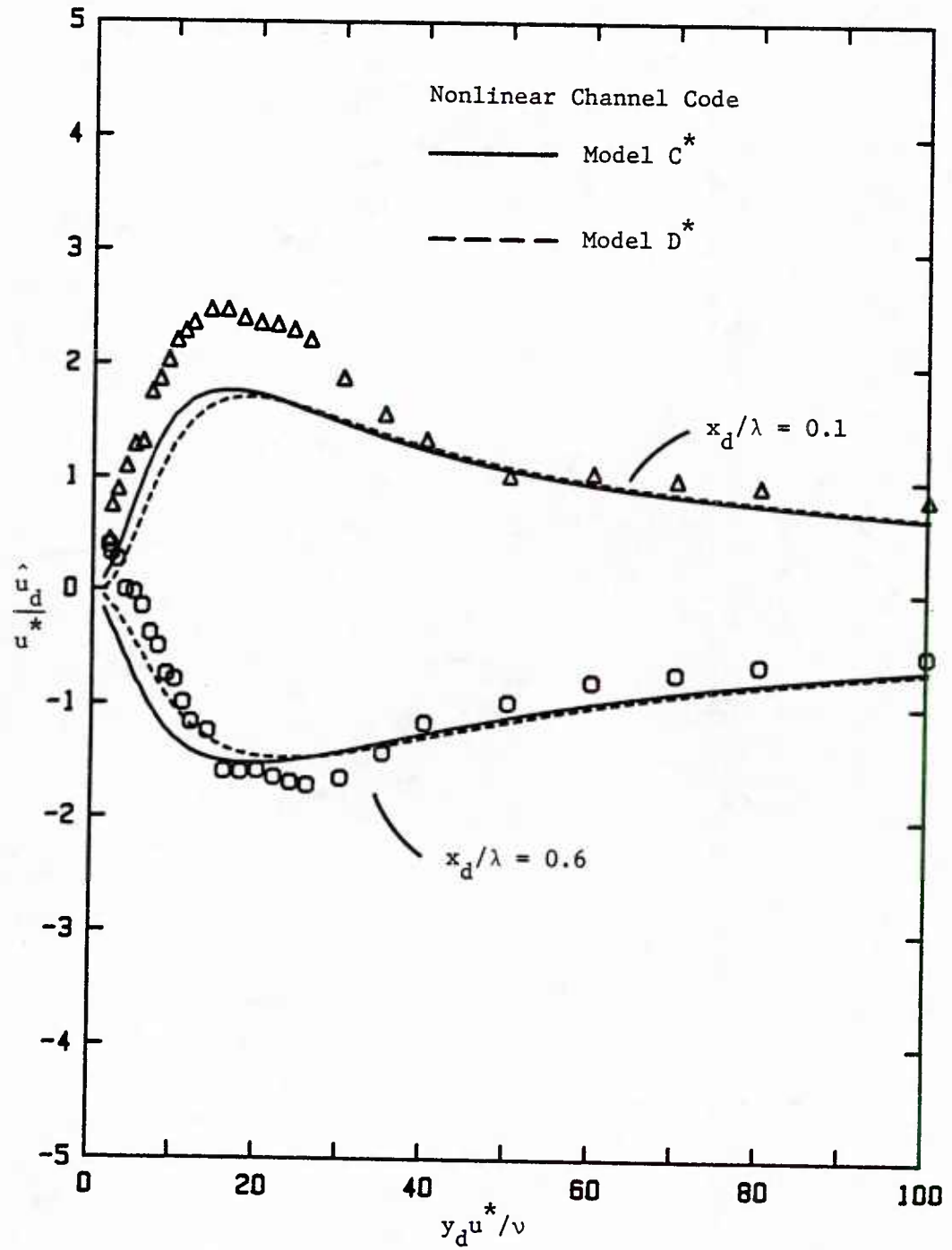


Figure 6.24 Wave-Induced Velocity Perturbations, $x_d/\lambda = 0.1$, 0.6 , $2a_d/\lambda = 0.03125$, $Re_b = 6400$, $2h_d/\lambda = 1.0$

The profiles of the wave-induced velocity perturbations are given in pairs at positions 180° apart along the wave surface. Abrams [2] has shown that for a perfectly linear response the perturbations are equal in magnitude and opposite in sign at half wavelength intervals. The data show that to a first approximation this characteristic of linear behavior is observed. However, small deviations can be seen. For instance, the magnitude of the perturbations at $x_d/\lambda = 0.3, 0.4,$ and 0.5 are larger than at the corresponding 180° distant positions of $x_d/\lambda = 0.8, 0.9,$ and 1.0 . The fluid in the trough region is moving slower than is expected from linear theory. This is not surprising since the conditions $2a_d/\lambda = 0.03125$ and $Re_b = 6400$ ($\alpha_d v/u^* = 0.008$) place this set of data close to the separated region. See Figure 3.1. Although no instantaneous separation was observed, the flow may be undergoing "incipient" separation. The location of this pre-separation behavior is consistent with the measurements of Kuzan [26] which show that separation first appears at approximately $x_d/\lambda = 0.4$.

A comparison of the data with predictions from the nonlinear channel code each using turbulence Models C^{*} and D^{*} is also shown in Figures 6.20-6.24. Here the calculated wavelength averaged profiles are used as the mean flowfield. Both models underpredict the disturbances in the viscous wall region. This is expected from previous comparisons of the theory with mean velocity profiles (Section I.C.) and the results of the Fourier analysis of the velocity field (Section I.D.).

G. Streamwise Intensities

The wavelength averaged profile of the streamwise intensity is shown in Figure 6.25. As with the case of the mean velocities, the intensities are averaged at constant heights measured vertically above the wave surface. Intensity measurements obtained over a flat surface in the same channel are also shown in Figure 6.25. A slight increase above flat channel intensities is observed in the viscous wall region.

Figure 6.26 gives all ten intensity profiles in Figure 5.15-5.24 plotted together. This figure shows the "envelope" of perturbation about the wavelength averaged profile. A maximum perturbation of ± 20 percent about the average occurs at $y_d u^* / \nu = 24$. The majority of the disturbances are found within the viscous wall region.

The observed deviations from the wavelength averaged intensity profile can be qualitatively explained in terms of pressure gradient effects on the turbulence. Because of the compression of the streamlines at the wave crest and the spreading of the streamlines at the trough the fluid pressure varies along the wave surface. This gives rise to a periodically varying pressure gradient along the wave surface that is roughly equal to that predicted by inviscid Kelvin-Helmholtz theory. That is, the pressure gradient is positive for $0 \leq x_d / \lambda \leq 0.5$ and negative for $0.5 \leq x_d / \lambda \leq 1.0$. Experimental studies [6,7,22,23,28,29,31] of turbulent boundary layers in slowly converging or diverging sections reveal that strong negative (favorable) pressure gradients cause a damping of turbulence close to the wall, and that positive (adverse) pressure gradients have

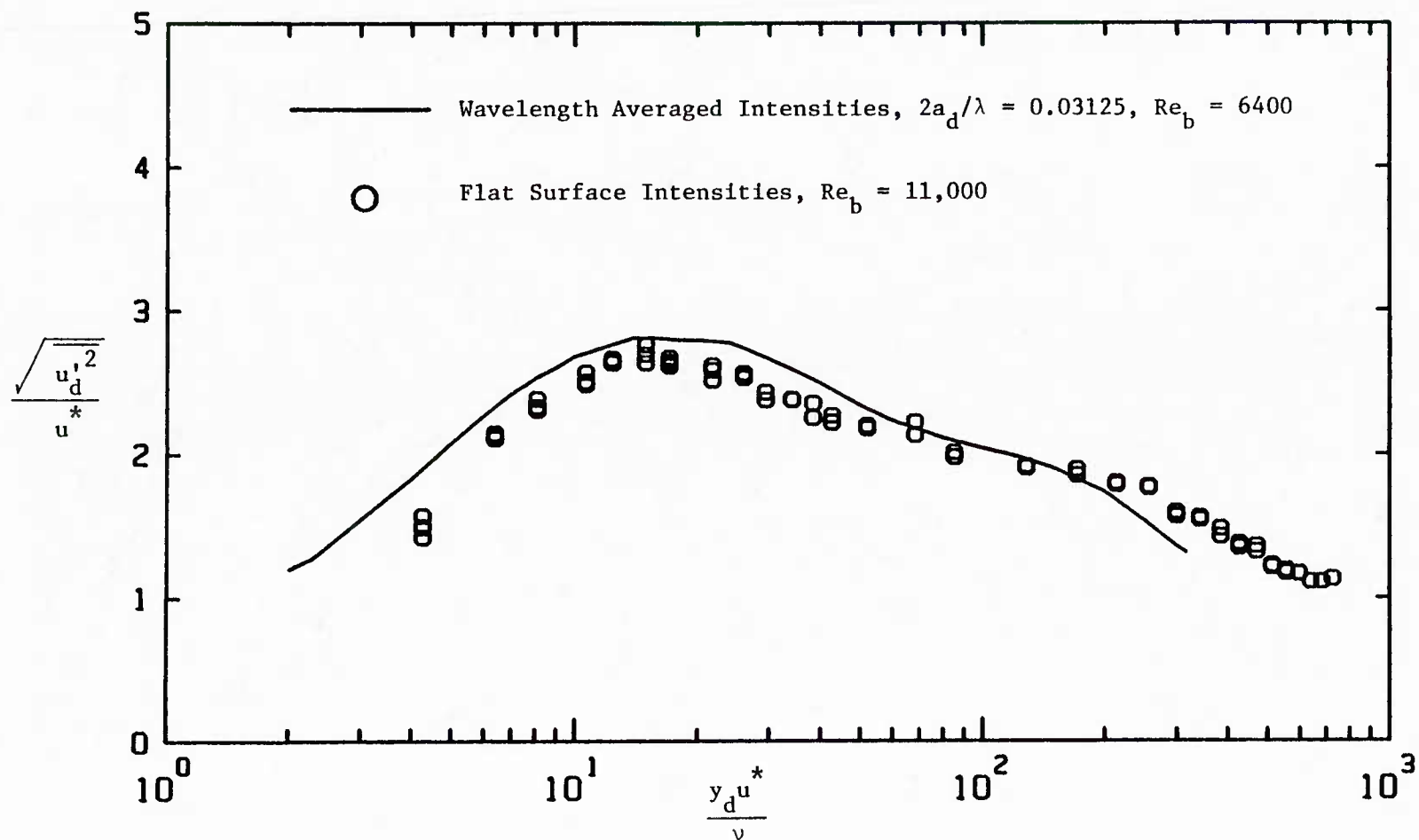












Figure 6.25 Comparison of Wavelength Averaged Intensity Profile with Flat Surface Intensity Profile

Legend for Figure 6.26

$\frac{x_d}{\lambda}$	Symbol
0.1	
0.2	
0.3	
0.4	
0.5	
0.6	
0.7	
0.8	
0.9	
1.0	

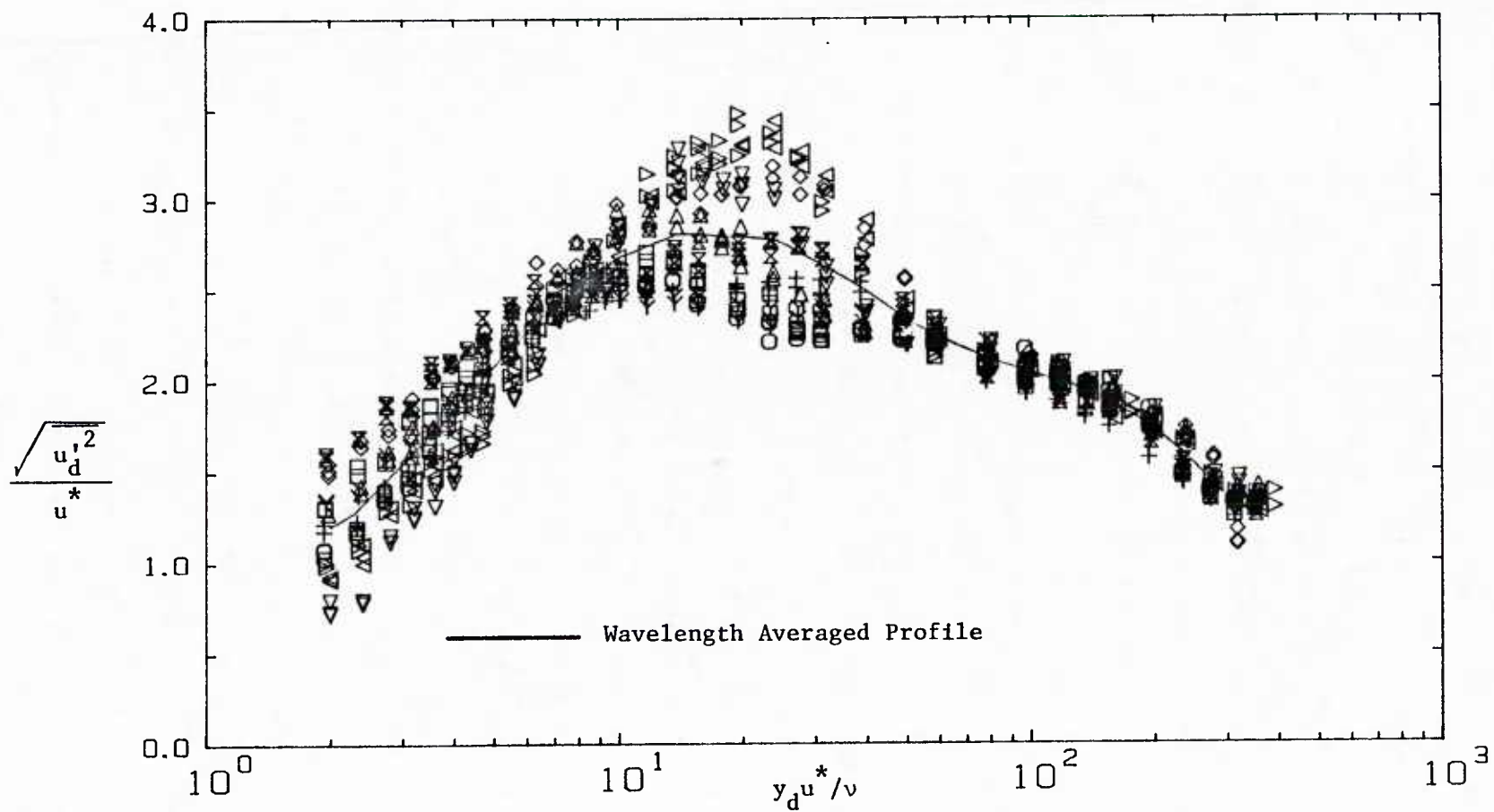


Figure 6.26 Envelope of Perturbations about Wavelength Averaged Intensity, $2a_d/\lambda = 0.03125$, $Re_b = 6400$, $2h_d/\lambda = 1.0$

just the opposite effect. These observations are confirmed by calculations of Finnicum [19] involving simple eddy modeling of the viscous wall region with constant pressure gradients. One might look for a similar phenomenon to occur at wave surfaces. However, in this case the pressure gradient is varying rapidly in the flow direction and its effect might not be as great as would be observed for an equilibrium flow because the flow does not adjust instantaneously.

The calculations in Section I.A. indicate that for $2a_d/\lambda = 0.03125$ and $Re_b = 6400$ the pressure field near the wave surface is shifted only slightly ($\approx 15^\circ$) downstream. Thus if the flow were to adjust instantaneously to the local pressure gradients, an enhancement and dampening of turbulence would be observed at approximately $0.0 \leq x_d/\lambda \leq 0.5$ and $0.5 \leq x_d/\lambda \leq 1.0$ respectively. However, lags in the reaction of the turbulence to the pressure gradients are observed. Figures 5.15-5.24 show that for $10 < y_d u^*/\nu < 60$ the actual positions of enhancement and dampening of the streamwise intensity are $0.3 \leq x_d/\lambda \leq 0.6$ and $0.8 \leq x_d/\lambda \leq 0.1$. It is also observed for $10 < y_d u^*/\nu < 60$ that this lag is a function of height above the wave surface with the lag increasing with increasing height. Turbulence Models C^* and D^* do not take into account this effect. Model C^* does not lag turbulence quantities and Model D^* uses a single lag constant at all heights.

For $y_d u^*/\nu > 60$ the intensities at all positions are approximately the same as the wavelength average. The influence of the wave is minimal here because inertial forces dominate the pressure gradient forces.

An interpretation of the intensity results below $y_d u^* / \nu = 10$ is less certain due to scatter in the responses. However, the data suggests that this portion of the intensity field responds faster to the local pressure gradient than the outer viscous wall region.

It should be noted that the pressure gradients along a wave surface are very large. The maximum negative pressure gradient predicted by the nonlinear channel code for $2a_d/\lambda = 0.03125$ and $Re_b = 6400$ is about 10 times the value of constant pressure gradients observed to cause relaminarization over a flat surface. Relaminarization was not observed. Thus an attenuation of the effect of the pressure gradients is seen as well as a lag.

The locations of the local intensity maxima in Figures 5.15-5.24 (marked by arrows) can be explained by drawing an analogy between the flowfield over a wave and a classical shear layer. This concept was first suggested by Buckles, Adrian and Hanratty [10]. The flowfield over a wave is similar to a shear layer because rapidly moving fluid from the crests passes over slowly moving fluid in the troughs. Figure 6.27 traces the loci of the intensity maxima over two wavelengths. The initial peak at $x_d/\lambda = 0.0$ becomes the second peak at about $x_d/\lambda = 0.6$ and then becomes the third peak at about $x_d/\lambda = 1.6$. This figure illustrates the "layering" effect of previous shear layers as their remnants pass over any given wave.

A two harmonic Fourier analysis of the intensity measurements was performed. The ratio of the amplitude of the second harmonic to the first, $|I_2|/|I_1|$, is shown in Figure 6.28. It can be seen

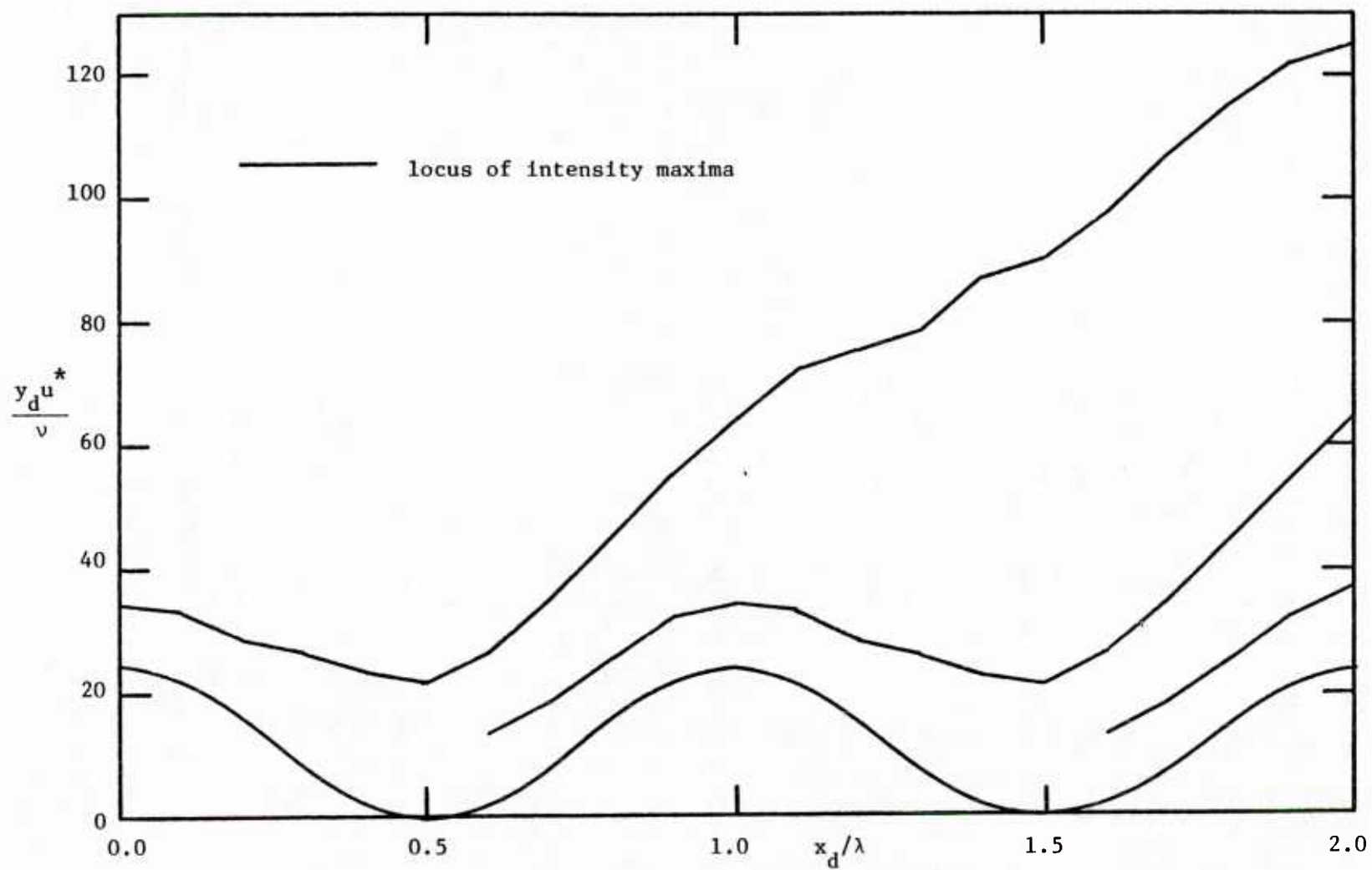


Figure 6.27 Locus of Maximum Intensities, $2a_d/\lambda = 0.03125$, $Re_b = 6400$, $2h_d/\lambda = 1.0$

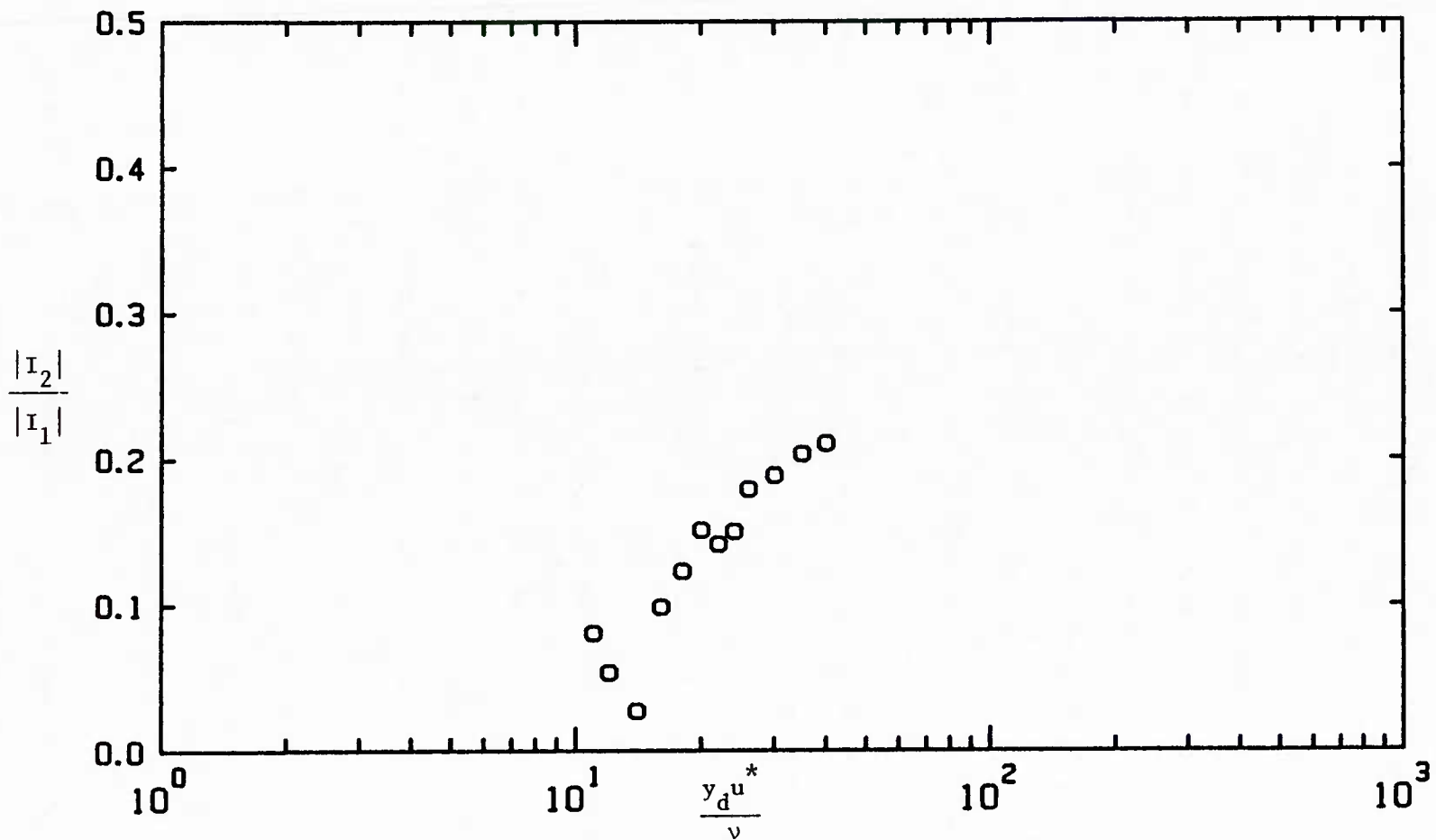


Figure 6.28 Intensity Amplitude Ratio of Second to First Harmonics,
 $2a_d/\lambda = 0.03125$, $Re_b = 6400$, $2h_d/\lambda = 1.0$

that the intensity response is nearly linear for $10 < y_d^* u^* / \nu < 40$. The results outside this range may be in error because here the amplitudes are small and of the same order as the scatter in the data.

The amplitudes of the first and second harmonics of the intensity response are given in Figure 6.30. The first harmonic is "spike" shaped with a maximum at $y_d^* u^* / \nu = 24$. The second harmonic has a maximum at approximately the same height above the wave but is much smaller and flatter. Figure 6.29 shows the intensity response at $y_d^* u^* / \nu = 24$ fitted to one and two harmonics. The amplitude of the intensity disturbance is negligible above $y_d^* u^* / \nu = 60$. The response at $y_d^* u^* / \nu = 60$ is given in Figure 6.31.

The phase shift upstream of the crest of the first harmonic of the intensity response is given in Figure 6.32. The phase varies from 222° at $y_d^* u^* / \nu = 10$ to 142° at $y_d^* u^* / \nu = 50$. The maximum intensity is in phase with the trough at about $y_d^* u^* / \nu \approx 28$.

II. Wave of Steepness $2a_d/\lambda = 0.05$

This section analyzes the velocity measurements for the wave of steepness $2a_d/\lambda = 0.05$ with $Re_b = 38,800$. The results, which are presented in the same form as in the previous section, show a flowfield with more nonlinear character than found over the $2a_d/\lambda = 0.03125$ wave. The ability of turbulence Models C^* and D^* to predict this behavior is discussed.

A. Wall Stresses

1. Surface Shear Stress

The surface shear stress responses predicted by the nonlinear channel code with turbulence Models C^* and D^* are shown in

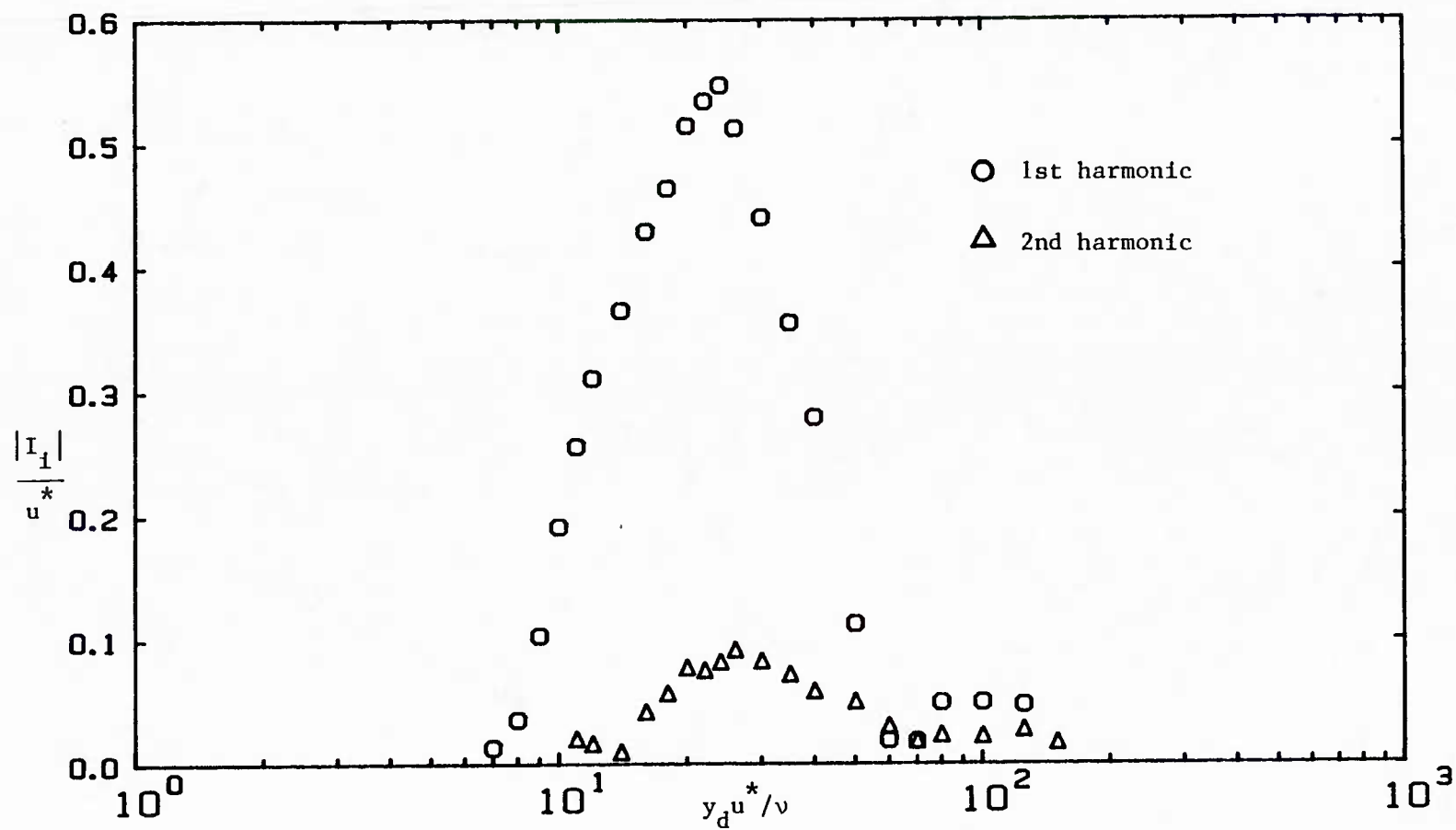


Figure 6.29 Amplitudes of First and Second Harmonics of Intensity Response, $2a_d/\lambda = 0.03125$, $Re_b = 6400$, $2h_d/\lambda = 1.0$

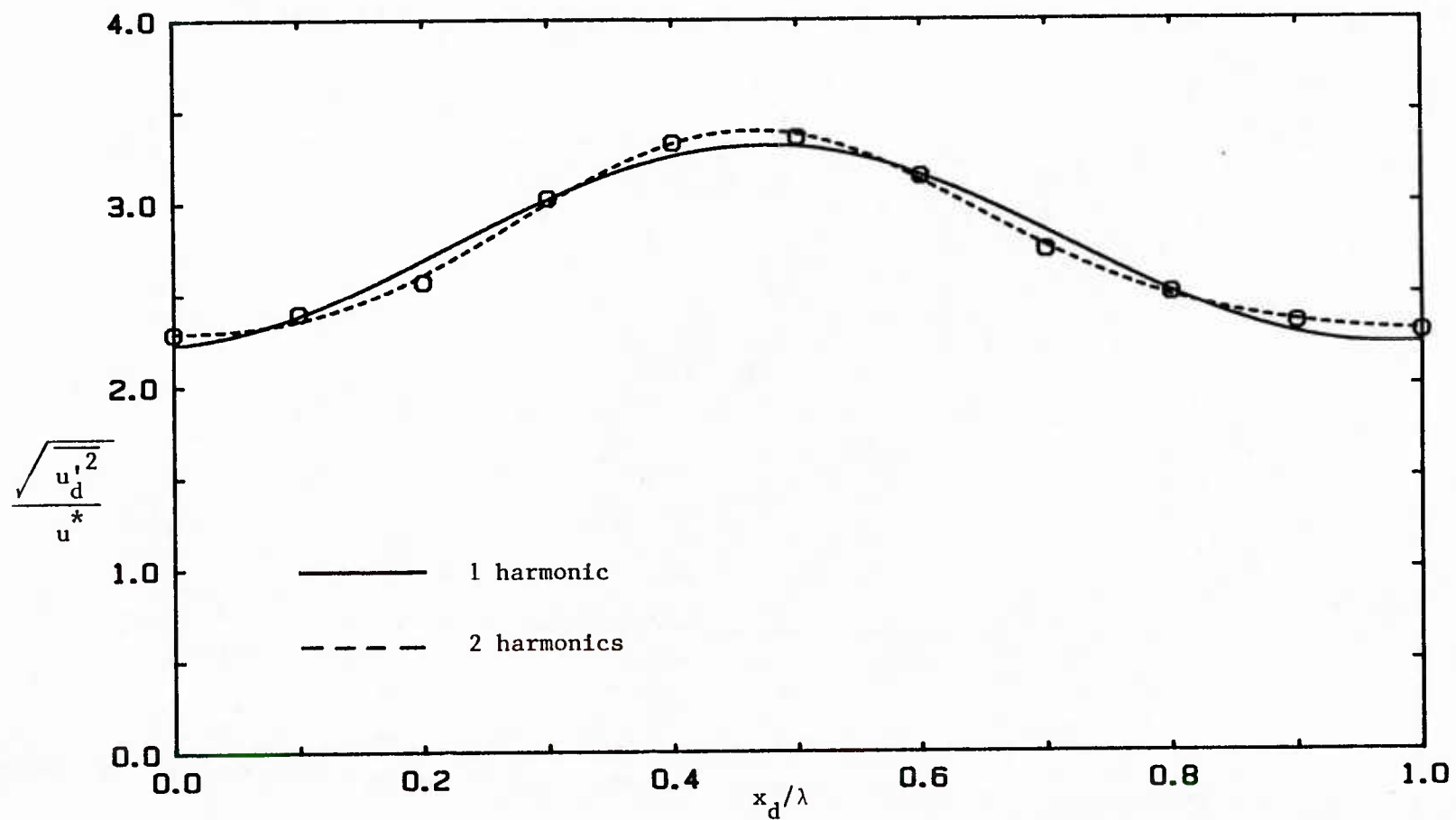


Figure 6.30 Intensity Response at $y_d u^* / \nu = 24$, $2a_d / \lambda = 0.03125$,
 $Re_b = 6400$, $2h_d / \lambda = 1.0$

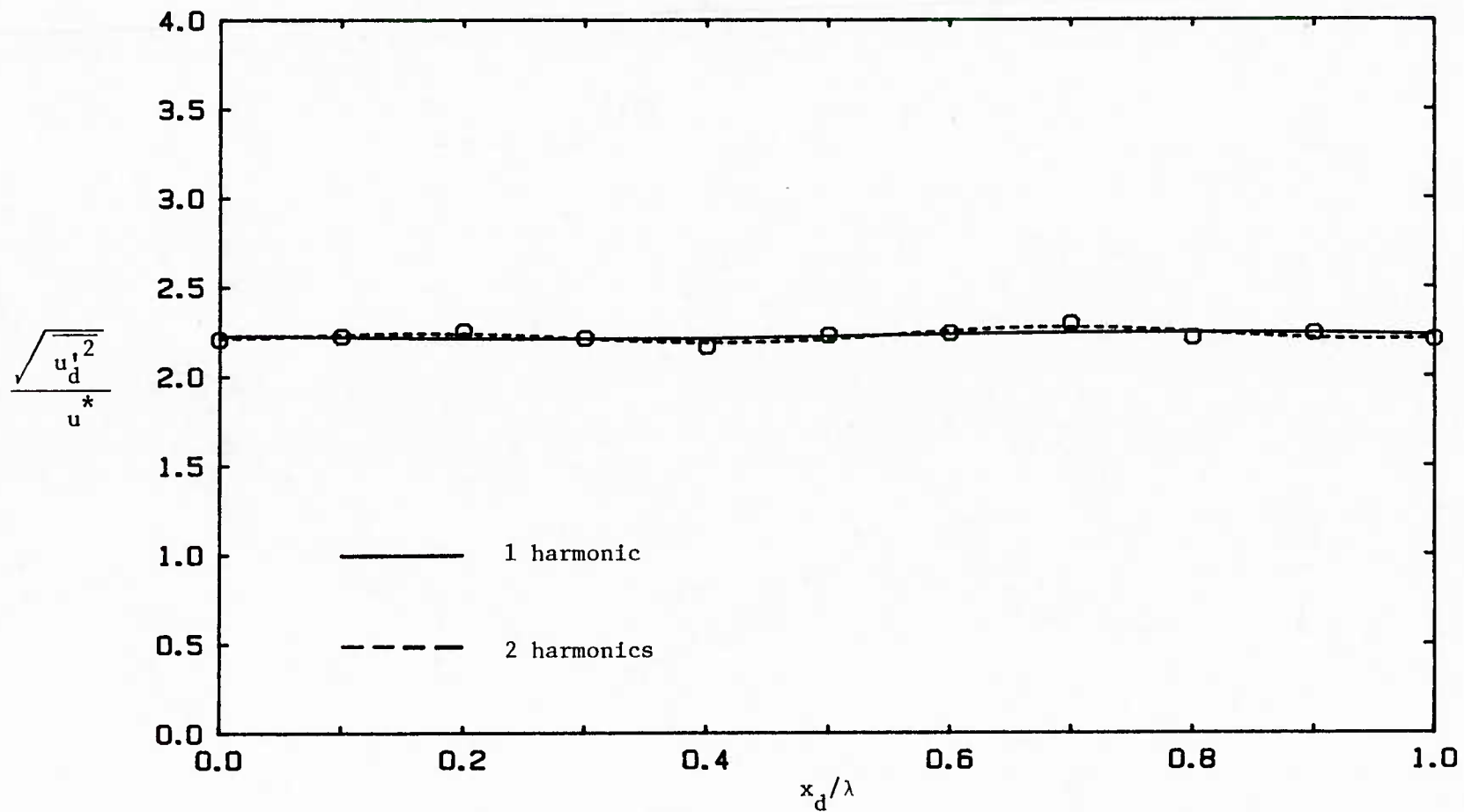


Figure 6.31 Intensity Response at $y_d^* u^* / \nu = 60$, $2a_d/\lambda = 0.03125$, $Re_b = 6400$, $2h_d/\lambda = 1.0$

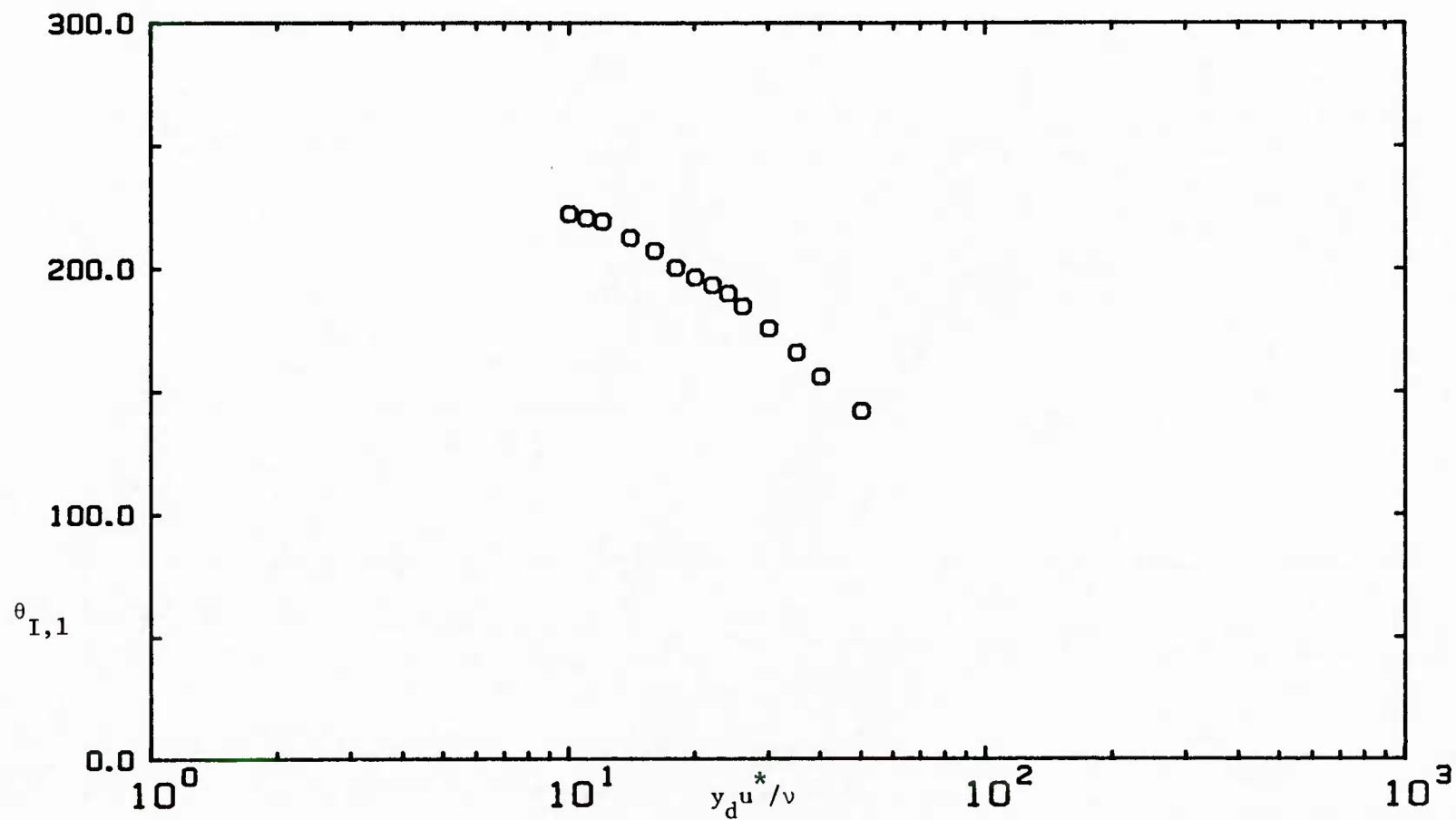


Figure 6.32 Phase Angle of First Harmonic of Intensity Response,
 $2a_d/\lambda = 0.03125$, $Re_b = 6400$, $2h_d/\lambda = 1.0$

Figure 6.33. This figure gives both the discrete grid points and the four harmonic Fourier fits of the spectral analysis. Recall that the code uses fitted curves to evaluate derivatives of quantities in the flow direction.

Figure 6.33 shows that Models C^* and D^* predict deviations from linearity for $2a_d/\lambda = 0.05$ and $Re_b = 38,800$. This is expected since $a_d u^*/\nu = 95.2$. Results of the code's spectral analysis are given in Table 6.4. Considerable differences between the models are seen in the degrees of linearity, in the amplitudes, and in the phases. Model D^* predicts the most nonlinear response with $|\hat{\tau}_d|_2 / |\hat{\tau}_d|_1 = 0.203$ as compared to 0.126 for Model C^* . The amplitude and phase of the first harmonics are $|\hat{\tau}_d|_1 / \rho u^{*2} = 0.7027$ and 0.5637 and $\theta_{\hat{\tau},1} = 48.5$ and 62.5 for Models C^* and D^* respectively. Both models predict a wavelength averaged shear stress that is approximately 10 percent below that found in a flat channel at the same flowrate. This is about the same reduction observed for the $2a_d/\lambda = 0.03125$ wave.

There are no shear stress data available for comparison with the above calculations. However, both models considerably underpredict the nonlinearities since Zilker [48] observed $|\hat{\tau}_d|_2 / |\hat{\tau}_d|_1 = 0.317$ for $2a_d/\lambda = 0.05$ with a smaller dimensionless wave amplitude of $a_d u^*/\nu = 80.3$. Models C^* and D^* also underpredict the phase angle of the shear stress. Zilker found that for a fixed flowrate the first harmonic of nonseparated nonlinear shear stress responses is approximately the same as that obtained over a wave with small enough steepness to give a linear response. Abrams and Hanratty [4]

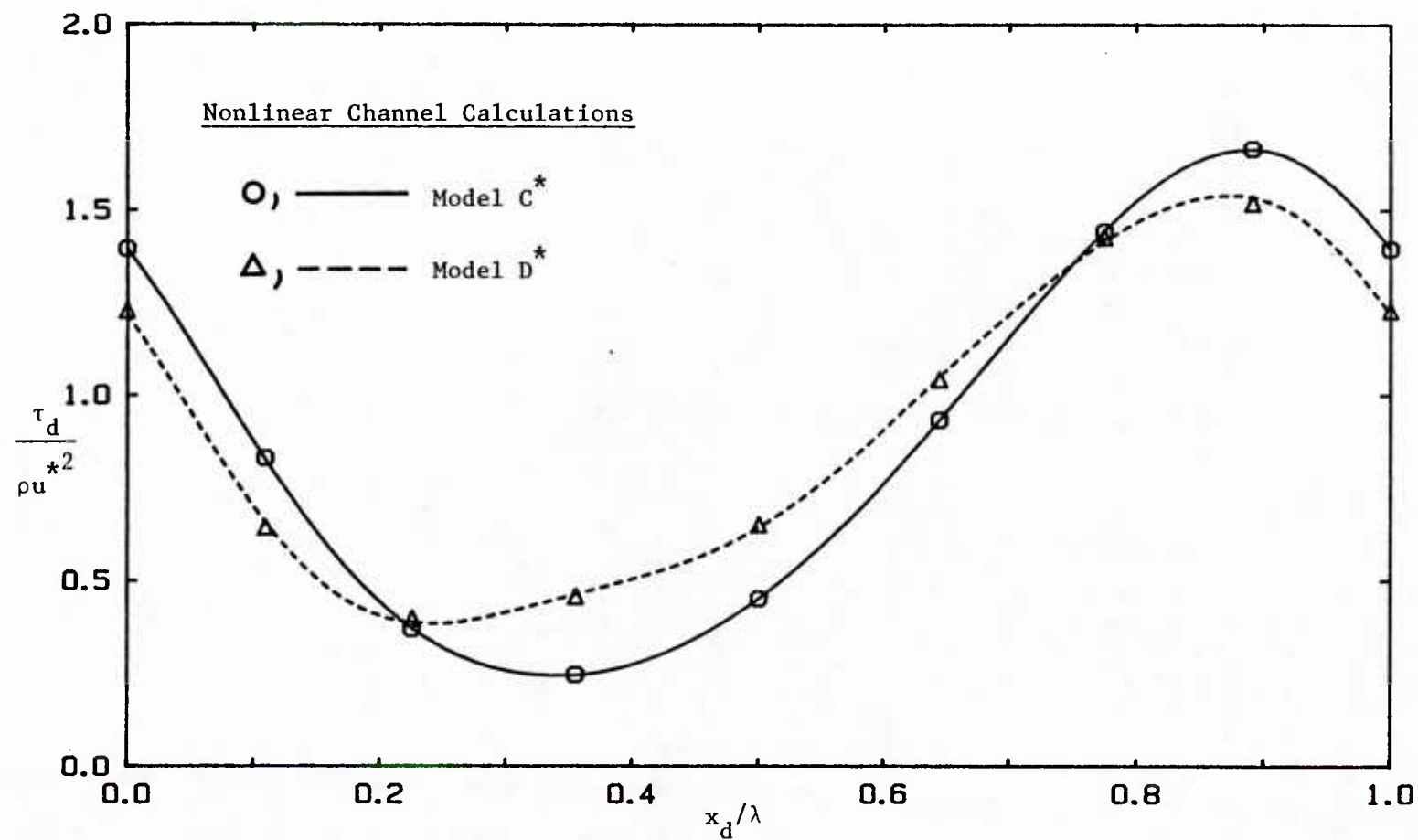


Figure 6.33 Calculated Surface Shear Stress Response, $2a_d/\lambda = 0.05$,
 $Re_b = 38,800$, $2h_d/\lambda = 1.0$

	<u>Model C*</u>	<u>Model D*</u>
$ \hat{\tau}_d _1/\rho u^{*2}$	0.7027	0.5637
$\theta_{\hat{\tau},1}$	48.5	62.5
$\bar{\tau}_d/\rho u^{*2}$	0.880	0.899
$ \hat{\tau}_d _2/ \hat{\tau}_d _1$	0.126	0.203
$ \hat{\tau}_d _3/ \hat{\tau}_d _1$	0.015	0.053

Table 6.4 Predictions of First Harmonic of
Surface Shear Stress Response,
 $2a_d/\lambda = 0.05$, $Re_b = 38,800$, $2h_d/\lambda = 1.0$

measured a linear response and a phase angle of $79 \pm 5^\circ$ for $2a_d/\lambda = 0.014$ and $Re_b = 38,800$.

The shape of the Model D^* response agrees qualitatively with that of all nonlinear shear stress responses observed by Zilker. The model exhibits a gradual variation of the wall shear stress on the windward side of the wave and a steep variation on the leeward side.

2. Surface Pressure

Predictions of the surface pressure by the nonlinear code with turbulence Models C^* and D^* are shown in Figure 6.34. The results of a two harmonic Fourier analysis of these discrete profiles is given in Table 6.5. Both models predict a linear response with nearly identical first harmonic amplitudes and phases. No data are available for comparison with these calculations.

3. Drag

Drag coefficients predicted by the nonlinear channel analysis are shown in Table 6.6. Both Models C^* and D^* give approximately a 10 percent decrease in the skin friction drag relative to a flat surface. The total drag for the wave surface increases by about 20 percent due to form drag which represents about 25 percent of the total drag for both models.

B. Wavelength Averaged Mean Velocity

The experimental wavelength averaged velocity profile over the wave with $2a_d/\lambda = 0.05$ is shown in Figure 6.35. This profile was obtained by averaging the ten profiles in Figures 5.25-5.34 and is thus constructed along Cartesian coordinates as discussed in

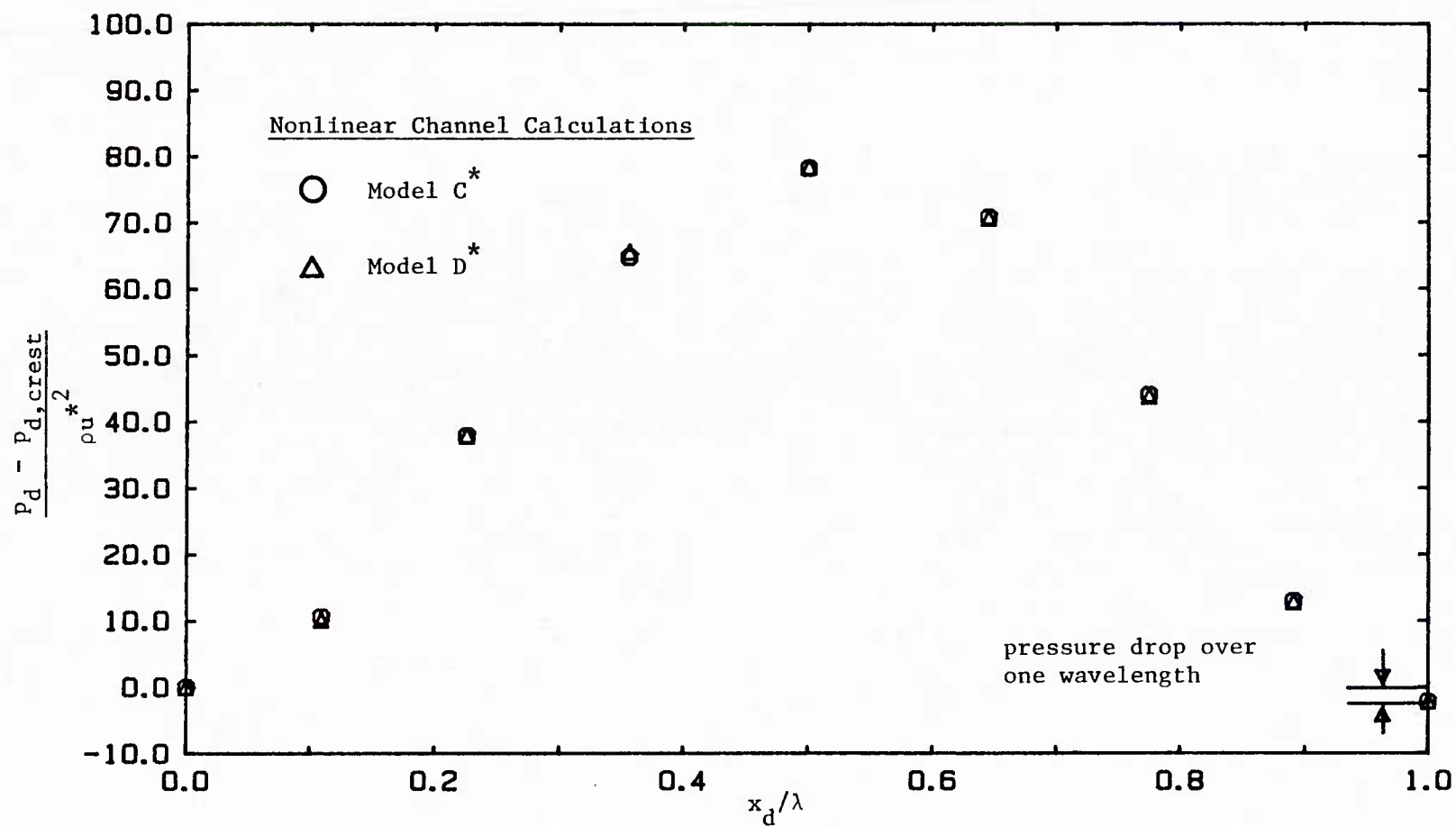


Figure 6.34 Calculated Pressure Response, $2a_d/\lambda = 0.05$, $Re_b = 38,800$,
 $2h_d/\lambda = 1.0$

	<u>Model C*</u>	<u>Model D*</u>
$ \hat{p}_d _1 / \rho u^*{}^2$	39.49	39.73
$\theta_{p,1}^{\wedge}$	174.5	174.8
$ \hat{p}_d _2 / \hat{p}_d _1$	0.108	0.106

Table 6.5 Surface Pressure Results of Nonlinear
Channel Analysis, $2a_d/\lambda = 0.05$,
 $Re_b = 38,000$, $2h_d/\lambda = 1.0$

Turbulence Model	C_s	C_p	$\frac{C_s}{C_s + C_p}$	$\frac{C_p}{C_s + C_p}$	$C_s + C_p$
C^*	0.880	0.315	0.736	0.264	1.19
D^*	0.899	0.296	0.752	0.248	1.20

Table 6.6 Drag Coefficients, $2a_d/\lambda = 0.05$,
 $Re_b = 38,800$, $2h_d/\lambda = 1.0$

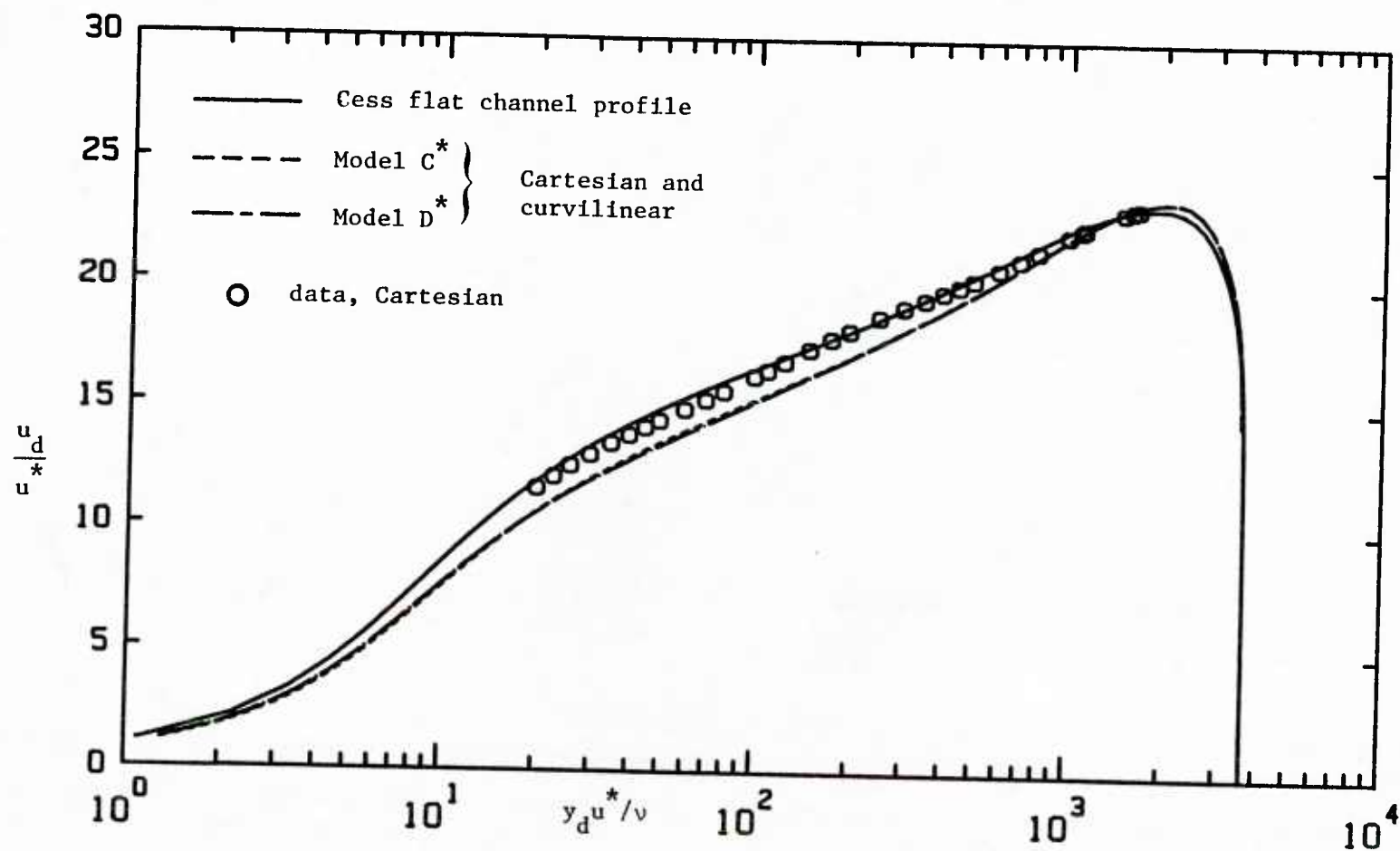


Figure 6.35 Wavelength Averaged Velocity Profiles, $2a_d/\lambda = 0.05$,
 $Re_b = 38,800$, $2h_d/\lambda = 1.0$

Section I.B. and shown in Figure 6.4. The Cartesian wavelength averaged profiles predicted by the nonlinear channel code with turbulence Models C^* and D^* are also shown in Figure 6.35. The differences between Models C^* and D^* are negligible. The wavelength averaged data are higher than the theory. This difference is believed to be slightly greater than the experimental error.

Predictions by the nonlinear code of wavelength averaged profiles formed along the curvilinear coordinates (Figure 6.5) were found to be nearly identical to the average profiles in Cartesian coordinates. The Cess flat channel profile is included in Figure 6.35. The calculated wavelength averaged profiles are significantly lower than the flat channel profile. The reason for this behavior is not known.

All of the wavelength averaged profiles discussed above are normalized with flat channel wall parameters.

C. Mean Velocity Profiles

The mean velocity profiles for the wave with $2a_d/\lambda = 0.05$ are shown in Figures 6.36-6.40, where they are compared with predictions of the nonlinear channel code with turbulence Models C^* and D^* . Significant differences between the two models are seen for $y_d^{u*}/\nu < 20$. In this region Model D^* predicts smaller perturbations about the mean flowfield than Model C^* . Both models considerably underestimate the measured disturbances at all heights above the wave.

The steepness of $2a_d/\lambda = 0.05$ was found to be small enough that the calculated profiles are independent of the type of distance y_d' used in the Cess equation. See equation (3.31).

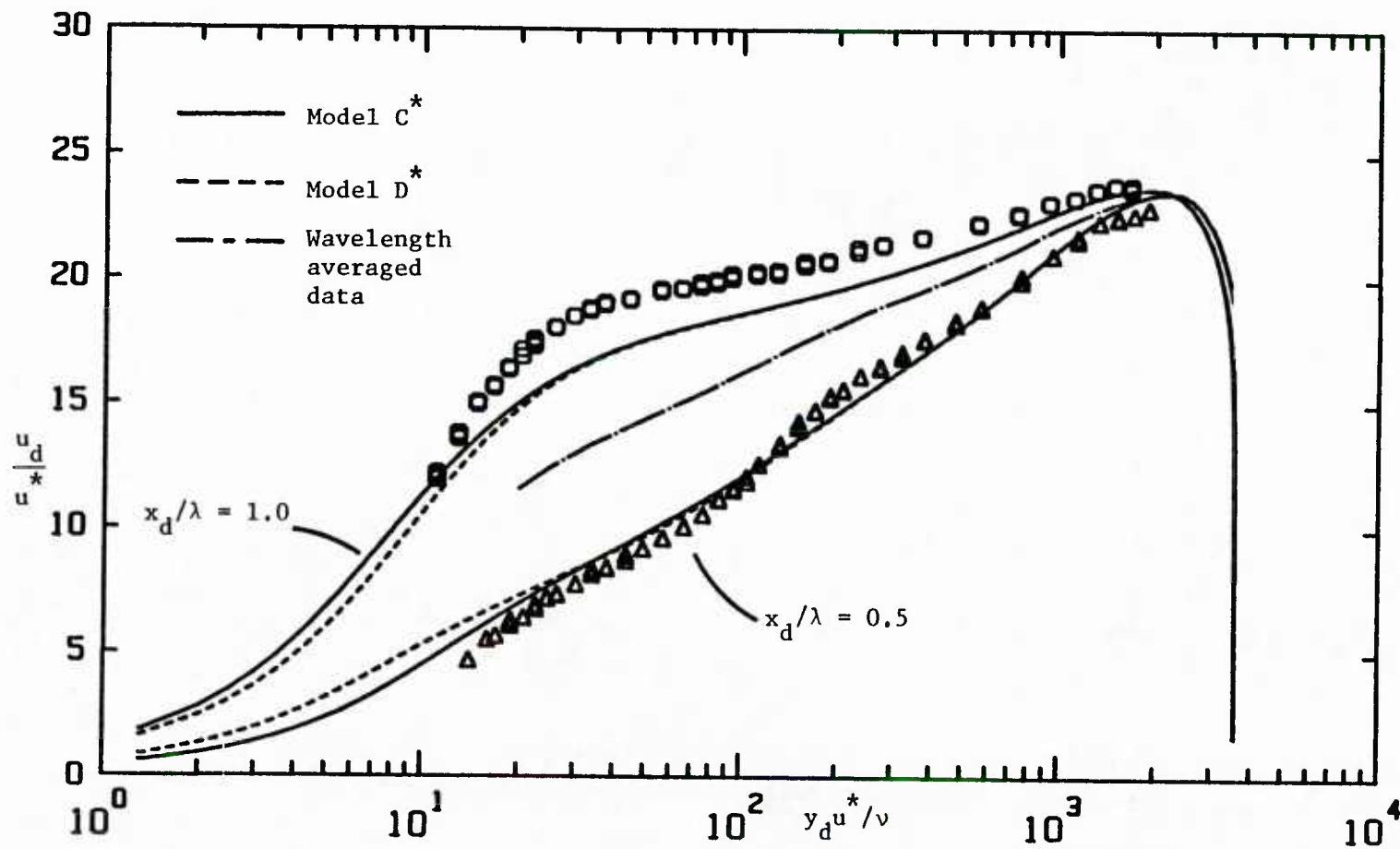


Figure 6.36 Comparison of Mean Velocity Measurements with Channel Calculations, $x_d/\lambda = 0.5, 1.0$, $2a_d/\lambda = 0.05$, $Re_b = 38,800$, $2h_d/\lambda = 1.0$

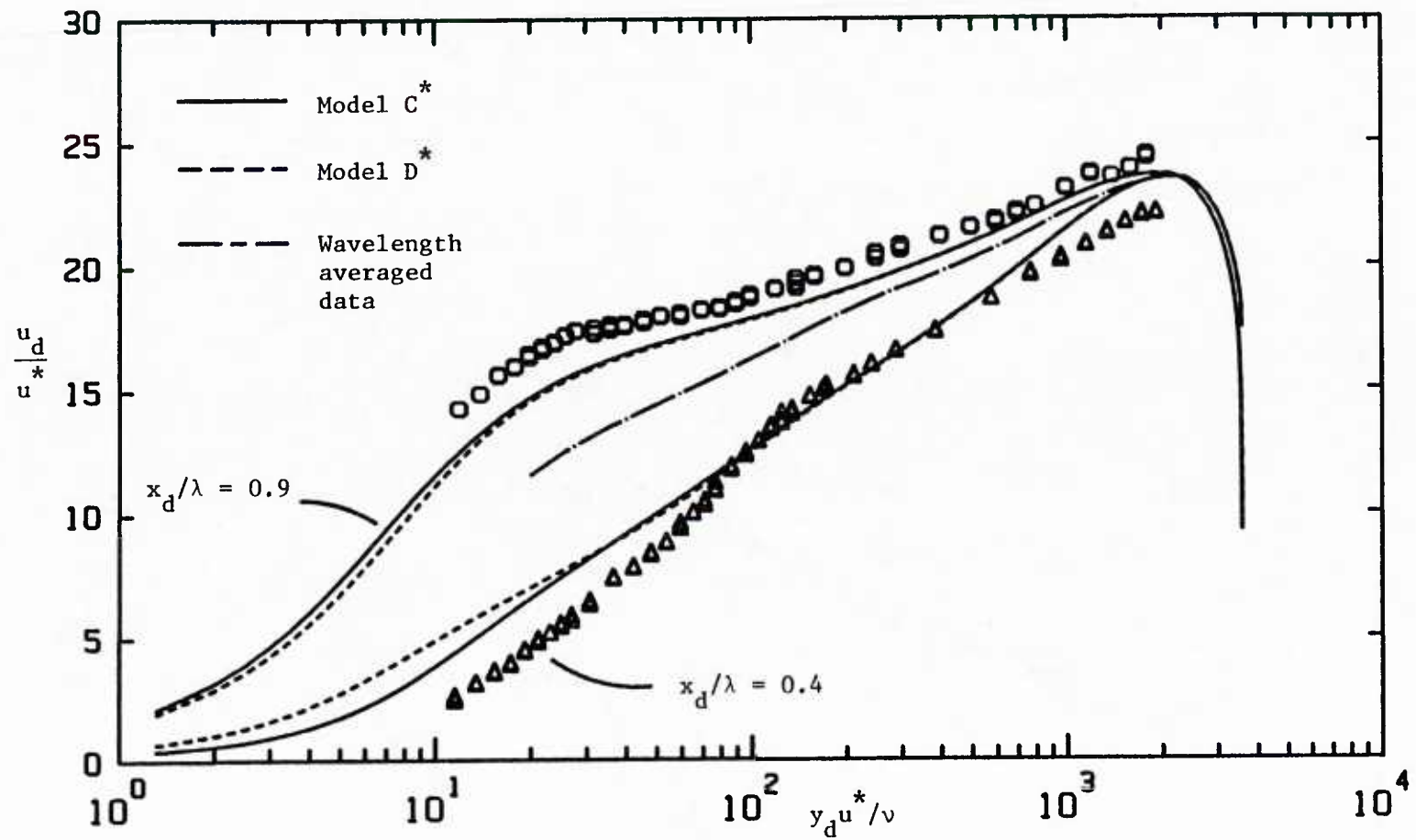


Figure 6.37 Comparison of Mean Velocity Measurements with Channel Calculations, $x_d/\lambda = 0.4, 0.9$, $2a_d/\lambda = 0.05$, $Re_b = 38,800$, $2h_d/\lambda = 1.0$

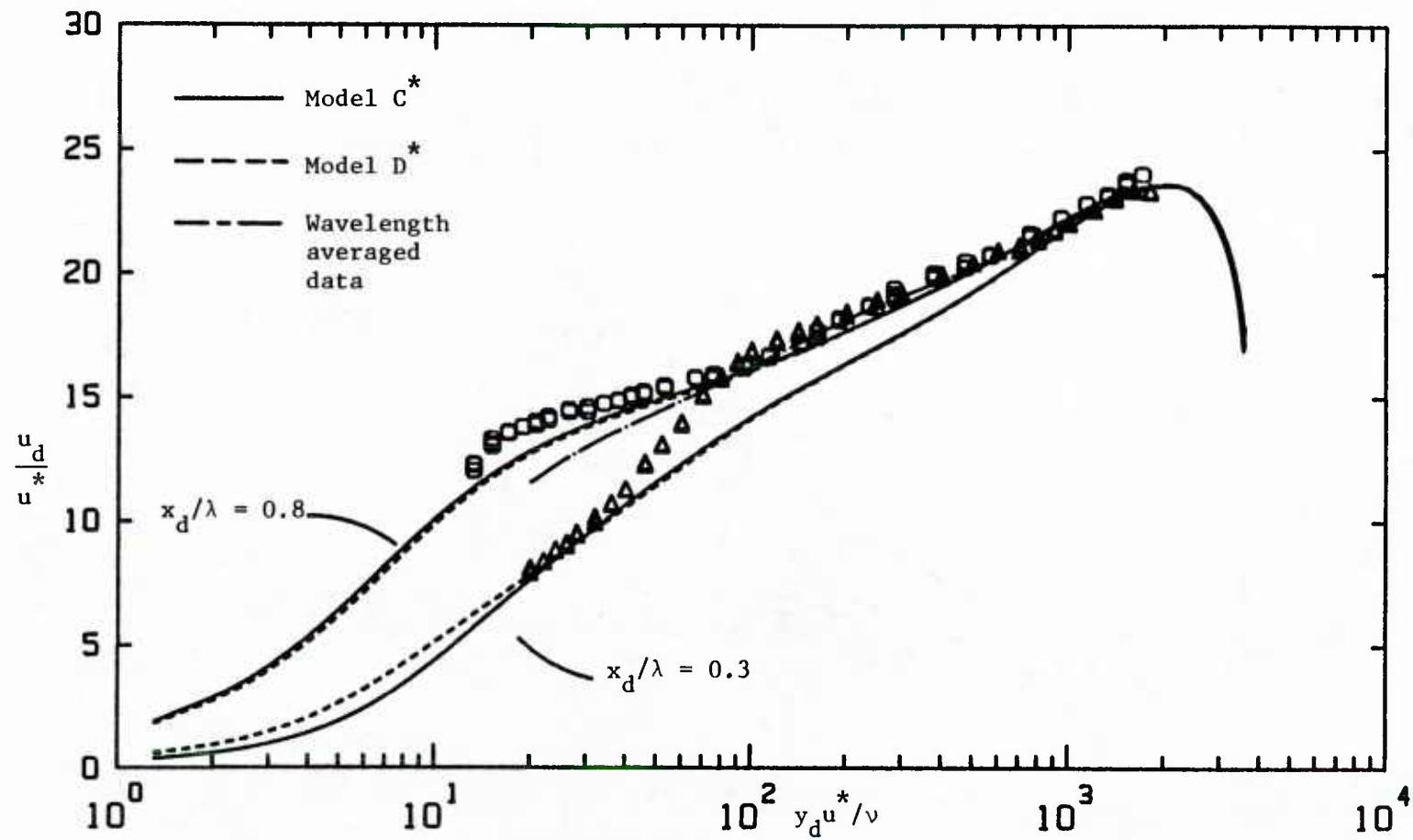


Figure 6.38 Comparison of Mean Velocity Measurements with Channel Calculations, $x_d/\lambda = 0.3, 0.8$, $2a_d/\lambda = 0.05$, $Re_b = 38,800$, $2h_d/\lambda = 1.0$

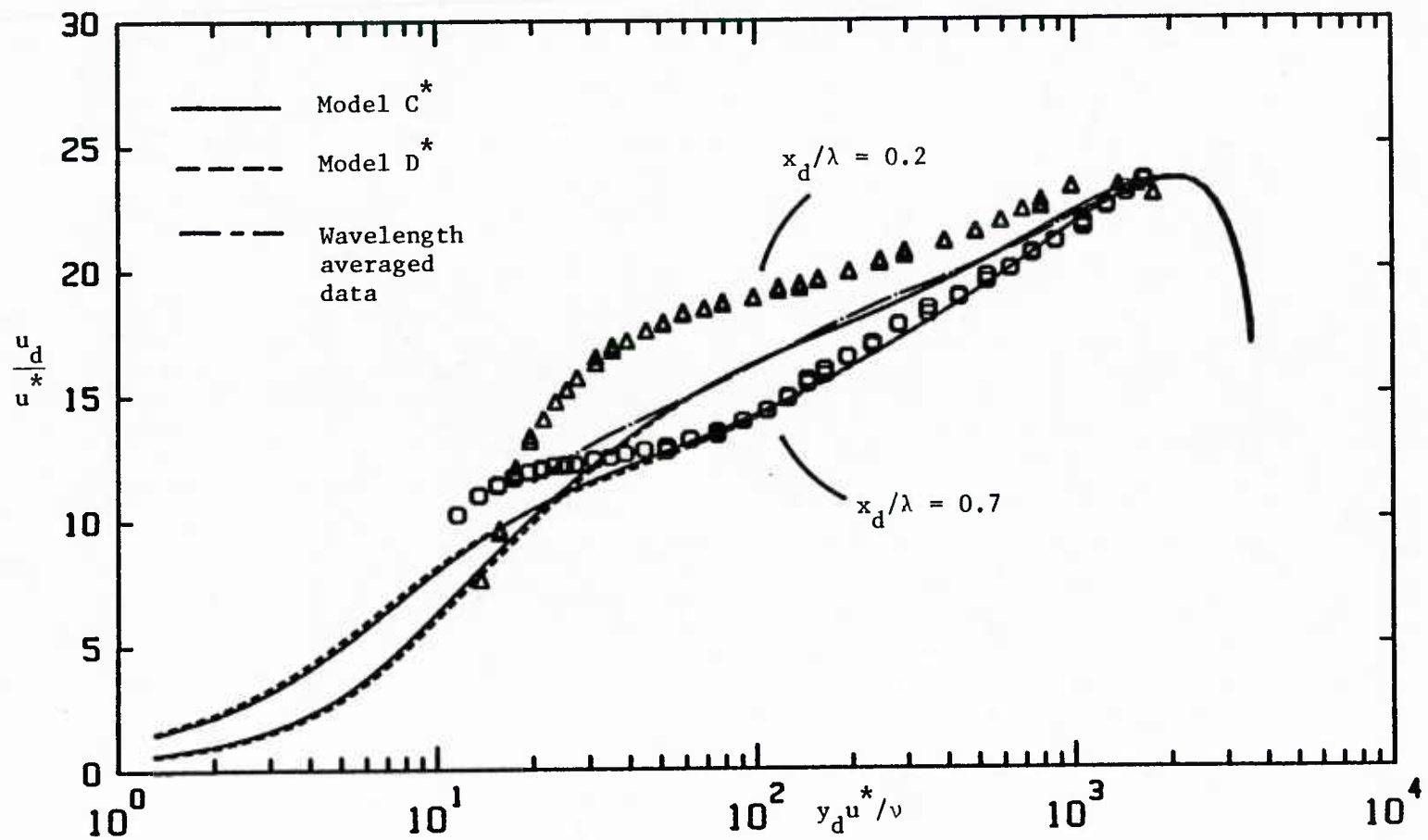


Figure 6.39 Comparison of Mean Velocity Measurements with Channel Calculations, $x_d/\lambda = 0.2, 0.7$, $2a_d/\lambda = 0.05$, $Re_b = 38,800$, $2h_d/\lambda = 1.0$

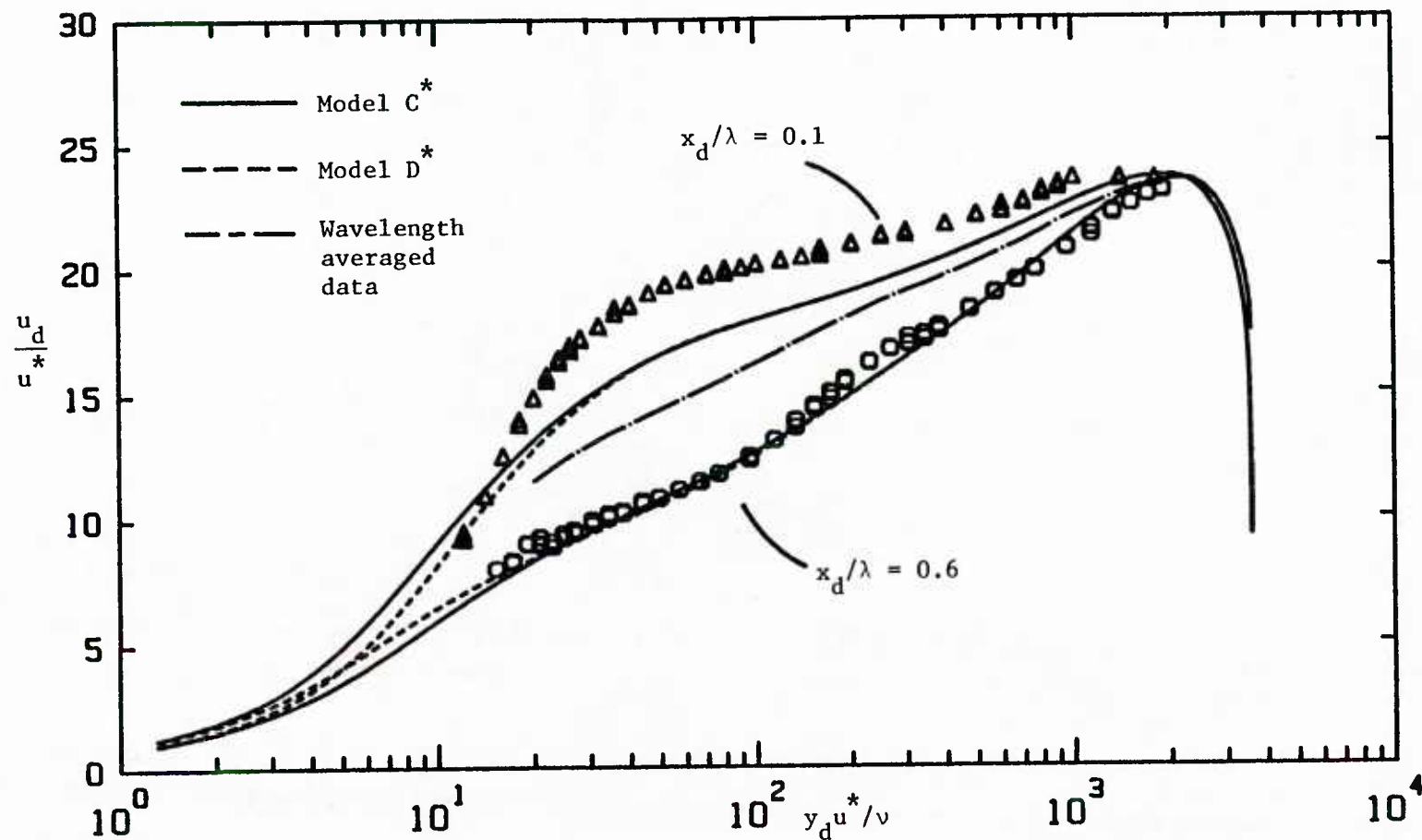


Figure 6.40 Comparison of Mean Velocity Measurements with Channel Calculations, $x_d / \lambda = 0.1, 0.6$, $2a_d / \lambda = 0.05$, $Re_b = 38,800$, $2h_d / \lambda = 1.0$

D. Mean Velocity Responses at Constant Heights above Wave

The velocity field at constant vertical heights above the wave surface is shown in Figure 6.41. The heights range from $y_d u^* / \nu = 20.4$ to $y_d u^* / \nu = 1500$. Moderate departures from a linear response are observed for roughly $y_d u^* / \nu < 100$. Here the velocity responses vary gradually on the windward side of the wave and steeply on the leeward side. This is the same shape that Zilker et al. [49] observed for nonlinear shear stress responses.

A two harmonic least squares Fourier analysis was performed on the curves in Figure 6.41. Figure 6.42 shows the ratio of the amplitude of the second to first harmonic as a function of distance above the wave. The response is observed to be nonlinear ($|\hat{u}_d|_2 / |\hat{u}_d|_1 > 0.116$) for $y_d u^* / \lambda < 100$ with a maximum ratio of 0.21 at $y_d u^* / \nu = 35$. These nonlinearities are surprisingly weak when it is considered that the dimensionless wave amplitude, $a_d u^* / \nu$, of the $2a_d / \lambda = 0.05$ wave is $95.2/12.3 = 7.7$ times that for the $2a_d / \lambda = 0.03125$ wave. The observed nonlinearities are underpredicted by both Models C* and D*.

Amplitudes of the first and second harmonics of the velocity response are shown in Figure 6.43. The shape of these profiles is similar to that found over the $2a_d / \lambda = 0.03125$ wave. The maximum value of the first harmonic amplitude is 5.6 at $y_d u^* / \nu = 26$. Figure 6.44 shows the response at $y_d u^* / \nu = 26$ where it is fitted to one and two harmonics. The amplitude of the second harmonic reaches a maximum at approximately $y_d u^* / \nu = 35$. Figure 6.45 shows the linear velocity response at $y_d u^* / \nu = 100$.

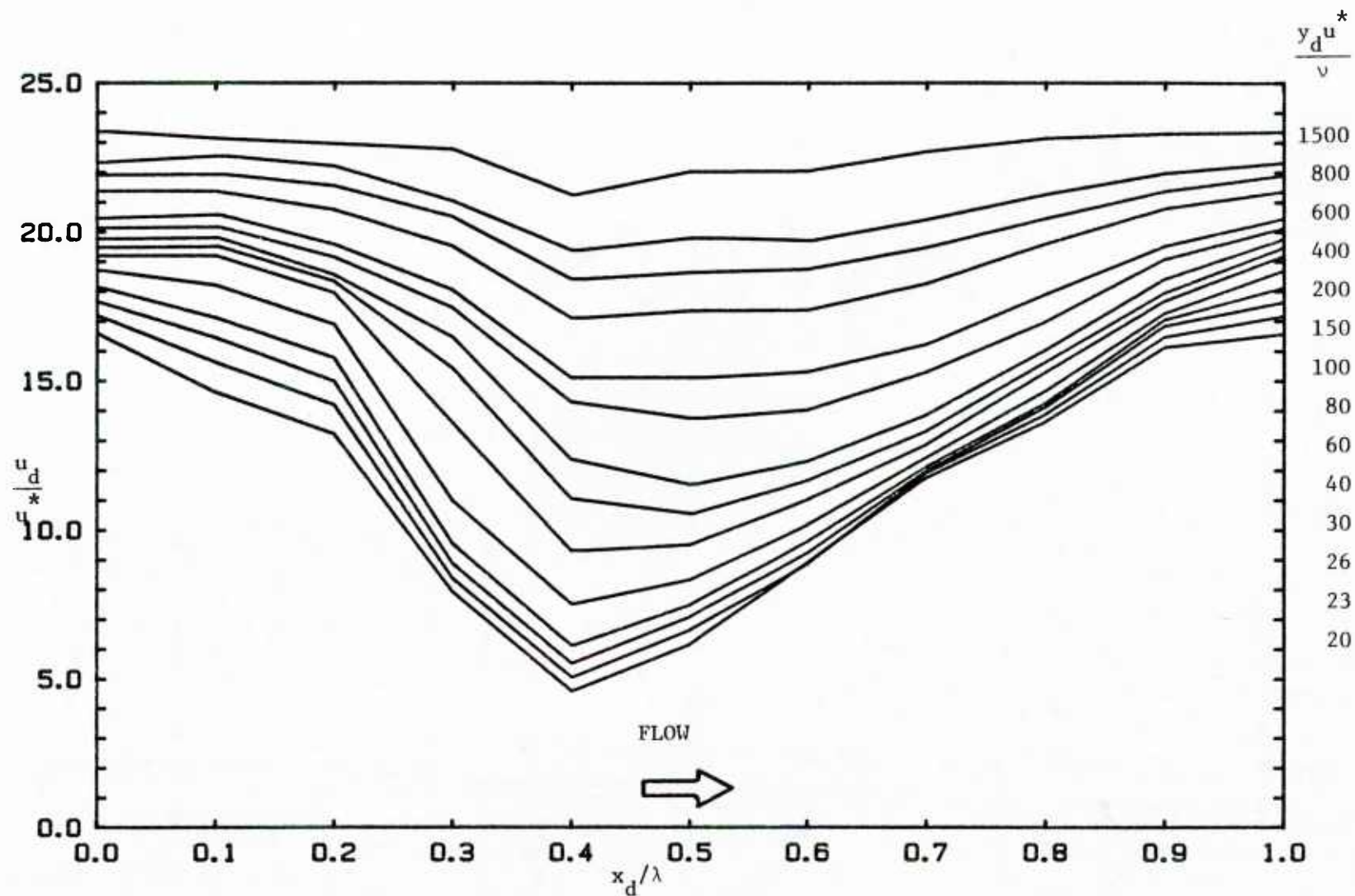


Figure 6.41 Mean Velocity Responses at Constant Heights above Wave Surface,
 $2a_d/\lambda = 0.05$, $Re_b = 38,800$, $2h_d/\lambda = 1.0$

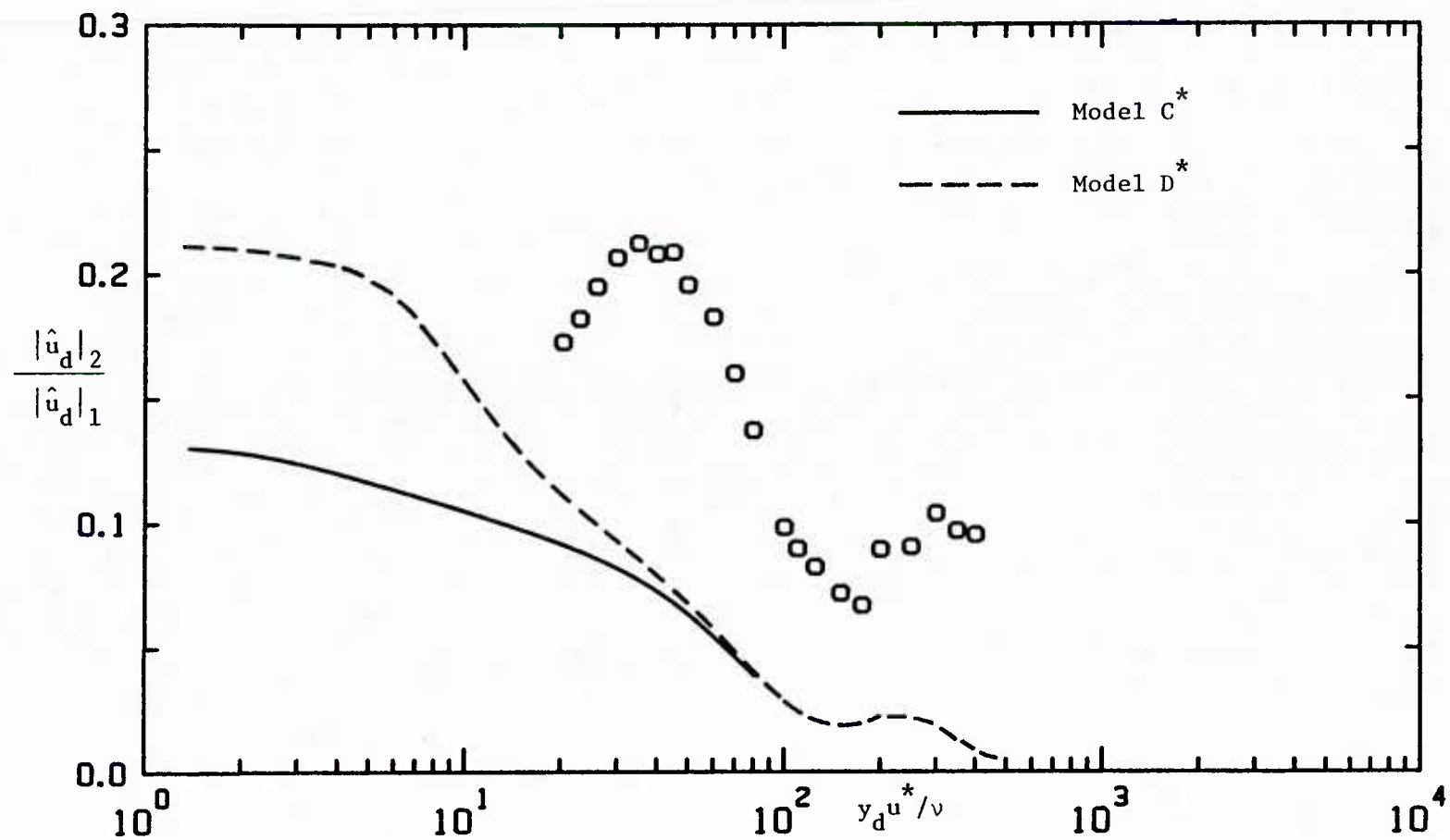


Figure 6.42 Velocity Amplitude Ratio of Second to First Harmonics,
 $2a_d/\lambda = 0.05$, $Re_b = 38,800$, $2h_d/\lambda = 1.0$

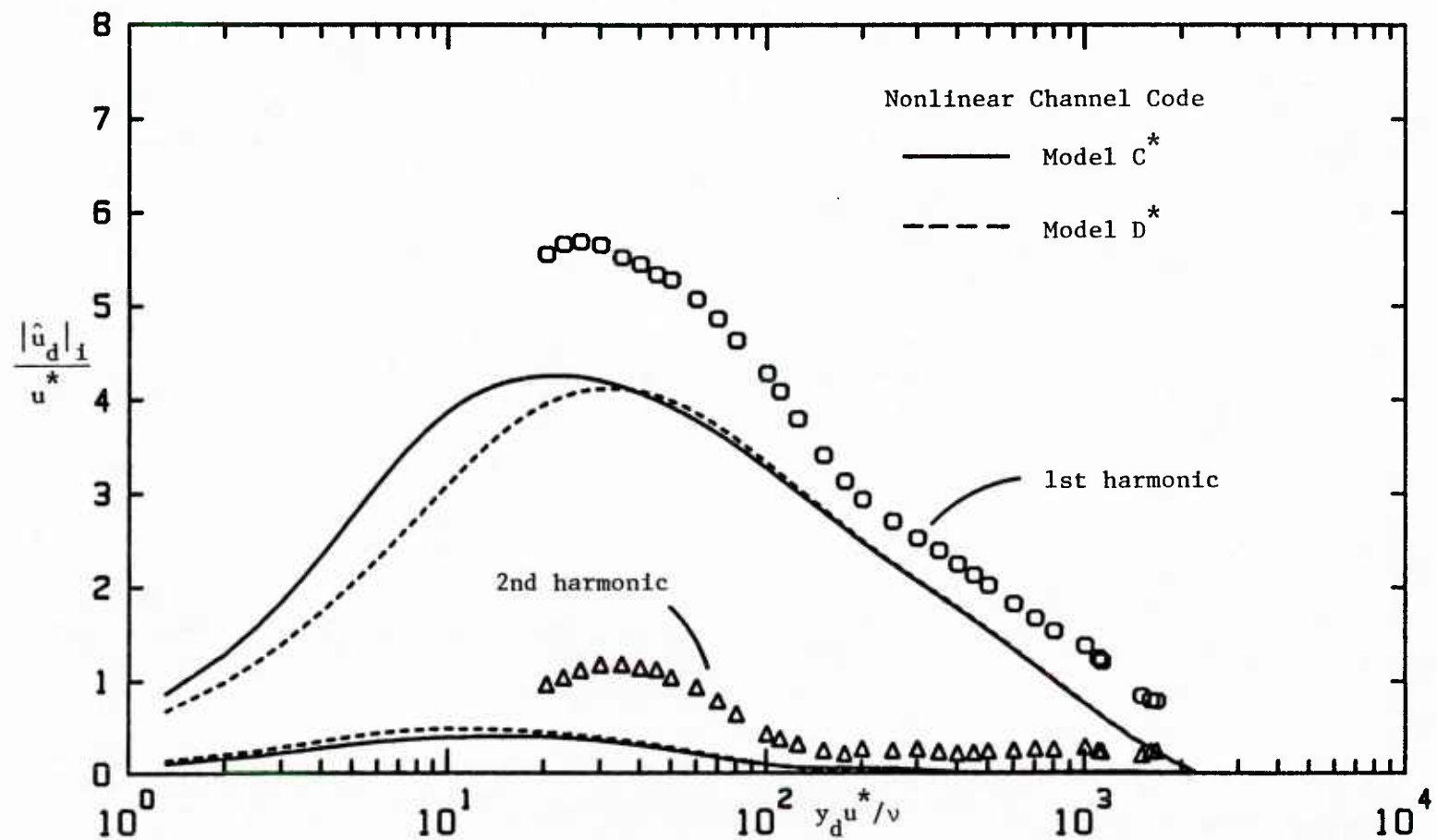


Figure 6.43 Amplitude of First and Second Harmonics of Velocity Response,
 $2a_d/\lambda = 0.05$, $Re_b = 38,800$, $2h_d/\lambda = 1.0$

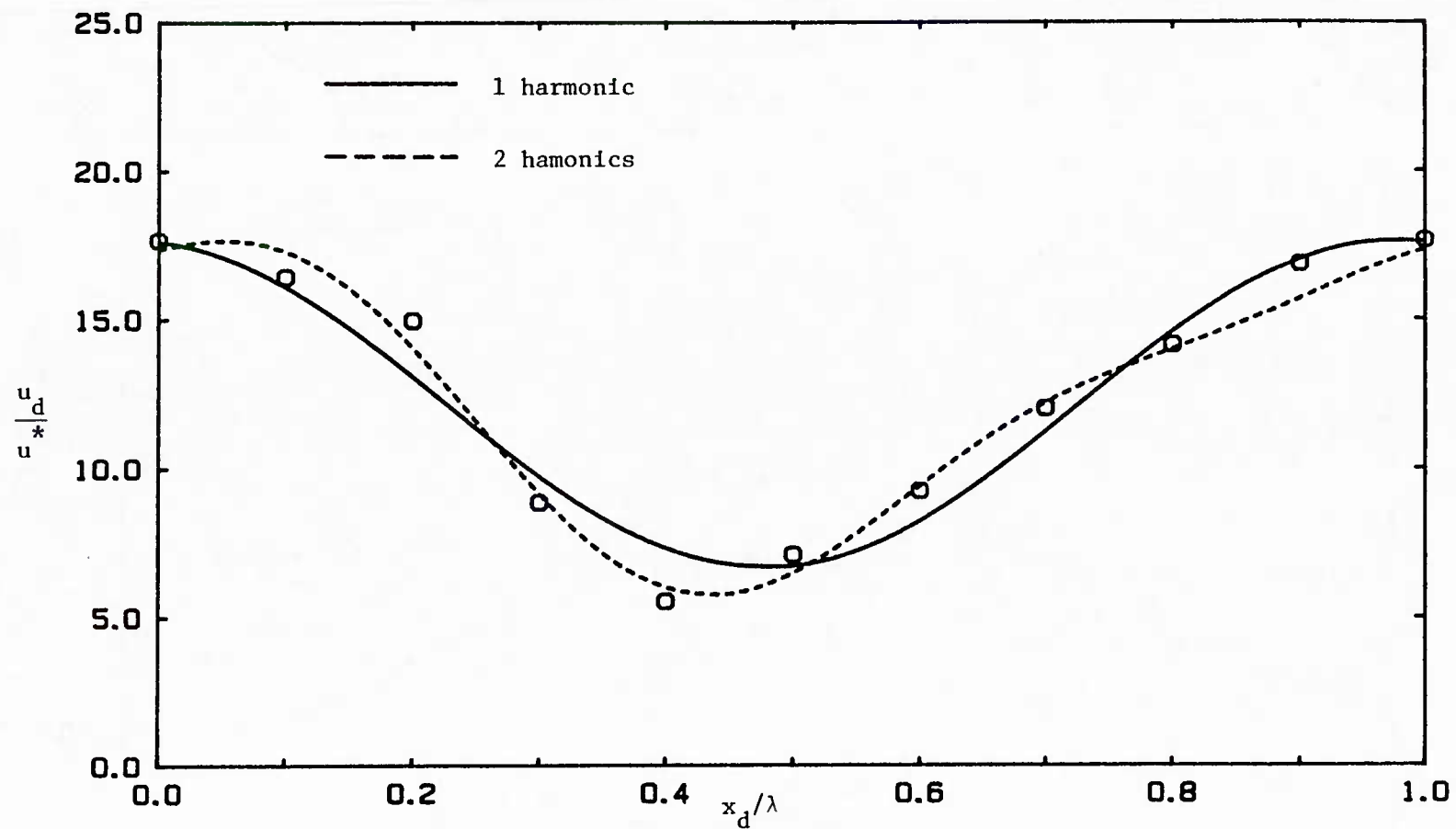


Figure 6.44 Velocity Response at $y_d u^*/\nu = 26$, $2a_d/\lambda = 0.05$, $Re_b = 38,800$, $2h_d/\lambda = 1.0$

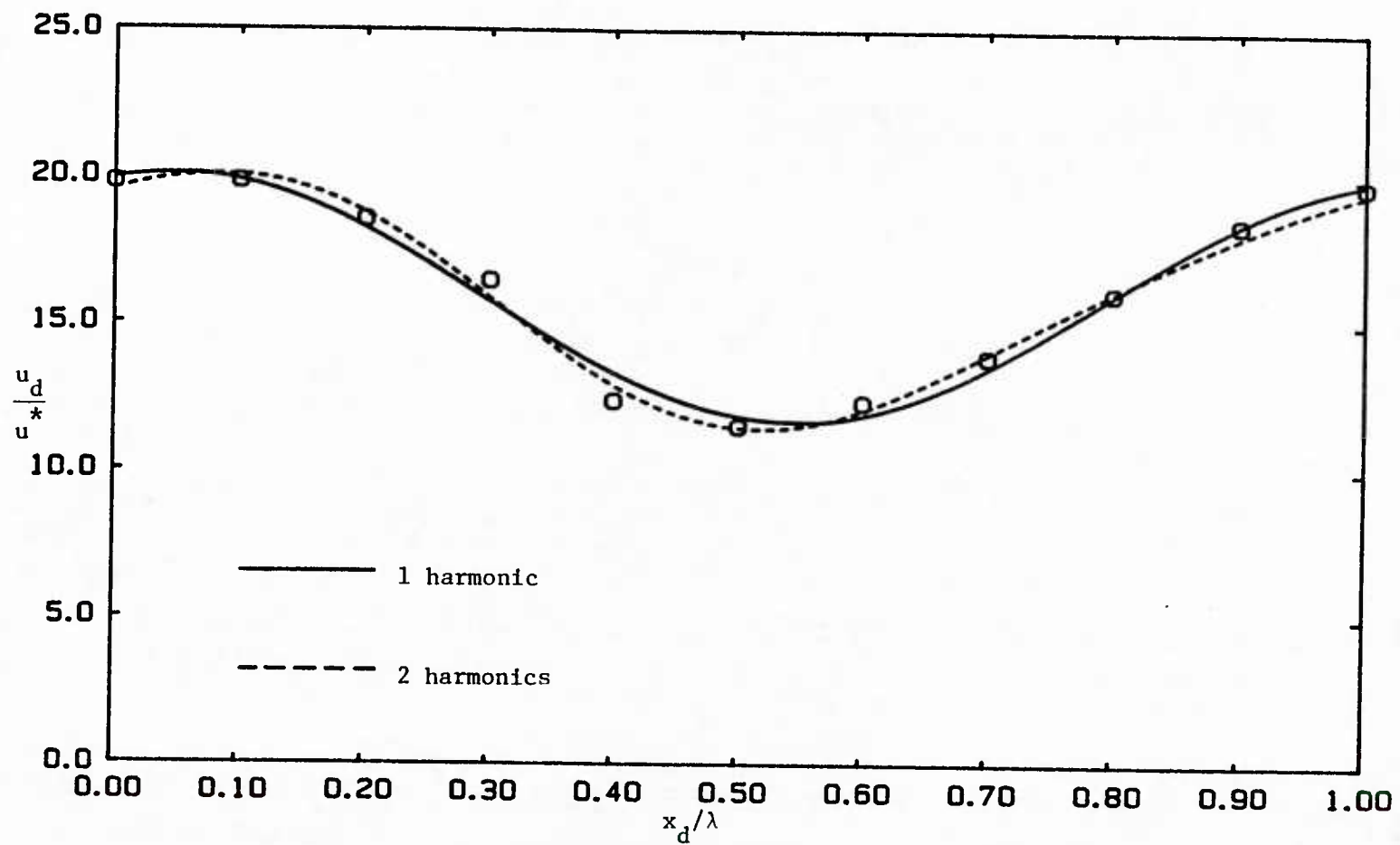


Figure 6.45 Velocity Response at $y_d u^*/\nu = 100$, $2a_d/\lambda = 0.05$, $Re_b = 38,800$, $2h_d/\lambda = 1.0$

Figure 6.43 differs from Figure 6.13 for the wave with $2a_d/\lambda = 0.03125$ in that the disturbances for the 0.05 wave extend well outside the viscous wall region. This is consistent with the linear theory calculations of Abrams [2] which predict that the penetration of disturbances increases with decreasing dimensionless wavenumber, $\alpha_d \nu / u^*$.

The amplitude predictions of Model C^* and D^* are also shown in Figure 6.43. Both models predict profiles with the same general shape as the data. The first harmonic responses of the two models are nearly identical for $y_d u^* / \nu > 40$. Below $y_d u^* / \nu = 40$ Model C^* gives larger first harmonic amplitudes than Model D^* . The second harmonic responses are similar for both turbulence models.

Models C^* and D^* significantly underestimate the amplitude observations for $y_d u^* / \nu < 100$. The explanation for the "failure" of these models is the same as given in Section I.D. for the wave with $2a_d/\lambda = 0.03125$ and $Re_b = 6400$. It is suggested that only a very simple model, with small wave-induced variations of the turbulence outside the near wall region, will provide a good fit to this portion of the velocity field. Supporting evidence for the above statement was obtained by running the linear boundary layer program of Abrams [2] with quasilaminar, C^* and D^* turbulence models for $\alpha_d \nu / u^* = 0.00165$ (equivalent to $Re_b = 38,800$). It is found that the quasilaminar model predicts a maximum wave-induced amplitude which is 41 percent and 42 percent higher than Models C^* and D^* respectively. However, it should not be forgotten that a quasilaminar model cannot predict the near wall region for

small dimensionless wavenumbers, $\alpha_d u^* / \nu$. Abrams has shown that for linear waves with $\alpha_d u^* / \nu = 0.00165$ it is necessary to use a model, such as Model D*, where turbulence properties are a function of the pressure gradient.

Determination of the amplitude of the shear stress response from the LDV measurements in Figure 6.43 is not possible because the closest measurements are well outside the viscous sublayer.

The phase angle of the first harmonic of the velocity response is shown in Figure 6.46. A value of 15.8° is observed at the closest measurement location of $y_d u^* / \nu = 20$. The phase angle falls to a minimum value of -16.9° at $y_d u^* / \nu = 125$ and tends toward zero far from the wall. The accuracy of the phase angles for $y_d u^* / \nu > 400$ is low because here scatter in the data becomes a significant fraction of the response amplitudes. Prediction of the phase angle by the nonlinear channel code with turbulence Models C* and D* are also shown in Figure 6.46. As in the case of the $2a_d / \lambda = 0.03125$ wave, neither model fits the data well outside the viscous wall region. The measurements approach the calculations at small $y_d u^* / \nu$ but do not extend close enough to the wave surface to test either model in the near wall region. Thus obtaining the phase angle of the wall shear stress by extrapolating the data to the wall is not possible for $2a_d / \lambda = 0.05$ and $Re_b = 38,800$. Electrochemical techniques are necessary to measure the wall shear stress response.

E. Wave-Induced Velocity Perturbations

Measured profiles of the wave-induced velocity perturbations about the experimental wavelength averaged profile are shown in

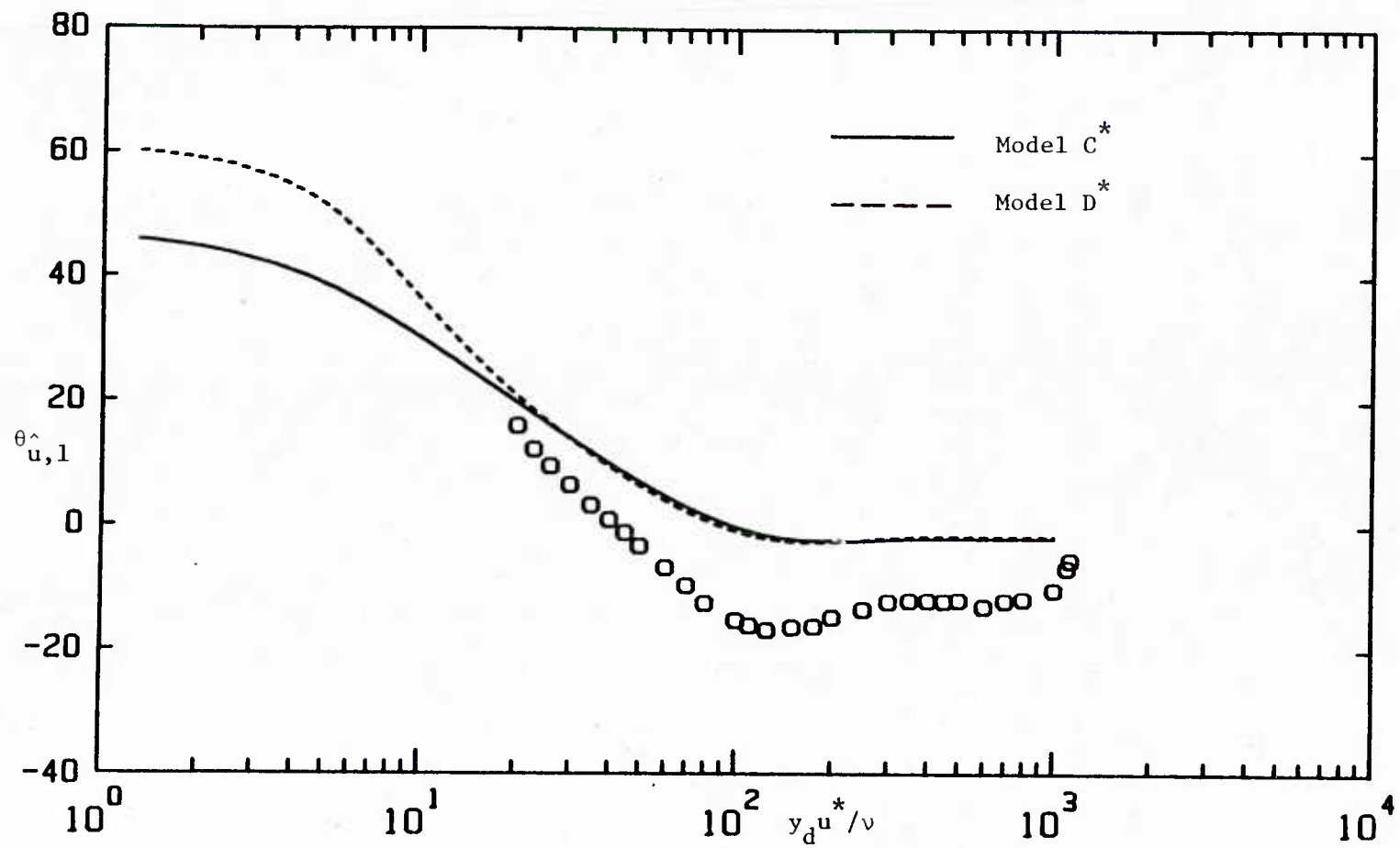


Figure 6.46 Phase Angle of First Harmonic of Velocity Response,
 $2a_d/\lambda = 0.05$, $Re_b = 38,800$, $2h_d/\lambda = 1.0$

Figures 6.47-6.51. These figures also contain predicted perturbations, by the nonlinear channel code with turbulence Models C^* and D^* , about calculated wavelength averaged profiles. It should be pointed out that in Figures 6.47-6.51 differences between the data and calculations are not due to differences in the experimental and calculated wavelength averaged profiles as is the case in Figures 6.47-6.51 for the mean velocity profiles. Both models underpredict the disturbances in the viscous wall region but have the same general shape as the data.

Figures 6.47-6.51 clearly show that disturbances penetrate outside the viscous wall region.

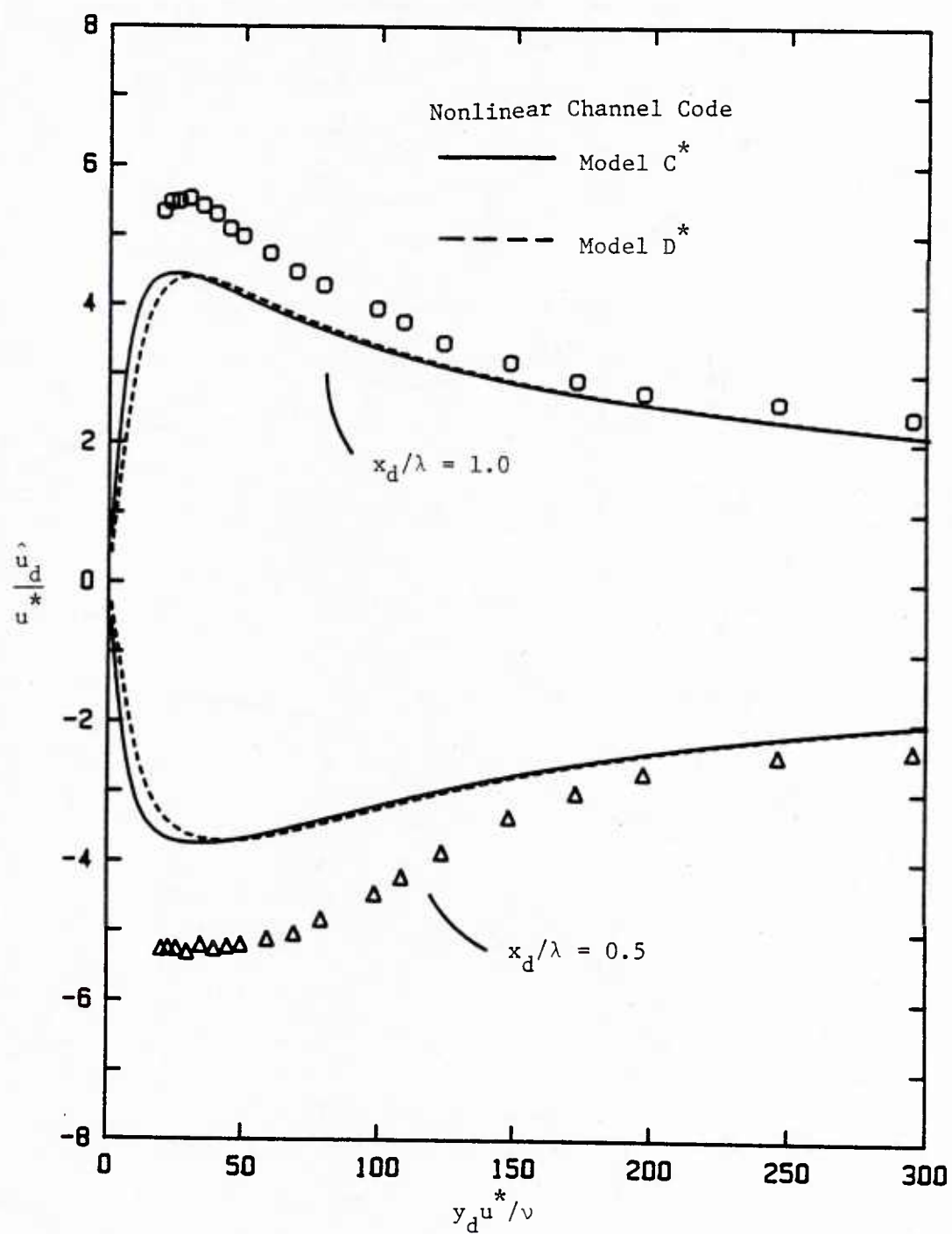


Figure 6.47 Wave-Induced Velocity Perturbations,
 $x_d/\lambda = 0.5, 1.0, 2a_d/\lambda = 0.05,$
 $Re_b = 38,800, 2h_d/\lambda_d = 1.0$

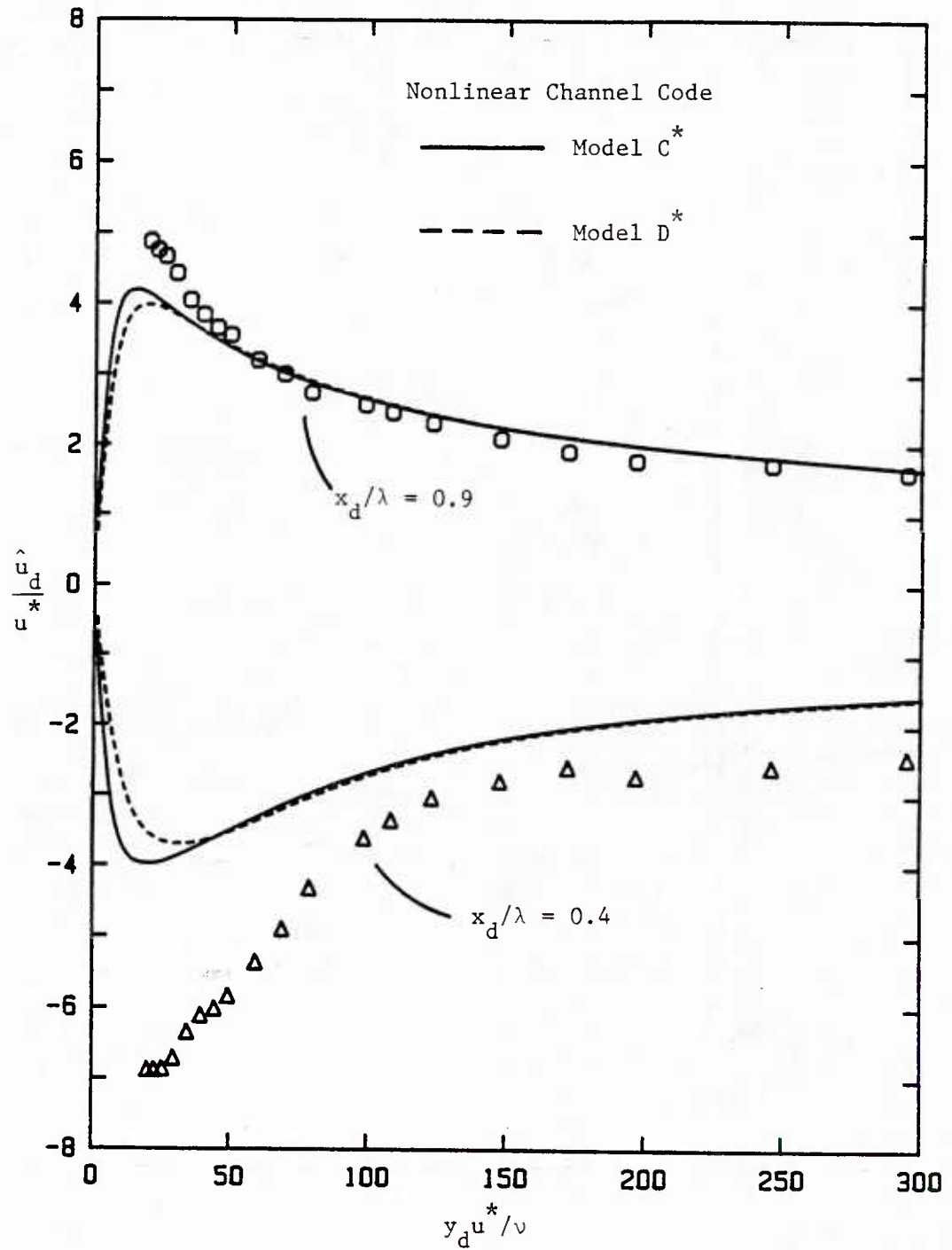


Figure 6.48 Wave-Induced Velocity Perturbations,
 $x_d / \lambda = 0.4, 0.9$, $2a_d / \lambda = 0.05$, $Re_b = 38,800$,
 $2h_d / \lambda = 1.0$

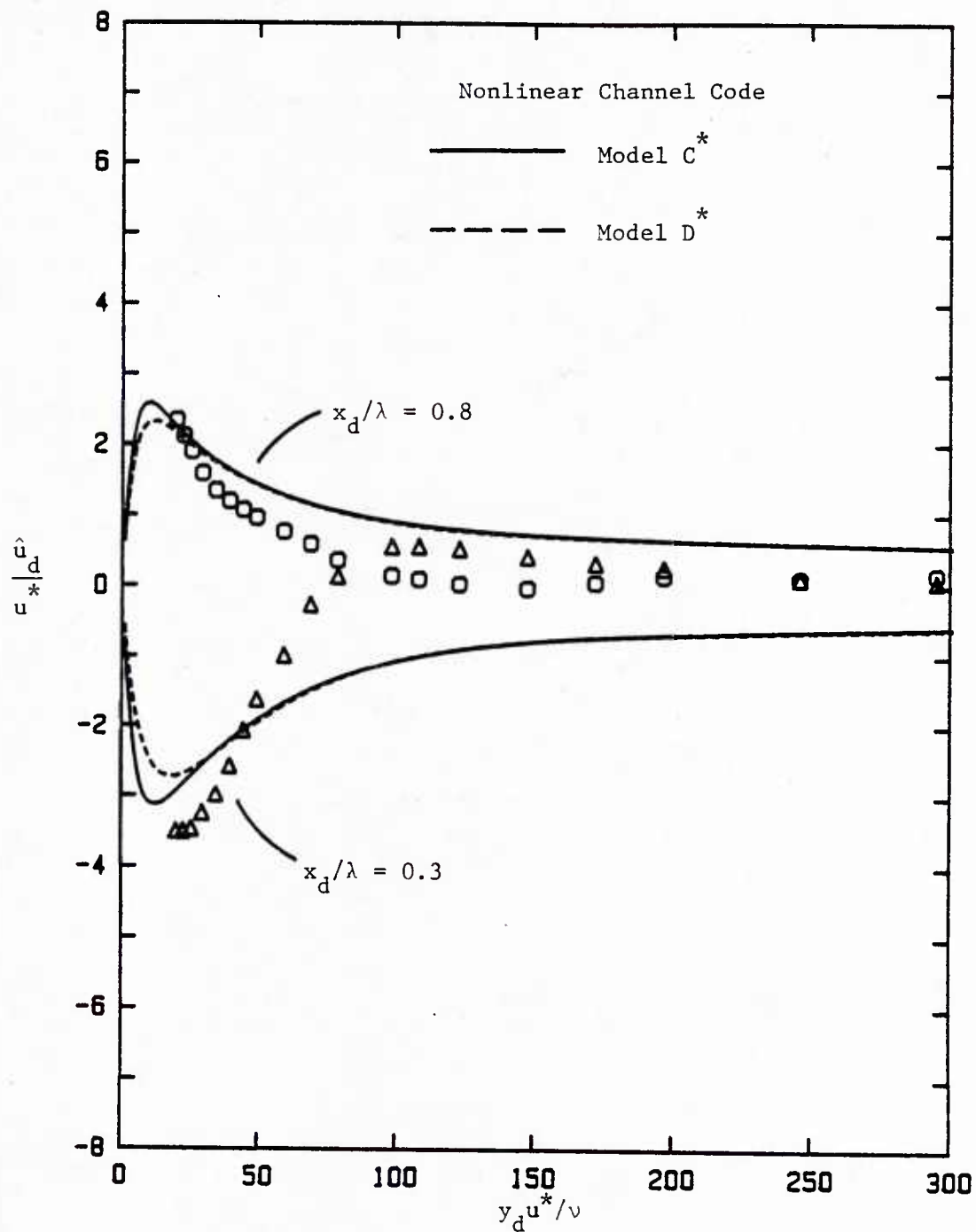


Figure 6.49 Wave-Induced Velocity Perturbations,
 $x_d / \lambda = 0.3, 0.8$, $2a_d / \lambda = 0.05$, $Re_b = 38,800$,
 $2h_d / \lambda = 1.0$

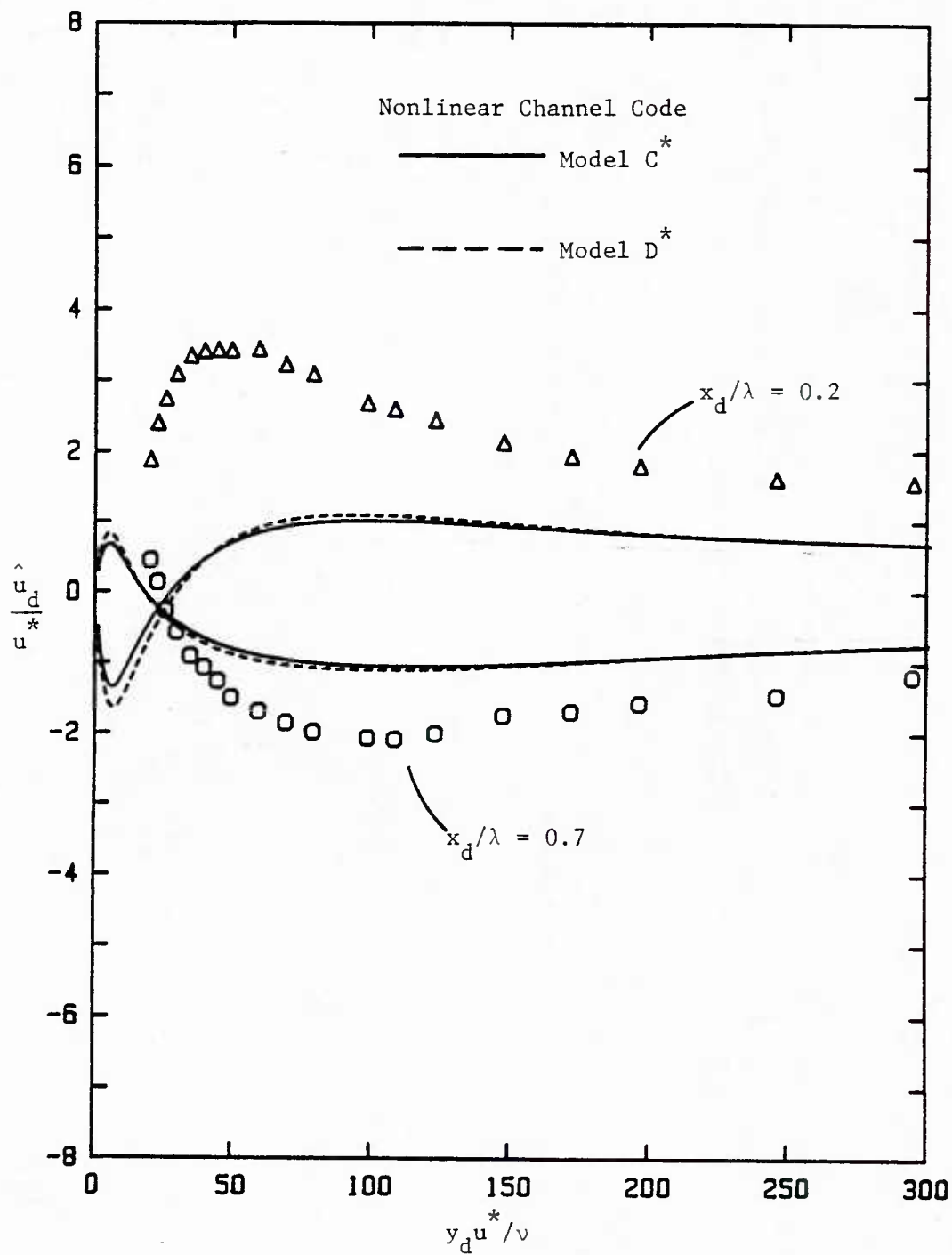


Figure 6.50 Wave-Induced Velocity Perturbations,
 $x_d/\lambda = 0.2, 0.7$, $2a_d/\lambda = 0.05$, $Re_b = 38,800$,
 $2h_d/\lambda = 1.0$

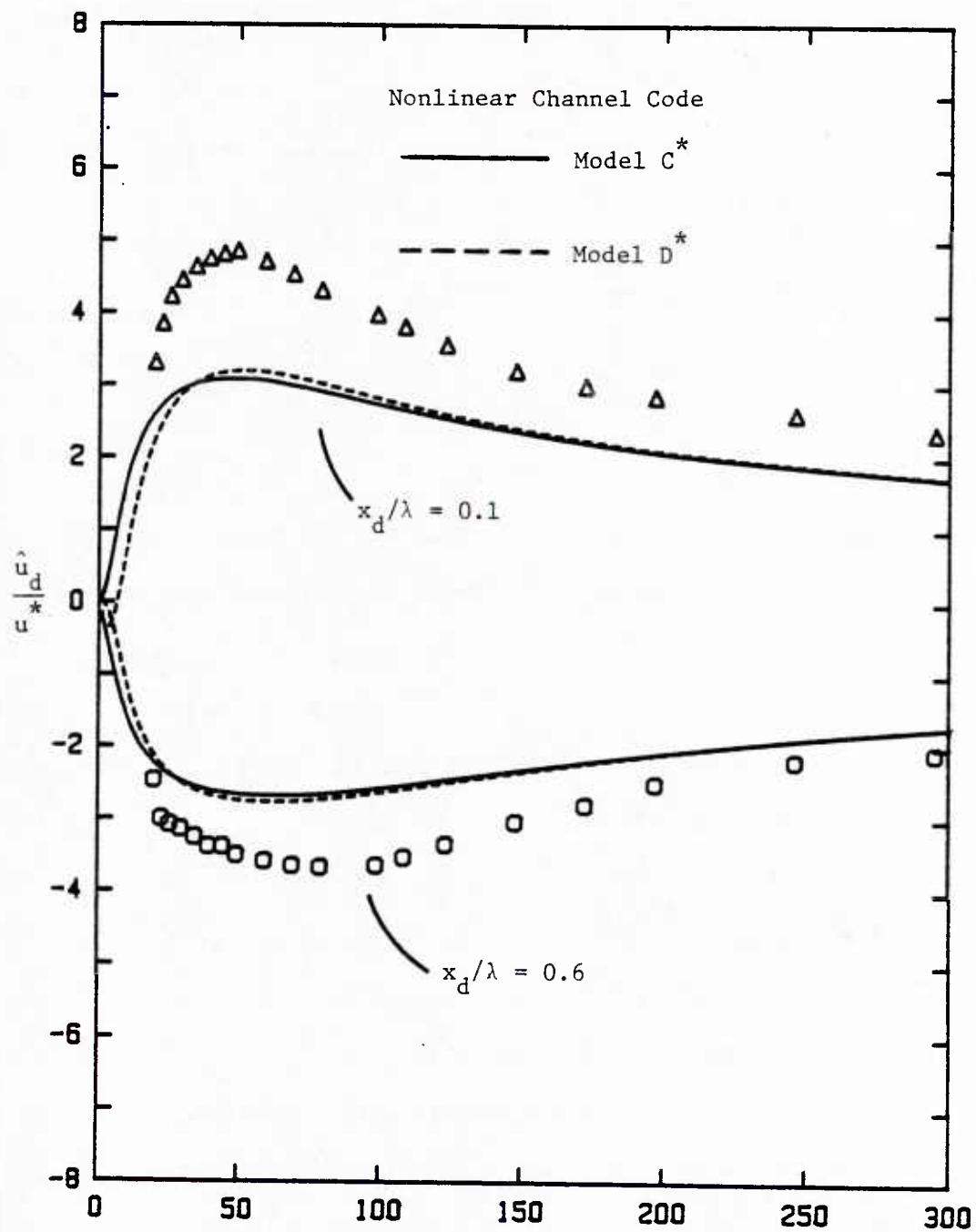


Figure 6.51 Wave-Induced Velocity Perturbations, $x_d/\lambda = 0.1, 0.6$,
 $2a_d/\lambda = 0.05$, $Re_b = 38,800$, $2h_d/\lambda = 1.0$

CHAPTER 7

SUMMARY AND CONCLUSIONS

This chapter summarizes the goals of this thesis, the approach taken to achieve these goals, and the major results which have emerged from the experiments and computations.

I. Goals and Approach

The purpose of the experimental effort was to extend previous studies of nonseparated flow over wavy surfaces by obtaining detailed measurements of the velocity field. Earlier investigators concentrated on the measurement of the surface shear stress and pressure and made only limited velocity measurements. This study presents the first set of velocity data with sufficient measurements to give an accurate representation of the spatial variation in the viscous wall region, $y_d u^* / \nu < 40$. The viscous wall region is of particular interest because the majority of wave-induced disturbances occur here and measurements within this region can be used as a test of the turbulence models of Thorsness [45] and Abrams [2]. Previous tests of their models, which are the best to date, have been limited to comparisons with surface stress data.

Two sets of velocity measurements over waves on the bottom wall of a channel were obtained at conditions corresponding to flows where linear and nonlinear shear stress responses are observed. The conditions were $2a_d/\lambda = 0.3125$, $Re_b = 6400$ and $2a_d/\lambda = 0.05$, $Re_b = 38,800$ respectively. The wavelength of the waves was 2 in. and the ratio of the channel height to the wavelength, $2h_d/\lambda$, was equal to one. The

measurements were taken with a single-channel dual-beam laser-Doppler velocimeter operated in the forward scatter mode. The unique feature of the LDV used in this study is an optics system containing two beam expanders. The beam expanders provided a small enough measurement volume to perform velocity measurements as close to the wave surface as $y_d u^* / \nu = 2$ and 10 for the waves with $2a_d / \lambda = 0.03125$ and 0.05 respectively. Fifteen to twenty data points were taken vertically within the viscous wall region and the measurements extended to the center of the channel. Good spatial resolution in the streamwise direction was achieved by conducting velocity measurements every tenth of a wavelength. Accurate location of the LDV was obtained with a lead screw type traversing mechanism which was constructed for this experiment. Careful filtering and seeding of the fluid was found to be critical for taking accurate LDV measurements.

The primary purpose of the computational effort was to extend the linear theory calculations of Thorsness [45] and Abrams [2] by developing a nonlinear computer code for predicting the flowfield above finite amplitude waves. The velocity measurements in this thesis were obtained over finite amplitude waves where the application of linear theory is uncertain. A secondary goal of the computational work was to perform the above calculations for a channel flow rather than a boundary layer as did Thorsness and Abrams. This is because all of the wavy surface measurements from this laboratory have been conducted in a channel. The computer code solves the nonlinear Reynolds-averaged Navier-Stokes equations using spectral methods in the flow direction and finite differences in the vertical

direction. For computational ease the wave surface was transformed to a flat surface via a conformal mapping. An explicit stretching in the vertical direction was introduced to resolve the steep velocity gradients near the wave and the top wall of the channel. Storage requirements were lowered with the use of a sparse matrix solver. The code is a modification of a boundary layer program by McLean [32].

Future applications of the nonlinear channel program may include the study of wave generation, drag reduction, asymmetric waves, and compliant surfaces. The program was also developed to be used as a "tool" for testing new turbulence models.

II. Results

Mean velocity responses at constant vertical heights above the wave of steepness $2a_d/\lambda = 0.03125$ with $Re_b = 6400$ were Fourier analyzed. The degree of linearity of the flowfield, the wavelength averaged flowfield, and the amplitudes and phases of the wave-induced responses were determined.

A weakly nonlinear flowfield is observed. This is consistent with the electrochemical shear stress measurements of Zilker [48] which show a borderline linear-nonlinear shear stress response for the same flow conditions. The maximum ratio of the amplitude of the second to first harmonics was found to be 0.17 at about $y_d u^*/\nu = 12$. Nonlinearities are negligible outside the viscous wall region.

The wavelength averaged flowfield is observed to be nearly the same as that found in a flat channel.

The majority of the wave-induced disturbances occur within the viscous wall region. The amplitude of the first harmonic is zero at the wave surface and rises sharply to a maximum of 3.6 plus units at $y_d u^* / \nu = 9$. This amplitude represents a 46% disturbance about the wavelength averaged velocity field. Above $y_d u^* / \nu = 9$ the amplitude of the first harmonic decreases rapidly to about the edge of the viscous wall region and then gradually decreases to zero at the center of the channel, $y_d u^* / \nu \approx 365$. At $y_d u^* / \nu = 40$ and 300 the disturbances about the mean flowfield were about 10% and 1% respectively.

A streamwise sequence of the mean velocity profiles clearly shows that the inner flow precedes the outer flow in reacting to pressure gradient changes along the wave surface. The inner flow responds more rapidly since the inertia of the fluid is less here than in the core. The phase angle of the first harmonic of the mean velocity response is a quantitative measure of these lags. The phase angle was found to vary rapidly in the viscous wall region. A maximum phase angle, with respect to the downstream crest, of 49° is observed at $y_d u^* / \nu = 2$ and phase has a minimum value of -23° at about $y_d u^* / \nu = 50$ and tends toward zero far from the wall where the influence of the wave on the fluid is not felt.

The streamwise turbulent intensity responses over the $2a_d / \lambda = 0.3125$ wave were also Fourier analyzed. The wavelength averaged profile of the intensity shows a slight increase above flat channel intensities. A near linear response is observed for $10 < y_d u^* / \nu < 40$. A maximum disturbance of 20% about the wavelength average occurs at

$y_d u^* / \nu = 24$. The amplitude of the wave-induced variation of the intensity is almost zero above $y_d u^* / \nu = 60$.

The periodic variation of the turbulent intensity along the wave is consistent with constant pressure gradient experiments in other laboratories [6, 7, 22, 23, 28, 29, 31]. It has been observed that strong negative (favorable) pressure gradients cause a dampening of turbulence close to the wall, and that positive pressure gradients (adverse) have just the opposite effect. However, in this case the pressure gradient is varying rapidly in the flow direction and the flow does not adjust instantaneously as it would for an equilibrium flow. Lags in the reaction of the turbulent intensity to the spatially varying pressure gradient are observed, with the reaction of the inner flow preceding the outer flow. The phase angle of the intensity response, with respect to the downstream crest, is 222° at $y_d u^* / \nu = 10$ and 142° at $y_d u^* / \nu = 50$. As a reference, instantaneous reaction of the fluid corresponds to a phase angle of about 270° since the variation of the pressure gradient along the wave is roughly that predicted by inviscid Kelvin-Helmholtz theory.

The above observation of the u-intensity lagging in reaction to a pressure gradient provides some physical basis for the highly empirical Model D^{*}. However, a better test of this model would be a comparison with uv-intensities. Experiments to measure the Reynolds stress with a two-component LDV are currently being designed in this laboratory. These measurements will provide a more direct test of turbulence models.

The LDV measurements are close enough to the wave surface to extrapolate linearly to obtain the phase angle but not the amplitude of the shear stress response. The extrapolated phase angle of 54° agrees with the electrochemical measurements of Zilker [48]. The amplitude of the shear stress response could not be obtained because the linear region in the velocity profiles does not extend to the closest measurements at $y_d u^* / \nu = 2$.

The mean velocity responses above the wave of steepness $2a_d/\lambda = 0.05$ with $Re_b = 38,800$ were also Fourier analyzed. The responses over this wave showed moderate departures from linear behavior for $y_d u^* / \nu < 100$. The maximum value of the ratio of the amplitude of the second harmonic to first harmonics is 0.21 at about $y_d u^* / \nu = 35$. The nonlinearities are surprisingly weak when it is considered that the dimensionless wave amplitude, $a_d u^* / \nu$, of this wave is 7.7 times that for the $2a_d/\lambda = 0.03125$ wave. The velocity responses varied gradually on the windward side of the wave and steeply on the leeward side. This is the same shape that Zilker [48] observed for all nonlinear shear stress responses. However, shear stress measurements of Zilker under similar conditions showed much greater nonlinearities at the wave surface than observed above the wave.

As in the case of the $2a_d/\lambda = 0.03125$ wave, the wavelength averaged flowfield was found to be very close to that observed in a flat channel.

The shape of the first harmonic amplitude profile is similar to that found over the $2a_d/\lambda = 0.03125$. However, in this case the disturbances extend well outside the viscous wall region. This is

consistent with the linear calculations of Abrams [2] which show that the penetration of disturbances increases with decreasing dimensionless wavenumber, $\alpha_d \nu / u^*$. The two sets of data suggest that this penetration is given by $(\alpha_d \nu / u^*)(y_d^* / \nu) = \text{constant}$. A maximum amplitude of 5.6 plus units is observed at $y_d^* / \nu = 26$. By coincidence, this is also a 46 percent disturbance about the wavelength averaged flowfield. Above $y_d^* / \nu = 26$ the disturbances decrease rapidly to $y_d^* / \nu = 200$ and then gradually to the center of the channel, $y_d^* / \nu \approx 1830$.

The phase angle of the first harmonic varied rapidly between the wave surface and $y_d^* / \nu = 100$. A value of 15.8° was observed at $y_d^* / \nu = 20$. A minimum value of -16.9° was found at $y_d^* / \nu = 125$ and the phase angle tended toward zero far from the wall. As found for the $2a_d / \lambda = 0.03125$ wave, the rapid phase changes are a result of mean velocity variations in the inner flow preceding the outer flow.

The nonlinear channel calculations were performed with turbulence Models C* and D* developed by Thorsness [44] and Abrams [2]. Both models used the Cess eddy viscosity profile which is an empirical equation derived by matching van Driest's wall region law with Reichardt's middle law. The Cess profile was chosen for the computations because it gives a good fit of eddy viscosity data in a flat channel and provides a smooth transition between the inner and core regions. For Model C* the flat channel value of the van Driest parameter is used in the Cess equation. However, turbulence properties are allowed to vary in the flow direction because the eddy viscosity is a function of the local shear stress and turbulent

stresses are a function of the local rate of strain. This model is appealing because it is a simple extension of the widely accepted Cess equation for a flat channel. In Model D^* the effect of pressure gradients on the turbulence is taken into account. The van Driest parameter is used as a scale factor for governing the thickness of the viscous wall region. This parameter is assumed to be a simple polynomial function of the pressure gradient with a single lag constant used to relax the flow. Model D^* was investigated because Abrams [2] has shown that it is necessary to include the effect of pressure gradients on the turbulence to predict the surface shear stress.

Three different types of physical distances from the wave surface in the Cess equation were investigated: normal, Cartesian, and curvilinear. It was found that the results are independent of the type of distance for waves of steepness $2a_d/\lambda \leq 0.05$.

The agreement between the computations and measurements is best for the wave of steepness $2a_d/\lambda = 0.03125$ with $Re_b = 6400$ and for these conditions the results using turbulence Models C^* and D^* are very similar.

Models C^* and D^* both predict the observed near linear response of the velocity field over the $2a_d/\lambda = 0.03125$ wave. However, the models significantly underpredict the weak nonlinearities found in the experimental velocity responses.

The amplitude and phase of the surface shear stress predicted by both models are within the experimental error of the electrochemical measurements of Zilber [48]. Zilker also observed a wavelength averaged shear stress which was the same as the flat

channel value. Models C^* and D^* predict a shear stress reduction of about 10 percent.

Turbulence Models C^* and D^* predict identical wavelength averaged velocity profiles over the $2a_d/\lambda = 0.03125$ wave that are within the experimental error of the wavelength averaged velocity data.

A comparison between the experimental mean velocity profiles and the mean profiles from Models C^* and D^* shows reasonably good agreement. Small differences between the two models is observed. The most important result for this wave is that Model C^* , which is an eddy viscosity model developed for a flat channel, predicts a good first approximation of the velocity field. However, two shortcomings of Models C^* and D^* are observed. First, both models predict smaller disturbances about the wavelength averaged profile than is found experimentally. Secondly, the observed variation of the phase angle of the velocity with height above the wave is larger than predicted.

Computations with turbulence Models C^* and D^* were also performed for the wave of steepness $2a_d/\lambda = 0.05$ with $Re_b = 38,800$. In general, agreement between the calculations and measurements is not as good as for the wave of lower steepness. However, the results are still semi-quantitative. Significant differences between the predictions of Models C^* and D^* are observed.

Models C^* and D^* correctly predict a nonlinear response of the velocity field. However, both models significantly underestimate observed nonlinearities. Model C^* is particularly poor because this

model predicts a weakly nonlinear response. The shape of the Model D^* response is qualitatively the same as the data. That is, the predicted velocity responses vary gradually on the windward side of the wave and steeply on the leeward side.

As in the case of the $2a_d/\lambda = 0.03125$ wave, the wavelength averaged velocity profiles predicted by Models C^* and D^* are nearly identical. However, these profiles are significantly lower than the measured wavelength average. The reason for this difference is not known.

The observed amplitude of the first harmonic of the velocity response for the wave with $2a_d/\lambda = 0.05$ is considerably underpredicted by both Models C^* and D^* . Linear theory calculations with a quasi-laminar turbulence model suggest that larger disturbances about the wavelength averaged flowfield are obtained with models predicting smaller wave-induced variations of the turbulence than Models C^* and D^* . However, Abrams [2] has shown that such models cannot predict the wall shear stress over a wide range of flowrates. Furthermore, models with small wave-induced variations do not predict strong nonlinearities. Thus there is an apparent contradiction in producing both the large wave-induced disturbances and the large nonlinearities which are observed in the data. It is not known how to "design" a turbulence model to resolve this problem. A lag constant in Model D^* that is a function of height above the wave may provide some improvement. However, it is suggested that a more fundamental approach such as a $k-\epsilon$ closure or solution of the unaveraged Navier-Stokes equations be investigated.

The variation with height of the phase angle of the velocity is underpredicted by Models C^{*} and D^{*}.

In summary, measurements were obtained of the viscous wall region over waves with nonseparated flows. It was found that the behavior of both the mean velocity field and the streamwise intensity field can be explained in terms of pressure gradient variations induced by the wave surface. It is observed that the outer flow lags the inner flow in reacting to the local pressure gradient. Of particular interest is a periodic enhancement and dampening of the streamwise intensity which is consistent with experiments for constant pressure gradient flows. A nonlinear computer code was developed to solve for the flow-field over finite amplitude waves in a channel. Two eddy viscosity turbulence models were investigated; one designed for a flat channel, and one where turbulent stresses are a function of the pressure gradient and relaxed with a single lag constant. Both models give semi-quantitative results but underpredict disturbances about the wavelength average flowfield, variations in the phase of the velocity, and nonlinearities.

NOMENCLATURE

a_d	Dimensional wave amplitude (cm)
A	van Driest parameter
A'	Dimensional area along wave surface, see equation (6.2) (cm^2)
\bar{A}	Average van Driest parameter, see equation (3.32)
b	Stretching coefficient in equation (3.23)
b_i	Coefficients in orthogonal transformation, see equations (3.8) and (3.9)
c_n	Coefficients in Fourier series defined by equation (6.1)
C'_p	Local wall pressure coefficient defined by Sigal
C_p	Pressure drag coefficient defined in equation (6.5)
C_s	Skin friction drag coefficient defined in equation (6.4)
d_n	Coefficients in Fourier series defined by equation (6.1)
f	Fanning friction factor
F_{x_d}	Dimensional x_d component of the total force that the fluid exerts on the wave (dyne)
h_d	Dimensional half height of channel (cm)
$ I_n $	Dimensional amplitude of nth harmonic of wave-induced streamwise intensity (cm/s)
J	Jacobian of orthogonal transformation defined by equations (3.8) and (3.9)
k_1, k_2	Coefficients defined in equation (3.32)
k_L	Lag parameter defined in equation (3.33)
P_d	Dimensional time-averaged pressure (dyne/cm^2)
$P_{d, \text{crest}}$	Dimensional time-averaged pressure at crest (dyne/cm^2)
$ \hat{P}_d _n$	Dimensional amplitude of nth harmonic of wave-induced surface pressure (dyne/cm^2)

p^+	Dimensionless pressure gradient in x_d direction
p_{eff}^+	Dimensionless effective pressure gradient defined by equation (3.54)
Re_b	Channel Reynolds number based on bulk velocity and half channel height
R_{ij}	Dimensional components of the time-averaged turbulent stress tensor (dyne/cm ²)
S	Dimensional distance along wave surface, see equations (6.4) and (6.5) (cm)
S_{ij}	Dimensional components of the time-averaged rate of strain tensor (1/s)
u^*	Friction velocity for flat surface (cm/s)
u_d	Dimensional time-averaged velocity in x_d direction (cm/s)
u'_d	Dimensional fluctuating component of turbulent velocity in x_d direction (cm/s)
\hat{u}_d	Dimensional wave-induced velocity in x_d direction (cm/s)
$ \hat{u}_d _n$	Dimensional amplitude of nth harmonic of wave-induced velocity in x_d direction (cm/s)
U_b	Bulk channel velocity (cm/s)
\bar{u}_d	Dimensional wavelength averaged velocity in x_d direction (cm/s)
v_d	Dimensional time-averaged velocity in y_d direction (cm/s)
v'_d	Dimensional fluctuating component of turbulent velocity in y_d direction (cm/s)
x_d	Dimensional horizontal Cartesian coordinate (cm)
y_d	Dimensional vertical Cartesian coordinate (cm)
y'_d	Dimensional normal, Cartesian, or curvilinear distance from the wave surface as illustrated in Figure 3.5 (cm)
y_T	Dimensional height of channel top wall in Cartesian coordinates (cm)
z	Unstretched coordinate defined by equation (3.23)

Greek

α_d	Dimensional wavenumber (cm)
β	Angle between the wave surface and the horizontal, see equation (6.3) ($^\circ$)
γ_k	Fourier coefficients in equations (3.27)-(3.29)
η	Dimensional transformed coordinate defined by equations (3.8) and (3.9)
η_T	Dimensional height of channel top wall in transformed coordinates (cm)
$\theta_{I,n}$	Phase lag of nth harmonic of wave-induced streamwise intensity from downstream crest ($^\circ$)
$\theta_{\hat{p},n}$	Phase lag of nth harmonic of wave-induced surface pressure from downstream crest ($^\circ$)
$\theta_{\hat{\tau},n}$	Phase lag of nth harmonic of wave-induced surface shear stress from downstream crest ($^\circ$)
$\theta_{\hat{u},n}$	Phase lag of nth harmonic of wave-induced velocity in x_d direction from downstream crest ($^\circ$)
κ	von Karman constant
λ	Dimensional wavelength (cm)
ν	Kinematic viscosity (cm^2/s)
ν_t	Turbulent viscosity (cm^2/s)
ϵ	Dimensional transformed coordinate defined by equations (3.8) and (3.9)
ρ	Density of fluid (gm/cm^3)
τ_d	Dimensional surface shear stress (dyne/cm)
$\bar{\tau}_d$	Dimensional wavelength averaged surface shear stress (dyne/cm)
$ \hat{\tau} _n$	Dimensional amplitude of nth harmonic of wave-induced surface shear stress (dyne/cm ²)
τ_w	Dimensional wall shear stress for flat surface (dyne/cm ²)

ϕ	Dimensional dependent variables in equations (3.24)-(3.29) which define finite difference and spectral approximations (cm^2/s) or $1/\text{s}$)
ψ_d	Dimensional time-averaged stream function (cm^2/s)
ω_d	Dimensional time-averaged vorticity ($1/\text{s}$)

REFERENCES

1. Abrams, J. (1979), "A Nonlinear Boundary Layer Analysis for Turbulent Flow Over a Solid Wavy Surface," M.S. Thesis, Department of Chemical Engineering, University of Illinois, Urbana.
2. Abrams, J. (1984), "Turbulent Flow Over Small Amplitude Solid Waves," Ph.D. Thesis, Department of Chemical Engineering, University of Illinois, Urbana.
3. Abrams, J., Frederick, K. A. and Hanratty, T. J. (1981), "Interaction Between a Turbulent Flow and a Wavy Surface," presented at National Meeting of the A.I.Ch.E., Detroit, Michigan; to be published in Physico Chemical Hydrodynamics.
4. Abrams, J. and Hanratty, T. J. (1985), "Relaxation Effects Over a Wavy Surface," J. Fluid Mech., 151, 443.
5. Adrian, R. J. (1980), "Laser Velocimetry," Department of Theoretical and Applied Mechanics, Report No. 422, University of Illinois, Urbana.
6. Anderson, P. S., Kays, W. M. and Moffat, R. J. (1972), "The Turbulent Boundary Layer on a Porous Plate: An Experimental Study of the Fluid Mechanics for Adverse Free-Stream Pressure Gradients," Stanford University, Thermosc. Div. Rep. HMT-15.
7. Badri Narayanan, M. A. and Ramjee, V. (1968), "On the Criteria for Reverse Transition in a Two Dimensional Boundary Layer Flow," India Inst. Sci. Rep. AE68FM1.
8. Beebe, P. S. (1972), "Turbulent Flow Over a Wavy Boundary," Ph.D. Thesis, Department of Civil Engineering, Colorado State University, Fort Collins.
9. Buckles, J. J. (1983), "Turbulent Separated Flow Over Wavy Surfaces," Ph.D., Thesis, Department of Chemical Engineering, University of Illinois, Urbana.
10. Buckles, J. J., Adrian, R. J., Hanratty, T. J. (1984), "Turbulent Flow Over Large-Amplitude Wavy Surfaces," J. Fluid Mech., 140, 27.
11. Caponi, E. A., Fornberg, B., Knight, D. D., McLean, J. W., Saffman, P. G. and Yuen, H. C. (1982), "Calculations of Laminar Viscous Flow Over a Moving Wavy Surface," J. Fluid Mech., 124, 347.

12. Cary, A. M., Jr., Weinstein, L. M. and Bushnell, D. M. (1980), "Drag Reduction Characteristics of Small Amplitude Rigid Surface Waves," in Viscous Flow Drag Reduction (ed. by G. R. Hough), Amer. Inst. Aero. Astro., New York, 144.
13. Cess, R. D. (1958), "A Survey of the Literature in Heat Transfer in Turbulent Tube Flow," Westinghouse Research Report 8-0529-R24.
14. Clark, J. A. (1968), "A Study of Incompressible Turbulent Boundary Layers in Channel Flow," J. Basic Eng., 455.
15. Cohen, L. S. (1964), "Interaction Between Turbulent Air and a Flowing Liquid Film," Ph.D. Thesis, Department of Chemical Engineering, University of Illinois, Urbana.
16. Compte-Bellot, G. (1965), "Écoulement Turbulent Entre Deux Parois Parallèles," Publ. Sci et Techn. du Ministère de l'Air, No. 419.
17. Cook, G. W. (1970), "Turbulent Flow Over Solid Wavy Surfaces," Ph.D. Thesis, Department of Chemical Engineering, University of Illinois, Urbana.
18. Eckelmann, H. and Reichardt, H. (1971), "An Experimental Investigation in a Turbulent Channel Flow with a Thick Viscous Sublayer," Proceedings of Symposium on Turbulence in Liquids, University of Missouri, Rolla.
19. Finnicum, D. S., Ph.D. Thesis, Department of Chemical Engineering, University of Illinois, Urbana, expected 1986.
20. Hsu, S. and Kennedy, J. F. (1971), "Turbulent Flow in Wavy Pipes," J. Fluid Mech., 47, 481.
21. Hussain, A. K. M. F. and Reynolds, W. C. (1970), "The Mechanics of a Perturbation Wave in Turbulent Shear Flow," Stanford University, Thermosc. Div. Rep. RM-6.
22. Jones, W. P. (1967), "Strongly Accelerated Turbulent Boundary Layers," M.Sc. Thesis, Imperial College.
23. Julien, H. L., Kays, W. M., and Moffat, R. J. (1969), "The Turbulent Boundary Layer over a Porous Plate: Experimental Hydrodynamics of Favorable Pressure Gradient Flows," Stanford University, Thermosc. Div. Rep. HMT-4.
24. Kendall, J. M. (1970), "The Turbulent Boundary Layer Over a Wall With Progressive Surface Waves," J. Fluid Mech., 41, 259.
25. Kuzan, J. D. (1983), "Separated Flow Over a Large Amplitude Wavy Surface," M.S. Thesis, Department of Chemical Engineering, University of Illinois, Urbana.

26. Kuzan, J. D., Ph.D. Thesis, Department of Chemical Engineering, University of Illinois, Urbana, expected 1986.
27. Larras, J. and Claria, A. (1960), "Recherches en soufflène sur l'action relative de la houle et du vent," *La Houille Blanche*, 6, 674.
28. Launder, B. E. and Jones, W. P. (1969), "Sink-Flow Turbulent Boundary Layers," *J. Fluid Mech.*, 38, 817.
29. Launder, B. E. and Stinchcombe, H. S. (1967), "Sink Flow Turbulent Boundary Layers," Imperial College, Mech. Engng. Dept. Rep. TWF/TN/21.
30. Lin, J. C., Walsh, M. J., Watson, R. D., and Balasubramanian, R. (1983), "Turbulent Drag Characteristic of Small Amplitude Rigid Surface Waves," AIAA-83-0228.
31. Loyd, R. J., Moffat, R. J. and Kays, W. M. (1970), "The Turbulent Boundary Layer on a Porous Plate: An Experimental Study of the Fluid Dynamics with Strong Favorable Pressure Gradients and Blowing," Stanford University Thermosc. Div. Rep. HMT-13.
32. McLean, J. W. (1983), "Computation of Turbulent Flow Over a Moving Wavy Boundary," *Phys. Fluids*, 26, 2065.
33. Morrisroe, P. E. (1970), "Flow Over Solid Wavy Surfaces," M.S. Thesis, Department of Chemical Engineering University of Illinois, Urbana.
34. Motzfeld, H. (1937), "Die Turbulente Strömung on welligen Wänden," *Z. angew. Math. Mech.*, 17, 193.
35. Orszag, S. A. (1971), "Numerical Simulation of Incompressible Flows within Simple Boundaries," *J. Fluid Mech.*, 49, 75.
36. Reichardt, H. (1951), *Arch. Ges. Warmetechnik*, 6/7, 129.
37. Reischman, M. M. and Tiederman, W. G. (1975), "Laser-Doppler Anemometer Measurements in Drag-Reducing Channel Flows," *J. Fluid Mech.*, 70, 369.
38. Reynolds, W. C. and Tiederman, W. G. (1967), "Stability of Turbulent Channel Flow, with Application to Malkus's Theory," *J. Fluid Mech.*, 27, 253.
39. Scott, M. R. and Watts, H. A., (1975) "Support a Computer Code for Two-Point Boundary-Value Problems via Orthonormalization," Rep. Sand. 75-0198, Sandia Labs., Albuquerque, NM.
40. Scott, M. R. and Watts, H. A. (1977), "Computational Solution of Linear Two-Point Boundary Value Problems via Orthonormalization," *SIAM Journal on Numerical Analysis*, 14, 40.

41. Sigal, A. (1971), "An Experimental Investigation of the Turbulent Boundary Layer Over a Wavy Wall," Ph.D. Thesis, Department of Aeronautical Engineering, California Institute of Technology, Pasadena.
42. Stadtherr, M. A. and Wood, E. S. (1984), "Sparse Matrix Methods for Equation-Based Chemical Process Flowsheeting-II," Comput. Chem. Engng., 6, 115.
43. Stanton, T., Marshall, D. and Houghton, R. (1932), "The Growth of Waves on Water Due to the Action of the Wind," Proc. Roy. Soc. A., 137, 283.
44. Thorsness, C. B. (1975), "Transport Phenomena Associated with Flow Over a Solid Wavy Surface." Ph.D. Thesis, Department of Chemical Engineering, University of Illinois, Urbana.
45. Thorsness, C. B., Morrisroe, P. E. and Hanratty, T. J. (1978), "A Comparison of Linear Theory with Measurements of the Variation of Shear Stress Along a Solid Wave." Chemical Engineering Science, 33, 579.
46. van Driest, E. R. (1957), "On Turbulent Flow Near a Wall," J. Aero. Sci., 73, 1007.
47. Zagustin, K., Hsu, F. Y., Street, R. L., and Perry, B. (1966), "Flow Over a Moving Boundary in Relation to Wind-Generated Waves," Technical Report No. 60, Department of Civil Engineering, Stanford University.
48. Zilker, D. P. (1976), "Flow Over Wavy Surfaces," Ph.D. Thesis, Department of Chemical Engineering, University of Illinois, Urbana.
49. Zilker, D. P., Cook, G. W. and Hanratty, T. J. (1977), "Influence of the Amplitude of a Solid Wavy Wall on a Turbulent Flow. Part 1, Non-Separated Flows." J. Fluid Mech., 82, 29.

APPENDIX A

LISTING OF NONLINEAR CHANNEL

COMPUTER PROGRAM

TEXT

PROGRAM MAIN

C

```

IMPLICIT REAL*8(A-H,O-Z)
IMPLICIT INTEGER*4(I-N)
REAL*8 JA,JN1,JS1
COMMON/PVAR/PO,P(2600),PS(2600),PN(2600)
& ,PSS(2600),PNN(2600),PNNN(2600),UZ(2600),US(32)
COMMON/XYD/PXX(2600),PYY(2600),PXY(2600)
COMMON/WVAR/W(2600),WS(2600),WN(2600)
COMMON/CON/N,M,NP1,NP2,N2,N3,MP1,MP2,RE,REI,RK,A,C,PI,DX,RKL
& ,RK1,LDA,LDJ,NE,DEL,DEL2
COMMON/SCALE/Z1(200),Z2(200),Z3(200),Z1H(200),Z2H(200),Z3H(200)
& ,ZA(200),ZB(200),Z1S(200),ETA(200)
COMMON/TRANS/SX(2600),SY(2600),SXX(2600),SXY(2600)
& ,SXS(2600),SYS(2600),SXSX(2600)
COMMON/MAT/DJ(300000),ICI(300000),IRP(3000),MAXA
COMMON/AMAT/ABD(32,32),IPVT(32)
COMMON/EDVIS/T(2600),TN(2600),TNN(2600),TXX(2600),
& TYY(2600),TXY(2600),TS(2600),TSS(2600),
& TW(2600),TWSS(2600),TWN(2600),TT(2600),
& EX(2600),AU(32),AS(32)
COMMON/NEW/JA(2600),JN1(2600),JS1(2600),B(15),YO,ZT
& ,HS(32),HSS(32),ZERO(32)
& ,DN(2600),DB(2600),SHR(32),SHI(32),ET(32),ETM(32)
COMMON/CDATA/XXX(400)
COMMON/FRED/RH
COMMON/KONST/CC1
COMMON/KUZ/ETAT
COMMON/TEST1/INDEX1
COMMON/BUM/NDUK
DIMENSION F1(2600),F(2600)

```

C**

```

WRITE(52,1001)
1001 FORMAT(' **TURBULENT CALCULATION SPECTRAL EQNS 2NTH MODES**'
& ,/, ' ** REVISION 12/10/85 MODEL C* OR D*, **'
& ,/, ' ** USING THE CESS EDDY VISCOSITY PROFILE **')
WRITE(52,1005)
1005 FORMAT(' THIS PROGRAM IS A MODIFICATION OF THE BOUNDARY
& LAYER CODE BY MCLEAN TO THE CASE OF CHANNEL FLOW ')
WRITE(52,1004)
1004 FORMAT(' MODIFIED BY K.A. FREDERICK & J.D. KUZAN ',/)
WRITE(52,1003)
1003 FORMAT(' THE DISTANCES USED TO EVALUATE THE EDDY VISCOSITY
& ARE ALONG LINES OF CONSTANT XI ')

```

C**

```

PI=4.DO*DATAN(1.DO)
LDA=32
DEL=1.D-6
DEL2=DEL+DEL

```

C** GENERATE CONFORMAL MAP & COMPUTE JACOBIAN

C** COMPUTE SCALE FACTORS FOR STRETCHING

*

*


```

      CALL INIT(ST)
      NE=NP1*M
C**  PARAMETERS FOR SPARSE MATRIX SOLVER
      CHKT=.0001D0
      PIVT=.0001D0
C**  INITIALIZE DATA FOR FFT
      CALL CINIT(NP1)
      CALL HSET(ST)
C**  COMPUTE BOUNDARY CONDITIONS
      CALL FLEXBC(F)
C**  GENERATE INITIAL GUESS FOR STREAMFUNCTION
      CALL GUESS(F)
      INDEX1=0
C**  START OF NEWTON ITERATION
100  INDEX1=INDEX1+1
C**  COMPUTE STREAMFUNCTION DERIVATIVES...VORTICITY & DERIVS **
      CALL PPRIME(F1)
      CALL XYDER
      CALL VORT
      CALL WPRIME(F1)
C**  COMPUTE EDDY VISCOSITY
      CALL MIX(F)
      CALL EDDY(F)
C**  COMPUTE RESIDUAL
      CALL RES(F)
      DO 250 NI=1,NP1*MP2
C**  PRINT OUT RESIDUALS
      WRITE(54,101)NI,F(NI)
101  FORMAT(1X,I5,3X,F30.20)
250  CONTINUE
      CLOSE(54)
      XA=0.D0
      DO 200 I=1,NP1*MP2
      XB=DABS(F(I))
200  IF (XA.LT.XB) XA=XB
C**  PRINT OUT MAXIMUM RESIDUAL
      WRITE(53,1002)INDEX1,XA
      CLOSE(53)
1002 FORMAT(' INDEX1= ',I3, ' MAXIMUM RESIDUAL IS: ',E12.6)
      IF (XA.LT.1.D-6) GOTO 1000
      IF (XA.GT.1.D7) GOTO 5000
      IF (INDEX1.EQ.10) GOTO 1000
      CALL PRESSURE(F)
C**  COMPUTE JACOBIAN AND SOLVE LINEAR SYSTEM
C**  (SPARSE MATRIX SOLVER BY M.A. STADTHERR)
      CALL FDJAC(F,F1)
      CALL TRANPR(NE)
      CALL LU1SOL(NE,CHKT,PIVT,F,F1)
C**  UPDATE STREAMFUNCTION, AT THE INTERIOR POINTS ONLY
      DO 300 I=1,NP1*M
      P(I+NP1)=P(I+NP1)-F1(I)
300  CONTINUE

```

```
NRQ=(NP1*MP2)-((2*NP1)-1)
P(NP1*MP2-NP1)=P(NRQ)
C** PRINT OUT STREAMFUNCTION SO THAT PROGRAM CAN BE
C  RESTARTED IF COMPUTER GOES DOWN
DO 301 I=1,NP1*MP2
301 WRITE(56,*) I,P(I)
CLOSE(56)
GOTO 100
C** END OF NEWTON ITERATION
1000 CONTINUE
C** OUTPUT RESULTS: NORMAL AND TANGENTIAL STRESSES ,DRAG COEFF, ETC. *
CALL PRESSURE(F)
CALL EXIT
5000 STOP
END
C** *
```

```

SUBROUTINE INIT(ST)
C**
C** SUBROUTINE TO GENERATE COORDINATE SCALINGS
C**
IMPLICIT REAL*8(A-H,O-Z)
IMPLICIT INTEGER*4(I-N)
REAL*8 JA,JN1,JS1
COMMON/CON/N,M,NP1,NP2,N2,N3,MP1,MP2,RE,REI,RK,A,C,PI,DX,RKL
& ,RK1,LDA,LDJ,NE,DEL,DEL2
COMMON/SCALE/Z1(200),Z2(200),Z3(200),Z1H(200),Z2H(200),Z3H(200)
& ,ZA(200),ZB(200),Z1S(200),ETA(200)
COMMON/TRANS/SX(2600),SY(2600),SXX(2600),SXY(2600)
& ,SXS(2600),SYS(2600),SXSX(2600)
COMMON/NEW/JA(2600),JN1(2600),JS1(2600),B(15),Y0,ZT
& ,HS(32),HSS(32),ZERO(32)
& ,DN(2600),DB(2600),SHR(32),SHI(32),ET(32),ETM(32)
COMMON/FRED/RH
COMMON/KUZ/ETAT
DIMENSION PSJ(32)
C**
C** INPUT PARAMETERS
C**
DATA RK,A,RK1,RKL/0.48D0,33.D0,-35.D0,1800.D0/
DATA RH,RE,C/0.2D0,77.89D0,0.D0/
DATA M,YT,BZ,N/59,1.D0,5.0D0,31/
C**
WRITE(52,1001)A,RK1,RKL
1001 FORMAT(' VAN-DRIEST: A=',F5.2,' K1=',F6.2,' KL=',F7.2)
WRITE(52,2000)RH
2000 FORMAT(' 2A/LAMBDA=',F12.5)
WRITE(52,2001)RE
2001 FORMAT(' REYNOLDS NUMBER=',F10.4)
WRITE(52,2002)C
2002 FORMAT(' C/U*=',F6.3)
WRITE(52,2003)M
2003 FORMAT(' # OF VERT INTERIOR MESH PTS =',I5)
WRITE(52,2004)YT

```

```

2004  FORMAT(' 2H/LAMBDA=',F6.3)
      WRITE(52,2005)BZ
2005  FORMAT(' VERT. STRETCHING PARAM.=',F5.2)
      WRITE(52,2006) N,RK
2006  FORMAT(' # OF HORIZ. INTERIOR MESH PTS =',I4,'VON KARMAN=',F5.2)
      AMP=PI*RH
      ZT=2.DO*PI*YT
      REI=1.DO/RE
      NP1=N+1
      NP2=NP1+1
      N2=NP2+NP1
      N3=NP1+N2
      MP1=M+1
      MP2=M+2
      DX=2.DO*PI/NP1
C**  COMPUTE FOURIER COEFFICIENTS OF CONFORMAL MAP
      CALL WALL(AMP,ZT,YO,PHS,B)
C**
C**  COMPUTE STRETCHING & VERTICAL SCALE FACTORS
C**
      CALL WHY(YO,ZT,BZ)
      DO 10 J=0,MP1
      J1=J+1
      Z1H(J1)=Z1(J1)/2.DO
      Z2H(J1)=Z2(J1)/2.DO
      Z3H(J1)=Z3(J1)/2.DO
      ZA(J1)=Z1(J1)*Z1(J1)*Z1(J1)/2.DO
      ZB(J1)=3.DO*Z1(J1)*Z2(J1)
      Z1S(J1)=Z1(J1)*Z1(J1)
10   CONTINUE
C**
C**  JACOBIAN OF TRANSFORMATION
C**
      NJ=-N
      DO 130 J=0,MP1
      NJ=NJ+NP1
      PSI=-DX
      DO 120 I=0,N
      PSI=PSI+DX
      NI=I+NJ
      XS=1.DO
      XN=0.DO
      XSS=0.DO
      XSN=0.DO
      DO 110 I1=1,14
      SN=DSIN(I1*PSI)
      CS=DCOS(I1*PSI)
      CH=DCOSH(I1*(ETAT-ETA(J+1)))/DSINH(I1*ETAT)
      SH=DSINH(I1*(ETAT-ETA(J+1)))/DSINH(I1*ETAT)
      XS=XS+B(I1)*CS*CH
      XN=XN-B(I1)*SN*SH
      XSS=XSS-I1*B(I1)*SN*CH

```

```

XSN=XSN-I1*B(I1)*CS*SH
110 CONTINUE
XJ=1.DO/(XS*XS+XN*XN)
JA(NI)=XJ
JS1(NI)=-2.DO*XJ*(XS*XSS+XN*XSN)
JN1(NI)=-2.DO*XJ*(XS*XSN-XN*XSS)
XJ3=XJ*XJ*XJ
XA=XS*(3.DO*XN*XN-XS*XS)
XB=XN*(3.DO*XS*XS-XN*XN)
SX(NI)=XS*XJ
SY(NI)=-XN*XJ
SXS(NI)=SX(NI)*SX(NI)
SYS(NI)=SY(NI)*SY(NI)
SXX(NI)=XJ3*(XSS*XA-XSN*XB)
120 SXY(NI)=XJ3*(XSS*XB+XSN*XA)
130 CONTINUE
C** TERMS FOR MIXING LENGTH *
C** COMPUTE TANGENTIAL DISTANCES AT SURFACE
ST=0.DO
DO 135 I=1,NP1
135 ST=ST+1.DO/DSQRT(JA(I))
ST=DX*ST/(2.DO*PI)
SC=RK1/(0.6DO*RE*DSQRT(ST*ST+(RKL/RE)**2))
ET(1)=SC
ETM(1)=1.DO
DO 150 I=1,N
S=-0.5DO/DSQRT(JA(1))-0.5DO/DSQRT(JA(I+1))
DO 140 K=0,I
140 S=S+1.DO/DSQRT(JA(K+1))
S=DX*S
TEE=S-I*DX*ST
ETM(I+1)=DEXP(-TEE*RE/RKL)
150 ET(I+1)=SC/ETM(I+1)
C**
C**
C** CALCULATE Y DISTANCES FOR EDDY VISCOSITY BY GOING
C ALONG COORDINATE OF CONSTANT XI
C (DISCRETE ARC LENGTH CALCULATION)
DO 186 I=1,NP1
NN=0
SUM=0.DO
SUM1=0.DO
PSJ(I)=((I-1)/8.DO)*2.DO*PI
DO 176 J=0,NP1*MP2-NP1,NP1
NI=I+J
NN=NN+1
DO 90 K=1,14
A1=DSINH(K*(ETAT-ETA(NN)))
A2=DSINH(K*ETAT)
SUM=SUM+(B(K)/K)*DCOS(K*PSJ(I))*A1/A2
90 CONTINUE

```

```

DO 95 KK=1,14
A3=DCOSH(KK*(ETAT-ETA(NN)))
A4=DSINH(KK*ETAT)
SUM1=SUM1+(B(KK)/KK)*DSIN(KK*PSJ(I))*A3/A4
95 CONTINUE
XX=(SUM1+PSJ(I))
Y=(ETA(NN)+YO-SUM)-AMP*DCOS(XX)
IF(J.EQ.0)GOTO 170
DN(NI)=DN(NI-NP1)+RK*DSQRT((XOLD-XX)**2 + (YOLD-Y)**2)
DB(NI)=- (DN(NI)/RK)*RE/A
IF(NI.GT.NP1*MP2-NP1)THEN
DMAX=DN(NI)
END IF
170 XOLD=XX
YOLD=Y
SUM=0.DO
SUM1=0.DO
176 CONTINUE
NSQT=NP1*MP2-NP1
NSQR=((NP1*MP2-NP1)/2)
DO 172 J=NSQT,NSQR,-NP1
NI=I+J
DN(NI)=DMAX-DN(NI)
DB(NI)=- (DN(NI)/RK)*RE/A
172 CONTINUE
186 CONTINUE
RETURN
END

C**
C**
SUBROUTINE WALL (AMP,ZT,YO,PHS,B)

C**
C** COMPUTE FOURIER COEFFICIENTS OF CONFORMAL MAP
IMPLICIT REAL*8(A-H,O-Z)
IMPLICIT INTEGER*4(I-N)
DIMENSION X(15),Y(15),Z(15),B(1),A(5),F(15),IPVT(15),DJ(15,15)

C**
LDJ=15
N=14
C** PARAMETERS FOR A RIGID SINUSOIDAL WALL
WRITE(52,1001)
1001 FORMAT(' SINUSOIDAL WAVE PROFILE')
A(1)=AMP
A(2)=0.DO
A(3)=0.DO
A(4)=0.DO
A(5)=0.DO
PHS=1.DO
NP1=N+1
INDEX=0
PI=4.DO*DATAN(1.DO)
XA=PI/NP1

```

*
*

*

```

C**      INITIAL GUESS                                     *
DO 10 I=1,NP1
Z(I)=(I-1)*XA
10      B(I)=0.DO
        B(1)=-AMP
        Y0=0.DO
C**      COMPUTE RESIDUAL                                   *
20      INDEX=INDEX+1
        DO 40 I=1,NP1
        S1=0.DO
        S2=0.DO
        DO 30 J=1,N
        S1=S1+B(J)*DSIN(J*Z(I))/(J*DTANH(J*ZT))
30      S2=S2+B(J)*DCOS(J*Z(I))/J
        X(I)=S1+Z(I)
        Y(I)=Y0-S2
        S1=0.DO
        DO 35 I1=1,5
35      S1=S1+A(I1)*DCOS(I1*X(I))
40      F(I)=S1-Y(I)
        XA=0.DO
        DO 50 I=1,NP1
        XB=DABS(F(I))
50      IF(XB.GT.XA)XA=XB
        IF (XA.LT.1.D-10) GOTO 1000
        IF (XA.GT.10.DO) GOTO 5000
        IF (INDEX.GT.10) GOTO 5000
C**      COMPUTE RESIDUAL                                   *
        DO 70 I=1,NP1
        S1=0.DO
        DO 55 I1=1,5
55      S1=S1+I1*A(I1)*DSIN(I1*X(I))
        DO 60 J=1,N
60      DJ(I,J)=(DCOS(J*Z(I))-S1*DSIN(J*Z(I))/DTANH(J*ZT))/J
70      DJ(I,NP1)=-1.DO
        JOB=0
        CALL DGEFA(DJ,LDJ,NP1,IPVT,INFO)
        CALL DGESL(DJ,LDJ,NP1,IPVT,F,JOB)
        DO 80 I=1,N
80      B(I)=B(I)-F(I)
        Y0=Y0-F(NP1)
        GOTO 20
1000     CONTINUE
        RETURN
5000     WRITE(52,1002)
1002     FORMAT(' THE CONFORMAL MAPPING DID NOT CONVERGE')
        CALL EXIT
        END
C**
SUBROUTINE WHY(Y0,ZT,BZ)
C**
IMPLICIT REAL*8(A-H,O-Z)

```

```

      IMPLICIT INTEGER*4(I-N)
      COMMON/CON/N,M,NP1,NP2,N3,MP1,MP2,RE,REI,RK,A,C,PI,DX,RKL
& ,RK1,LDA,LDJ,NE,DEL,DEL2
      COMMON/SCALE/Z1(200),Z2(200),Z3(200),Z1H(200),Z2H(200),Z3H(200)
& ,ZA(200),ZB(200),Z1S(200),ETA(200)
      COMMON/KUZ/ETAT

C**
C**  COMPUTE  STRETCHING IN THE NORMAL DIRECTION
C**
C**
C**  MODIFIED TO STRETCH AT BOTH TOP AND
C**  BOTTOM WALLS
C**
      DZ=1.DO/MP1
      ETAT=ZT-YO
      C1=DATAN(BZ)
      C2=DATAN(-BZ)
      C3=BZ*ETAT
      C4=BZ**2.DO
      C5=BZ*4.DO
      C6=C1/ETAT
      C7=C6*C5
      ETA(1)=0.DO
      DO 18 J=0,MP1
      Z8=J*DZ
      A1=(1-2.DO*Z8)
      A11=DATAN(-BZ*A1)
      A2=A1**2.DO
      IF (J.EQ.0) THEN
      ETA(1)=0.DO
      GO TO 1
      END IF
      ETA(J+1)=ETAT*((A11-C2)/(2.DO*C1))
1      ETA(1)=0.DO
      Z1(J+1)=((1.DO+C4*A2)*C1)/C3
      Z2(J+1)=((C1/ETAT)*(-C5*A1))*Z1(J+1)
      Z3(J+1)=(C7*((-A1*Z2(J+1))+(2.DO*(Z1(J+1)**2.DO))))/DZ
      Z2(J+1)=Z2(J+1)/DZ
      Z1(J+1)=Z1(J+1)/DZ
18     CONTINUE
      RETURN
      END

C**
C**
      SUBROUTINE HSET(ST)

C**
C**  COMPUTES FACTORS TO TAKE DERIVATES BY FFT
C**  COMPUTES FACTORS TO SHIFT PHASE BY FFT
C**
      IMPLICIT REAL*8(A-H,O-Z)
      IMPLICIT INTEGER*4(I-N)
      REAL*8 JA,JN1,JS1

```

*
*


```

COMMON/CON/N,M,NP1,NP2,N2,N3,MP1,MP2,RE,REI,RK,A,C,PI,DX,RKL
& ,RK1,LDA,LDJ,NE,DEL,DEL2
COMMON/NEW/JA(2600),JN1(2600),JS1(2600),B(15),Y0,ZT
& ,HS(32),HSS(32),ZERO(32)
& ,DN(2600),DB(2600),SHR(32),SHI(32),ET(32),ETM(32)

C**
  PI2=2.DO*PI
  RN=1.DO/NP1
  NH=NP1/2-1
  STS=ST*ST
  RS=(RKL/RE)**2
  DO 20 I=0,NH
    HS(I+1)=RN*I
    HSS(I+1)=-I*I*RN
    SCI=DSQRT((STS+RS)/(STS+I*I*RS))
    IF (I.EQ.0) SCI=1.DO
    PHI=DATAN(I*RKL/(RE*ST))
    SHR(I+1)=RN*DCOS(PHI)*SCI
20  SHI(I+1)=-RN*DSIN(PHI)*SCI
    DO 30 I=NH+1,N
      K=I-NP1
      HS(I+1)=RN*K
      HSS(I+1)=-K*K*RN
      SCI=DSQRT((STS+RS)/(STS+K*K*RS))
      PHI=DATAN(K*RKL/(RE*ST))
      SHR(I+1)=RN*DCOS(PHI)*SCI
30  SHI(I+1)=-RN*DSIN(PHI)*SCI
    DO 40 I=1,NP1
40  ZERO(I)=0.DO
    RETURN
  END

C**
C**
SUBROUTINE FLEXBC(F)

C**
C** COMPUTES BOUNDARY CONDITIONS
IMPLICIT REAL*8(A-H,O-Z)
IMPLICIT INTEGER*4(I-N)
REAL*8 JA,JN1,JS1
COMMON/PVAR/PO,P(2600),PS(2600),PN(2600)
& ,PSS(2600),PNN(2600),PNNN(2600),UZ(2600),US(32)
COMMON/WVAR/W(2600),WS(2600),WN(2600)
COMMON/CON/N,M,NP1,NP2,N2,N3,MP1,MP2,RE,REI,RK,A,C,PI,DX,RKL
& ,RK1,LDA,LDJ,NE,DEL,DEL2
COMMON/TRANS/SX(2600),SY(2600),SXX(2600),SXY(2600)
& ,SXS(2600),SYS(2600),SXXSY(2600)
COMMON/EDVIS/T(2600),TN(2600),TNN(2600),TXX(2600),
& TYY(2600),TXY(2600),TS(2600),TSS(2600),
& TW(2600),TWSS(2600),TWNN(2600),TT(2600),
& EX(2600),AU(32),AS(32)
COMMON/NEW/JA(2600),JN1(2600),JS1(2600),B(15),Y0,ZT
& ,HS(32),HSS(32),ZERO(32)

```

*
*
*

```

& ,DN(2600),DB(2600),SHR(32),SHI(32),ET(32),ETM(32)
DIMENSION F(1)
C**
  NJ=1+NP1*MP1
C**  BOUNDARY CONDIIONS AT WALL *
  DO 20 I=0,N
  P(I+1)=0.DO
  PS(I+1)=0.DO
  PSS(I+1)=0.DO
  TT(I+1)=0.DO
  T(I+1)=REI
  TS(I+1)=0.DO
  TSS(I+1)=0.DO
  PN(I+1)=-C/SX(I+1)
  US(I+1)=-JA(I+1)*PN(I+1)*PN(I+1)/2.DO
C**  BOUNDARY CONDITIONS AT UPPER BOUNDARY *
  NI=I+NJ
  TT(NI)=0.DO
  T(NI)=REI
C**  THE UPPER B.C.'S ON TS &TSS ARE ACTUALLY SET IN SUBR EDDY
  TS(NI)=0.DO
  TSS(NI)=0.DO
C  *****
C  THE FOLLOWING IS CALCULATED IN GUESS
C
C  P(NI)=PO
C
C  *****
C  PS(NI)=0.DO
C  PSS(NI)=0.DO
C  PN(NI)=0.DO
20  CONTINUE
    CALL PF(NP1,US,ZERO,1,F(1),F(NP2),1)
    DO 30 I=1,NP1
    US(I)=-HS(I)*F(I+NP1)
30  F(I)=HS(I)*F(I)
    CALL FP(NP1,US,F,1,US,F,1)
    RETURN
  END
C**
C**
  SUBROUTINE GUESS(F)
C
C**  INITIAL GUESS FOR STREAMFUNCTION
C
  IMPLICIT REAL*8(A-H,O-Z)
  IMPLICIT INTEGER*4(I-N)
  REAL*8 JA,JN1,JS1
  COMMON/PVAR/PO,P(2600),PS(2600),PN(2600)
& ,PSS(2600),PNN(2600),PNNN(2600),UZ(2600),US(32)
  COMMON/CON/N,M,NP1,NP2,N2,N3,MP1,MP2,RE,REI,RK,A,C,PI,DX,RKL
& ,RK1,LDA,LDJ,NE,DEL,DEL2

```

```

COMMON/SCALE/Z1(200),Z2(200),Z3(200),Z1H(200),Z2H(200),Z3H(200)
& ,ZA(200),ZB(200),Z1S(200),ETA(200)
COMMON/EDVIS/T(2600),TN(2600),TNN(2600),TX(2600),
&          TYY(2600),TXY(2600),TS(2600),TSS(2600),
&          TW(2600),TWSS(2600),TWNN(2600),TT(2600),
&          EX(2600),AU(32),AS(32)
COMMON/NEW/JA(2600),JN1(2600),JS1(2600),B(15),YO,ZT
& ,HS(32),HSS(32),ZERO(32)
& ,DN(2600),DB(2600),SHR(32),SHI(32),ET(32),ETM(32)
COMMON/TRANS/SX(2600),SY(2600),SXX(2600),SXY(2600)
& ,SXS(2600),SYS(2600),SXSX(2600)
COMMON/MIXL/RL(100)
DIMENSION F(1),PSI(200),TTINIT(200)

C
  PN(1)=-C/SX(1)
C.....USE THE SAME STREAMFUNCTION
C  AT ALL X POSITIONS
  READ(40,*)(PSI(J),J=1,MP2)
C  (INITIAL GUESS FOR STREAMFUNCTION MUST BE INPUT.
C  OBTAIN INITIAL GUESS BY RUNNING FLAT CHANNEL
C  PROGRAM.)
  DO 70 J=1,MP2
    NJ=1+NP1*(J-1)
    DO 60 I=0,N
      TT(I+NJ)=TTINIT(J)
60    P(I+NJ)=PSI(J)
70    CONTINUE
C.....STREAMFUNCTION AT UPPER BOUNDARY (MASS FLOWRATE)
  PO=P(1+NP1*MP1)
80  CONTINUE
  RETURN
  END

C**
C**
SUBROUTINE PPRIME(F)

C**
C**  COMPUTE STREAMFUNCTION DERIVATIVES
IMPLICIT REAL*8(A-H,O-Z)
IMPLICIT INTEGER*4(I-N)
REAL*8 JA,JN1,JS1
COMMON/PVAR/PO,P(2600),PS(2600),PN(2600)
& ,PSS(2600),PNN(2600),PNNN(2600),UZ(2600),US(32)
COMMON/CON/N,M,NP1,NP2,N2,N3,MP1,MP2,RE,REI,RK,A,C,PI,DX,RKL
& ,RK1,LDA,LDJ,NE,DEL,DEL2
COMMON/SCALE/Z1(200),Z2(200),Z3(200),Z1H(200),Z2H(200),Z3H(200)
& ,ZA(200),ZB(200),Z1S(200),ETA(200)
COMMON/NEW/JA(2600),JN1(2600),JS1(2600),B(15),YO,ZT
& ,HS(32),HSS(32),ZERO(32)
& ,DN(2600),DB(2600),SHR(32),SHI(32),ET(32),ETM(32)
DIMENSION F(1)
C**  COMPUTE TANGENTIAL (S) DERIVATIVES
  NJ=1

```

```

DO 20 J=1,M
NJ=NJ+NP1
CALL PF(NP1,P(NJ),ZERO,1,F(1),F(NP2),1)
DO 10 I=0,N
NI=I+NJ
PS(NI)=-HS(I+1)*F(I+NP2)
F(I+N2)=HS(I+1)*F(I+1)
PSS(NI)=HSS(I+1)*F(I+1)
10 F(I+NP2)=HSS(I+1)*F(I+NP2)
CALL FP(NP1,PS(NJ),F(N2),1,PS(NJ),F(N2),1)
CALL FP(NP1,PSS(NJ),F(NP2),1,PSS(NJ),F(NP2),1)
20 CONTINUE
C** COMPUTE NORMAL (N) DERIVATIVES AT INTERIOR POINTS *
NJ=1
DO 40 J=1,M
J1=J+1
NJ=NJ+NP1
DO 30 I=0,N
NI=I+NJ
NP=NI+NP1
NPP=NI+NP1+NP1
NM=NI-NP1
NMM=NI-NP1-NP1
PZ=P(NP)-P(NM)
PZZ=P(NP)-P(NI)-P(NI)+P(NM)
IF (NMM.LE.0) GO TO 21
PZZZ=P(NPP)-P(NP)-P(NP)+P(NM)+P(NM)-P(NMM)
PNNN(NI)=ZA(J1)*PZZZ+ZB(J1)*PZZ+Z3H(J1)*PZ
21 CONTINUE
PN(NI)=Z1H(J1)*PZ
PNN(NI)=Z1S(J1)*PZZ+Z2H(J1)*PZ
UN=JA(NI)*(PNN(NI)+JN1(NI)*PN(NI)-PSS(NI)-JS1(NI)*PS(NI))
UZ(NI)=DABS(UN)
30 CONTINUE
40 CONTINUE
C** COMPUTES Y DERIVATIVES AT Z=0,H *
DO 50 I=0,N
I1=I+1
PB=P(I1+NP1)-PN(I1)/Z1H(1)
PNN(I1)=Z1S(1)*(P(I1+NP1)+PB)+Z2H(1)*(P(I1+NP1)-PB)
UN=JA(I1)*(PNN(I1)+JN1(I1)*PN(I1))
UZ(I1)=DABS(UN)
NI=I1+NP1
NM=I1
NP=NI+NP1
NPP=NI+NP1+NP1
PZ=P(NP)-P(NM)
PZZ=P(NP)-P(NI)-P(NI)+P(NM)
PZZZ=P(NPP)-P(NP)-P(NP)+P(NM)+P(NM)-PB
PNNN(NI)=ZA(2)*PZZZ+ZB(2)*PZZ+Z3H(2)*PZ
50 CONTINUE
RETURN

```

```

END
C**
C**
SUBROUTINE XYDER
C**
C** COMPUTE CARTESIAN DERIVATIVES OF STREAMFUNCTION
IMPLICIT REAL*8(A-H,O-Z)
IMPLICIT INTEGER*4(I-N)
COMMON/PVAR/PO,P(2600),PS(2600),PN(2600)
& ,PSS(2600),PNN(2600),PNNN(2600),UZ(2600),US(32)
COMMON/XYD/PXX(2600),PYY(2600),PXY(2600)
COMMON/CON/N,M,NP1,NP2,N2,N3,MP1,MP2,RE,REI,RK,A,C,PI,DX,RKL
& ,RK1,LDA,LDJ,NE,DEL,DEL2
COMMON/SCALE/Z1(200),Z2(200),Z3(200),Z1H(200),Z2H(200),Z3H(200)
& ,ZA(200),ZB(200),Z1S(200),ETA(200)
COMMON/TRANS/SX(2600),SY(2600),SXX(2600),SXY(2600)
& ,SXS(2600),SYS(2600),SXSX(2600)
COMMON/TEST1/INDEX1
C**
DO 20 J=1,M
NJ=1+NP1*J
J1=J+1
DO 10 I=0,N
NI=I+NJ
PSN=Z1H(J1)*(PS(NI+NP1)-PS(NI-NP1))
X1=(SXSX(NI)+SXSX(NI))*PSN-SXX(NI)*PS(NI)+SXY(NI)*PN(NI)
PXX(NI)=PSS(NI)*SXS(NI)+PNN(NI)*SYS(NI)-X1
PYY(NI)=PSS(NI)*SYS(NI)+PNN(NI)*SXS(NI)+X1
PXY(NI)=SXSX(NI)*(PSS(NI)-PNN(NI))+(SXS(NI)-SYS(NI))*PSN
& +PS(NI)*SXY(NI)+PN(NI)*SXX(NI)
10 CONTINUE
20 CONTINUE
RETURN
END
C**
C**
SUBROUTINE VORT
C**
C** COMPUTE VORTICITY
IMPLICIT REAL*8(A-H,O-Z)
IMPLICIT INTEGER*4(I-N)
REAL*8 JA,JN1,JS1
COMMON/PVAR/PO,P(2600),PS(2600),PN(2600)
& ,PSS(2600),PNN(2600),PNNN(2600),UZ(2600),US(32)
COMMON/WVAR/W(2600),WS(2600),WN(2600)
COMMON/CON/N,M,NP1,NP2,N2,N3,MP1,MP2,RE,REI,RK,A,C,PI,DX,RKL
& ,RK1,LDA,LDJ,NE,DEL,DEL2
COMMON/NEW/JA(2600),JN1(2600),JS1(2600),B(15),Y0,ZT
& ,HS(32),HSS(32),ZERO(32)
& ,DN(2600),DB(2600),SHR(32),SHI(32),ET(32),ETM(32)
C**
NJ=-N

```

```

DO 20 J=0,M
NJ=NJ+NP1
DO 10 I=0,N
NI=I+NJ
10 W(NI)=-JA(NI)*(PSS(NI)+PNN(NI))
20 CONTINUE
RETURN
END

C**
C**
SUBROUTINE WPRIME(F)

C**
C** COMPUTE DERIVATIVES OF THE VORTICITY
IMPLICIT REAL*8(A-H,O-Z)
IMPLICIT INTEGER*4(I-N)
REAL*8 JA,JN1,JS1
COMMON/PVAR/PO,P(2600),PS(2600),PN(2600)
& ,PSS(2600),PNN(2600),PNNN(2600),UZ(2600),US(32)
COMMON/WVAR/W(2600),WS(2600),WN(2600)
COMMON/CON/N,M,NP1,NP2,N2,N3,MP1,MP2,RE,REI,RK,A,C,PI,DX,RKL
& ,RK1,LDA,LDJ,NE,DEL,DEL2
COMMON/SCALE/Z1(200),Z2(200),Z3(200),Z1H(200),Z2H(200),Z3H(200)
& ,ZA(200),ZB(200),Z1S(200),ETA(200)
COMMON/NEW/JA(2600),JN1(2600),JS1(2600),B(15),Y0,ZT
& ,HS(32),HSS(32),ZERO(32)
& ,DN(2600),DB(2600),SHR(32),SHI(32),ET(32),ETM(32)
DIMENSION F(1)

C**
C** COMPUTE TANGENTIAL DERIVATIVES
DO 25 J=0,M
NJ=1+NP1*J
CALL PF(NP1,W(NJ),ZERO,1,F(1),F(NP2),1)
DO 10 I=0,N
NI=I+NJ
WS(NI)=-HS(I+1)*F(I+NP2)
F(I+1)=HS(I+1)*F(I+1)
C** COMPUTE NORMAL DERIVATIVES
IF (NI.LE.8) GO TO 10
WN(NI)=(Z1H(J+1)*(PSS(NI-NP1)-PSS(NI+NP1))-PNNN(NI))*JA(NI)
& +JN1(NI)*W(NI)
10 CONTINUE
CALL FP(NP1,WS(NJ),F(1),1,WS(NJ),F(1),1)
25 CONTINUE
RETURN
END

C**
C**
SUBROUTINE MIX(F)

C**
C** COMPUTE EDDY VISCOSITY BY NEWTONS METHOD
C** VAN-DRIEST CORRECTION:
C** WALL VALUES FOR PRESSURE...LAG EQUATION FOR PRESSURE

```

```

C** LOCAL VALUES FOR SHEAR STRESS
C**
      IMPLICIT REAL*8(A-H,O-Z)
      IMPLICIT INTEGER*4(I-N)
      REAL*8 JA,JN1,JS1
      COMMON/PVAR/PO,P(2600),PS(2600),PN(2600)
& ,PSS(2600),PNN(2600),PNNN(2600),UZ(2600),US(32)
      COMMON/WVAR/W(2600),WS(2600),WN(2600)
      COMMON/CON/N,M,NP1,NP2,N2,N3,MP1,MP2,RE,REI,RK,A,C,PI,DX,RKL
& ,RK1,LDA,LDJ,NE,DEL,DEL2
      COMMON/SCALE/Z1(200),Z2(200),Z3(200),Z1H(200),Z2H(200),Z3H(200)
& ,ZA(200),ZB(200),Z1S(200),ETA(200)
      COMMON/AMAT/ABD(32,32),IPVT(32)
      COMMON/EDVIS/T(2600),TN(2600),TNN(2600),TXX(2600),
& ,TYY(2600),TXY(2600),TS(2600),TSS(2600),
& ,TW(2600),TWSS(2600),TWN(2600),TT(2600),
& ,EX(2600),AU(32),AS(32)
      COMMON/NEW/JA(2600),JN1(2600),JS1(2600),B(15),YO,ZT
& ,HS(32),HSS(32),ZERO(32)
& ,DN(2600),DB(2600),SHR(32),SHI(32),ET(32),ETM(32)
      COMMON/BUM/NDUK
      COMMON/NFRED/NC
      COMMON/MIXL/RL(100)
      DIMENSION F(1),RES(32),QT(2600)

C** INDEX=0
C** COMPUTE TWNN FROM MOMENTUM EQN AT Z=0
      DO 10 I=0,N
        I1=I+1
10      TW(I1)=T(I1)*W(I1)
        CALL PF(NP1,TW,ZERO,1,F(1),F(NP2),1)
        DO 20 I=1,NP1
          TWSS(I)=HSS(I)*F(I)
20      F(I)=HSS(I)*F(I+NP1)
        CALL FP(NP1,TWSS,F,1,TWSS,F,1)
        DO 30 I=1,NP1
          TWNN(I)=WS(I)*PN(I)-TWSS(I)
30      TWNN(I)=WS(I)*PN(I)-TWSS(I)
C** START OF ITERATION FOR MIXING LENGTH
40      INDEX=INDEX+1
        NJ=NP2
        DO 50 I=0,N
          NI=I+NJ
          TT(NI)=RL(NI)*RL(NI)*UZ(NI)
          T(NI)=TT(NI)+REI
50      TW(NI)=T(NI)*W(NI)
C** COMPUTE UNSHIFTED PRESSURE TERM
      XA=0.DO
      DO 70 I=0,N
        I1=I+1
        TM=(TWN(I1)+2.DO*Z1S(1)*TW(I1)-(Z1S(1)+Z2H(1))*TW(I1+NP1))
& /(Z1S(1)-Z2H(1))
        TN(I1)=Z1H(1)*(TW(I1+NP1)-TM)

```



```

70    AU(I1)=ET(I1)*(US(I1)-TN(I1))
C**  SHIFT THE PRESSURE BY FFT
      CALL PF(NP1,AU,ZERO,1,F(1),F(NP2),1)
      DO 80 I=0,N
        I1=I+1
        AS(I1)=SHR(I1)*F(I1)-SHI(I1)*F(I+NP2)
80    F(I1)=SHR(I1)*F(I+NP2)+SHI(I1)*F(I1)
      CALL FP(NP1,AS,F,1,AS,F,1)
C**  COMPUTE MODIFIED VAN-DRIEST FACTOR
      DO 81 I=1,NP1
        PR=ETM(I)*AS(I)
81    AS(I)=1.DO+0.6DO*DTANH(PR)
C**  COMPUTE THE RESIDUAL
      DO 90 I=0,N
        NI=I+NJ
C**  COMMENT THE FOLLOWING LINE FOR MODEL D*
C    AS(I+1)=1.0
      EX(NI)=DB(NI)*DSQRT(T(NI)*UZ(NI))/AS(I+1)
C    EX(NI)=DB(NI)
C**  CONSTANT BOUNDARY LAYER THICKNESS EQUAL TO THE HALF
C    HEIGHT OF A FLAT CHANNEL WITH THE SAME AVERAGE
C    CROSS SECTION
      DELTA=ZT/2.DO
      RES(NI-NP1)=RL(NI)-DN(NI)*(1.DO-DEXP(EX(NI)))
      XB=DABS(RES(NI-NP1))
90    IF (XA.LT.XB) XA=XB
      JF (XA.LT.1.D-11) GOTO 120
      IF (INDEX.GT.100) GOTO 500
      IF (XA.GT.1.D3) GOTO 500
C**  COMPUTE THE JACOBIAN AND SOLVE
      CALL AJAC(F)
      JOB=0
      CALL DGEFA(ABD,LDA,NP1,IPVT,INFO)
      CALL DGESL(ABD,LDA,NP1,IPVT,RES,JOB)
      DO 110 I=1,NP1
110   RL(I+NP1)=RL(I+NP1)-RES(I)
      GOTO 40
C**  END OF NEWTON ITERATION AT Z=0
120  CONTINUE
      INDEX=0
C**  START OF NEWTON FOR EDDY VISCOSITY AT INTERIOR POINTS
200  INDEX=INDEX+1
      XA=0.DO
      DO 220 J=2,M
        NJ=1+NP1*J
        DO 210 I=0,N
          NI=I+NJ
          T(NI)=TT(NI)+REI
C**  COMMENT THE FOLLOWING LINE FOR MODEL D*,
C**  UNCOMMENT THE LINE FOR MODEL C*
C    AS(I+1)=1.0
      EX(NI)=DB(NI)*DSQRT(T(NI)*UZ(NI))/AS(I+1)

```



```

IF(J.EQ.MP1/2)EX(NI)=-1000.DO
IF(J.GT.MP1/2)EX(NI)=DB(NI)
A1=(2.0*RK*RE*(DN(NI)/RK)/3.0)**2
A2=(1.0-0.5*DN(NI)/(RK*DELTA))**2
A3=(3.0-4.0*DN(NI)/(RK*DELTA)+2.0*(DN(NI)/(RK*DELTA))**2)**2
A4=(1.0-EXP(EX(NI)))**2
QT(NI)=0.5*(1.0/RE)*SQRT(1.0+A1*A2*A3*A4)-0.5*(1.0/RE)
F(NI)=TT(NI)-QT(NI)
XB=DABS(F(NI))
210 IF (XA.LT.XB) XA=XB
220 CONTINUE
IF (XA.LT.1.D-11) GOTO 300
IF (XA.GT.1.D3) GOTO 500
IF (INDEX.GT.100) GOTO 500
DO 240 J=2,M
NJ=1+NP1*J
DO 230 I=0,N
NI=I+NJ
Y=DN(NI)/RK
YH=Y/DELTA
C** COMMENT THE FOLLOWING LINE FOR MODEL D*,
C** UNCOMMENT THE LINE FOR MODEL C*
C AS(I+1)=1.0
Z=-(RE*Y/A)*DSQRT(T(NI)*UZ(NI))/AS(I+1)
IF(J.EQ.MP1/2)Z=-1000.DO
ZP=(RE*Y*UZ(NI)/(2.DO*A))/AS(I+1)
ZP=-ZP*(1.DO/DSQRT(T(NI)*UZ(NI)))
ZZ=(1.DO/(2.DO*RE))**2
ZZZ=(3.DO-4.DO*YH+2.DO*YH**2)**2
ZZZ=ZZZ*(1.DO-0.5DO*YH)**2
ZZZ=ZZZ*(2.DO*K*RE*Y/3.DO)**2
ZZZ=ZZZ*ZZ
DF=2.DO*ZZZ*(1.DO-DEXP(Z))*(-ZP*DEXP(Z))
DF=DF*(1.DO/DSQRT(ZZ+ZZZ*(1.DO-DEXP(Z))**2))
DF=1.DO-0.5DO*DF
IF(J.GT.MP1/2)DF=1.DO
TT(NI)=TT(NI)-F(NI)/DF
230 CONTINUE
240 CONTINUE
GOTO 200
C** END OF NEWTON AT INTERIOR POINTS
C** COMPUTE OTHER VARIABLES AT THE UPPER BOUNDARY
300 NJ=1+NP1*MP1
DO 305 I=0,N
NI=I+NJ
IF (NDUK.GT.0) THEN
JP=NC+2*NP1
PNN(JP)=2.DO*Z1S(MP2)*(P(JP-NP1)-P(JP))
W(JP)=-JA(JP)*PNN(JP)
GO TO 597
END IF
PNN(NI)=-RE/JA(NI)

```

```

      W(NI)=RE
C**  Y DERIVATIVE AT Z=1,1-H
597  PT=(PMN(NI)+2.DO*Z1S(MP2)*P(NI)-(Z1S(MP2)-Z2H(MP2))*P(NI-NP1))
      & /(Z1S(MP2)+Z2H(MP2))
      NI=NI-NP1
      NP=NI+NP1
      NM=NI-NP1
      NMM=NI-NP1-NP1
      PZ=P(NP)-P(NM)
      PZZ=P(NP)-P(NI)-P(NI)+P(NM)
      PZZZ=PT-P(NP)-P(NP)+P(NM)+P(NM)-P(NMM)
      PNNN(NI)=ZA(MP1)*PZZZ+ZB(MP1)*PZZ+Z3H(MP1)*PZ
305  WN(NI)=(Z1H(MP1)*(PSS(NI-NP1)-PSS(NI+NP1))-PNNN(NI))*JA(NI)
      & +JN1(NI)*W(NI)
      RETURN
500  WRITE(52,1001)
1001  FORMAT(' BOMBED OUT COMPUTING EDDY VISCOSITY')
      CALL EXIT
      END
C**

```

*

C**

SUBROUTINE AJAC(F)

C**

C**

FINITE DIFFERENCE JACOBIAN FOR MIXING LENGTH COMPUTATION

IMPLICIT REAL*8(A-H,O-Z)

IMPLICIT INTEGER*4(I-N)

REAL*8 JA,JN1,JS1

COMMON/PVAR/PO,P(2600),PS(2600),PN(2600)

& ,PSS(2600),PNN(2600),PNNN(2600),UZ(2600),US(32)

COMMON/WVAR/W(2600),WS(2600),WN(2600)

COMMON/CON/N,M,NP1,NP2,N2,N3,MP1,MP2,RE,REI,RK,A,C,PI,DX,RKL

& ,RK1,LDA,LDJ,NE,DEL,DEL2

COMMON/AMAT/ABD(32,32),IPVT(32)

COMMON/EDVIS/T(2600),TN(2600),TNN(2600),TXX(2600),

& TYY(2600),TXY(2600),TS(2600),TSS(2600),

& TW(2600),TWSS(2600),TWN(2600),TT(2600),

& EX(2600),AU(32),AS(32)

COMMON/NEW/JA(2600),JN1(2600),JS1(2600),B(15),YO,ZT

& ,HS(32),HSS(32),ZERO(32)

& ,DN(2600),DB(2600),SHR(32),SHI(32),ET(32),ETM(32)

COMMON/MIXL/RL(100)

DIMENSION ASP(32),ASM(32),F(1)

C**

NJ=NP2

DO 30 I=0,N

NIO=I+NJ

RLO=RL(NIO)

RL(NIO)=RLO+DEL

T(NIO)=RL(NIO)*RL(NIO)*UZ(NIO)+REI

TW(NIO)=T(NIO)*W(NIO)

CALL ASTAR(I,ASP,F)

RL(NIO)=RLO-DEL

```

T(NIO)=RL(NIO)*RL(NIO)*UZ(NIO)+REI
TW(NIO)=T(NIO)*W(NIO)
CALL ASTAR(I,ASM,F)
RL(NIO)=RLO
T(NIO)=RL(NIO)*RL(NIO)*UZ(NIO)+REI
TW(NIO)=T(NIO)*W(NIO)
DO 10 I1=0,N
NI=I1+NJ
DA=(ASP(I1+1)-ASM(I1+1))/DEL2
ABD(NI-NP1,NIO-NP1)=-DN(NI)*DEXP(EX(NI))*EX(NI)*DA/AS(I1+1)
10 CONTINUE
ABD(NIO-NP1,NIO-NP1)=1.DO+DN(NIO)*EX(NIO)*DEXP(EX(NIO))*RL(NIO)
& *UZ(NIO)/T(NIO)+ABD(NIO-NP1,NIO-NP1)
30 CONTINUE
RETURN
END

C**
C**
SUBROUTINE ASTAR(I,ASN,F)

C**
C** COMPUTE NEW PRESSURE CORRECTION FOR MIXING LENGTH JACOBIAN
IMPLICIT REAL*8(A-H,O-Z)
IMPLICIT INTEGER*4(I-N)
REAL*8 JA,JN1,JS1
COMMON/PVAR/PO,P(2600),PS(2600),PN(2600)
& ,PSS(2600),PNN(2600),PNNN(2600),UZ(2600),US(32)
COMMON/CON/N,M,NP1,NP2,N2,N3,MP1,MP2,RE,REI,RK,A,C,PI,DX,RKL
& ,RK1,LDA,LDJ,NE,DEL,DEL2
COMMON/SCALE/Z1(200),Z2(200),Z3(200),Z1H(200),Z2H(200),Z3H(200)
& ,ZA(200),ZB(200),Z1S(200),ETA(200)
COMMON/EDVIS/T(2600),TN(2600),TNN(2600),TXX(2600),
& TYY(2600),TXY(2600),TS(2600),TSS(2600),
& TW(2600),TWSS(2600),TWN(2600),TT(2600),
& EX(2600),AU(32),AS(32)
COMMON/NEW/JA(2600),JN1(2600),JS1(2600),B(15),Y0,ZT
& ,HS(32),HSS(32),ZERO(32)
& ,DN(2600),DB(2600),SHR(32),SHI(32),ET(32),ETM(32)
DIMENSION ASN(1),F(1),AUN(32)

C**
DO 10 I1=1,NP1
10 AUN(I1)=AU(I1)
TM=(TWN(I1)+2.DO*Z1S(1)*TW(I1)-(Z1S(1)+Z2H(1))*TW(I1+NP2))
& /(Z1S(1)-Z2H(1))
TN(I1)=Z1H(1)*(TW(I1+NP2)-TM)
AUN(I1)=ET(I1)*(US(I1)-TN(I1))
CALL PF(NP1,AUN,ZERO,1,F(1),F(NP2),1)
DO 20 I1=1,NP1
ASN(I1)=SHR(I1)*F(I1)-SHI(I1)*F(I1+NP1)
20 F(I1)=SHR(I1)*F(I1+NP1)+SHI(I1)*F(I1)
CALL FP(NP1,ASN,F,1,ASN,F,1)
DO 30 I1=1,NP1
PR=ETM(I1)*ASN(I1)

```

```

30   ASN(I1)=1.DO+0.6DO*DTANH(PR)
      RETURN
      END
C**
C**
      SUBROUTINE EDDY(F)
C**
C**   COMPUTE DERIATIVES OF EDDY VISCOSITY *
      IMPLICIT REAL*8(A-H,O-Z)
      IMPLICIT INTEGER*4(I-N)
      REAL*8 JA,JN1,JS1
      COMMON/PVAR/PO,P(2600),PS(2600),PN(2600)
& ,PSS(2600),PNN(2600),PNNN(2600),UZ(2600),US(32)
      COMMON/WVAR/W(2600),WS(2600),WN(2600)
      COMMON/CON/N,M,NP1,NP2,N2,N3,MP1,MP2,RE,REI,RK,A,C,PI,DX,RKL
& ,RK1,LDA,LDJ,NE,DEL,DEL2
      COMMON/SCALE/Z1(200),Z2(200),Z3(200),Z1H(200),Z2H(200),Z3H(200)
& ,ZA(200),ZB(200),Z1S(200),ETA(200)
      COMMON/TRANS/SX(2600),SY(2600),SXX(2600),SXY(2600)
& ,SXS(2600),SYS(2600),SXSX(2600)
      COMMON/EDVIS/T(2600),TN(2600),TMN(2600),TXX(2600),
& ,TYY(2600),TXY(2600),TS(2600),TSS(2600),
& ,TW(2600),TWSS(2600),TWN(2600),TT(2600),
& ,EX(2600),AU(32),AS(32)
      COMMON/NEW/JA(2600),JN1(2600),JS1(2600),B(15),YO,ZT
& ,HS(32),HSS(32),ZERO(32)
& ,DN(2600),DB(2600),SHR(32),SHI(32),ET(32),ETM(32)
      DIMENSION F(1)
C**
C**   COMPUTE TW AT INTERIOR POINTS
      DO 10 J=2,MP1
      NJ=1+NP1*J
      DO 10 I=0,N
      NI=I+NJ
10    TW(NI)=T(NI)*W(NI)
C**   COMPUTE TANGENTIAL (S) DERIVATIVES OF T AND TW *
      NJ=1
      DO 80 J=1,MP1
      NJ=NJ+NP1
      CALL PF(NP1,T(NJ),ZERO,1,F(1),F(NP2),1)
      CALL PF(NP1,TW(NJ),ZERO,1,F(N2),F(N3),1)
      DO 70 I=0,N
      NI=I+NJ
      XA=F(I+NP2)
      TS(NI)=-HS(I+1)*F(I+NP2)
      IF(NJ.EQ.1+NP1*MP1)TS(NI)=0.DO
      F(I+NP2)=HS(I+1)*F(I+1)
      TSS(NI)=HSS(I+1)*F(I+1)
      IF(NJ.EQ.1+NP1*MP1)TSS(NI)=0.DO
      F(I+1)=HSS(I+1)*XA
      TWSS(NI)=HSS(I+1)*F(I+N2)
70    F(I+N2)=HSS(I+1)*F(I+N3)

```

```

      CALL FP(NP1,TS(NJ),F(NP2),1,TS(NJ),F(NP2),1)
      CALL FP(NP1,TSS(NJ),F(1),1,TSS(NJ),F(1),1)
      CALL FP(NP1,TWSS(NJ),F(N2),1,TWSS(NJ),F(N2),1)
80    CONTINUE
C**  COMPUTE NORMAL (N) DERIVATIVES OF T AND TW          *
      NJ=1
      DO 100 J=1,M
      NJ=NJ+NP1
      J1=J+1
      DO 90 I=0,N
      NI=I+NJ
      TN(NI)=Z1H(J1)*(T(NI+NP1)-T(NI-NP1))
      TNN(NI)=Z1S(J1)*(T(NI+NP1)-T(NI)-T(NI)+T(NI-NP1))
& +Z2H(J1)*(T(NI+NP1)-T(NI-NP1))
      CZ=TW(NI+NP1)-TW(NI-NP1)
      CZZ=TW(NI+NP1)-TW(NI)-TW(NI)+TW(NI-NP1)
      TWNN(NI)=Z1S(J1)*CZZ+Z2H(J1)*CZ
C**  COMPUTE CARTESIAN DERIVATIVES OF EDDY VISCOSITY      *
      TYX=Z1H(J1)*(TS(NI+NP1)-TS(NI-NP1))
      X1=(SXXSY(NI)+SXXSY(NI))*TYX-SXX(NI)*TS(NI)+SXY(NI)*TN(NI)
      TXX(NI)=TSS(NI)*SXS(NI)+TNN(NI)*SYS(NI)-X1
      TYY(NI)=TSS(NI)*SYS(NI)+TNN(NI)*SXS(NI)+X1
90    TXY(NI)=SXXSY(NI)*(TSS(NI)-TNN(NI))+(SXS(NI)-SYS(NI))*TYX
& +TS(NI)*SXY(NI)+TN(NI)*SXX(NI)
100   CONTINUE
      RETURN
      END
C**  ...  *

```

```

C**                                     *
SUBROUTINE RES(F)
C**                                     *
C** COMPUTE THE RESIDUAL AT INTERIOR POINTS
IMPLICIT REAL*8(A-H,O-Z)
IMPLICIT INTEGER*4(I-N)
REAL*8 JA,JN1,JS1
COMMON/PVAR/PO,P(2600),PS(2600),PN(2600)
& ,PSS(2600),PNN(2600),PNNN(2600),UZ(2600),US(32)
COMMON/XYD/PXX(2600),PYY(2600),PXY(2600)
COMMON/WVAR/W(2600),WS(2600),WN(2600)
COMMON/CON/N,M,NP1,NP2,N2,N3,MP1,MP2,RE,REI,RK,A,C,PI,DX,RKL
& ,RK1,LDA,LDJ,NE,DEL,DEL2
COMMON/EDVIS/T(2600),TN(2600),TNN(2600),TXX(2600),
& TYY(2600),TXY(2600),TS(2600),TSS(2600),
& TW(2600),TWSS(2600),TWN(2600),TT(2600),
& EX(2600),AU(32),AS(32)
COMMON/NEW/JA(2600),JN1(2600),JS1(2600),B(15),YO,ZT
& ,HS(32),HSS(32),ZERO(32)
& ,DN(2600),DB(2600),SHR(32),SHI(32),ET(32),ETM(32)
COMMON/NFRED/NC
DIMENSION F(1)
C**
NJ=1

```

```

DO 20 J=1,M
NJ=NJ+NP1
DO 10 I=0,N
NI=I+NJ
F(NI-NP1)=WS(NI)*PN(NI)-WN(NI)*PS(NI)-TWSS(NI)-TWNN(NI)
& -2.DO*(PXX(NI)*TYY(NI)-2.DO*PXY(NI)*TXY(NI)
& +PYY(NI)*TXX(NI))/JA(NI)
10 CONTINUE
20 CONTINUE
RETURN
END

C**
SUBROUTINE FDJAC(FP,FM)
C**
C** FINITE DIFFERENCE JACOBIAN: **
IMPLICIT REAL*8(A-H,O-Z)
IMPLICIT INTEGER*4(I-N)
COMMON/PVAR/PO,P(2600),PS(2600),PN(2600)
& ,PSS(2600),PNN(2600),PNNN(2600),UZ(2600),US(32)
COMMON/CON/N,M,NP1,NP2,N2,N3,MP1,MP2,RE,REI,RK,A,C,PI,DX,RKL
& ,RK1,LDA,LDJ,NE,DEL,DEL2
COMMON/MAT/DJ(300000),ICI(300000),IRP(3000),MAXA
COMMON/TEST1/INDEX1
COMMON/NFRED/NC
DIMENSION FP(1),FM(1)
C** CENTERED DIFFERENCES AT INTERIOR POINTS
C FDJAC FILLS THE MATRIX COLUMN WISE
C THE FOLLOWING PARAMETERS ARE USED BY TRANPR AND MATRIX
C MAXA IS THE TOTAL NUMBER OF NON-ZERO ENTRIES
C L IS THE POSITION NUMBER; L(MAX)=MAXA
C IRP POINTS TO THE BEGINNING OF EACH NEW COLUMN
C ICI IS THE POSITION VECTOR
C DJ IS THE MATRIX ELEMENT
C ON EXIT FROM TRANPR, THE ELEMENTS ARE ROW ORIENTED
MAXA=0
L=0
IRP(1)=1
DO 300 J=1,M
NJO=1+NP1*J
DO 200 I=0,N
NIO=I+NJO
NC=NIO-NP1
POLD=P(NIO)
P(NIO)=POLD+DEL
CALL STARDER(J,FP)
P(NIO)=POLD-DEL
CALL STARDER(J,FM)
P(NIO)=POLD
DO 130 I1=1,NE
Q=(FP(I1)-FM(I1))/DEL2
IF (Q.NE.0.DO) THEN
L=L+1

```



```
MAXA=MAXA+1
DJ(L)=Q
ICI(L)=I1
END IF
130 CONTINUE
WRITE(58,*) MAXA
IRP(NC+1)=L+1
200 CONTINUE
300 CONTINUE
WRITE(52,*)MAXA
CLOSE(58)
RETURN
END
```

C**

*

```

C**                                     *
SUBROUTINE STARDER(J,F)
C**
COMMON/CON/N,M,NP1,NP2,N2,N3,MP1,MP2,RE,REI,RK,A,C,PI,DX,RKL
& ,RK1,LDA,LDJ,NE,DEL,DEL2
COMMON/NFRED/NC
COMMON/BUM/NDUK
DIMENSION F(1)
C**
IF(NC.GE.NP1*M-N)NDUK=10
CALL PPRIME(F)
CALL XYDER
CALL VORT
CALL WPRIME(F)
CALL MIX(F)
CALL EDDY(F)
CALL RES(F)
NDUK=0
RETURN
END
C**
C**
SUBROUTINE PRESSURE(F)
C**
C** OUTPUT: NORMAL AND TANGENTIAL STRESSES, DRAG COEFFICIENTS, ETC. *
IMPLICIT REAL*8(A-H,O-Z)
IMPLICIT INTEGER*4(I-N)
REAL*8 JA,JN1,JS1
COMMON/PVAR/PO,P(2600),PS(2600),PN(2600)
& ,PSS(2600),PNN(2600),PNNN(2600),UZ(2600),US(32)
COMMON/XYD/PXX(2600),PYY(2600),PXY(2600)
COMMON/WVAR/W(2600),WS(2600),WN(2600)
COMMON/CON/N,M,NP1,NP2,N2,N3,MP1,MP2,RE,REI,RK,A,C,PI,DX,RKL
& ,RK1,LDA,LDJ,NE,DEL,DEL2
COMMON/SCALE/Z1(200),Z2(200),Z3(200),Z1H(200),Z2H(200),Z3H(200)
& ,ZA(200),ZB(200),Z1S(200),ETA(200)
COMMON/TRANS/SX(2600),SY(2600),SXX(2600),SXY(2600)
& ,SXS(2600),SYS(2600),SXSX(2600)

```

```

COMMON/EDVIS/T(2600),TN(2600),TNN(2600),TXX(2600),
&          TYY(2600),TXY(2600),TS(2600),TSS(2600),
&          TW(2600),TWSS(2600),TWNN(2600),TT(2600),
&          EX(2600),AU(32),AS(32)
COMMON/NEW/JA(2600),JN1(2600),JS1(2600),B(15),Y0,ZT
& ,HS(32),HSS(32),ZERO(32)
& ,DN(2600),DB(2600),SHR(32),SHI(32),ET(32),ETM(32)
COMMON/FRED/RH
COMMON/KUZ/ETAT
DIMENSION X(200),Y(200),PR(200),SIG(200),STR(200),F(1),PSJ(20)

C
C** COMPUTE PHYSICAL COORDINATES OF WAVY SURFACE
DO 110 I=0,NP1
  I1=I+1
  PSI=I*DX
  X(I1)=PSI
  Y(I1)=Y0
  DO 100 K=1,14
    X(I1)=X(I1)+B(K)*DSIN(K*PSI)/(K*DTANH(K*ETAT))
100  Y(I1)=Y(I1)-B(K)*DCOS(K*PSI)/K
110  X(I1)=X(I1)/(2.DO*PI)
C** COMPUTE NORMAL DERIVATIVE OF TW AT WALL *
C** TN HERE IS THE NORMAL DERIVATIVE OF TW
C** FIRST COMPUTE BY FINITE (FORWARD) DIFFERENCES *
DO 200 I=1,NP1
200  TN(I)=Z1H(1)*(-3.DO*TW(I)+4.DO*TW(I+NP1)-TW(I+NP1+NP1))
  WRITE(52,1002)
1002  FORMAT(' TWN FROM FORWARD DIFFERENCES')
  WRITE(52,1001)(TN(I),I=1,NP1)
1001  FORMAT(8(2X,F12.6))
C** THEN COMPUTE BY USING THE MOMENTUM EQN AT THE WALL *
CALL PF(NP1,TW,ZERO,1,TWSS,TWNN,1)
DO 120 I=1,NP1
  TWSS(I)=HSS(I)*TWSS(I)
120  TWNN(I)=HSS(I)*TWNN(I)
  CALL PF(NP1,TWSS,TWNN,1,TWSS,TWNN,1)
  DO 130 I=1,NP1
    TWNN(I)=WS(I)*PN(I)-TWSS(I)
    TM=(TWNN(I)+2.DO*Z1S(1)*TW(I)-(Z1S(1)+Z2H(1))*TW(I+NP1))
    & /(Z1S(1)-Z2H(1))
130  TN(I)=Z1H(1)*(TW(I+NP1)-TM)
  WRITE(52,1003)
1003  FORMAT(' TWN AT Z=0 FROM EQUATION:')
  WRITE(52,1001)(TN(I),I=1,NP1)
C** WS HERE IS THE CROSS TERM PSIXY
DO 140 I=1,N-1
140  WS(I+1)=(PN(I+2)-PN(I))/(2.DO*DX)
  WS(1)=(PN(2)-PN(NP1))/(2.DO*DX)
  WS(NP1)=(PN(1)-PN(N))/(2.DO*DX)
C** PRESSURE AND SHEAR DRAG COEFFICIENTS *
CP=0.DO
CS=0.DO

```

```

DO 310 I=0,N
  I1=I+1
  CP=CP+Y(I1)*(TN(I1)-US(I1))
310  CS=CS-TW(I1)*SX(I1)/JA(I1)
  CP=CP/NP1
  CS=CS/NP1
  WRITE(52,1005)CS+CP
  WRITE(52,1006)CS,CS/(CS+CP)
  WRITE(52,1007)CP,CP/(CS+CP)
1005  FORMAT(' THE TOTAL DRAG AT THE SURFACE IS: ',F10.7)
1006  FORMAT(' SHEAR DRAG COEFFICIENT ',F10.7,' NORMALIZED: ',F10.7)
1007  FORMAT(' PRESSURE DRAG COEFFICIENT: ',F10.7,' NORMALIZED '
    & ',F10.7)
C**  COMPUTE PRESSURE AT THE WAVY SURFACE *
  XA=JA(1)*PN(1)*PN(1)
  DO 420 I=0,N
    I1=I+1
    PR(I1)=- (TN(1)+TN(I1))/2.DO
    DO 400 K=0,I
400   PR(I1)=PR(I1)+TN(K+1)
    PR(I1)=(XA-JA(I1)*PN(I1)*PN(I1))/2.DO-DX*PR(I1)
    SIG(I1)=JA(I1)*(PNN(I1)+JN1(I1)*PN(I1))/RE
420   STR(I1)=-PR(I1)-JA(I1)*(2.DO*WS(I1)+PN(I1)*JS1(I1))/RE
C**  COMPUTE TERMS AT THE ENDPOINT: X=LAMDA *
C**  COMPUTE AMPLITUDE AND PHASE OF VARIATIONS OF PRESSURE AND SHEAR
  PR(NP2)=0.DO
  TAVE=0.DO
  S1=0.DO
  S2=0.DO
  S3=0.DO
  S4=0.DO
  SP1=0.DO
  SP2=0.DO
  DO 500 K=0,N
    XS=SX(K+1)/JA(K+1)
    S1=S1-SIG(K+1)*DSIN(2.DO*PI*X(K+1))*XS
    S2=S2+SIG(K+1)*DCOS(2.DO*PI*X(K+1))*XS
    S3=S3-SIG(K+1)*DSIN(4.DO*PI*X(K+1))*XS
    S4=S4+SIG(K+1)*DCOS(4.DO*PI*X(K+1))*XS
    SP1=SP1-PR(K+1)*DSIN(2.DO*PI*X(K+1))*XS
    SP2=SP2+PR(K+1)*DCOS(2.DO*PI*X(K+1))*XS
    TAVE=TAVE+SIG(K+1)
500   PR(NP2)=PR(NP2)+TN(K+1)
  PR(NP2)=-DX*PR(NP2)
  TAVE=TAVE/NP1
  SAVE=2.DO*DSQRT(S1*S1+S2*S2)/NP1
  S2AVE=2.DO*DSQRT(S3*S3+S4*S4)/NP1
  PAVE=2.DO*DSQRT(SP1*SP1+SP2*SP2)/NP1
  TPH=DATAN2(S1,S2)
  TPR=DATAN2(SP1,SP2)
  TPH=180.DO*TPH/PI
  TPR=180.DO*TPR/PI

```

```

W(NP2)=W(1)
SIG(NP2)=SIG(1)
STR(NP2)=STR(1)+PR(1)-PR(NP2)
WRITE(52,3000)
DO 430 I=1,NP2
430  WRITE(52,4000)X(I),W(I),PR(I),SIG(I),STR(I),SIG(I)/TAVE
      WRITE(52,1008)TAVE,SAVE,S2AVE
      WRITE(52,1009)TPH,TPR,PAVE
1008  FORMAT(' THE AVERAGE STRESS AT THE SURFACE IS: ',F12.7
& ', ' ENERGY IN FUNDAMENTAL: ',F12.7,' SECOND HARMONIC: ',F12.7)
1009  FORMAT(' THE PHASE OF THE WALL STRESS IS: ',F12.7
& ', ' WALL PRESSURE: ',F12.7,' WALL PRES AMP: ',F12.7)
3000  FORMAT(6X,'X COORDINATE',10X,'VORTICITY',11X,'PRESSURE',
& 7X,'TANGENTIAL STRESS',6X,'NORMAL STRESS',9X,'T/<T>')
4000  FORMAT(6(4X,E16.8))
C**
C**
C**  ALL OF THE FOLLOWING LINES HAVE BEEN ADDED TO THE
C**  ORIGINAL MCLEAN PROGRAM
C**
      WRITE(52,6002)Y0,ZT
6002  FORMAT('// ' Y0=',F10.5,' ZT=',F10.5//)
      DO 50 I=1,15
      WRITE(52,6003)B(I)
6003  FORMAT(F20.10)
      50  CONTINUE
      APLUS=RH*PI*RE
      NN=0
      DO 80 I=1,NP1
      SUM=0.DO
      SUM1=0.DO
      SUM2=0.DO
      PSJ(I)=((I-1)/FLOAT(NP1))*2.DO*PI
      DO 70 J=0,NP1*MP2-NP1,NP1
      NN=NN+1
      DO 90 K=1,14
      A1=DSINH(K*(ETAT-ETA(NN)))
      A2=DSINH(K*ETAT)
      SUM=SUM+(B(K)/K)*DCOS(K*PSJ(I))*A1/A2
90  CONTINUE
      DO 95 KK=1,14
      A3=DCOSH(KK*(ETAT-ETA(NN)))
      A4=DSINH(KK*ETAT)
      SUM1=SUM1+(B(KK)/KK)*DSIN(KK*PSJ(I))*A3/A4
      SUM2=SUM2+(B(KK)/KK)*DCOS(KK*PSJ(I))*A3/A4
95  CONTINUE
      XX=(SUM1+PSJ(I))/(2.DO*PI)
      DNDY=1.DO/(1.DO+SUM2)
      YPCART=RE*(ETA(NN)+Y0-SUM)
      FACTOR=APLUS*DCOS(2.DO*PI*XX)
      YPSURF=YPCART-FACTOR
C**  CALCULATE THE VELOCITY IN CARTESIAN COORDINATES

```

```

      PY=DNDY*PN(I+J)+SY(I+J)*PS(I+J)
      WRITE(52,7000)PSJ(I),XX,ETA(NN),YPSURF,PY,DNDY,PN(I+J),
&      SY(I+J),PS(I+J)
7000  FORMAT(9F12.5)
      SUM=0.DO
      SUM1=0.DO
      SUM2=0.DO
      70  CONTINUE
      NN=0
      80  CONTINUE
C**  CALCULATE THE SURFACE STRESSES IN PLUS UNITS
C    (MAGNITUDE,REAL PART,IMAGINARY PART)
      PMAG=PAVE/APLUS
      PRE=-PMAG/DSQRT((DTAN(TPR*PI/180.DO))**2+1.DO)
      PIM=PRE*DTAN(TPR*PI/180.DO)
      TMAG=SAVE/APLUS
      TR=TMAG/DSQRT((DTAN(TPH*PI/180.DO))**2+1.DO)
      TI=TR*DTAN(TPH*PI/180.DO)
      WRITE(52,7001)APLUS,PMAG,PRE,PIM,TMAG,TR,TI
7001  FORMAT(///7F15.8)
      CLOSE(52)
      RETURN
      END

```

APPENDIX B

TABULATED FLAT CHANNEL

INTENSITY MEASUREMENTS

4.25496	1.49553	170.19876	1.84975
4.25496	1.48892	170.19876	1.89131
4.25496	1.56770	212.74840	1.78409
4.25496	1.41903	212.74840	1.79723
6.38245	2.10770	255.29814	1.76228
6.38245	2.14275	255.29814	1.77324
6.38245	2.12518	297.84778	1.56325
8.08445	2.30673	297.84778	1.59169
8.08445	2.38107		
8.08445	2.32637		
10.63741	2.56469		
10.63741	2.48156		
10.63741	2.50131		
12.33942	2.63251	340.39752	1.55674
12.33942	2.63251	340.39752	1.54144
12.33942	2.65867	382.94717	1.42337
14.89237	2.68927	382.94717	1.47806
14.89237	2.63024	425.49689	1.37529
14.89237	2.75493	425.49689	1.34686
17.01986	2.63685	468.04654	1.35554
17.01986	2.61059	468.04654	1.31843
17.01986	2.66746	510.59628	1.22445
21.70030	2.61276	510.59628	1.20914
21.70030	2.50999	553.14594	1.18940
21.70030	2.57999	553.14594	1.16758
		595.69562	1.16314
25.95526	2.54287	595.69562	1.16314
25.95526	2.52757	638.24530	1.10855
25.95526	2.55817	680.79492	1.10855
		723.34454	1.12819
29.35927	2.37228		
29.35927	2.42697		
34.03971	2.37662		
34.03971	2.37445		
38.29468	2.24987		
38.29468	2.35046		
42.54964	2.21709		
42.54964	2.26517		
51.91062	2.19300		
51.91062	2.17770		
68.07952	2.21926		
68.07952	2.12962		
85.09938	2.00938		
85.09938	1.97650		
127.64912	1.91313		
127.64912	1.90217		

Table B.1 Flat Channel Intensity Data, $Re_b = 11,000$

APPENDIX C

TABULATED VELOCITY MEASUREMENTS OVER WAVES

	<u>$2a_d/\lambda = 0.03125$</u>	<u>$2a_d/\lambda = 0.05$</u>
Re_b	6370	38,840
U_b (cm/s)	24.6	147.4
u^* (cm/s)	1.44	6.88
v (cm ² /s)	0.009316	0.009155
h_d (cm)	2.413	2.413

$y_d \frac{u^*}{\nu}$	$\frac{u_d}{u^*}$	$y_d \frac{u^*}{\nu}$	$\frac{u_d}{u^*}$
1. 946	2. 361	38. 884	15. 267
1. 946	2. 383	48. 604	15. 457
2. 335	3. 185	48. 604	15. 598
2. 335	3. 138	48. 604	15. 620
2. 724	3. 493	58. 325	16. 047
2. 724	3. 446	58. 325	16. 259
3. 113	4. 036	58. 325	16. 000
3. 113	4. 248	58. 325	16. 259
3. 113	4. 176	58. 325	16. 022
3. 501	4. 554	77. 765	16. 777
3. 501	4. 554	77. 765	16. 824
3. 501	4. 625	97. 206	17. 320
3. 890	5. 025	97. 206	17. 367
3. 890	5. 025	97. 206	17. 414
3. 890	4. 956	116. 647	17. 744
4. 279	5. 617	116. 647	17. 816
4. 279	5. 474	116. 647	17. 793
4. 279	5. 592	116. 647	17. 910
4. 668	5. 898	116. 647	17. 744
4. 668	5. 898	136. 088	18. 312
4. 668	5. 947	136. 088	18. 171
5. 445	6. 606	136. 088	18. 358
5. 445	6. 678	136. 088	18. 287
5. 445	6. 631	155. 529	18. 689
6. 223	7. 149	155. 529	18. 452
6. 223	7. 220	155. 529	18. 664
7. 001	8. 306	194. 411	19. 256
7. 001	8. 165	194. 411	19. 160
7. 778	8. 637	233. 292	19. 681
7. 778	8. 920	233. 292	19. 681
7. 778	8. 708	272. 174	20. 058
8. 556	9. 298	272. 174	20. 152
8. 556	9. 510	311. 056	20. 389
9. 722	10. 242	311. 056	20. 364
9. 722	10. 430	349. 937	20. 246
11. 667	11. 328	349. 937	20. 246
11. 667	11. 421		
11. 667	11. 350		
13. 611	12. 248		
13. 611	12. 248		
15. 555	12. 860		
15. 555	12. 907		
19. 443	13. 780		
19. 443	13. 711		
23. 331	14. 466		
23. 331	14. 394		
27. 219	14. 843		
27. 219	14. 819		
31. 107	14. 843		
31. 107	14. 772		
31. 107	14. 937		
31. 107	15. 127		
38. 884	15. 267		

Table C.1 Time-Averaged Velocity Data, $x_d/\lambda = 0.1$,
 $2a_d/\lambda = 0.03125$, $\alpha_d \nu/u^* = 0.008$

$y_d \frac{u^*}{v}$	$\frac{u_d}{u^*}$	$y_d \frac{u^*}{v}$	$\frac{u_d}{u^*}$
1. 977	1. 463	39. 557	14. 843
1. 977	1. 417	49. 447	15. 433
2. 372	1. 699	49. 447	15. 504
2. 372	1. 722	49. 447	15. 362
2. 768	2. 431	59. 337	15. 882
2. 768	2. 336	59. 337	15. 975
3. 163	2. 548	79. 116	16. 565
3. 163	2. 453	79. 116	16. 518
3. 163	2. 643	79. 116	16. 472
3. 163	2. 548	98. 895	17. 108
3. 559	2. 785	98. 895	17. 084
3. 559	2. 619	118. 675	17. 650
3. 955	3. 138	118. 675	17. 816
3. 955	3. 326	138. 454	18. 006
4. 350	3. 445	138. 454	18. 006
4. 350	3. 516	138. 454	18. 028
4. 746	3. 823	158. 234	18. 311
4. 746	3. 846	158. 234	18. 382
5. 537	4. 365	197. 792	18. 996
5. 537	4. 413	197. 792	19. 067
5. 537	4. 648	237. 351	19. 681
5. 537	4. 696	237. 351	19. 657
6. 328	5. 404	237. 351	19. 610
6. 328	5. 238	276. 910	19. 940
7. 119	5. 899	276. 910	19. 940
7. 119	6. 064	316. 469	20. 105
7. 910	6. 347	316. 469	20. 081
7. 910	6. 347	316. 469	20. 247
8. 702	7. 055	356. 027	20. 198
8. 702	6. 962	356. 027	20. 105
9. 888	8. 118	356. 027	20. 247
9. 888	8. 093		
11. 866	9. 698		
11. 866	9. 581		
13. 844	10. 549		
13. 844	10. 595		
15. 822	11. 515		
15. 822	11. 846		
17. 800	11. 963		
17. 800	12. 388		
17. 800	12. 083		
17. 800	12. 105		
19. 778	12. 766		
19. 778	12. 836		
19. 778	12. 648		
23. 734	13. 546		
23. 734	13. 687		
27. 690	14. 087		
27. 690	14. 087		
31. 646	14. 560		
31. 646	14. 512		
39. 557	14. 984		
39. 557	15. 102		

Table C.2 Time-Averaged Velocity Data, $x_d/\lambda = 0.2$,
 $2a_d/\lambda = 0.03125$, $\alpha_d v/u^* = 0.008$

$y_d \frac{u^*}{v}$	$\frac{u_d}{u^*}$	$y_d \frac{u^*}{v}$	$\frac{u_d}{u^*}$
1. 979	0. 354	17. 990	9. 628
1. 979	0. 472	19. 991	10. 525
1. 979	0. 425	19. 991	10. 525
2. 379	0. 449	19. 991	10. 547
2. 379	0. 472	23. 994	11. 798
2. 780	0. 992	23. 994	11. 563
2. 780	0. 992	27. 996	12. 625
3. 180	1. 180	27. 996	12. 696
3. 180	1. 038	31. 999	13. 356
3. 180	1. 180	31. 999	12. 979
3. 180	1. 109	31. 999	13. 143
3. 580	1. 204	40. 004	13. 969
3. 580	1. 510	40. 004	13. 947
3. 580	1. 368	50. 011	14. 702
3. 980	1. 463	50. 011	14. 536
3. 980	1. 651	50. 011	14. 819
3. 980	1. 581	50. 011	14. 677
3. 980	1. 629	50. 011	14. 631
4. 381	1. 700	60. 017	15. 078
4. 381	1. 676	60. 017	14. 914
4. 381	1. 722	60. 017	15. 007
4. 781	1. 959	60. 017	15. 102
4. 781	2. 076	80. 031	15. 786
4. 781	2. 030	80. 031	15. 904
4. 781	2. 123	80. 031	15. 810
5. 582	2. 525	100. 044	16. 612
5. 582	2. 406	100. 044	16. 494
5. 582	2. 406	120. 057	17. 085
6. 382	2. 950	120. 057	17. 132
6. 382	2. 738	120. 057	17. 132
6. 382	2. 831	120. 057	17. 108
7. 183	3. 280	140. 070	17. 699
7. 183	3. 398	140. 070	17. 508
7. 983	3. 893	160. 083	17. 982
7. 983	3. 847	160. 083	18. 123
8. 784	4. 484	160. 083	18. 287
8. 784	4. 247	200. 109	18. 830
8. 784	4. 436	200. 109	18. 712
8. 784	4. 272	240. 136	19. 445
9. 985	4. 956	240. 136	19. 421
9. 985	5. 332	280. 162	19. 704
9. 985	5. 002	280. 162	19. 870
9. 985	5. 332	320. 188	19. 963
11. 986	6. 348	320. 188	20. 080
11. 986	6. 299	320. 188	20. 058
13. 987	7. 953	320. 188	20. 129
13. 987	7. 457	320. 188	20. 129
13. 987	7. 174	360. 214	20. 175
13. 987	7. 411	360. 214	20. 175
13. 987	7. 669		
15. 988	8. 613		
15. 988	8. 495		
17. 990	9. 721		

Table C.3 Time-Averaged Velocity Data, $x_d/\lambda = 0.3$,
 $2a_d/\lambda = 0.03125$, $\alpha_d v/u^* = 0.008$

$y_d \frac{u}{v}^*$	$\frac{u_d}{u}^*$	$y_d \frac{u}{v}^*$	$\frac{u_d}{u}^*$
1. 959	0. 472	48. 886	14. 159
1. 959	0. 518	48. 886	14. 088
2. 350	0. 591	58. 663	14. 466
2. 350	0. 684	58. 663	14. 607
2. 741	0. 778	58. 663	14. 441
2. 741	0. 873	78. 216	15. 385
3. 132	0. 920	78. 216	15. 315
3. 132	0. 990	97. 769	16. 117
3. 523	1. 226	97. 769	15. 906
3. 523	1. 250	117. 322	16. 777
3. 914	1. 321	117. 322	16. 730
3. 914	1. 321	136. 875	17. 297
4. 305	1. 581	136. 875	17. 132
4. 305	1. 557	156. 428	17. 769
4. 305	1. 486	156. 428	17. 698
4. 696	1. 746	156. 428	17. 674
4. 696	1. 652	175. 982	18. 170
4. 696	1. 557	175. 982	18. 194
5. 478	2. 053	175. 982	18. 311
5. 478	2. 218	195. 535	18. 501
5. 478	1. 934	195. 535	18. 430
6. 261	2. 430	234. 641	19. 160
6. 261	2. 501	234. 641	19. 209
6. 261	2. 408	273. 747	19. 727
7. 043	2. 880	273. 747	19. 727
7. 043	2. 880	312. 853	20. 011
7. 825	3. 092	312. 853	19. 963
7. 825	3. 116	351. 959	20. 128
8. 607	3. 870	351. 959	20. 153
8. 607	3. 823	391. 065	20. 128
9. 780	4. 483	391. 065	20. 223
9. 780	4. 318	391. 065	20. 082
11. 736	5. 286		
11. 736	5. 332		
13. 691	6. 254		
13. 691	6. 088		
13. 691	6. 254		
15. 646	6. 913		
15. 646	6. 891		
15. 646	7. 149		
17. 602	8. 071		
17. 602	8. 117		
19. 557	8. 825		
19. 557	8. 920		
19. 557	8. 825		
23. 467	9. 863		
23. 467	10. 053		
27. 378	10. 832		
27. 378	11. 067		
31. 289	12. 199		
31. 289	12. 247		
39. 110	13. 238		
39. 110	13. 286		

Table C.4 Time-Averaged Velocity Data, $x_d/\lambda = 0.4$,
 $2a_d/\lambda = 0.03125$, $\alpha_d v/u^* = 0.008$

$y_d \frac{u^*}{v}$	$\frac{u_d}{u^*}$	$y_d \frac{u^*}{v}$	$\frac{u_d}{u^*}$
1. 983	0. 520	32. 003	11. 066
1. 983	0. 566	32. 003	11. 044
1. 983	0. 566	40. 008	12. 082
2. 383	0. 709	40. 008	12. 224
2. 383	0. 803	50. 014	13. 286
2. 383	0. 803	50. 014	13. 380
2. 383	0. 803	60. 021	13. 946
2. 783	1. 132	60. 021	14. 065
2. 783	1. 156	80. 034	14. 749
3. 184	1. 274	80. 034	14. 749
3. 184	1. 274	100. 047	15. 598
3. 184	1. 345	100. 047	15. 528
3. 584	1. 415	120. 061	16. 188
3. 584	1. 509	120. 061	16. 164
3. 584	1. 652	120. 061	16. 306
3. 584	1. 581	140. 074	16. 896
3. 984	1. 676	140. 074	16. 848
3. 984	1. 840	140. 074	16. 754
3. 984	1. 864	160. 087	17. 250
3. 984	1. 628	160. 087	17. 274
4. 384	2. 029	160. 087	17. 320
4. 384	2. 029	200. 113	18. 147
4. 785	2. 384	200. 113	18. 217
4. 785	2. 218	200. 113	18. 217
5. 585	2. 525	240. 139	18. 972
5. 585	2. 689	240. 139	18. 901
5. 585	2. 573	280. 165	19. 327
6. 386	3. 163	280. 165	19. 373
6. 386	3. 069	320. 192	19. 845
7. 186	3. 681	320. 192	19. 845
7. 186	3. 562	360. 218	19. 917
7. 987	3. 988	360. 218	19. 799
7. 987	3. 751	360. 218	19. 963
7. 987	3. 799		
8. 787	4. 247		
8. 787	4. 319		
9. 988	5. 074		
9. 988	4. 837		
9. 988	4. 955		
11. 989	5. 804		
11. 989	5. 852		
13. 991	6. 583		
13. 991	6. 348		
15. 992	6. 890		
15. 992	7. 361		
15. 992	7. 315		
19. 995	7. 951		
19. 995	8. 024		
23. 997	9. 298		
23. 997	9. 180		
23. 997	9. 439		
28. 000	10. 029		
28. 000	10. 288		

Table C.5 Time-Averaged Velocity Data, $x_d/\lambda = 0.5$,
 $2a_d/\lambda = 0.03125$, $\alpha_d v/u^* = 0.008$

$y_d \frac{u^*}{v}$	$\frac{u_d}{u^*}$	$y_d \frac{u^*}{v}$	$\frac{u_d}{u^*}$
1.982	2.431	79.121	15.031
1.982	2.406	79.121	15.315
1.982	2.431	79.121	15.409
2.377	2.760	98.900	16.000
2.377	2.713	98.900	15.763
2.773	3.067	98.900	16.210
2.773	3.091	98.900	16.094
3.168	3.469	118.680	16.636
3.168	3.611	118.680	16.589
3.168	3.492	118.680	16.517
3.564	3.729	138.459	17.036
3.564	3.893	138.459	17.180
3.564	3.893	158.238	17.674
3.960	4.011	158.238	17.793
3.960	4.036	197.797	18.547
4.751	4.956	197.797	18.688
4.751	4.672	237.356	19.279
4.751	4.719	237.356	19.351
4.751	4.743	276.915	19.964
5.542	5.097	276.915	19.940
5.542	5.309	316.473	20.365
5.542	5.262	316.473	20.271
6.333	5.804	316.473	20.318
6.333	5.829	316.473	20.224
7.124	6.229		
7.124	6.088		
7.915	6.561		
7.915	6.536		
8.706	6.843		
8.706	6.820		
9.893	7.599		
9.893	7.293		
9.893	7.503		
11.871	7.810		
11.871	8.094		
13.849	8.519		
13.849	8.779		
15.827	8.848		
15.827	8.895		
17.805	9.321		
17.805	9.439		
19.783	9.887		
19.783	9.840		
23.739	10.478		
27.695	10.972		
27.695	11.044		
31.650	11.633		
31.650	11.610		
39.562	12.766		
49.452	13.639		
49.452	13.544		
59.342	14.323		
59.342	14.276		

Table C.6 Time-Averaged Velocity Data, $x_d/\lambda = 0.6$,
 $2a_d/\lambda = 0.03125$, $\alpha_d v/u^* = 0.008$

$y_d \frac{u^*}{v}$	$\frac{u_d}{u^*}$	$y_d \frac{u^*}{v}$	$\frac{u_d}{u^*}$
1. 954	3. 115	31. 284	12. 341
1. 954	3. 044	31. 284	12. 105
2. 345	3. 705	39. 105	13. 096
2. 345	3. 800	39. 105	13. 144
2. 737	4. 271	48. 882	13. 733
2. 737	4. 177	48. 882	13. 685
2. 737	4. 223	58. 658	14. 110
3. 128	4. 860	58. 658	14. 229
3. 128	4. 719	58. 658	14. 466
3. 519	5. 285	78. 211	15. 316
3. 519	5. 285	78. 211	15. 268
3. 519	5. 450	78. 211	15. 433
3. 519	5. 380	97. 765	15. 717
3. 910	5. 805	97. 765	16. 046
3. 910	5. 829	97. 765	15. 834
4. 301	6. 018	117. 317	16. 519
4. 301	6. 018	117. 317	16. 495
4. 692	6. 324	117. 317	16. 447
4. 692	6. 276	117. 317	16. 519
4. 692	6. 347	136. 871	17. 061
4. 692	6. 300	136. 871	17. 132
5. 474	6. 796	156. 424	17. 486
5. 474	6. 891	156. 424	17. 509
5. 474	6. 820	195. 530	18. 383
6. 256	7. 481	195. 530	18. 452
6. 256	7. 338	195. 530	18. 383
6. 256	7. 362	234. 636	19. 090
7. 038	7. 670	234. 636	19. 090
7. 038	7. 834	234. 636	19. 042
7. 820	8. 023	273. 742	19. 374
7. 820	7. 999	273. 742	19. 491
8. 602	8. 496	273. 742	19. 397
8. 602	8. 589	312. 848	19. 846
9. 384	8. 849	312. 848	19. 703
9. 384	8. 754	351. 955	19. 963
10. 167	8. 990	351. 955	19. 846
10. 167	9. 061		
11. 731	9. 463		
11. 731	9. 510		
13. 686	9. 911		
13. 686	9. 981		
15. 642	10. 312		
15. 642	10. 217		
15. 642	10. 288		
19. 552	10. 666		
19. 552	11. 043		
19. 552	10. 854		
23. 463	11. 375		
23. 463	11. 303		
23. 463	11. 303		
27. 373	11. 893		
27. 373	11. 893		
31. 284	11. 988		

Table C.7 Time-Averaged Velocity Data, $x_d/\lambda = 0.7$,
 $2a_d/\lambda = 0.03125$, $\alpha_d v/u^* = 0.008$

$y_d \frac{u^*}{v}$	$\frac{u_d}{u^*}$	$y_d \frac{u^*}{v}$	$\frac{u_d}{u^*}$
1. 939	1. 959	23. 205	12. 648
1. 939	1. 959	23. 205	12. 696
2. 326	2. 926	27. 071	12. 861
2. 326	2. 950	27. 071	12. 861
2. 326	3. 091	30. 937	13. 426
2. 713	3. 611	30. 937	13. 214
2. 713	3. 492	30. 937	13. 308
2. 713	3. 540	38. 670	13. 828
3. 099	4. 176	38. 670	13. 852
3. 099	4. 247	48. 336	14. 512
3. 486	4. 742	48. 336	14. 442
3. 486	4. 837	58. 002	14. 984
3. 873	5. 405	58. 002	15. 149
3. 873	5. 451	77. 334	15. 833
4. 259	5. 852	77. 334	15. 716
4. 259	6. 159	77. 334	15. 833
4. 259	5. 971	77. 334	15. 951
4. 259	6. 183	96. 666	16. 565
4. 646	6. 418	96. 666	16. 471
4. 646	6. 418	115. 998	17. 013
5. 419	7. 102	115. 998	17. 061
5. 419	7. 056	115. 998	17. 107
5. 419	7. 078	115. 998	17. 085
5. 419	7. 127	115. 998	17. 061
6. 193	7. 622	135. 330	17. 533
6. 193	8. 046	135. 330	17. 581
6. 193	7. 881	135. 330	17. 462
6. 193	8. 094	154. 662	17. 840
6. 966	8. 684	154. 662	18. 004
6. 966	8. 542	154. 662	18. 028
6. 966	8. 471	154. 662	17. 958
7. 739	9. 037	193. 326	18. 642
7. 739	9. 085	193. 326	18. 759
8. 512	9. 487	193. 326	18. 618
8. 512	9. 581	231. 989	19. 397
8. 512	9. 698	231. 989	19. 255
9. 286	10. 053	231. 989	19. 255
9. 286	10. 053	270. 653	19. 632
10. 059	10. 288	270. 653	19. 704
10. 059	10. 077	309. 317	19. 917
10. 059	10. 241	309. 317	19. 987
11. 605	10. 878	347. 981	20. 058
11. 605	10. 524	347. 981	19. 939
11. 605	10. 430	347. 981	20. 081
13. 539	11. 255	347. 981	20. 058
13. 539	11. 255		
15. 472	11. 705		
15. 472	11. 845		
19. 338	12. 106		
19. 338	12. 602		
19. 338	12. 459		
19. 338	12. 224		
23. 205	12. 790		

Table C.8 Time-Averaged Velocity Data, $x_d/\lambda = 0.8$,
 $2a_d/\lambda = 0.03125$, $\alpha_d v/u^* = 0.008$

$y_d \frac{u^*}{v}$	$\frac{u_d}{u^*}$	$y_d \frac{u^*}{v}$	$\frac{u_d}{u^*}$
1. 955	2. 194	31. 285	14. 441
1. 955	2. 265	31. 285	14. 299
2. 346	3. 634	39. 106	14. 984
2. 346	3. 729	39. 106	14. 583
2. 346	3. 729	39. 106	14. 559
2. 737	4. 390	48. 883	15. 101
2. 737	4. 436	48. 883	15. 150
3. 128	5. 121	48. 883	15. 314
3. 128	5. 192	58. 659	15. 410
3. 520	5. 781	58. 659	15. 598
3. 520	5. 640	58. 659	15. 740
3. 911	6. 207	58. 659	15. 740
3. 911	6. 371	78. 212	16. 305
3. 911	6. 278	78. 212	16. 588
4. 302	6. 867	78. 212	16. 495
4. 302	6. 867	78. 212	16. 447
4. 302	6. 914	97. 765	17. 060
4. 693	7. 222	97. 765	17. 085
4. 693	7. 457	117. 318	17. 297
4. 693	7. 598	117. 318	17. 273
4. 693	7. 244	117. 318	17. 557
4. 693	7. 481	117. 318	17. 462
5. 475	8. 330	136. 872	17. 603
5. 475	8. 046	136. 872	17. 982
6. 257	9. 085	136. 872	17. 840
6. 257	9. 179	156. 425	18. 359
7. 039	9. 770	156. 425	18. 264
7. 039	9. 817	195. 531	18. 878
7. 821	10. 453	195. 531	18. 878
7. 821	10. 548	195. 531	19. 019
8. 603	10. 902	195. 531	19. 044
8. 603	10. 807	234. 637	19. 609
9. 385	11. 279	234. 637	19. 420
9. 385	11. 326	234. 637	19. 445
10. 168	11. 492	273. 743	19. 775
10. 168	11. 751	273. 743	19. 868
11. 732	12. 201	312. 849	20. 081
11. 732	12. 294	312. 849	20. 034
13. 687	12. 719	351. 956	20. 247
13. 687	12. 932	351. 956	20. 247
15. 642	13. 143		
15. 642	12. 954		
15. 642	13. 262		
19. 553	13. 451		
19. 553	13. 663		
19. 553	13. 475		
23. 464	13. 710		
23. 464	13. 827		
23. 464	13. 922		
23. 464	13. 922		
27. 374	14. 277		
27. 374	14. 229		
31. 285	14. 370		

Table C.9 Time-Averaged Velocity Data, $x/\lambda = 0.9$,
 $2a_d/\lambda = 0.03125$, $\alpha_d v/u^* = 0.008$

$y_d \frac{u^*}{v}$	$\frac{u_d}{u^*}$	$y_d \frac{u^*}{v}$	$\frac{u_d}{u^*}$
1.935	2.525	23.200	14.181
1.935	2.525	23.200	14.276
1.935	2.595	27.067	14.631
2.322	3.092	27.067	14.631
2.322	3.162	27.067	14.441
2.322	3.116	27.067	14.488
2.708	3.823	30.933	14.748
2.708	3.751	30.933	14.702
2.708	3.729	30.933	14.843
3.095	4.201	30.933	14.748
3.095	4.437	30.933	14.960
3.095	4.223	38.666	15.361
3.095	4.318	38.666	15.149
3.482	4.697	38.666	15.008
3.482	4.884	48.332	15.385
3.482	4.838	48.332	15.645
3.482	4.673	48.332	15.575
3.868	5.405	48.332	15.692
3.868	5.380	57.998	16.069
3.868	5.475	57.998	15.811
4.255	5.782	57.998	15.881
4.255	5.804	77.330	16.613
4.642	6.465	77.330	16.684
4.642	6.371	77.330	16.660
4.642	6.419	96.662	17.250
5.415	7.409	96.662	17.438
5.415	7.621	96.662	17.438
5.415	7.621	115.993	17.864
6.188	8.258	115.993	17.864
6.188	8.188	115.993	17.815
6.188	8.188	115.993	17.815
6.962	9.180	135.326	18.358
6.962	9.061	135.326	18.311
6.962	9.061	135.326	18.287
7.735	9.674	154.657	18.594
7.735	9.462	154.657	18.547
7.735	9.722	154.657	18.618
8.508	10.430	154.657	18.666
8.508	10.477	193.321	19.326
9.281	10.902	193.321	19.231
9.281	11.067	193.321	19.231
9.281	10.832	231.985	19.467
10.055	11.398	231.985	19.562
10.055	11.350	231.985	19.539
11.601	12.082	270.649	19.917
11.601	11.987	270.649	19.822
13.534	12.578	309.313	20.153
13.534	12.671	309.313	19.963
15.468	13.191	309.313	20.128
15.468	13.050	347.977	20.223
15.468	13.120	347.977	20.128
19.334	13.899	347.977	20.128
19.334	13.875		

Table C.10 Time-Averaged Velocity Data, $x_d/\lambda = 1.0$,
 $2a_d/\lambda = 0.03125$, $\alpha_d v/u^* = 0.008$

$y_d \frac{u^*}{v}$	$\sqrt{u_d'^2/u^*}$	$y_d \frac{u^*}{v}$	$\sqrt{u_d'^2/u^*}$
1. 944	1. 304	38. 882	2. 242
1. 944	1. 296	38. 882	2. 275
2. 333	1. 534	48. 602	2. 269
2. 333	1. 483	48. 602	2. 226
2. 722	1. 551	48. 602	2. 263
2. 722	1. 571	58. 322	2. 336
3. 111	1. 775	58. 322	2. 120
3. 111	1. 793	58. 322	2. 263
3. 111	1. 779	58. 322	2. 224
3. 499	1. 789	58. 322	2. 216
3. 499	1. 869	77. 763	2. 081
3. 499	1. 863	77. 763	2. 134
3. 888	1. 842	97. 204	2. 061
3. 888	1. 957	97. 204	1. 951
3. 888	1. 934	97. 204	2. 004
4. 277	1. 989	97. 204	2. 012
4. 277	1. 957	116. 645	2. 059
4. 277	2. 022	116. 645	2. 049
4. 666	2. 067	116. 645	1. 967
4. 666	2. 018	116. 645	1. 965
4. 666	2. 169	116. 645	2. 063
4. 666	2. 006	136. 086	1. 877
5. 444	2. 277	136. 086	1. 969
5. 444	2. 177	136. 086	1. 879
5. 444	2. 208	136. 086	1. 867
6. 221	2. 346	155. 527	1. 849
6. 221	2. 342	155. 527	1. 993
6. 999	2. 422	155. 527	1. 822
6. 999	2. 507	194. 408	1. 732
7. 776	2. 489	194. 408	1. 746
7. 776	2. 579	233. 290	1. 477
7. 776	2. 499	233. 290	1. 461
8. 554	2. 630	272. 172	1. 365
8. 554	2. 605	272. 172	1. 344
9. 720	2. 599	311. 053	1. 273
9. 720	2. 616	311. 053	1. 247
11. 665	2. 577	349. 935	1. 275
11. 665	2. 705		
11. 665	2. 658		
13. 609	2. 644		
13. 609	2. 677		
15. 553	2. 603		
15. 553	2. 552		
19. 441	2. 440		
19. 441	2. 387		
23. 329	2. 475		
23. 329	2. 365		
27. 217	2. 267		
27. 217	2. 277		
27. 217	2. 254		
31. 105	2. 214		
31. 105	2. 334		
31. 105	2. 326		
31. 105	2. 322		

Table C.11 Intensity Data, $x_d/\lambda = 0.1$, $2a_d/\lambda = 0.03125$,
 $\alpha_d v/u^* = 0.008$

$y_d \frac{u^*}{v}$	$\sqrt{u_d'^2/u^*}$	$y_d \frac{u^*}{v}$	$\sqrt{u_d'^2/u^*}$
1. 978	1. 267	39. 559	2. 261
1. 978	1. 269	49. 448	2. 354
2. 374	1. 384	49. 448	2. 261
2. 374	1. 421	49. 448	2. 213
2. 769	1. 609	59. 338	2. 267
2. 769	1. 568	59. 338	2. 241
3. 165	1. 625	79. 117	2. 184
3. 165	1. 582	79. 117	2. 140
3. 165	1. 748	79. 117	2. 124
3. 165	1. 696	98. 897	2. 043
3. 560	1. 750	98. 897	2. 049
3. 560	1. 738	118. 676	1. 968
3. 956	1. 855	118. 676	1. 938
3. 956	1. 908	138. 456	1. 962
4. 352	1. 958	138. 456	1. 926
4. 352	1. 942	138. 456	1. 952
4. 747	2. 067	158. 235	1. 960
4. 747	2. 106	158. 235	1. 940
5. 538	2. 243	197. 794	1. 754
5. 538	2. 170	197. 794	1. 710
5. 538	2. 376	237. 352	1. 722
5. 538	2. 292	237. 352	1. 659
6. 329	2. 445	237. 352	1. 694
6. 329	2. 421	276. 911	1. 425
7. 121	2. 570	276. 911	1. 449
7. 121	2. 566	316. 470	1. 405
7. 912	2. 597	316. 470	1. 330
7. 912	2. 760	316. 470	1. 370
8. 703	2. 726	356. 029	1. 372
8. 703	2. 706	356. 029	1. 411
9. 890	2. 791	356. 029	1. 338
9. 890	2. 938		
11. 868	2. 831		
11. 868	2. 940		
11. 868	2. 882		
13. 846	2. 906		
13. 846	2. 843		
15. 823	2. 799		
15. 823	2. 908		
17. 802	2. 795		
17. 802	2. 779		
17. 802	2. 728		
17. 802	2. 769		
19. 779	2. 843		
19. 779	2. 623		
19. 779	2. 670		
23. 735	2. 593		
23. 735	2. 554		
27. 691	2. 470		
27. 691	2. 467		
31. 647	2. 439		
31. 647	2. 350		
39. 559	2. 257		
39. 559	2. 302		

Table C.12 Intensity Data, $x_d/\lambda = 0.2$, $2a_d/\lambda = 0.03125$,
 $\alpha_d v/u^* = 0.008$

$y_d \frac{u^*}{\nu}$	$\sqrt{u_d'^2}/u^*$	$y_d \frac{u^*}{\nu}$	$\sqrt{u_d'^2}/u^*$
2.001	0.716	18.012	3.054
2.001	0.789	20.013	2.969
2.001	0.724	20.013	3.084
2.401	0.775	20.013	3.139
2.401	0.791	20.013	3.074
2.802	1.117	24.016	2.997
2.802	1.149	24.016	3.050
3.202	1.238	28.018	2.797
3.202	1.249	28.018	2.748
3.202	1.303	32.021	2.523
3.202	1.245	32.021	2.623
3.602	1.311	32.021	2.568
3.602	1.439	40.026	2.400
3.602	1.400	40.026	2.370
4.003	1.447	50.033	2.319
4.003	1.485	50.033	2.250
4.003	1.568	50.033	2.246
4.003	1.500	50.033	2.190
4.403	1.623	50.033	2.297
4.403	1.663	60.039	2.175
4.403	1.661	60.039	2.297
4.803	1.781	60.039	2.157
4.803	1.815	60.039	2.216
4.803	1.896	80.052	2.194
4.803	1.852	80.052	2.210
5.604	2.001	80.052	2.161
5.604	1.918	100.066	2.088
5.604	1.902	100.066	2.099
6.404	2.090	120.079	2.090
6.404	2.145	120.079	2.016
6.404	2.094	120.079	1.973
7.205	2.368	120.079	2.044
7.205	2.329	140.092	1.967
8.005	2.507	140.092	1.989
8.005	2.463	160.105	1.916
8.806	2.578	160.105	1.997
8.806	2.554	160.105	1.892
8.806	2.742	200.131	1.837
8.806	2.479	200.131	1.797
8.806	2.527	240.158	1.645
10.007	2.857	240.158	1.663
10.007	2.752	280.184	1.475
10.007	2.845	280.184	1.435
10.007	2.790	320.210	1.423
12.008	2.963	320.210	1.457
12.008	2.985	320.210	1.356
14.009	3.046	320.210	1.362
14.009	3.126	320.210	1.313
14.009	3.205	360.236	1.366
14.009	3.280	360.236	1.330
14.009	3.116		
16.010	3.135		
16.010	3.094		
18.012	3.108		

Table C.13 Intensity Data, $x_d/\lambda = 0.3$, $2a_d/\lambda = 0.03125$,
 $\alpha_d \nu/u^* = 0.008$

$y_d \frac{u^*}{v}$	$\sqrt{u_d'^2/u^*}$	$y_d \frac{u^*}{v}$	$\sqrt{u_d'^2/u^*}$
1.955	0.978	39.106	2.688
1.955	1.000	48.883	2.327
2.346	1.069	48.883	2.309
2.346	1.103	58.659	2.218
2.737	1.283	58.659	2.125
2.737	1.341	58.659	2.156
3.128	1.319	78.212	2.156
3.128	1.404	78.212	2.144
3.520	1.513	97.765	2.047
3.520	1.555	97.765	2.087
3.911	1.595	117.318	2.087
3.911	1.551	117.318	2.081
4.302	1.714	136.872	1.970
4.302	1.625	136.872	1.964
4.693	1.646	156.425	1.997
4.693	1.658	156.425	1.849
4.693	1.726	156.425	1.880
4.693	1.702	175.978	1.882
5.475	2.029	175.978	1.817
5.475	2.144	175.978	1.807
5.475	1.986	195.531	1.757
6.257	2.174	195.531	1.775
6.257	2.039	234.637	1.660
6.257	2.083	234.637	1.666
7.039	2.352	273.743	1.474
7.039	2.396	273.743	1.428
7.821	2.362	312.849	1.379
7.821	2.420	312.849	1.363
8.603	2.616	351.956	1.371
8.603	2.660	351.956	1.331
9.777	2.769	391.062	1.383
9.777	2.773	391.062	1.293
11.732	3.017	391.062	1.293
11.732	3.142		
13.687	3.045		
13.687	3.241		
13.687	3.178		
13.687	3.168		
15.642	3.279		
15.642	3.140		
15.642	3.315		
17.598	3.196		
17.598	3.326		
17.598	3.227		
19.553	3.408		
19.553	3.241		
19.553	3.473		
23.464	3.313		
23.464	3.366		
27.374	3.223		
27.374	3.237		
31.285	2.932		
31.285	2.981		
39.106	2.587		

Table C.14 Intensity Data, $x_d/\lambda = 0.4$, $2a_d/\lambda = 0.03125$,
 $\alpha_d v/u^* = 0.008$

$y_d \frac{u^*}{\nu}$	$\sqrt{u_d'^2/u^*}$	$y_d \frac{u^*}{\nu}$	$\sqrt{u_d'^2/u^*}$
2.001	0.907	28.018	3.265
2.001	0.923	32.021	3.036
2.001	0.901	32.021	3.129
2.401	0.995	40.026	2.774
2.401	1.036	40.026	2.882
2.401	1.102	50.033	2.392
2.401	1.108	50.033	2.446
2.802	1.266	60.039	2.242
2.802	1.309	60.039	2.214
3.202	1.399	80.052	2.099
3.202	1.461	80.052	2.087
3.202	1.473	100.066	2.063
3.602	1.459	100.066	2.047
3.602	1.541	120.079	2.017
3.602	1.626	120.079	1.969
3.602	1.553	120.079	1.955
4.003	1.620	140.092	1.945
4.003	1.712	140.092	1.907
4.003	1.750	140.092	1.923
4.403	1.622	160.105	1.868
4.403	1.878	160.105	1.778
4.403	1.836	160.105	1.856
4.803	1.951	200.131	1.788
4.803	1.943	200.131	1.702
5.604	2.093	200.131	1.770
5.604	2.099	240.158	1.636
5.604	2.013	240.158	1.660
6.404	2.286	280.184	1.413
6.404	2.282	280.184	1.409
7.205	2.400	320.210	1.325
7.205	2.479	320.210	1.313
8.005	2.603	360.236	1.294
8.005	2.374	360.236	1.264
8.005	2.575	360.236	1.325
8.005	2.537		
8.806	2.551		
8.806	2.615		
10.007	2.868		
10.007	2.685		
10.007	2.826		
12.008	3.020		
12.008	2.988		
12.008	2.982		
14.009	3.033		
14.009	3.125		
16.010	3.179		
16.010	3.269		
16.010	3.199		
20.013	3.306		
20.013	3.291		
24.016	3.434		
24.016	3.281		
24.016	3.348		
28.018	3.179		

Table C.15 Intensity Data, $x_d/\lambda = 0.5$, $2a_d/\lambda = 0.03125$,
 $\alpha_d \nu/u^* = 0.008$

$y_d \frac{u^*}{v}$	$\sqrt{u_d'^2/u^*}$	$y_d \frac{u^*}{v}$	$\sqrt{u_d'^2/u^*}$
1. 978	1. 548	59. 338	2. 214
1. 978	1. 505	79. 117	2. 120
1. 978	1. 482	79. 117	2. 034
2. 374	1. 672	79. 117	2. 061
2. 374	1. 638	98. 897	2. 108
2. 769	1. 736	98. 897	2. 141
2. 769	1. 703	98. 897	2. 061
3. 165	1. 846	98. 897	2. 089
3. 165	1. 903	118. 676	2. 014
3. 360	1. 811	118. 676	2. 087
3. 360	2. 008	118. 676	2. 055
3. 360	2. 030	138. 456	1. 944
3. 956	2. 022	138. 456	1. 961
3. 956	2. 106	158. 235	1. 936
4. 747	2. 079	158. 235	1. 869
4. 747	2. 284	197. 794	1. 805
4. 747	2. 167	197. 794	1. 795
4. 747	2. 235	237. 352	1. 676
5. 538	2. 277	237. 352	1. 732
5. 538	2. 408	276. 911	1. 574
5. 538	2. 374	276. 911	1. 556
6. 329	2. 400	316. 470	1. 098
6. 329	2. 521	316. 470	1. 090
7. 121	2. 652	316. 470	1. 169
7. 121	2. 547		
7. 912	2. 609		
7. 912	2. 635		
8. 703	2. 766		
8. 703	2. 674		
9. 890	2. 715		
9. 890	2. 840		
9. 890	2. 760		
11. 868	2. 971		
11. 868	2. 860		
13. 846	2. 840		
13. 846	3. 011		
15. 823	3. 003		
15. 823	2. 917		
17. 802	3. 028		
17. 802	3. 024		
19. 779	3. 022		
19. 779	3. 067		
23. 735	3. 075		
23. 735	3. 114		
27. 691	3. 181		
27. 691	3. 020		
31. 647	3. 120		
31. 647	3. 071		
39. 559	3. 044		
39. 559	2. 832		
49. 448	2. 740		
49. 448	2. 549		
59. 338	2. 562		
	2. 276		

Table C.16 Intensity Data, $x_d/\lambda = 0.6$, $2a_d/\lambda = 0.03125$,
 $\alpha_d v/u^* = 0.008$

$y_d \frac{u^*}{\nu}$	$\sqrt{u_d'^2/u^*}$	$y_d \frac{u^*}{\nu}$	$\sqrt{u_d'^2/u^*}$
1. 955	1. 596	27. 374	2. 740
1. 955	1. 576	27. 374	2. 730
2. 346	1. 690	31. 285	2. 661
2. 346	1. 686	31. 285	2. 716
2. 737	1. 807	31. 285	2. 708
2. 737	1. 862	39. 106	2. 643
2. 737	1. 880	39. 106	2. 633
3. 128	1. 846	48. 883	2. 402
3. 128	1. 856	48. 883	2. 434
3. 520	2. 059	58. 659	2. 331
3. 520	2. 099	58. 659	2. 297
3. 520	2. 001	58. 659	2. 299
3. 520	2. 059	78. 212	2. 085
3. 911	2. 111	78. 212	2. 011
3. 911	2. 091	78. 212	2. 083
4. 302	2. 158	97. 765	2. 055
4. 302	2. 178	97. 765	2. 001
4. 693	2. 188	97. 765	1. 993
4. 693	2. 349	117. 318	2. 053
4. 693	2. 222	117. 318	1. 977
4. 693	2. 202	117. 318	1. 894
5. 475	2. 317	117. 318	1. 870
5. 475	2. 422	136. 872	1. 870
5. 475	2. 385	136. 872	1. 864
6. 257	2. 547	156. 425	1. 834
6. 257	2. 353	156. 425	1. 839
6. 257	2. 436	195. 531	1. 733
7. 039	2. 440	195. 531	1. 652
7. 039	2. 394	195. 531	1. 691
7. 821	2. 557	234. 637	1. 547
7. 821	2. 462	234. 637	1. 501
8. 603	2. 468	234. 637	1. 551
8. 603	2. 533	273. 743	1. 455
9. 385	2. 553	273. 743	1. 336
9. 385	2. 494	273. 743	1. 398
9. 385	2. 583	312. 849	1. 314
10. 168	2. 577	312. 849	1. 336
10. 168	2. 603	351. 956	1. 249
11. 732	2. 591	351. 956	1. 273
11. 732	2. 532		
13. 687	2. 710		
13. 687	2. 732		
13. 687	2. 641		
13. 687	2. 649		
15. 642	2. 597		
15. 642	2. 762		
15. 642	2. 662		
19. 553	2. 716		
19. 553	2. 756		
19. 553	2. 686		
23. 464	2. 680		
23. 464	2. 772		
23. 464	2. 762		
27. 374	2. 803		

Table C.17 Intensity Data, $x_d/\lambda = 0.7$, $2a_d/\lambda = 0.03125$,
 $\alpha_d \nu/u^* = 0.008$

$y_d \frac{u}{v}^*$	$\sqrt{u_d'^2/u}^*$	$y_d \frac{u}{v}^*$	$\sqrt{u_d'^2/u}^*$
1. 933	1. 168	23. 198	2. 495
1. 933	1. 210	27. 065	2. 507
2. 320	1. 202	27. 065	2. 559
2. 320	1. 228	30. 931	2. 461
2. 320	1. 200	30. 931	2. 474
2. 707	1. 425	30. 931	2. 549
2. 707	1. 345	38. 664	2. 479
2. 707	1. 389	38. 664	2. 537
3. 093	1. 479	48. 330	2. 346
3. 093	1. 505	48. 330	2. 332
3. 480	1. 584	57. 996	2. 242
3. 480	1. 598	57. 996	2. 212
3. 866	1. 782	77. 328	2. 188
3. 866	1. 728	77. 328	2. 019
4. 253	1. 832	77. 328	2. 165
4. 253	1. 893	77. 328	2. 063
4. 253	1. 931	96. 660	1. 999
4. 253	1. 852	96. 660	1. 987
4. 640	1. 943	115. 992	1. 951
4. 640	1. 945	115. 992	2. 011
5. 413	2. 196	115. 992	1. 967
5. 413	2. 093	115. 992	1. 931
5. 413	2. 129	115. 992	1. 957
5. 413	2. 165	115. 992	1. 881
6. 186	2. 278	135. 324	1. 788
6. 186	2. 234	135. 324	1. 826
6. 186	2. 304	135. 324	1. 804
6. 186	2. 304	154. 655	1. 820
6. 959	2. 360	154. 655	1. 738
6. 959	2. 378	154. 655	1. 836
6. 959	2. 420	154. 655	1. 778
7. 733	2. 410	193. 319	1. 564
7. 733	2. 402	193. 319	1. 708
8. 506	2. 509	193. 319	1. 716
8. 506	2. 585	231. 983	1. 491
8. 506	2. 386	231. 983	1. 547
9. 279	2. 434	231. 983	1. 564
9. 279	2. 434	270. 647	1. 431
10. 053	2. 441	270. 647	1. 419
10. 053	2. 495	309. 311	1. 353
10. 053	2. 521	309. 311	1. 323
11. 599	2. 577	347. 975	1. 319
11. 599	2. 457	347. 975	1. 341
11. 599	2. 501	347. 975	1. 371
13. 532	2. 621	347. 975	1. 270
13. 532	2. 495		
15. 465	2. 509		
15. 465	2. 503		
19. 332	2. 479		
19. 332	2. 499		
19. 332	2. 511		
19. 332	2. 527		
23. 198	2. 537		
23. 198	2. 461		

Table C.18 Intensity Data, $x_d/\lambda = 0.8$, $2a_d/\lambda = 0.03125$,
 $\alpha_d v/u^* = 0.008$

$y_d \frac{u^*}{v}$	$\sqrt{u_d'^2/u^*}$	$y_d \frac{u^*}{v}$	$\sqrt{u_d'^2/u^*}$
1. 955	1. 329	31. 285	2. 315
1. 955	1. 343	31. 285	2. 402
2. 346	1. 369	31. 285	2. 372
2. 346	1. 414	39. 106	2. 374
2. 346	1. 363	39. 106	2. 364
2. 737	1. 556	39. 106	2. 313
2. 737	1. 596	48. 883	2. 285
3. 128	1. 661	48. 883	2. 315
3. 128	1. 643	48. 883	2. 303
3. 520	1. 728	58. 659	2. 234
3. 520	1. 718	58. 659	2. 287
3. 911	1. 829	58. 659	2. 295
3. 911	1. 888	58. 659	2. 184
3. 911	1. 892	78. 212	2. 210
4. 302	1. 884	78. 212	1. 991
4. 302	1. 963	78. 212	1. 981
4. 302	1. 967	78. 212	2. 095
4. 693	2. 133	78. 212	2. 068
4. 693	2. 018	97. 765	1. 918
4. 693	2. 133	97. 765	1. 924
4. 693	2. 089	117. 318	2. 012
4. 693	2. 052	117. 318	1. 929
5. 475	2. 196	117. 318	1. 906
5. 475	2. 208	117. 318	1. 931
6. 257	2. 354	136. 872	1. 920
6. 257	2. 402	136. 872	1. 874
7. 039	2. 419	136. 872	1. 902
7. 039	2. 344	156. 425	1. 797
7. 821	2. 498	156. 425	1. 809
7. 821	2. 494	195. 531	1. 688
8. 603	2. 510	195. 531	1. 740
8. 603	2. 463	195. 531	1. 663
9. 385	2. 477	195. 531	1. 716
9. 385	2. 459	234. 637	1. 424
10. 168	2. 486	234. 637	1. 473
10. 168	2. 443	234. 637	1. 473
11. 732	2. 449	273. 743	1. 325
11. 732	2. 480	273. 743	1. 335
11. 732	2. 401	312. 849	1. 256
13. 687	2. 421	312. 849	1. 238
13. 687	2. 463	351. 956	1. 301
15. 642	2. 417	351. 956	1. 284
15. 642	2. 459		
15. 642	2. 394		
19. 553	2. 319		
19. 553	2. 354		
19. 553	2. 415		
23. 464	2. 291		
23. 464	2. 329		
23. 464	2. 392		
23. 464	2. 317		
27. 374	2. 336		
27. 374	2. 396		
31. 285	2. 429		

Table C.19 Intensity Data, $x_d/\lambda = 0.9$, $2a_d/\lambda = 0.03125$,
 $\alpha_d v/u^* = 0.008$

$y_d \frac{u^*}{v}$	$\sqrt{u_d'^2/u^*}$	$y_d \frac{u^*}{v}$	$\sqrt{u_d'^2/u^*}$
1.933	1.025	23.198	2.321
1.933	1.073	23.198	2.313
1.933	1.067	27.065	2.392
2.320	1.147	27.065	2.283
2.320	1.194	27.065	2.222
2.320	1.174	27.065	2.315
2.707	1.402	30.931	2.382
2.707	1.373	30.931	2.265
2.707	1.335	30.931	2.277
3.093	1.472	30.931	2.216
3.093	1.537	30.931	2.243
3.093	1.414	38.664	2.283
3.093	1.464	38.664	2.269
3.480	1.694	38.664	2.281
3.480	1.726	48.330	2.313
3.480	1.654	48.330	2.218
3.480	1.611	48.330	2.251
3.866	1.813	48.330	2.232
3.866	1.793	57.996	2.239
3.866	1.748	57.996	2.190
4.253	1.863	57.996	2.224
4.253	1.896	77.328	2.130
4.640	2.023	77.328	2.059
4.640	1.950	77.328	2.077
4.640	1.998	96.660	2.071
5.413	2.150	96.660	1.974
5.413	2.210	96.660	2.011
5.413	2.210	96.660	2.166
6.186	2.247	115.992	1.958
6.186	2.295	115.992	2.053
6.186	2.224	115.992	2.023
6.959	2.355	115.992	2.007
6.959	2.450	135.324	1.934
6.959	2.347	135.324	1.978
7.733	2.400	135.324	1.944
7.733	2.400	154.655	1.930
7.733	2.434	154.655	1.896
8.506	2.497	154.655	1.827
8.506	2.529	154.655	1.922
9.279	2.579	154.655	1.884
9.279	2.573	193.319	1.746
9.279	2.585	193.319	1.787
10.053	2.567	193.319	1.835
10.053	2.533	231.983	1.488
11.599	2.511	231.983	1.462
11.599	2.529	231.983	1.476
13.532	2.545	270.647	1.383
13.532	2.553	270.647	1.373
15.465	2.434	309.311	1.317
15.465	2.531	309.311	1.323
15.465	2.416	309.311	1.331
19.332	2.390	347.975	1.315
19.332	2.339	347.975	1.295
23.198	2.208	347.975	1.317

Table C.20 Intensity Data, $x_d/\lambda = 1.0$, $2a_d/\lambda = 0.03125$,
 $\alpha_d v/u^* = 0.008$

$y_d \frac{u^*}{v}$	$\frac{u_d}{u^*}$	$y_d \frac{u^*}{v}$	$\frac{u_d}{u^*}$
12.006	9.484	200.105	20.991
12.006	9.186	200.105	20.942
12.006	9.384	250.132	21.238
14.007	10.915	250.132	21.336
14.007	10.964	300.158	21.436
16.008	12.495	300.158	21.336
16.008	12.544	300.158	21.485
18.010	13.780	400.211	21.732
18.010	13.978	400.211	21.732
18.010	13.780	500.263	22.126
20.011	14.866	500.263	22.077
20.011	14.817	600.316	22.226
22.012	15.705	600.316	22.522
22.012	15.509	600.316	22.275
22.012	15.756	700.369	22.571
24.013	16.446	700.369	22.669
24.013	16.299	800.422	23.114
24.013	16.250	800.422	22.965
26.014	16.940	800.422	22.916
26.014	16.693	900.474	23.212
26.014	16.793	900.474	23.361
28.015	17.236	900.474	23.163
28.015	17.138	900.474	23.212
32.017	17.730	1000.527	23.560
32.017	17.681	1000.527	23.560
36.019	18.423	1400.738	23.560
36.019	18.175	1400.738	23.459
36.019	18.224	1800.948	23.511
40.021	18.472		
40.021	18.569		
40.021	18.569		
46.024	19.014		
46.024	19.014		
52.027	19.362		
52.027	19.310		
60.032	19.509		
60.032	19.558		
70.037	19.707		
70.037	19.805		
80.042	19.805		
80.042	19.805		
80.042	20.003		
80.042	19.854		
90.047	20.052		
90.047	20.003		
100.053	20.152		
100.053	20.201		
120.063	20.299		
120.063	20.348		
140.074	20.448		
140.074	20.448		
160.084	20.644		
160.084	20.497		
160.084	20.793		

Table C.21 Time-Averaged Velocity Data, $x_d/\lambda = 0.1$,
 $2a_d/\lambda = 0.050$, $\alpha_d v/u^* = 0.00165$

$y_d \frac{u^*}{v}$	$\frac{u_d}{u^*}$	$y_d \frac{u^*}{v}$	$\frac{u_d}{u^*}$
13.698	7.606	587.073	21.879
13.698	7.606	587.073	21.879
15.655	9.484	684.918	22.324
15.655	9.632	684.918	22.324
17.612	12.101	782.764	22.422
17.612	11.902	782.764	22.719
19.569	13.335	782.764	22.522
19.569	13.137	978.455	23.262
21.526	14.027	978.455	23.214
21.526	14.027	1369.837	23.312
23.483	14.718	1565.528	23.312
23.483	14.718	1565.528	23.362
25.440	15.211	1761.219	22.917
25.440	15.163	1761.219	22.965
27.397	15.656		
27.397	15.656		
31.311	16.250		
31.311	16.496		
31.311	16.250		
35.224	16.941		
35.224	16.742		
35.224	16.891		
39.138	17.137		
39.138	17.137		
45.009	17.534		
45.009	17.534		
50.880	17.781		
50.880	17.879		
58.707	18.175		
58.707	18.274		
68.492	18.374		
68.492	18.422		
78.276	18.668		
78.276	18.570		
97.845	18.817		
97.845	18.867		
117.415	19.113		
117.415	19.262		
136.984	19.214		
136.984	19.360		
136.984	19.410		
156.553	19.508		
156.553	19.608		
195.691	19.855		
195.691	19.905		
244.614	20.199		
244.614	20.348		
293.536	20.496		
293.536	20.644		
293.536	20.695		
391.382	21.089		
391.382	21.039		
489.227	21.484		
489.227	21.434		

Table C.22 Time-Averaged Velocity Data, $x_d/\lambda = 0.2$,
 $2a_d/\lambda = 0.050$, $\alpha_d v/u^* = 0.00165$

$y_d \frac{u^*}{v}$	$\frac{u_d}{u^*}$	$y_d \frac{u^*}{v}$	$\frac{u_d}{u^*}$
20.011	8.101	700.369	20.892
20.011	7.902	700.369	21.138
20.011	8.101	700.369	21.089
22.012	8.395	800.422	21.533
22.012	8.346	800.422	21.287
24.013	8.790	800.422	21.484
24.013	8.842	900.474	21.682
26.014	8.989	900.474	21.781
26.014	9.136	1000.527	21.979
28.015	9.531	1000.527	22.028
28.015	9.433	1200.632	22.570
32.017	10.174	1200.632	22.521
32.017	9.977	1400.738	23.115
32.017	9.926	1400.738	22.965
36.019	10.718	1600.843	23.360
36.019	10.667	1600.843	23.311
40.021	11.261	1800.948	23.262
40.021	11.261	1800.948	23.311
46.024	12.347		
46.024	12.249		
52.027	13.039		
52.027	13.088		
60.032	13.976		
60.032	13.927		
60.032	13.878		
70.037	15.112		
70.037	15.014		
80.042	15.706		
80.042	15.853		
90.047	16.349		
90.047	16.447		
100.053	16.744		
100.053	16.891		
100.053	16.793		
120.063	17.335		
120.063	17.188		
140.074	17.534		
140.074	17.681		
160.084	17.929		
160.084	17.929		
200.105	18.422		
200.105	18.422		
200.105	18.275		
250.132	18.621		
250.132	18.915		
250.132	19.866		
300.158	19.163		
300.158	19.163		
400.211	19.806		
400.211	19.953		
500.263	20.397		
500.263	20.397		
600.316	20.892		
600.316	20.892		

Table C.23 Time-Averaged Velocity Data, $x_d/\lambda = 0.3$,
 $2a_d/\lambda = 0.050$, $\alpha_d v/u^* = 0.00165$

$y_d \frac{u^*}{v}$	$\frac{u_d}{u^*}$	$y_d \frac{u^*}{v}$	$\frac{u_d}{u^*}$
11.481	2.671	114.807	13.543
11.481	2.576	124.374	14.068
11.481	2.481	124.374	13.733
11.481	2.481	124.374	13.638
13.394	3.194	133.941	14.020
13.394	3.148	133.941	14.210
15.308	3.576	133.941	14.115
15.308	3.671	153.076	14.736
17.221	3.958	153.076	14.687
17.221	4.005	172.210	15.164
17.221	3.910	168.383	14.974
19.135	4.530	168.383	15.021
19.135	4.435	210.479	15.498
21.048	4.815	210.479	15.593
21.048	4.959	239.181	16.023
22.961	5.198	239.181	15.975
22.961	5.198	287.017	16.547
24.875	5.580	287.017	16.547
24.875	5.436	382.690	17.311
26.788	5.675	382.690	17.311
26.788	5.865	382.690	17.358
26.788	5.913	574.035	18.645
30.615	6.342	574.035	18.645
30.615	6.485	765.380	19.600
30.615	6.342	765.380	19.694
36.355	7.439	956.724	20.315
36.355	7.391	956.724	20.172
42.096	7.819	1148.070	20.839
42.096	7.868	1148.070	20.792
47.836	8.440	1339.414	21.267
47.836	8.345	1339.414	21.364
53.576	8.822	1530.759	21.744
53.576	8.869	1530.759	21.698
59.317	9.441	1722.104	21.983
59.317	9.633	1722.104	22.078
59.317	9.394	1722.104	22.032
65.057	10.015	1913.449	22.127
65.057	10.062	1913.449	22.078
70.798	10.349	1913.449	22.078
70.798	10.539		
76.538	10.921		
76.538	11.016		
76.538	11.254		
86.105	11.778		
86.105	11.922		
95.673	12.350		
95.673	12.494		
95.673	12.494		
105.240	12.922		
105.240	12.922		
114.807	13.448		
114.807	13.494		
114.807	13.494		
114.807	13.399		

Table C.24 Time-Averaged Velocity Data, $x_d/\lambda = 0.4$,
 $2a_d/\lambda = 0.050$, $\alpha_d v/u^* = 0.00165$

$y_d \frac{u^*}{v}$	$\frac{u_d}{u^*}$	$y_d \frac{u^*}{v}$	$\frac{u_d}{u^*}$
14.007	4.646	207.993	15.557
16.008	5.485	207.993	15.509
17.018	5.631	236.356	16.101
17.018	5.631	236.356	16.101
18.909	6.026	274.173	16.496
18.909	6.124	274.173	16.397
18.909	6.273	321.444	16.941
18.909	6.174	321.444	16.843
20.799	6.371	321.444	17.039
20.799	6.371	378.169	17.582
22.690	6.866	378.169	17.532
22.690	6.718	472.711	18.274
22.690	6.766	472.711	18.176
24.581	7.161	472.711	18.324
24.581	7.113	567.254	18.818
26.472	7.309	567.254	18.866
26.472	7.261	756.339	20.101
30.253	7.704	756.339	19.905
30.253	7.704	945.423	20.941
34.035	8.298	945.423	20.941
34.035	8.099	1134.508	21.681
34.035	8.150	1134.508	21.533
37.817	8.346	1323.592	22.275
37.817	8.396	1323.592	22.275
43.489	8.643	1323.592	22.275
43.489	8.889	1512.677	22.471
43.489	8.842	1512.677	22.423
49.162	9.136	1701.762	22.572
49.162	9.136	1890.846	22.818
56.725	9.581	1890.846	22.818
56.725	9.581		
66.180	10.027		
66.180	10.027		
75.634	10.520		
75.634	10.520		
85.088	11.161		
85.088	11.113		
94.542	11.509		
94.542	11.607		
103.996	12.052		
103.996	11.853		
113.451	12.545		
113.451	12.545		
132.359	13.237		
132.359	13.385		
151.268	14.027		
151.268	14.274		
151.268	14.125		
170.176	14.669		
170.176	14.719		
189.085	15.262		
189.085	15.262		
189.085	15.212		
189.085	15.310		

Table C.25 Time-Averaged Velocity Data, $x_d/\lambda = 0.5$,
 $2a_d/\lambda = 0.050$, $\alpha_d v/u^* = 0.00165$

$y_d \frac{u^*}{v}$	$\frac{u_d}{u^*}$	$y_d \frac{u^*}{v}$	$\frac{u_d}{u^*}$
15.214	8.006	266.245	16.743
17.116	8.247	304.280	17.237
17.116	8.346	304.280	16.989
19.017	8.988	304.280	16.941
19.017	9.039	342.315	17.385
20.919	9.285	342.315	17.187
20.919	9.237	342.315	17.337
20.919	8.940	342.315	17.139
20.919	9.039	380.350	17.682
22.821	9.138	380.350	17.631
22.821	9.087	380.350	17.484
22.821	8.889	380.350	17.583
22.821	8.889	475.438	18.324
24.723	9.433	475.438	18.373
24.723	9.237	570.526	18.966
24.723	9.237	570.526	19.015
26.625	9.582	665.613	19.510
26.625	9.433	665.613	19.459
26.625	9.532	760.701	19.954
30.428	9.778	760.701	19.904
30.428	9.877	950.876	20.744
30.428	9.976	950.876	20.792
34.231	10.225	1141.051	21.287
34.231	10.075	1141.051	21.584
38.035	10.321	1141.051	21.534
38.035	10.225	1331.226	22.128
43.740	10.618	1331.226	22.224
43.740	10.717	1521.402	22.521
49.446	10.865	1521.402	22.521
49.446	10.816	1711.577	22.867
57.053	11.162	1711.577	22.867
57.053	11.162	1901.752	23.016
66.561	11.507	1901.752	23.065
66.561	11.459		
76.070	11.804		
76.070	11.804		
95.088	12.495		
95.088	12.347		
114.105	13.137		
114.105	13.137		
133.123	13.878		
133.123	13.632		
133.123	13.927		
152.140	14.373		
152.140	14.521		
171.158	14.767		
171.158	14.965		
171.158	15.064		
190.175	15.557		
190.175	15.410		
190.175	15.410		
228.210	16.199		
228.210	16.250		
266.245	16.793		

Table C.26 Time-Averaged Velocity Data, $x_d/\lambda = 0.6$,
 $2a_d/\lambda = 0.050$, $\alpha_d v/u^* = 0.00165$

$y_d \frac{u}{v}^*$	$\frac{u_d}{u}^*$	$y_d \frac{u}{v}^*$	$\frac{u_d}{u}^*$
11.573	10.225	279.680	17.780
11.573	10.225	347.190	18.175
13.502	11.014	347.190	18.423
13.502	10.964	433.987	18.818
15.431	11.457	433.987	18.916
15.431	11.358	530.428	19.460
17.360	11.756	530.428	19.706
17.360	11.657	530.428	19.658
19.288	11.903	626.870	19.954
19.288	11.953	626.870	20.002
21.217	12.100	732.955	20.546
21.217	12.001	732.955	20.645
23.146	12.150	867.974	21.039
23.146	12.198	867.974	21.090
25.075	12.150	1060.856	21.831
25.075	12.249	1060.856	21.583
27.004	12.249	1060.856	21.733
27.004	12.198	1253.739	22.423
27.004	12.198	1253.739	22.522
27.004	12.249	1446.622	22.965
30.861	12.396	1446.622	22.965
30.861	12.446	1446.622	23.165
34.719	12.495	1639.506	23.461
34.719	12.495	1639.506	23.559
38.577	12.644	1639.506	23.509
38.577	12.644		
44.363	12.793		
44.363	12.793		
52.078	12.793		
52.078	12.892		
52.078	12.743		
52.078	12.940		
52.078	12.841		
61.722	13.236		
61.722	13.188		
75.224	13.532		
75.224	13.385		
90.655	13.927		
90.655	13.927		
108.015	14.372		
108.015	14.324		
125.374	14.817		
125.374	14.916		
144.662	15.410		
144.662	15.607		
144.662	15.559		
163.951	15.756		
163.951	15.953		
163.951	16.002		
192.883	16.495		
192.883	16.447		
231.460	17.039		
231.460	16.892		
279.680	17.730		

Table C.27 Time-Averaged Velocity Data, $x_d/\lambda = 0.7$,
 $2a_d/\lambda = 0.050$, $\alpha_d v/u^* = 0.00165$

$y_d \frac{u^*}{v}$	$\frac{u_d}{u^*}$	$y_d \frac{u^*}{v}$	$\frac{u_d}{u^*}$
13.240	12.018	283.718	19.361
13.240	12.304	283.718	18.932
13.240	12.256	283.718	19.121
15.132	13.067	283.718	19.121
15.132	13.019	378.291	19.980
15.132	13.115	378.291	19.791
15.132	13.304	378.291	19.884
17.023	13.542	472.863	20.218
17.023	13.590	472.863	20.458
18.914	13.782	472.863	20.218
18.914	13.782	567.436	20.743
20.806	13.878	567.436	20.695
20.806	14.019	756.581	21.603
22.697	14.211	756.581	21.459
22.697	14.067	945.727	22.222
26.480	14.497	945.727	22.222
26.480	14.401	1134.872	22.795
30.263	14.401	1134.872	22.795
30.263	14.593	1324.017	23.129
30.263	14.593	1324.017	23.174
34.046	14.734	1324.017	23.081
34.046	14.734	1513.162	23.556
37.829	14.878	1513.162	23.604
37.829	14.830	1513.162	23.748
41.612	15.068	1513.162	23.700
41.612	14.974	1513.162	23.700
41.612	15.068	1702.308	23.986
45.395	15.116		
45.395	15.212		
52.961	15.402		
52.961	15.356		
52.961	15.450		
66.201	15.783		
66.201	15.738		
75.658	15.927		
75.658	15.738		
75.658	15.879		
94.573	16.261		
94.573	16.165		
94.573	16.309		
113.487	16.594		
113.487	16.690		
141.859	17.120		
141.859	17.216		
141.859	17.168		
160.773	17.597		
160.773	17.691		
160.773	17.406		
189.145	18.073		
189.145	18.169		
189.145	18.169		
236.432	18.646		
236.432	18.694		
283.718	19.121		

Table C.28 Time-Averaged Velocity Data, $x_d/\lambda = 0.8$,
 $2a_d/\lambda = 0.050$, $\alpha_d v/u^* = 0.00165$

$y_d \frac{u^*}{v}$	$\frac{u_d}{u^*}$	$y_d \frac{u^*}{v}$	$\frac{u_d}{u^*}$
11. 872	14. 233	158. 290	19. 508
13. 850	14. 825	158. 290	19. 607
15. 829	15. 557	158. 290	19. 508
15. 829	15. 606	197. 862	19. 853
17. 808	15. 903	197. 862	19. 903
17. 808	15. 952	247. 328	20. 448
19. 786	16. 298	247. 328	20. 251
19. 786	16. 396	247. 328	20. 498
19. 786	16. 446	296. 793	20. 597
21. 765	16. 594	296. 793	20. 794
21. 765	16. 742	296. 793	20. 646
21. 765	16. 693	395. 725	21. 189
23. 743	16. 940	395. 725	21. 140
23. 743	16. 841	494. 656	21. 535
25. 722	17. 187	494. 656	21. 486
25. 722	17. 137	593. 587	21. 831
27. 701	17. 335	593. 587	21. 683
27. 701	17. 384	692. 518	22. 177
31. 658	17. 236	692. 518	22. 029
31. 658	17. 285	791. 449	22. 375
31. 658	17. 483	791. 449	22. 375
31. 658	17. 236	989. 312	23. 066
31. 658	17. 483	989. 312	23. 115
35. 615	17. 631	1187. 174	23. 609
35. 615	17. 384	1187. 174	23. 708
35. 615	17. 483	1385. 036	23. 560
35. 615	17. 483	1582. 899	23. 906
39. 572	17. 532	1582. 899	23. 856
39. 572	17. 582	1780. 761	24. 449
39. 572	17. 631	1780. 761	24. 301
45. 508	17. 829		
45. 508	17. 680		
45. 508	17. 730		
51. 444	17. 977		
51. 444	17. 927		
59. 359	17. 927		
59. 359	18. 076		
59. 359	17. 977		
69. 252	18. 224		
69. 252	18. 174		
79. 145	18. 224		
79. 145	18. 273		
79. 145	18. 322		
89. 038	18. 421		
89. 038	18. 569		
98. 931	18. 816		
98. 931	18. 668		
98. 931	18. 767		
118. 717	19. 014		
118. 717	19. 063		
138. 504	19. 261		
138. 504	19. 458		
138. 504	19. 063		
138. 504	19. 458		

Table C.29 Time-Averaged Velocity Data, $x_d/\lambda = 0.9$,
 $2a_d/\lambda = 0.050$, $\alpha_d v/u^* = 0.00165$

$y_d \frac{u^*}{v}$	$\frac{u_d}{u^*}$	$y_d \frac{u^*}{v}$	$\frac{u_d}{u^*}$
11.082	12.065	157.000	20.648
11.082	12.208	157.000	20.505
11.082	12.112	184.706	20.743
11.082	11.922	184.706	20.648
11.082	11.969	230.882	21.076
12.929	13.782	230.882	21.269
12.929	13.544	277.059	21.365
12.929	13.639	277.059	21.412
14.776	14.925	277.059	21.365
14.776	14.925	369.411	21.698
14.776	15.020	369.411	21.650
16.624	15.594	554.117	22.270
16.624	15.689	554.117	22.174
18.471	16.404	738.823	22.651
18.471	16.309	738.823	22.555
20.318	17.118	923.529	23.079
20.318	16.833	923.529	23.032
22.165	17.264	1108.234	23.272
22.165	17.406	1108.234	23.222
22.165	17.549	1292.940	23.558
25.859	17.978	1292.940	23.606
25.859	18.026	1292.940	23.606
29.553	18.454	1477.646	23.796
29.553	18.454	1477.646	23.749
33.247	18.788	1477.646	23.796
33.247	18.692	1477.646	23.749
36.941	18.978	1662.352	23.796
36.941	19.026	1662.352	23.606
36.941	18.978	1662.352	23.701
36.941	18.931	1662.352	23.749
44.329	19.169		
44.329	19.121		
55.412	19.457		
55.412	19.552		
55.412	19.505		
64.647	19.552		
64.647	19.600		
73.882	19.790		
73.882	19.838		
73.882	19.647		
83.118	19.886		
83.118	19.933		
83.118	19.790		
83.118	19.886		
92.353	20.171		
92.353	20.076		
92.353	19.981		
110.823	20.267		
110.823	20.124		
129.294	20.171		
129.294	20.267		
129.294	20.314		
129.294	20.267		
157.000	20.695		

Table C.30 Time-Averaged Velocity Data, $x_d/\lambda = 1.0$
 $2a_d/\lambda = 0.050$, $\alpha_d v/u^* = 0.00165$

APPENDIX D

COMPARISON OF LINEAR THEORY
WITH VELOCITY MEASUREMENTS

Calculations of the flowfield over waves of infinitesimal amplitude were performed with the linear boundary layer code of Abrams [2]. Abrams solved the Orr-Sommerfeld equation using the SUPPORT code developed at Sandia Laboratories. (See references [34] and [40].) The linear analysis predicts wave-induced velocity perturbations that are normalized with the amplitude of the wave. The perturbations were multiplied by the wave amplitude in order to compare the infinitesimal wave results with the finite amplitude wave measurements. The calculations were made with three turbulence models: a quasilaminar model, Model C^{*}, and Model D^{*}.

The predicted amplitudes and phases of the wave-induced velocity responses for $2a_d/\lambda = 0.0125$ and $\alpha_d \nu/u^* = 0.008$ (equivalent to $Re_b = 6400$) are shown in Figures D.1 and D.2 respectively. Amplitude and phase results for the wave with $2a_d/\lambda = 0.05$ and $\alpha_d \nu/u^* = 0.00165$ (equivalent to $Re_b = 38,8000$) are shown in Figures D.3 and D.4.

Only semi-quantitative comparisons with the data are appropriate since the linear calculations are for a boundary layer rather than a channel flow and are strictly valid only for waves of infinitesimal amplitude. The purpose of the above calculations was to show the relative amplitude and phase differences between the three turbulence models at the flow conditions of the data.

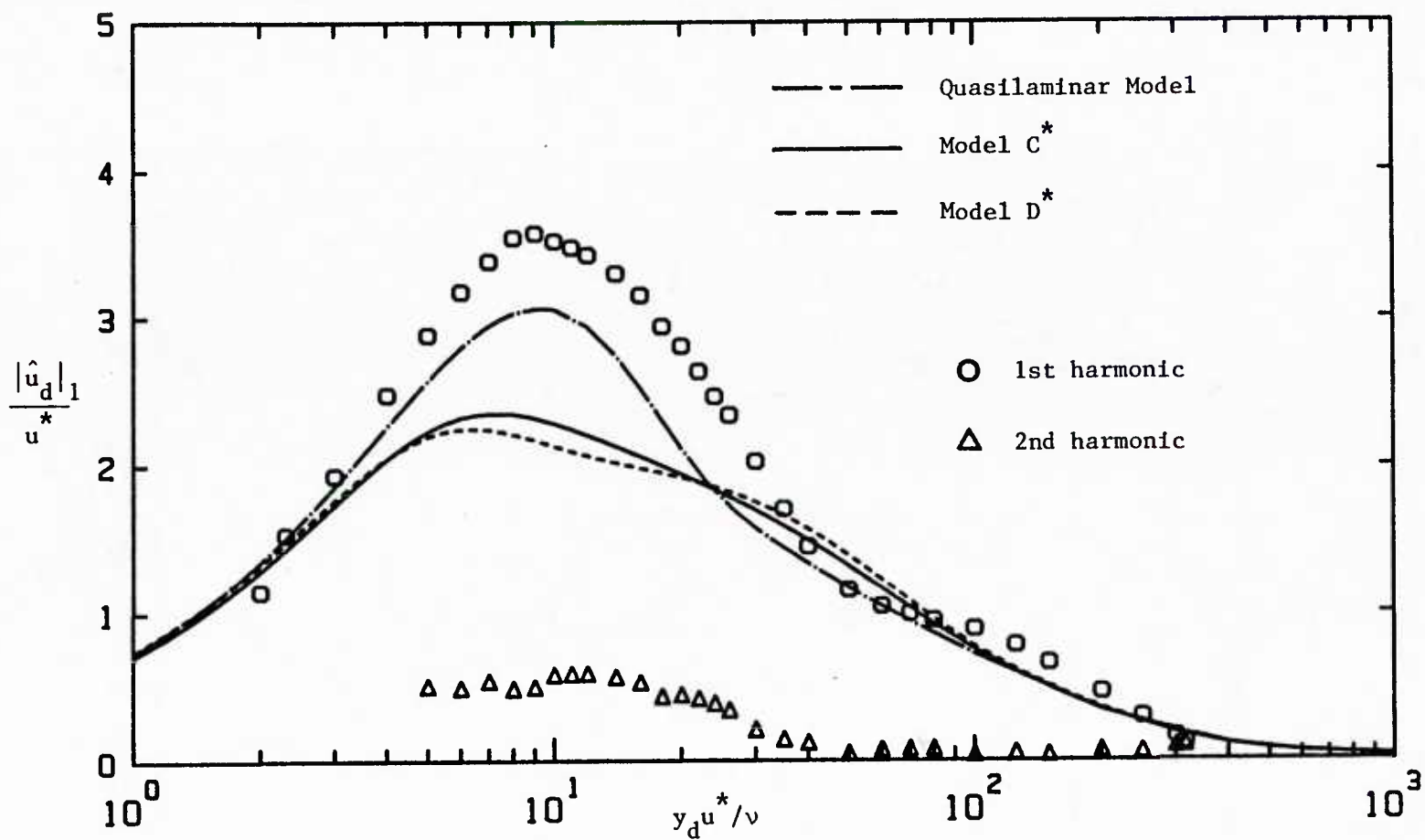


Figure D.1 Comparison of Linear Theory with Measurements,
 $\frac{|\hat{u}_d|_1}{u^*}$ ($2a_d/\lambda = 0.03125$, $\alpha_d \nu / u^* = 0.008$)

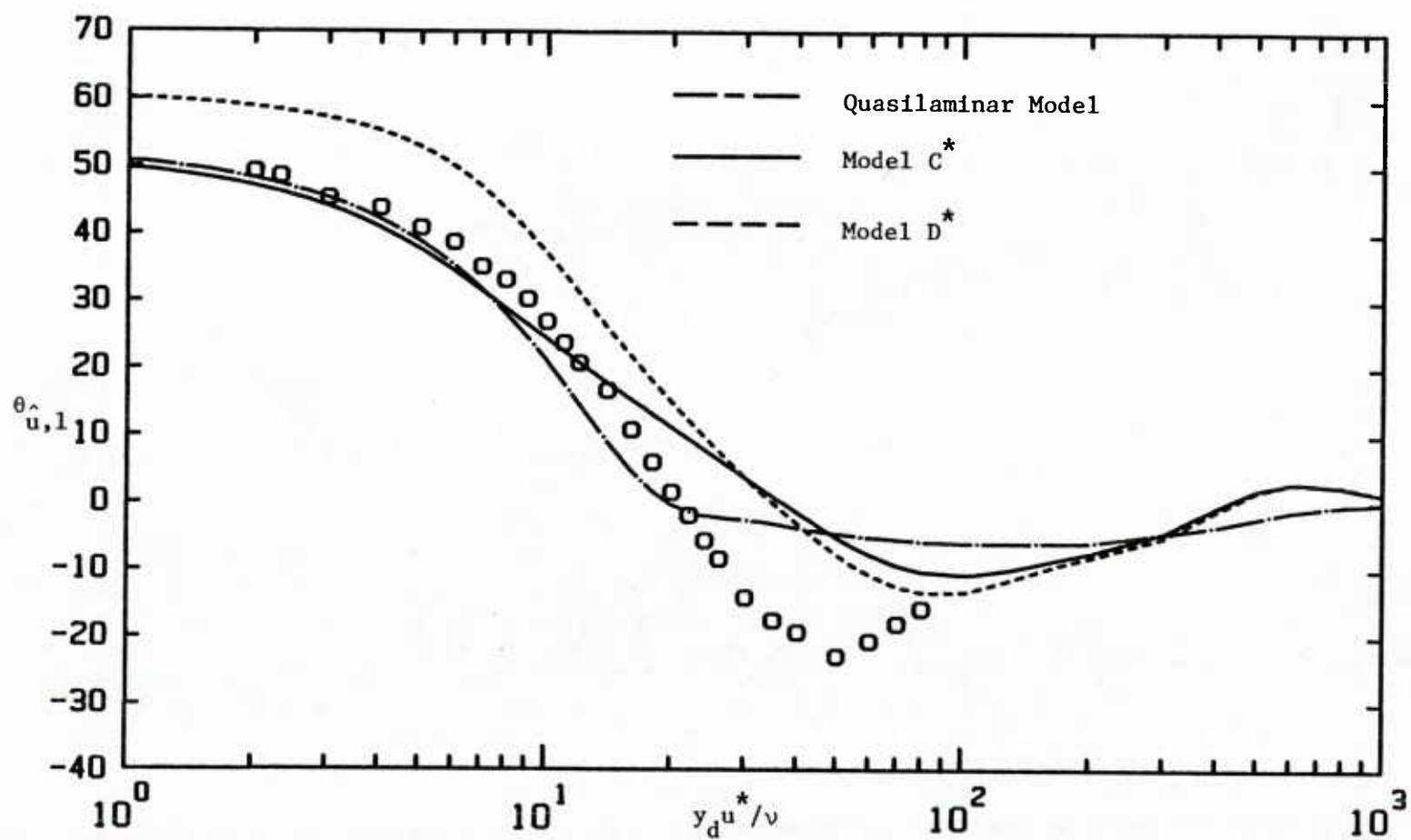


Figure D.2 Comparison of Linear Theory with Measurements, $\theta_{u,1}$
 $(2a_d/\lambda = 0.03125, \alpha_d \nu/u^* = 0.008)$

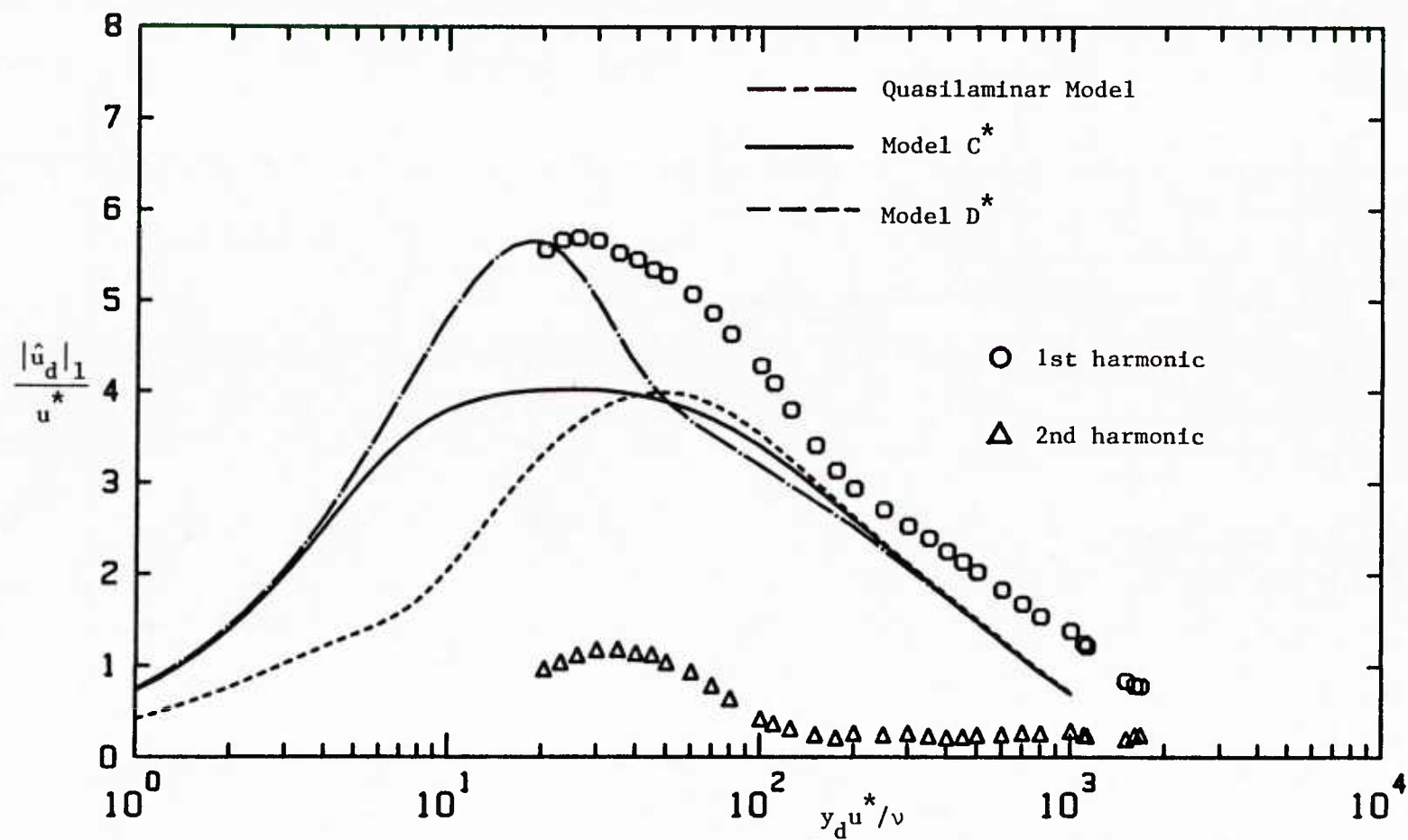


Figure D.3 Comparison of Linear Theory with Measurements, $|u_d|_1$
 $(2a_d/\lambda = 0.05, \alpha_d \nu / u^* = 0.00165)$

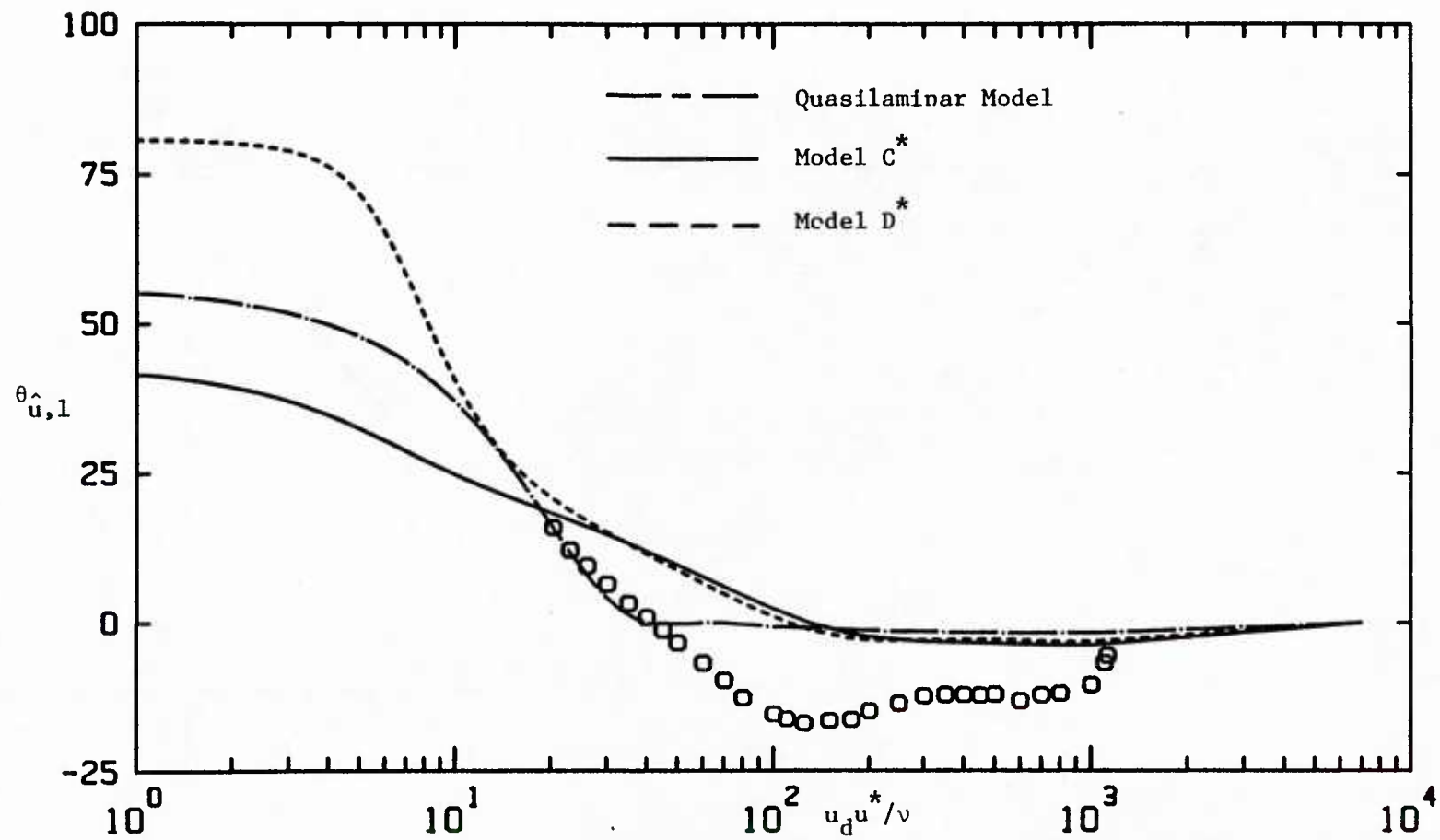


Figure D.4 Comparison of Linear Theory with Measurements, $\theta_{u,1}$
 ($2a_d/\lambda = 0.05$, $\alpha_d \nu/u^* = 0.00165$)

Professor R. E. Kaplan
Department of Aero Engineering
University of Southern California
University Park
Los Angeles, CA 90007

Dr. Phillip S. Klebanoff
National Bureau of Standards
Mechanics Section
Washington, DC 20234

Professor Louis Landweber
The University of Iowa
Institute of Hydraulic Research
Iowa City, IA 52242

Professor L. Gary Leal
California Institute of Technology
Division of Chemistry and
Chemical Engineering
Pasadena, CA 91125

Library of Congress
Science and Technology Division
Washington, DC 20540

Professor H. W. Liepmann
California Institute of Technology
Graduate Aeronautical Laboratories
Pasadena, CA 91125

Lorenz G. Straub Library
University of Minnesota
St. Anthony Falls Hydraulic Laboratory
Minneapolis, MN 55414

Professor John L. Lumley
Cornell University
Sibley School of Mechanical
and Aerospace Engineering
Ithaca, NY 14853

Donald McEligot
Gould Defense Systems Inc.
1 Corporate Park
Middletown, RI 02840

Dr. D. K. McLaughlin
Dynamics Technology Inc.
21311 Hawthorne Blvd., Suite 200
Torrance, CA 90503

Dr. Jim McMichael
Air Force Office of Scientific
Research/NA
Building 410
Bolling AFB
Washington, DC 20332

Dr. Arthur B. Metzner
University of Delaware
Department of Chemical Engineering
Newark, DE 19711

Professor Richard W. Miksad
The University of Texas at Austin
Department of Civil Engineering
Austin, TX 78712

NASA Scientific and Technical
Information Facility
P. O. Box 8757
Baltimore/Washington International
Airport
Maryland 21240

Professor Paul M. Naghdi
University of California
Department of Mechanical Engineering
Berkeley, CA 94720

Technical Library
Naval Coastal System Laboratory
Panama City, FL 32401

Technical Library
Naval Missile Center
Point Mugu, CA 93041

Technical Library
Naval Ocean Systems Center
San Diego, CA 92151

Library
Naval Postgraduate School
Monterey, CA 93940

Library
Naval Sea Systems Command A
Code 09GS
Washington, DC 20362

Mr. Thomas E. Peirce
Naval Sea Systems Command B
Code 63R21
Washington, DC 20362

Librarian
Naval Surface Weapons Center
White Oak Laboratory
Silver Spring, MD 20910

Technical Library
Naval Underwater Systems Center
Newport, RI 02840

Library
Naval Weapons Center
China Lake, CA 93555

Office of Naval Research
Code 1132F
800 N. Quincy Street
Arlington, VA 22217 3 copies

Director
Office of Naval Research
Eastern/Central Regional Office
Building 114, Section D
666 Summer Street
Boston, MA 02210

Director
Office of Naval Research
Western Regional Office
1030 E. Green Street
Pasadena, CA 91101

Professor T. Francis Ogilvie
The University of Michigan
Department of Naval Architecture
and Marine Engineering
Ann Arbor, MI 48109

Professor S. I. Pai
University of Maryland
Institute of Fluid Dynamics
and Applied Mathematics
College Park, MD 20742

Professor Eli Reshotko
Case Western Reserve University
Department of Mechanical and
Aerospace Engineering
Cleveland, OH 44106

Professor A. Roshko
California Institute of Technology
Graduate Aeronautical Laboratories
Pasadena, CA 91125

The Society of Naval Architects and
Marine Engineers
One World Trade Center, Suite 1369
New York, NY 10048

Professor W. G. Tiederman
School of Mechanical Engineering
Purdue University
West Lafayette, IN 47907

Professor P. S. Virk
Massachusetts Institute of Technology
Department of Chemical Engineering
Cambridge, MA 02139

Professor John V. Wehausen
University of California
Department of Naval Architecture
Berkeley, CA 94720

Professor W. W. Willmarth
The University of Michigan
Department of Aerospace Engineering
Ann Arbor, MI 48109

Professor Theodore Y. Wu
California Institute of Technology
Engineering Science Department
Pasadena, CA 91125

Professor C. -S. Yih
The University of Michigan
Department of Engineering Mechanics
Ann Arbor, MI 48109

Library
Naval Weapons Center
China Lake, CA 93555

Office of Naval Research
Code 1132F
800 N. Quincy Street
Arlington, VA 22217 3 copies

Director
Office of Naval Research
Eastern/Central Regional Office
Building 114, Section D
666 Summer Street
Boston, MA 02210

Director
Office of Naval Research
Western Regional Office
1030 E. Green Street
Pasadena, CA 91101

Professor T. Francis Ogilvie
The University of Michigan
Department of Naval Architecture
and Marine Engineering
Ann Arbor, MI 48109

Professor S. I. Pai
University of Maryland
Institute of Fluid Dynamics
and Applied Mathematics
College Park, MD 20742

Professor Eli Reshotko
Case Western Reserve University
Department of Mechanical and
Aerospace Engineering
Cleveland, OH 44106

Professor A. Roshko
California Institute of Technology
Graduate Aeronautical Laboratories
Pasadena, CA 91125

The Society of Naval Architects and
Marine Engineers
One World Trade Center, Suite 1369
New York, NY 10048

Professor W. G. Tiederman
School of Mechanical Engineering
Purdue University
West Lafayette, IN 47907

Library
U.S. Naval Academy
Annapolis, MD 21402

Professor P. S. Virk
Massachusetts Institute of Technology
Department of Chemical Engineering
Cambridge, MA 02139

Professor John V. Wehausen
University of California
Department of Naval Architecture
Berkeley, CA 94720

Professor W. W. Willmarth
The University of Michigan
Department of Aerospace Engineering
Ann Arbor, MI 48109

Professor Theodore Y. Wu
California Institute of Technology
Engineering Science Department
Pasadena, CA 91125

Professor C. -S. Yih
The University of Michigan
Department of Engineering Mechanics
Ann Arbor, MI 48109

U224339